ADVERTIMENT. La consulta d'aquesta tesi queda condicionada a l'acceptació de les següents condicions d'ús: La difusió d'aquesta tesi per mitjà del servei TDX (www.tesisenxarxa.net) ha estat autoritzada pels titulars dels drets de propietat intel·lectual únicament per a usos privats emmarcats en activitats d'investigació i docència. No s'autoritza la seva reproducció amb finalitats de lucre ni la seva difusió i posada a disposició des d'un lloc aliè al servei TDX. No s'autoritza la presentació del seu contingut en una finestra o marc aliè a TDX (framing). Aquesta reserva de drets afecta tant al resum de presentació de la tesi com als seus continguts. En la utilització o cita de parts de la tesi és obligat indicar el nom de la persona autora.

ADVERTENCIA. La consulta de esta tesis queda condicionada a la aceptación de las siguientes condiciones de uso: La difusión de esta tesis por medio del servicio TDR (www.tesisenred.net) ha sido autorizada por los titulares de los derechos de propiedad intelectual únicamente para usos privados enmarcados en actividades de investigación y docencia. No se autoriza su reproducción con finalidades de lucro ni su difusión y puesta a disposición desde un sitio ajeno al servicio TDR. No se autoriza la presentación de su contenido en una ventana o marco ajeno a TDR (framing). Esta reserva de derechos afecta tanto al resumen de presentación de la tesis como a sus contenidos. En la utilización o cita de partes de la tesis es obligado indicar el nombre de la persona autora.

WARNING. On having consulted this thesis you're accepting the following use conditions: Spreading this thesis by the TDX (www.tesisenxarxa.net) service has been authorized by the titular of the intellectual property rights only for private uses placed in investigation and teaching activities. Reproduction with lucrative aims is not authorized neither its spreading and availability from a site foreign to the TDX service. Introducing its content in a window or frame foreign to the TDX service is not authorized (framing). This rights affect to the presentation summary of the thesis as well as to its contents. In the using or citation of parts of the thesis it's obliged to indicate the name of the author

Exploiting Nonlinearity and Noise in Optical Tweezers and Semiconductor Lasers:

from Resonant Damping to Stochastic Logic Gates and Extreme Pulses

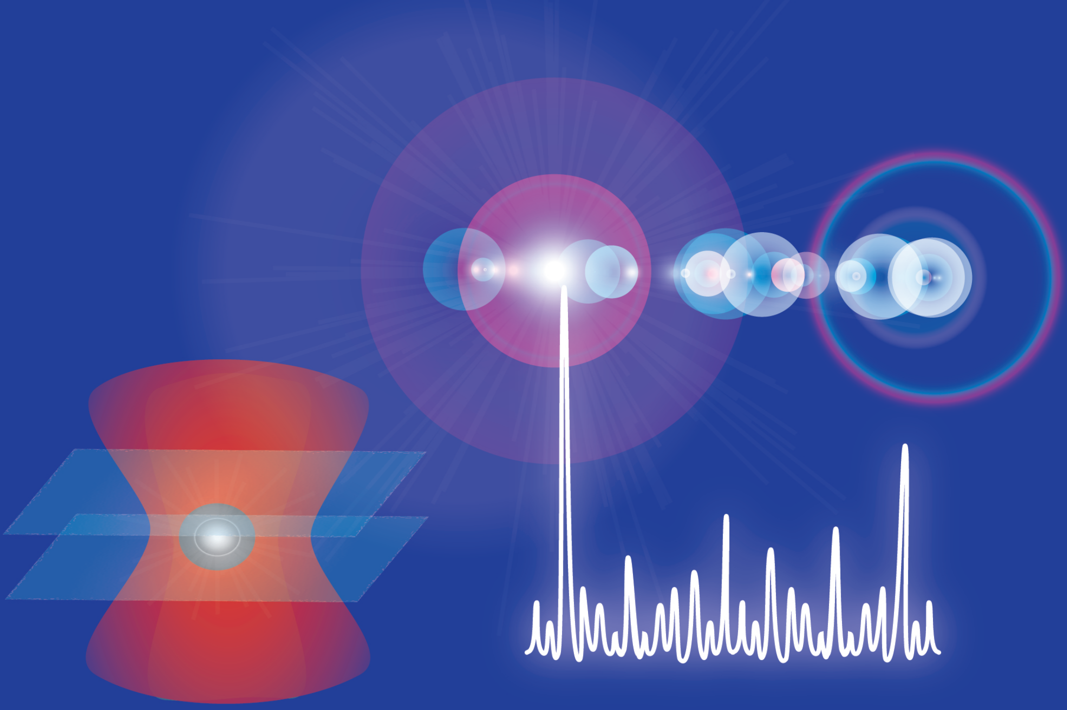

Sandro Perrone
sandro.perrone@gmail.com

Doctoral Thesis
February 2014

Exploiting nonlinearity and noise in optical tweezers and semiconductor lasers:

from resonant damping to stochastic logic gates

and extreme pulses.

Sandro Perrone
Memòria presentada per a optar al grau de doctor per la
Universitat Politècnica de Catalunya

Directors
Prof. Dr. Cristina Masoller
Prof. Dr. Ramon Vilaseca

Departamento de Fisíca i Enginyeria Nuclear
Universitat Politecnica de Catalunya
Nonlinear Dynamics, Nonlinear Optics and Lasers Group.

Terrassa 2014

To my family and all those loving me

Acknowledgements

First of all I would like to acknowledge continued support from my supervisors and PhD directors: Professors Cristina Masoller and Ramon Vilaseca.

Special thanks to Cristina, who invested her time, money resources and energies to training me and betting on my skills and my talent. She gave me always the way to aim the research, making me more responsible and autonomous and, giving me the possibility to express my creativity and my critic point of view. I really appreciated the brainstorming with her and other colleagues, in which we could deal with the more philosophical research sides, which helped us to assemble the big puzzle, and proposing innovative solutions. Her willingness to glimpse and emphasize my quality have been of inestimable value. She has been and always will be one of the most important references for me, source of knowledge and new ideas. Thank you!

Ramon to always worried about me and my research giving me the most useful advices. I have to say that without him perhaps I would not stay here writing these lines. He has been incredibly patient during all the time for the redaction of this manuscript, where I did countless small mistakes that I could not to note for my inexperience. He helped me very much with important suggestions, and useful discussions which lead me to see some physical situations from other perspectives. In some controversial situations his wisdom has directed me along the right path. Thank you!

A first part of this thesis has been devoted to an experimental study of stochastic effects by means optical traps. For all this part, without any doubt, my guide and director has been Professor Dmitri Petrov. With his infinite patience he taught me how to deal with an experimental study. Looking him at work in the laboratory, giving life to an optical setup has been very inspiring. He gave me the idea on how the artists during the Renaissance period could work. I have never met anyone like him with a great desire to teach and learn at the same time, compete and find out. He gave me all the tools to make research, and his constant presence has been crucial in the development and understanding of the physical phenomena studied. Thank you!

I thank all the confidence they had in me since the first day and continually demonstrated to me. I always tried to deserve all this with effort and dedication.

Special thanks also to professors Carme Torrent, Kestutis Staliunas, Crina Cojocaru, Toni Pons, Simone Pigolotti for the fruitful scientific discussions, which have been strong stimulus to bring new insights into the research fields, and also for the confidence and cool environment that they have been able to establish.

I would like to say thanks to my colleagues and friends: Andrés Aragoneses, Giulio Tirabassi, Ignacio Deza, Dani Malagarriga, Shubham Kumar, Lina Maigyté, Ricard Menchon, Juan José Cardenas, Cristian Fernandez Oto, Thomas Michalski, Petya Petkova, Yu-Chieh Cheng, Damiano Rotondo, Nikhil Pradeep Kumar, Safae BenDali, Bingxia Wang, Heather Taterka. Thanks to all of you for the useful scientific discussions and for the funny and cool moments past together.

Thanks to my friends: Enrico Zecca and his wife Ada, Gianpiero Galati, Maurizio de Sensi, Rita Domenech, Verena Markert, Niels Agatz and Stefania Urbani, that despite the long distance we still stay in contact, and when I go back from time to time to Italy we enjoy good moments. Thank you friends!

Thanks to my brother Francesco and his wife Alina Dziergwa, who helped me all moments that I was in difficulty, and for giving me the great joy of becoming uncle with the small beautiful Alessandra. Thank you!

Finally, but the most important, a special Thanks to my parents Cosimo Perrone and Osilda Maritati, for their constant support during the worse moment and and for having lean on each decision I made. Thank you to be the very special parents that you are!

Terrassa, 13 December 2013

"To predict the behavior of ordinary people in advance, you only have to assume that they will always try to escape a disagreeable situation with the smallest possible expenditure of intelligence."

- Friedrich Nietzsche

"An experiment is a question which science poses to Nature and a measurement is the recording of Nature's answer."

- Max Planck, Scientific Autobiography and Other Papers

"An expert is a person who has made all the mistakes that can be made in a very narrow field."

- Niels Bohr

Contents

List of Figures **9**

List of Tables **27**

Glossary **29**

1 Introduction to stochastic effects in nonlinear systems **37**

1.1 Introduction 37

1.2 General overview about stochastic phenomena 37

1.3 Stochastic Resonance 39

1.4 Mechanism of Stochastic Resonance 42

1.4.1 Langevin equation 45

1.5 Coherence Resonance 49

1.5.1 Mechanism of Coherence Resonance 50

1.6 Logical Stochastic Resonance 53

1.6.1 Mechanism of Logical Stochastic Resonance . . . 54

2 Resonance phenomena in noisy systems by optical trap technique **57**

2.1 Introduction 57
  2.2 Experimental techniques 58
    2.2.1 Optical tweezers 58
      2.2.1.1 Ray optics regime 59
      2.2.1.2 Rayleigh regime 62
      2.2.1.3 Optimization of trapping force 63
    2.2.2 Force detection and calibration 65
      2.2.2.1 Brownian motion and power spectral density 67
      2.2.2.2 Conversion to physical units 69
    2.2.3 The Photonic Force Microscope 71
      2.2.3.1 Trapping optics 72
      2.2.3.2 Imaging optics 73
      2.2.3.3 Detection optics 73
      2.2.3.4 Acousto-Optic Deflection 74
2.3 Introduction to the experimental theoretical outcomes . . 76
    2.3.1 Optical setup 77
2.4 Stochastic Resonant Damping: theory and experiments . 79
    2.4.1 Introduction 79
    2.4.2 Mathematical Model 80
    2.4.3 Experimental Verification 85
    2.4.4 Experimental Setup 85
      2.4.4.1 Colored Gaussian noise generation . . . 87
      2.4.4.2 Data analysis 87
    2.4.5 Experimental Results 88
    2.4.6 Conclusions 90
2.5 Stochastic Resonant Damping versus Stochastic Resonance 92
    2.5.1 Theoretical model and simulations of Stochastic Resonance in a double well system 92
    2.5.2 SR in a double well potential moved harmonically 94
    2.5.3 Experimental Results and discussion 96

2.6 Maximum in the Signal-to-Noise ratio in a monostable system . . . 99
  2.6.1 Mathematical description of a particle held in an oscillating cuartic optical potential . . . 101
  2.6.2 Experimental procedures and Data analysis . . . 101
  2.6.3 Experimental outcomes . . . 102
2.7 10-fold increasing detection range in position sensing for photonic force microscope . . . 105
  2.7.1 Introduction . . . 105
  2.7.2 Experimental procedures and Results . . . 107
  2.7.3 Final comments . . . 110

3 Semiconductor Laser with Optical Injection 113
3.1 Introduction . . . 113
  3.1.1 Historic overview and types of semiconductor laser 114
    3.1.1.1 Basic physical principles of laser . . . 114
    3.1.1.2 Vertical Cavity Surface Emitting Laser VCSEL . . . 118
    3.1.1.3 Advancement of VCSEL . . . 118
3.2 Semiconductor Laser with Optical Injection . . . 120
3.3 Rate equations and steady state solutions . . . 122
  3.3.1 Stability analysis . . . 124
  3.3.2 Injection locking conditions . . . 126
3.4 Nonlinear dynamics induced by optical injection . . . 129
  3.4.1 Experimental mapping technique . . . 129
  3.4.2 Optical injection induced dynamics . . . 131
3.5 Influence of side mode excitation . . . 137
3.6 Enhancement of modulation bandwidth by strong optical injection . . . 138
  3.6.1 Origin of modulation bandwidth enhancement . . 140
3.7 Frequency Chirping suppression by strong optical injection 143

3.8 High frequency chaotic oscillation by strong optical injection 146

4 All optical implementation of Stochastic Logic Gate 147

4.1 Theoretical model for VCSELs 147

4.1.1 The spin-flip model 149

4.1.2 Steady state solutions of the Spin-Flip Model . . 153

4.2 Polarization switching and bistability 156

4.3 Numerical results for all optical implementation of Stochastic Logic Gate 161

4.3.1 Introduction 161

4.3.2 Spin-Flip Model for optically injected VCSELs . . 163

4.3.3 Encoding scheme of the logical response 164

4.3.4 Results 166

4.3.5 Conclusions 173

5 Rogue Waves in a semiconductor laser with optical injection and current modulation 175

5.1 Introduction 175

5.2 Rate equation model for a seminconductor laser with optical injection and current modulation 179

5.3 Statistical description 180

5.4 Numerical Results 182

5.4.1 Relaxation oscillation frequency of the free running laser 182

5.4.2 Dynamic regimes with optical injection and without current modulation 183

5.4.3 Dynamics at strong current modulation 187

5.4.4 RWs maps in the parameter space ($\Delta\nu$, μ), without modulation 195

5.4.5 RWs maps in the parameter space (f_{mod} A_{mod}) . . 197

5.5 Conclusions 202

6 Conclusions: Summary of results and future work 205
6.1 Summary of results 206
6.2 Perspectives for future work 209

A Brownian motion 211
A.1 Diffusion relation 211
A.2 Diffusion and mobility 213

B Numerical integration techniques 215

References
At the end of each reference we indicate the pages where it is cited in this Memory. 219

List of Figures

1.1 double well potential. The trace represent the jiggling trajectory of the particle in time. Below: description diagram of a noisy bistable system with a potential modulation . 43

1.2 Residence time distributions N(T) for the symmetric bistable system. Reproduced from (1) 44

1.3 Characterization of stochastic resonance. (a) A typical power spectral density ($S\nu$) vs frequency n for the case of the quartic double-well potential. (b) Strength of the first delta spike, Eq. 1.14 , and the SNR, Eq. 1.15 , vs D (in units of Δ V). Reported from (2) 48

1.4 The dynamics of the Fitz HughNagumo system (Eqs. 1.16-1.17) for a=1.05, $\epsilon = 0.01$, and different noise amplitudes: (c) D= 0.02, (b) D= 0.07, and (a) D = 0.25. The mean durations of pulses are 7, 4, and 3.5, respectively.(d)-(e)-(f) are the respective autocorrelation function of (a)-(b)-(c). The activation and the excursion times for one pulse are depicted. Reproduced from (3) 52

1.5 Correlation time t_c (solid line) and the noise-to-signal ratio R (Eq. 1.20, dashed line) vs noise amplitude for the Fitz HughNagumo system.Reproduced from (3) 52

1.6 Schematic of a noisy nonlinear system forced by an input signal yielding a logic output. 54

1.7 (a) Response in quadrature of the resonator as a function of the driving frequency for different values of the drive amplitude. (b) Response in quadrature of the resonator as a function of the drive amplitude for a fixed frequency (3.158 MHz) in the bistable regime. (c) Micrograph of the resonator and experimental setup. Reported from (4) . . 55

2.1 **Trapping regimes**. Trapping regimes and typical objects that are trapped in optical manipulation experiments. . . 59

2.2 Principle of optical trapping of a microsphere. [a] A trapped bead in the laser focus, slightly displaced in a direction perpendicular to that of the laser light. Incoming rays with different intensities (arrows) are refracted by the transparent bead. Because of momentum conservation, the direction of the force on the bead is opposite to the momentum change of the photon field. The net force is composed of the inward gradient force F_{grad} and an upward component. [b] Forces acting on a bead positioned slightly above the laser focus. Due to refraction of high incident angle rays, the net force on the bead is in the downward direction. This force can overcome the upward pointing scattering force F_{scat} (not shown). 60

2.3 **Forces in the Rayleigh.** Scattering and gradient forces in the Rayleigh regime. 62

2.4 Objective NA and overfilling. [a] When the trapping laser does not (over)fill the back aperture of the objective, the highest-angle rays are smaller than Θ_{max} and thus the high NA is not fully exploited. [b] The scattering force is more efficiently counteracted by an expanded beam. The parameters used in Eq. 2.6 are depicted. 64

2.5 Back-focal-plane interferometry. Configuration for the detection of lateral displacement of a trapped sphere from the trap center. The condensers Back Focal Plane (BFP) is imaged onto a Quadrant Photo Detector (QPD). Reading out the differential signals $(I_1 + I_3) - (I_2 + I_4)$ and $(I_1+I_2)-(I_3+I_4)$ (both normalized by the total intensity), displacement signals for x and y are obtained, respectively. 65

2.6 Intensity distribution signals D_x and D_y constructed from the light intensities I_j on the four individual segments of a quadrant photodiode. 66

2.7 Detector response for $\omega_0 = 0.53\ \mu m$ and d = 0.5 μm. Reported from (5) 66

2.8 Power spectrum plus fit. The 'noise' is in fact the Brownian motion of the bead in the trap. The corner frequency f_0 of this spectrum is $\sim$ 1000 Hz, taken with a 2.1 μm polystyrene bead. This yields a trap stiffness of 125 pNμm^{-1} 68

2.9 **Basic PFM setup.** The main components are: laser, high-NA objective (O), sample, quadrant photo-detector (QPD), and CCD camera. Other optical components: telescope (L_1, L_2), Dichroic Mirror DM, mirror (M), and illuminating light source (LED). 71

2.10 The trapping optics is constituted by two lenses which expand the laser beam to overfill an high-NA objective (O), which focused create the optical trap inside the liquid solution where the object to be trapped is suspended. Besides, a dichroic mirror (Dichroic Mirror (DM)) is used to reflect the Near Infra-Red (NIR) beam and allowing to pass the visible light direct to the Charge-Coupled Device (CCD) camera and the detection beam. 72

2.11 **Imaging optics.** An objective C (usually called condenser) focuses a white or green light (LED) on the sample. The light is then recollected by a second objective (O) and projected onto a CCD camera connected to a monitor. 73

2.12 **Detection optics.** A QPD, connected to an acquisition system, receives the forward scattered laser light by a trapped particle, after it is collimated by an objective (O) and collected by a condenser C. 73

2.13 Light scattering off the wavefronts of a plane acoustic wave traveling through a crystal. The figure shows the case for Bragg diffraction, where the incidence angle should be the Bragg angle θ_B given by equation 2.18 The total beam deviation equals $2\theta_B$ 74

2.14 Experimental setup: O and C are objective and condenser, respectively; DM_1, DM_2, and DM_3 are dichroic mirrors; M is mirror; AOM/D is acousto-optic modulator/ deflector; L_1 and L_2 are lenses of an optical system which conjugates the output plane of the AOM/D and the input plane of the objective O; PH is a pinhole; 77

2.15 Output system variance σ_x^2 as a function of the confinement effort C ($D = 1$, $A = 1$) for harmonic (a) and colored Gaussian (b) parametric noise for various values of the frequency f_0: from bottom to top $f_0 = 100, 31, 10, 3, 1$ (thick curve), $0.3, 0.1, 0.03, 0.01 Hz$. The thick line indicates the σ_x^2 minima. The shaded area represent the range of accessible output variance for a given value of the confinement effort. The additional axis shows the system intrinsic noise cutoff frequency f_c. Insets: a typical example of x_0 in time and frequency domain ($f_0 = 1$). 84

2.16 Intrinsic system output (gray filled area) and system output in the presence of a sinusoidal modulation (f_0 =1, D=1, A=1) (red dashed curve) for three states of the system, indicated by dots in Fig. 2.15(a) for the modulation frequency f_0=1Hz: (i) C=0.4 (f_c=0.064 Hz), (ii) C=2 (f_c=0.32 Hz) corresponding to the absolute variance minimum, and (iii) C=10 (f_c=1.6 Hz). The output variance always exceeds the intrinsic variance. 84

2.17 (a) Experimental and theoretical σ_x^2 as a function of the laser power in the presence of harmonic modulation of the trap center. From the bottom to the top the various sets of values correspond to $f_0 = 5,\ 50,\ 500,\ 5000,\ Hz$. The bar represent one standard deviation. The solid lines represent the theoretical prediction for the experimental parameters ($k = 0.4\,pN/\mu m\, mW \times$ TrappingPower $[mW]$, $\gamma = 1.1 \cdot 10^{-8}\,Ns/m$, $A = 100\,nm$). The disagreement between experimental data and theoretical results for right end of the $5\,Hz$ dataset is observed because for such values of the confinement effort and intrinsic noise frequency the trapping potential is not harmonic anymore. (b) Data for the non-modulated direction y. The two additional axes show the value of the confinement effort and the corresponding cutoff frequency of the intrinsic noise. 88

2.18 Experimental σ_x^2 as a function of the noise amplitude. Various sets of values are presented for $A = 55,\ 70,\ 85\,nm$. The bars represent one standard deviation. The solid line represent the theoretical prediction for the experimental parameters ($k = 0.7\,pN/\mu m\, mW \times$ TrappingPower $[mW]$, $\gamma = 1.9 \cdot 10^{-8}\,Ns/m$). The two additional axes show the value of the confinement effort and the corresponding cutoff frequency of the intrinsic noise. 91

2.19 Experimental and theoretical σ_x^2 as a function of the trapping power obtained with colored Gaussian forcing of the equilibrium position. Various sets of values are presented for $f_0 = 5,\ 500,\ 50,\ 5,\ Hz$. The bars represent one standard deviation. The solid line represent the theoretical prediction for the experimental parameters ($k = 0.7\,pN/\mu m\,mW \times$ TrappingPower $[mW]$, $\gamma = 1.9 \cdot 10^{-8}\,Ns/m$, $A = 70\,nm$). The disagreement between experimental data and theoretical results for right end of the $5\,Hz$ dataset is observed because for such values of the confinement effort and intrinsic noise frequency the trapping potential is not harmonic anymore. The two additional axes show the value of the confinement effort and the corresponding cutoff frequency of the intrinsic noise. 91

2.20 Panel (a) displays the numerical results of the Langevin equation for a monostable system described from the equation 2.20, while panel (b) shows the numerical results of the system from the equations set 2.28. In both situations, the center trap is modulated sinusoidally. The blue, green, red, blue-light and magenta curves (from the highest variance values to the lowest) represent modulation frequencies 1, 3, 5, 10, 20 Hz. 93

2.21 Concept of the double well optical landscape. The particle is jiggling from one well to the other. Dashed line indicate the movement of the center of 100 nm. The distance from the minimums is fixed at 240 nm. The sides graphs show the shapes changes due to the stiffness. 94

2.22 Power spectral density and traces of features SR. The particle is jiggling in a double well potential where the center trap is modulated sinusoidally at 0.2 Hz for three different powers (from the top to the bottom 3, 7, 12 pN/nm). . . 94

2.23 SNR of a double well optical potential versus the power stiffness “K”, at three different frequency. Blue 200 Hz, red 20 Hz, black 0.2 Hz. 95

2.24 Experimental evidence of Stochastic Resonance vs Stochastic Resonant Damping: (a) Signal to Noise Ratio (SNR) as a function of the trap stiffness for a single well system.(b) SNR as a function of K for a double well potential. (c) System output variance σ_x^2 for a single well. (d) System variance as a function of the trap stiffness for a double well potential. In each subplot, different curves are plotted for different values of the frequency f_0 of the external modulated forcing (blue 200 Hz, red 20 Hz, black 0.2 Hz). 98

2.25 (a) Potentials $V_1(x)$, $V_2(x)$, $V_3(x)$ for the maximum value of $h_t(d)$ (solid line) and for the minimum value (dashed line).(b) Behavior of the SNR for the three potentials.(c) Power spectrum corresponding to $V_1(x)$ for noise strength D=0.1 and D=1000). Reported from (6) 100

2.26 Potential energy of the ferromagnetic particle as a function of θ for the maximum value of $h_t(d)$ (solid line) and for the minimum (dashed line). (b) SNR for the previous values of the parameters obtained through computer simulations. (c) Power spectrum for noise strength D= 0.05, 0.15, 0.35, and 1. Reported from (6) 100

2.27 Experimental realization of an optical x^4 potential by an Opto Acoustic Deflector/Modulator (AOD). 102

2.28 Power Spectral Densities for three amplitude sinusoidal modulation (from the top to the bottom A=100,240,650 nm) 104

2.29 (a) SNR as a function of the modulation amplitude at 20 Hz frequency modulation. (b) SNR as a function of the modulation strength for three different frequencies (2, 20, 200 Hz). 104

2.30 Concept of the detection. We record the QPD signals V_x and V_z while we scan the probe along the direction x through the detection beam. The QPD gives three signals that are proportional to the probe position in the trap: Vx=$(VI + VIII) - (VII + VIV)$, $Vy = (VI + V_{II}) - (V_{III} + V_{IV})$, and $V_z = V_I + V_{II} + V_{III} + V_{IV}$, where VI, V_{II}, V_{III}, and V_{IV} are the signals associated to the four quadrants of the QPD. 106

2.31 Experimental data. [(a)(c)] V_x (solid line) and V_z (dash line) signals obtained by moving the probe sinusoidally. [(d)(f)] Averaged signals $\langle V_x \rangle$ (solid line) and $\langle V_z \rangle$ (dash line) in function of the probe position x. The dotted lines represent the signals of the photo-detector if its response would be linear. The amplitude of the sinusoidal movement of the trap center is [(a) and (d)] A=18 nm, [(b) and (e)] A=180 nm, and [(c) and (f)] A=720 nm. 108

2.32 Calibration curve (solid line) $\langle V_x \rangle(x_{trap})$, $\langle V_z \rangle(x_{trap})$ parameterized on the trap position x_{trap} (dots). 109

2.33 Variances of $\langle V_x \rangle$ and $\langle V_z \rangle$ depend on the position of the trap. 109

2.34 Calculated probe position x^* (gray line) for the signals presented in 2.31. The known trap center position (black line) is shown for comparison. The amplitude of the sinusoidal movement of the trap center are (a) A_1 =18 nm, (b) A_2=180 nm, and (c) A_3=720 nm. 110

3.1 Schematic edge-emitting semiconductor laser diode. Lasing occurs in the plane of the junction. 116

3.2 Schematic heterostructure (left) and homostructure (right) Semiconductor Laser (SCL). In heterostructure laser a layer of low bandgap materials (gray) is sandwiched between two layers of high bandgap material (white). Homostructure is a p-n union of the same type semiconductor materials. 117

3.3 Schematic of VCSEL. 118

3.4 Typical setup of a CW master laser and a follower laser coupled by an optical isolator 120

3.5 Carrier fluctuations normalized by the averaged value in injection-locked semiconductor laser modulated at resonance frequency for (a) different injection rates at $\Delta f=$ 0.5 GHz and (b) different detuned frequencies at r_{inj} = 40%. Reported from (7) 125

3.6 Locking and unlocking regions in the phase space of frequency detuning versus injection ratio. SL: stable locking. NL: nonlinear dynamics. FWM: Four-Wave Mixing. The FWM boundaries are obtained from the steady-state analysis of 3.12, and the SL boundary is calculated from the stability analysis of 3.15. The diagrams are drawn for pump current J = $1.3J_{th}$, where J is the threshold current. Reported from (7, 8). 128

3.7 Schematic of the apparatus used to build the spectra after shown. Reported from (9) 130

3.8 Spectra with injection at the free-running optical frequency showing the transition from stable to limit cycle dynamics. The left column contains the optical spectra and the right column consists of the regenerative amplification spectra. The Injection Field is proportional to the square root of the injected power. The free-running regenerative amplification spectrum has been corrected for background noise and the variation of local oscillator power during the scan so that it can be compared to the model calculation, shown as a thin line. Reported from (9) 132

3.11 Mapping of the observed dynamics based on the experimentally measured spectra of the DFB laser under optical injection when biased at twice the threshold current. The full diamonds mark the saddle node bifurcation between stable and unlockedlocked operation while the open diamonds mark the unlockinglocking transition in a region of bistability (see (9)). Squares mark the Hopf bifurcation between stable and limit cycle operation. The triangles bound regions of period two operation. Within the period two regions are regions of complex dynamics marked by the shaded lines and crosses and a region of period four operation that is bounded by the circles. At injection levels below the saddle node bifurcation line and at low offset frequencies, multiwave mixing and Adler-type frequency pulling to locking are observed in the lightly shaded regions. Reported from (9) 134

3.9 Experimental optical frequencies and rf power spectra corresponding to chaotic bifurcation in semiconductor lasers under optical injection. Left side are the optical spectra and in the right side the rf power spectra. The relaxation oscillation frequency at the solitary oscillation is 4.7 GHz. The injection current rate is changed as (a) 0.14, (b) 0.23, (c) 0.41 (d) 0.52. Reported from (9) 135

3.10 Experimental optical frequencies and rf power spectra corresponding to chaotic bifurcation in semiconductor lasers under optical injection. Left side are the optical spectra and in the right side the rf power spectra. The relaxation oscillation frequency at the solitary oscillation is 4.7 GHz. The injection current rate is changed as (e) 0.77, (f) 1.02, (g) 1.30 (h) 3.01. Reported from (9) 136

3.12 Bifurcation diagram as a function of the injection ratio at a frequency detuning of 2 GHz. (a) Bifurction diagram for large gain defect μ_d=0.1. The laser oscillates at a single mode. (b) Bifurcation diagram for small gain defect of μ_d=0.001. Reported from (9) 137

3.13 Experimental modulation response of a semiconductor laser at J=2.4J_{th}. (a) free running laser; (b) very weak injection of $S_{inj}/S_s = 0.011$;(c) $S_{inj}/S_s = 0.092$; (d) $S_{inj}/S_s = 0.44$. Where S_{inj} is the injected photon number and S_s steady state value of the free running laser. Reported from (10) 140

3.14 Resonant condition of a semiconductor laser in the presence of optical injection. (a) Spectrum before optical injection. ω_0 is the angular frequency of the solitary laser, ω_{inj} is the frequency of the shifted light, and $\Delta\omega_{inj}$ is the frequency detuning between them. (b) Cavity resonant condition under injection locking. ω_{shift} is the cavity resonance frequency shifted from ω_0 by $\Delta\omega_{shift}(n)$ due to optical injection. Reported from (7) 142

3.15 Effective chirping parameter. Dash-dotted curve: Injection locking at $\Delta\nu$=1 GHz. Solid curve: Injection locking at $\Delta\nu$=-10 GHz. Dashed curve: Injection locking at $\Delta\nu$=-18 GHz. Dotted curve: Free-running. Reported from (11) 144

3.16 (a-b) Time series and (c-d) power spectra (respectively for (a) and (b)) of chaotic oscillations in the transmitter laser with and without optical injection. Reproduced from (12) 146

4.1 Four level model for polarization dynamics in QW VCSELs.151

4.2 Polarizatyion stability diagram in the parameter space (γ_p, μ) for (a) γ_a = 0.5 and (b) $\gamma_a = -0.2\ ns^{-1}$. Reproduced from (13) 154

4.3 Polarization Resolved (PR) light-current characteristics of a solitary VCSEL. Reproduced from (14) 156

4.4 (Color online) Numerical calculated L-I curve for γ_a=0.5 and γ_p=30 GHz. (a) ΔT = 200 ns; (b) ΔT = 0.25 ns; circles identifies the dynamic for increasing current, while triangle identifies the dynamic for decreasing current. The green curve below the L-I characteristic is the current-time dependence. 157

4.5 (a) Light-current characteristic for the intensity of each linearly polarized mode (solid dots: $\hat{x}$-polarized; open circles: $\hat{y}$-polarized) and the associated fractional polarization (FP). $Re(E_x)$ versus $Re(Ey)$ plots; (b) optical spectra of the field amplitudes E_x (solid line) and E_y (dashed line) for the solutions labeled on the light-current characteristic, and N-1 versus n. Reproduced from (15) 159

4.6 (Color online) Numerically calculated polarization resolved versus injection power curve. The red curve represents the x polarization mode, while the blue curve is the y mode. Red squares and blue dots represent the dynamics for increasing injected power. For both curves triangles indicate the dynamics for decreasing injected power. On the top a schematic of the optical potential referring to the polarization modes. The laser parameters are as in Table 4.1 160

4.7 Time trace of the injected field amplitude within a bit. . 165

4.8 Schematic representations of the effective potential at four different pump current values, corresponding to the labels I to IV in Fig. The solid square indicates the three values that can be used for implementing a logic AND; the dashed square indicates the three values that can be used for implementing a logic OR. 167

4.9 Time trace of the intensity of the X polarization (red line) for three noise levels (a), (b) $\beta_{sp} = 105$; (c),(d) $\beta_{sp} = 0.1$; and (e), (f) $\beta_{sp} = 1$; $T_{bit} = 5ns$, other parameters are as indicated in the text. The black dashed line represents the three-level injection strength and the stars mark bits with wrong logic output. The panels (b), (d) and (f) indicate a zoom of (a), (c) and (e). 168

4.10 Probability of success of an OR logic gate as function of the bit time (a), (b) and as a function of the noise strength (c), (d). The red, black and blue lines indicate the probability calculated using the 90/10, 80/20 and 70/30 criteria respectively (see text for details). ΔE is 0.0015 in panels (a), (c); and 0.005 in (b), (d), the bit time is 7 ns in panels (c), (d), other parameters are as indicated in the text. . . 169

4.11 Probability of correct operation (in color code) as a function of the noise strength and the bit time (a), (b); and as a function of bit time and the modulation amplitude (c), (d). The probability is calculated over 500 bits using the 80/20 criterium of success logic OR operation. The parameters are $\Delta E = 0.0015$ (a), $\Delta E = 0.005$ (b), $\beta_{sp} = 10^{-4}$ (c) and $\beta_{sp} = 0.1$ (d), other parameters as in the text. . . 171

4.12 Success probability, P, as a function of the optical injection parameters (the injection modulation amplitude and the frequency detuning) for two bit times, 7 ns (a) and 5 ns (b); P as a function of the laser parameters (the birefringence and the spin-flip rate) (c), (the dichroism and the pump current) (d). The probability is calculated over 500 bits using the 80/20 criterium of success logic OR operation. The parameters are $\delta E = 0.003$, $\beta_{sp} = 10^{-4}$, other parameters are as indicated in the text. 172

5.1 Both figures are reproduced from (16) 178

5.2 Output time traces (a-c), and corresponding probability function of the amplitudes detected over the threshold (b-d). The red dot line correspond with the threshold defined with “const” equal to 6. While for the blue dot line “const” is equal to 8. The figure (a) and (c) are relative to the set of input parameters $\Delta\nu$=0 GHz, $\mu = 1.8$, and (b) and (d) to the set $\Delta\nu$=-1.86 GHz, $\mu = 1.96$ 181

5.3 Numerical calculated Power Spectral Density (a) and respective temporal series (b), without OI ($E_{inj} = 0$) and in the absence of periodic current modulation A_{mod}=0%, f_{mod}=0. Constant bias current with value of μ=1.8; 2.4; 3; respectively red, blue, green curves. Frequency detuning between master and slave $\Delta\nu = 0$ GHz; Power injected $E_{inj} = 0$. 183

5.4 Numerical calculated Power Spectral Density (a-c) and respective temporal series (b-d), without periodic current modulation A_{mod}=0%, f_{mod}=0. Constant bias current with value of μ=1.8; 2.4; 3; respectively red, blue, green curves. Frequency detuning between master and slave $\Delta\nu = 0.22$ GHz; Power injected $E_{inj} = 60$. 185

5.5 Numerical calculated Power Spectral Density (a-c) and respective temporal series (b-d), without periodic current modulation A_{mod}=0%, f_{mod}=0. Constant bias current with value of μ=1.8; 2.4; 3; respectively red, blue, green curves. Frequency detuning between master and slave $\Delta\nu = -0.24$ GHz; Power injected $E_{inj} = 60$. 186

5.6 Numerical calculated Power Spectral Density and respective temporal series with OI in the cases of modulation bias current and with constant bias current. Average currents values of μ=1.8; 2.4; 3; respectively red, blue, green curves. Noise strength $D = 10^{-4}$; $\Delta\nu$=0.22 GHz; $E_{inj} = 60$; A_{mod}=16% of the μ_{bias}; 189

5.7 Numerical calculated Power Spectral Density and respective temporal series with OI in the cases of modulation bias current and with constant bias current. Average currents values of μ=1.8; 2.4; 3; respectively red, blue, green curves. Noise strength $D = 10^{-4}$. $\Delta\nu$=0.22 GHz; $E_{inj} = 60$; A_{mod}=16% of the μ_{bias}; 190

5.8 Numerical calculated Power Spectral Density and respective temporal series of the output intensity with OI, in the cases of modulation bias current and with constant bias current. Average currents values of μ=1.8; 2.4; 3; respectively red, blue, green curves. Noise strength $D = 10^{-4}$. $\Delta\nu$=-0.24 GHz; $E_{inj} = 60$; A_{mod}=16% of the μ_{bias}; 193

5.9 Numerical calculated Power Spectral Density and respective temporal series with OI, in the cases of modulation bias current and with constant bias current. Average currents values of μ=1.8; 2.4; 3; respectively red, blue, green curves. Noise strength $D = 10^{-4}$. $\Delta\nu$=-0.24 GHz; $E_{inj} = 60$; A_{mod}=16% of the μ_{bias}; 194

5.10 Number of detected RWs in the parameter space μ, $\Delta\nu$, when no current modulation is applied. The color code is plotted in logarithmic scale in order to increase the contrast of the regions with a small number of RWs. (a) Noise strength $D = 0$, (b) Noise strength $D = 10^{-4}$, (c) Noise strength $D = 10^{-3}$,(d) Noise strength $D = 10^{-2}$. The two parameters to be used in next section are labeled as A ($\mu = 2.4$, $\Delta\nu = 0.22$ GHz) and B ($\mu = 2.4$, $\Delta\nu = -0.24$ GHz). 196

5.11 Number of detected RWs in the parameter space f_{mod}, A_{mod}. The color code is plotted in logarithmic scale in order to increase the contrast of the regions with a small number of RWs. (a) Noise strength $D = 0$, (b) Noise strength $D = 10^{-4}$, (c) Noise strength $D = 10^{-3}$,(d) Noise strength $D = 10^{-2}$. The input parameters used for the master laser are those labeled with A ($\mu = 2.4$, $\Delta\nu = 0.22$). 199

5.12 Number of detected RWs in the parameter space f_{mod}, A_{mod}. The color code is plotted in logarithmic scale in order to increase the contrast of the regions with a small number of RWs. (a) Noise strength $D = 0$, (b) Noise strength $D = 10^{-4}$, (c) Noise strength $D = 10^{-3}$,(d) Noise strength $D = 10^{-2}$. The input parameters used for the master laser are those labeled, in Fig. 5.10, with B ($\mu = 2.4$, $\Delta\nu = -0.24$ GHz). 201

List of Tables

1.1 Scheme of the AND, NAND, OR, NOR logical operations. 55

2.1 Table of refractive index of plastic and polystyrene. . . . 63

4.1 Typical VCSEL parameters and values used in this chapter. 153
4.2 Input/output combinations for an OR gate: the input is codified with the injection strength on the Y polarization; the response is decoded from the output polarization. . . 162
4.3 First scheme: Relationship between the two inputs and the output of the logical operations, and the encoding power levels. 166
4.4 Second scheme: Relationship between the two inputs and the output of the logical operations, and the encoding power levels. 166
4.5 Relationship between the two inputs and the output of the logical operations. 167

Glossary

AOD	Opto Acoustic Deflector/Modulator
ATP	Adenosine triphosphate
BFP	Back Focal Plane
CCD	Charge-Coupled Device
CD	Compact Disc
CR	Coherence Resonance
CW	Continous Wave
DFB	Distributed Feedback
DM	Dichroic Mirror
EEL	edge-emitting semiconductor laser
FIR	Finite Impulse Response
FS	Forward Scattering

FWM	Four-Wave Mixing
high-NA	high-Numerical Aperture
LCD	Liquid Crystal Display
LED	Light Emitted Diode
LSR	Logical Stochastic Resonance
ML	Master Laser
NIR	Near Infra-Red
NLS	Nonlinear Schrödinger
OI	Optical Injection or Optically Injected
PC	Personal Computer
PDF	Probability Density Function
PFM	Photonic Force Microscope
PN	Positive doped-Negative doped
PS	Polarization Switching or Power Switching
PSD	Power Spectral Density
QPD	Quadrant Photo Detector
QW	Quantum Well
RO	Relaxation Oscillation
ROC	Receiver Operating Characteristic
RW	Rogue Wave
SCL	Semiconductor Laser
SFM	Spin-Flip model

SL	Slave Laser
SNR	Signal to Noise Ratio
SR	Stochastic Resonance
SRD	Stochastic Resonant Damping
TE	Transverse Electric
VCSEL	Vertical-Cavity Surface-Emitting Laser

Summary

Although the methodology used to perform the research contained in this thesis is firmly within the fields of physics, the motivation is interdisciplinary in nature. The initial open question that inspired this PhD research was, how might noise in nature have a constructive role? In some systems the influence of noise is not restricted to destructive and thermodynamic effects, but can have positive outcomes.

This thesis is focused on the study of stochastic and nonlinear dynamics in optical systems. First, we study experimentally the dynamics of a Brownian nanometer particle in an optical trap subjected to an external forcing. Specifically, we consider the effects of parametric noise added to a monostable or bistable optical trap and discovered a new effect which we named stochastic resonant damping (SRD). SRD concerns the minimization of the output variance position of a particle held in a harmonic trap, when an external parametric noise was added to the position trap. We compared the classical stochastic resonance (SR) with SRD and found that they are two phenomena which coexist in the same system but in different regimes. The experimentally studied monostable system showed a maximum in the signal to noise ratio, a clear signature of a resonance. We also developed a new technique to increase 10-fold the detection range of the quadrant photodiode that we used in this study, which exploits the channel crosstalk.

Second, we study the stochastic dynamics of a type of semiconductor laser (SCL), known as vertical-cavity surface-emitting laser (VCSEL), that exhibits polarization

bistability and hysteresis, either when the injection current or when the optically injected power are varied. We have shown how these properties can be exploited for logic operations due to the effect of the spontaneous emission noise. Two logical input signals have been encoded in three levels of optically injected power from a master laser, and the logical output response was decoded from the emitted polarization of the injected VCSEL. Correct and robust operation was obtained when the three levels of injected power were adjusted to favor one polarization at two levels and to favor the orthogonal polarization at the third level. We numerically demonstrated that the VCSEL-based logic operator allows to reproduce the truth table for the OR and NOR logic operators, while the extension to AND and NAND is straightforward. With this all-optical configuration we have been able to reduce the minimum bit time required for correct operation from 30 ns, obtained in a previous work with an optoelectronic configuration, to 5 ns.

The third focus of this thesis is the study of the chaotic nonlinear dynamics of a SCL optically injected, in the regime where it can display sporadic huge intensities pulses, referred to as Rogue Waves (RWs). We found that, when adding optical noise, the region where RWs appear becomes wider. This behavior is observed for high enough noise; however, on the contrary, for very weak noise we found that noise diminishes the number of RW events in certain regions. In order to suppress or induce extreme pulses, we investigated the effects of an external periodic modulation of the laser current. We found that the modulation at specific frequencies modifies the dynamics from chaotic to periodic. Depending on the parameter region, current modulation can contribute to an increased threshold for RWs. Therefore, we concluded that the modulation can be effective for suppressing the RWs dynamics.

Then, we have structured this Thesis in the following way:

Chapter 1 sets the historical background of the main phenomena associated with noise. We pay particular attention to those that are related with our research, such as Stochastic Resonance, Logical Stochastic Resonance and Coherence Resonance. For the latter, we describe the underlying physical mechanism. These notions become indispensable to understand what happen in the other physical situations described in chapters 2/4 and 5.

Chapter 2 is entirely dedicated to noise phenomena in optical traps. We give a soft-background about how optical tweezers are composed, and how can they be used as a tool to study statistical physics. Then, we explain in detail our experimental outcomes: Stochastic Resonant Damping and its comparison with classical stochastic resonance, and the experimental observation of a maximum in the SNR in a monostable optical trap. Finally, we describe a technique that we invented to analyse the data in order to reach a 10-fold increase in the detection range.

With chapter 3 we start to analyse the nonlinear dynamics in optically injected semiconductor laser systems. We introduce the spin-flip model, which has been extensively employed to perform numerical analysis in chapter 4. Moreover chapter 3 intends to give a strong enough background for the interpretation of the nonlinear output dynamics, which has been extensively used in chapter 5. Finally, we give the main motivations for the popular optical injection technique.

In chapter 4 we show the results of the numerical simulations of noise controlled Vertical-Cavity Surface-Emitting Laser (VCSEL)s dynamics in an (Optical Injection or Optically Injected (OI)) configuration. We introduce a general form of multimode rate equations for VCSELs, then we illustrate the spin-flip model for the circularly polarized and linearly polarized fields, for the two preferred oscillation modes. We describe the effects of bistability and the hysteresis, for both an opto-electronic and an all-optical configuration. Finally, we demonstrate how an OI VCSEL can be used as a stochastic logic gate, describing our numerical results and all implications in possible real applications.

In chapter 5 we introduce the concept of extreme event, and we describe the output dynamics as a function of the input parameters, also under the influence of noise and studying its effects when it is varied. Interestingly enough, during this research we detect the phenomenon of coherence resonance, which is given by a more periodic behaviour. Importantly, we employe a periodic external modulation of the bias current to control the output response, and our findings bring us to new insights into the chaotic behavior of OI SCL, at high frequency regime.

Chapter 6 is dedicated to summarize the main results presented in this Thesis and to discuss the various possible future research lines. Finally, we list the publications and conferences where we presented our results, and the bibliography cited in all pages of this thesis.

We hope that this thesis can contribute to a better understanding of the different stochastic and nonlinear dynamics in nature and in semiconductor lasers, taking into account all the positive synergies that can sometimes occur between nonlinearity and noise.

1

Introduction to stochastic effects in nonlinear systems

1.1 Introduction

This Chapter is intended to set the context for the original work contained in this thesis. First of all, we set an historic background about noise phenomena, and then we focus on resonance phenomena in nonlinear systems such as stochastic, logic and coherence resonance. We briefly explore their history, highlighting in which research fields they have been observed. Moreover we elucidate the theoretical mechanism underlying each of these phenomena.

1.2 General overview about stochastic phenomena

Noise is ubiquitous in nature as well in many technological fields. Although often it is considered as a drawback to eliminate, in some specific cases, it can help to create some dynamics otherwise impossible to generate. Successively, we report some findings in different fields from the last decades where positive outcomes of noise have been observed.

In signal transmission a bistable medium with a nonzero value of noise intensity can be considered as an information channel, where string of bits also nonperiodic can be transmitted (17). On the other hand, random fluctuations, when they interact with certain system's nonlinearities, can give rise to spatial order. Many experimental observations of self-organized behavior arising out of noise have been described (18).

In (19), the joint action of two noise sources has been studied, in the framework of doubly stochastic effects where ordering occurs. This concept has been applied to several basic noise-induced phenomena: stochastic resonance, noise-induced propagation and coherence resonance. Moreover, it has been shown that **non equilibrium phase transitions** might be controlled by correlation time and length of a coloured noise (20). Noise-induced phase transitions to excitability, noise-sustained structures in excitable media, and domain growth of spatial structures in their way towards steady state, have been reported where noise is essential for their appearance (21, 22). The joint action of noise and coupling resulted in a stabilization of the system. This regime also showed characteristic traits of stochastic resonance and wave propagation (23).

In biophysics the mechanism of motor protein motion in cytoskeleton has been successfully modeled by Brownian ratchets: the motor protein kinesin can be driven by the action of both the thermal noise and an additive colored noise, whose finite correlation time corresponds to the kinesin binding events and subsequent energy release through hydrolysis (24), (25), (26). Numerous studies have also discussed both, at the **single-cell level and in cellular populations** , the important influence of noise on intercellular coupling (27). In (28) noise is also employed in the dynamics of cortical neuronal networks, where it induces up/down dynamics when noisy inputs are applied to low-degree (nonhub) network nodes, but not when they act upon network hubs.

In (29) the interplay between an externally added noise and the intrinsic noise of systems that relax fast towards a stationary state was analyzed theoretically and it was found that increasing the intensity of the external noise could reduce the total noise of the system. This is similar to the mechanism of noise-induced activation (30), (31), in which a minimal averaged residence time occurs at an optimal time-scale of the modulation of a potential barrier.

In chaotic laser systems, the role of noise is essential, is essential to establish secure communications, which have been developed by using chaos and nonlinear dynamics. Moreover, communication through the use of chaotic waveforms as carriers of information has been demonstrated by several groups, both in free space and through fiber channels. Information signals transmitted and received include digital and analog waveforms, and several different encoding and decoding schemes have been recently proposed and demonstrated (32). Intensity and phase correlations in the noise-driven dynamics of two coupled lasers have also been investigated. These correlations induce noise reduction phenomena which are robust against frequency detuning and for pump power well above threshold (33). In (34) it has been found that weak near resonant injection leads to complex dynamics, which consist in sudden irregular pulses. These bursting dynamics can be interpreted as the result of the wandering of the laser frequency through the (small) injection locking range of the system. Also numerical studies by a simple and general model for a two-level laser system describes how the chaotic behaviour could be suppressed by a slow periodic modulation current (35, 36). Also, the effect of spontaneous emission noise on the light circulating in a ring cavity with a nonlinear absorbing medium was studied by means of a set of stochastic delay-differential equations, where noise fluctuations were found to be amplified as the system was approaching to the first bifurcation (37).

1.3 Stochastic Resonance

In the last two decades the phenomenon of Stochastic Resonance (SR) has been predictor in nonlinear sciences. SR is often described as a counter-intuitive phenomenon. This is largely due to its historical background, since in the first decade and a half since its “discovery” in 1980, virtually all research into SR considered only systems driven by periodic-most often a sine wave input signals and broadband noise. In such systems, a natural measure of the systems performance is the output SNR, or also, often the ratio of the output Power Spectral Density (PSD) at the input frequency, to the output noise floor PSD. In general it is implicitly assumed that noise is a problem, usually with good reason. Hence, observations of presence of noise in a system providing the maximum output SNR are often seen to be highly counter-intuitive.

The concept of stochastic resonance was originally put forward in the seminal papers by Benzi and collaborators (38, 39, 40) wherein they addressed the problem of the periodically recurrent ice ages. The suggestion that SR might rule the periodicity of the primary cycle of recurrent ice ages was raised independently by Nicolis (41, 42, 43, 44). A statistical analysis of continental ice volume variations over the last 10^6 years shows that the glaciations sequence has an average periodicity of about 10^5 yr. Since its introduction, SR it has been a very attracting subject, increasing the attention from several fields of science such as electronic circuits (45, 46, 47), differential equations (48), lasers (49, 49, 50, 51) in the adiabatic limit (44, 52, 53) and in the full non adiabatic regime (44, 54), neural models (55, 56, 57), physiological neural populations (58, 59, 60), or enhancement of the evoked responses in the peripheral nervous system (61, 62). In biology SR has been demonstrated in mechanoreceptor neurons located in the tail fan of crayfish (61) and in hair cells of crickets (63, 64). It has also been described in networks (65), chemical reactions (66), ion channels (67), in the behavior of feeding paddlefish (68, 69, 70), ecological models (71), cell biology (72, 73), financial models (74), psychophysics (where SR has also been used as a measuring tool to quantify the ability of the human brain to interpret noise contaminated visual patterns (55, 75, 76, 77, 78, 79)), carbon-nanotube transistors (80, 81), nanomechanical oscillators (82, 83), organic semiconductor chemistry (84), and even in social systems (85).

Most recently, the notion of SR has been extended into the domain of microscopic and mesoscopic physics by addressing the quantum analog of SR (86, 87, 88, 89) and also into the world of spatially extended, pattern-forming systems (spatiotemporal SR) (90, 91, 92, 93, 94, 95). Stochastic resonance has also been observed through monostable media where harmonic signal were induced by external fluctuations (6, 47, 96). In the last two decades several papers and reviews about SR have been written (2, 97), in order to give a deep and complete description of the simple mechanism hidden by this counterintuitive phenomenon. Let us briefly resume how and when the SR takes place. SR is a rather paradoxical concept, which characterize a new group of effects, where addition of a right amount of noise causes an enhancement of the order degree of the system (98). Randomness is usually considered as a disturb or something deleterious for the systems, nevertheless it can act as a positive factor under some specific conditions. SR can be observed by means of the addition of the right amount of noise to a weak input signal, than the detection of the output signal is improved. Further increasing the noise strength, however, causes the system to show a worse response. Therefore, noise can be employed to improve the formation of regular signal structures, to increase the coherence degree, to enhance signal-to-noise ratio, etc., improving the overall system performance rather than deteriorating it.

Commonly in the scientific community, a direct measure of SR is associated with the maximization of the SNR curve or even to the statistics of the *resident time*, which exhibits peaks at the Kramers rate and its multiples as shown in Figure 1.2. Although all that being true, it is convenient to clarify that these two criteria are generally adopted when a “periodic” signal is masked from a background of noise. Therefore, the detection is improved by means a certain amount of noise, which helps the weak signal to overcome the threshold. However, other kind of measures are used for aperiodic signals such as the mutual information or correlation functions.

Finally, the basic ingredient to observe SR are:

- a weak periodic (or aperiodic) signal,
- a detection threshold (or potential barrier),
- an internal source of noise which drives the state-variable to defeat the threshold, or the barrier in the case of a double well bistable system.

Then, the response of the system exhibits a resonance function of the noise, which is due to the synchronization between the coherent input signal and the stochastic process governed by the noise. SR does not depend on the physical nature of the system it is rather a distinctive feature of nonlinear systems, where the noise can control its characteristic time scales. As mentioned, SR was initially considered to be restricted to the case of periodic input signals. However, now it is used as an all encompassing term, whether or not the input signal is a periodic sine-wave, a periodic broadband signal, or aperiodic. An appropriate measure of the output response depends on the task at hand, and of the form of the input signal. For example, for periodic signals and broadband noise, SNR is often used, but for random aperiodic signals, mutual information or correlation based measures are more appropriate.

1.4 Mechanism of Stochastic Resonance

The mechanism of SR can be explained considering a heavily damped particle of mass m and viscous friction γ, moving in a symmetric doublewell potential $V(x)$ (Figure 1.1). The particle is subject to fluctuational forces that are, for example, induced by coupling to a heat bath. Such a model is archetypal for investigations in reaction-rate theory (99). The fluctuational forces cause transitions between the neighboring potential wells with a rate given by the famous Kramers rate (100), i.e.,

$$r_k = \frac{\omega_0 \omega_B}{2\pi\gamma} e^{\frac{-\Delta V}{D}} \tag{1.1}$$

with $\omega_0^2 = \frac{V''(x_m)}{m}$ being the squared angular frequency of the potential in the potential minima at $\pm x_m$, and $\omega_B^2 = \frac{V''(x_b)}{m}$ the squared angular frequency at the top of the barrier, located at x_b; ΔV is the height of the potential barrier separating the two minima. The noise strength $D = k_{BT}$ is related to the temperature T. If we apply a weak periodic forcing to the particle, the double-well potential is tilted asymmetrically up and down, periodically raising and lowering the potential barrier, as shown in Figure 1.1. Although the periodic forcing is too weak to let the particle roll periodically from one potential well into the other one, noise induced hopping between the potential wells can become synchronized with the weak periodic forcing. This statistical synchronization takes place when the average waiting time $T_k(D) = 1/r_k$ between two noise-induced interwell transitions is comparable with half the period T_Ω of he periodic forcing. This yields the time-scale *matching condition* for SR, i.e.,

$$2T_k(D) = T_\Omega \tag{1.2}$$

In short, SR in a symmetric double well potential manifests itself by a synchronization of activated hopping events between the potential minima with the weak periodic forcing (52). For a given period of the forcing T_Ω, the time-scale matching condition can be fulfilled by tuning the noise level D_{max} to the value determined by Eq. 1.2.

Initial studies of SR focused on systems driven by a periodic signal, and hence

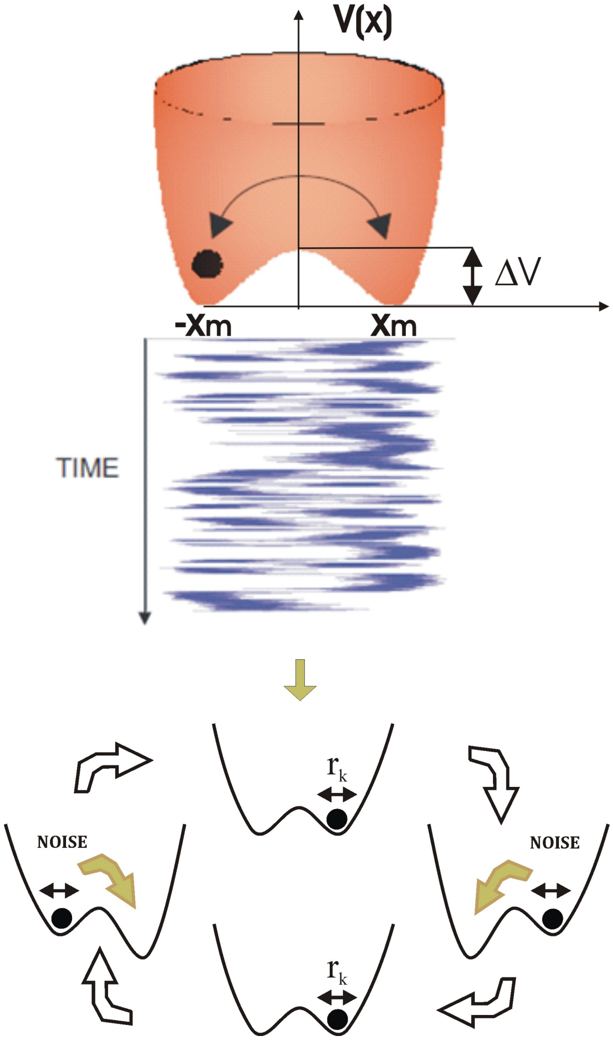
V(x)
ΔV
-Xm
Xm
TIME
r_k
NOISE
NOISE
r_k

Figure 1.1: double well potential. The trace represent the jiggling trajectory of the particle in time. Below: description diagram of a noisy bistable system with a potential modulation

used a signal-to-noise ratio based measure for comparison between the input and output of the system. It has been pointed out that for the more general case of aperiodic signals other performance measures are necessary, such as cross-correlation or information theoretical tools.

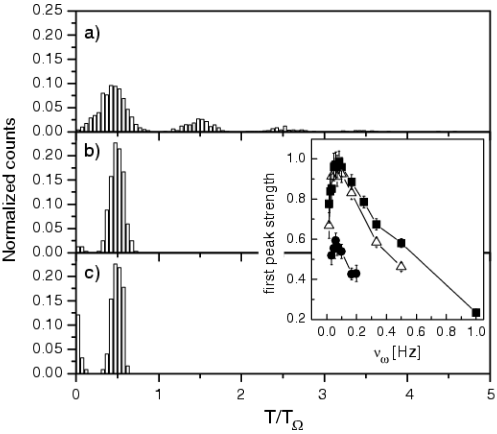

Figure 1.2: Residence time distributions N(T) for the symmetric bistable system. Reproduced from (1)

SR has been measured in many different ways. Examples include SNR (38), spectral power amplification ((101, 102), correlation coefficient (103), mutual information (63), Kullback entropy (104), channel capacity (105), Fisher information (68), ϕ divergences (106, 107), and mean square distortion (108). It has also been analysed in terms of residence time distributions (1, 109) as shown in Figure 1.2 and of Receiver Operating Characteristic (ROC) curves (110, 111, 112), which are based on probabilities of detecting a signal, or falsely detecting a non-existing signal (113). It was first thought that SR occurs only in bistable dynamical systems, generally driven by a periodic input signal, $Asin(\omega_0 t + \phi)$, and broadband noise. Since the input to such systems is a simple sinusoid, the SNR is a natural measure to use, with the following usual definition,

$$SNR = \frac{P(\omega_0)}{S_N(\omega_0)} \tag{1.3}$$

where $P(\omega_0)$ is the input signal power and $S_N(\omega_0)$ is the power of the PSD noisy background at the frequency of ω_0. SR occurs when the ratio of the output power at frequency ω_0 to the background noise PSD at ω_0, is maximized by a nonzero value of noise intensity.

Although SNR has been the first estimator of SR, researcher in the last decades have noticed that in many practical situation it is meaningless, specially for an aperiodic input signal. However, for our experimental research, where we add an harmonic component at a given frequency, we always computed SNR as estimator of SR. In the next Section we provide a general expression for the Signal to Noise Ratio derived from the Langevin equation for a brownian particle in a potential $V(x)$ and with a driving periodic input signal, as an estimator of SR.

1.4.1 Langevin equation

We consider the overdamped motion of a Brownian particle in a bistable potential in the presence of noise and periodic forcing:

$$\dot{x}(t) = -V'(x) + A_0 cos(\Omega t + \phi) + \varepsilon(t) \tag{1.4}$$

Where $V(x)$ denotes the reflection symmetric quartic potential

$$V(x) = -\frac{a}{2}x^2 + \frac{b}{4}x^4 \tag{1.5}$$

A_0 and Ω are the amplitude and frequency of the harmonic input signal, and $\varepsilon(t)$ denotes a zero-mean, Gaussian white noise with intensity D and autocorrelation function

$$\langle \varepsilon(t)\varepsilon(0) \rangle = 2D\delta(t) \tag{1.6}$$

In the absence of periodic forcing, $x(t)$ fluctuates around its local stable states with a statistical variance proportional to the noise intensity D. Noise-induced hopping between the local equilibrium states with the Kramers rate:

$$r_k = \frac{1}{\sqrt{2}\pi} e^{-\frac{\Delta V}{D}} \tag{1.7}$$

enforces the mean value $\langle x(t)\rangle$ to vanish. In the presence of periodic forcing, the reflection symmetry of the system is broken and the mean value $\langle x(t)\rangle$ does not vanish. This can be intuitively understood as the consequence of the periodic biasing towards one or the other potential well. An important quantifier of SR is based on the power spectrum. More in specific we are interested in the SNR. Therefore, we define the phase averaged power spectral density $S(\omega)$

$$S_\omega = \int\limits_{-\infty}^{+\infty} e^{-i\omega\tau}\langle\langle x(t+\tau)x(t)\rangle\rangle d\tau \tag{1.8}$$

where the inner brackets denote the ensemble average over the realizations of noise and the outer brackets indicate the average over the input initial phase ϕ. For a bistable system, $S(\omega)$ may be described as the superposition of a background power spectral density and a structure of delta spikes centered at $\omega = (2n+1)\Omega$ with $n = 0, \pm 1, \pm 2, ...$ Thanks to the approximation $A_0 x_m \ll \Delta V$, where x_m represents the minima of the bistable system (located at $\pm x_m$), we are led to separate $x(t)$ into a noisy background (which coincides, apart from a normalization constant, with the unperturbed output signal) and a periodic component with $\langle x(t)_{as}\rangle$, with amplitude $\bar{x}$, and phase lag $\bar{\phi}$ where

$$\langle x(t)_{as}\rangle = \bar{x}cos(\Omega t - \bar{\Phi}) \tag{1.9}$$

$$\bar{x}(D) = \frac{A_0\langle x^2\rangle_0}{D}\frac{2r_k}{\sqrt{4r_k^2+\Omega^2}} \tag{1.10}$$

$$\bar{\Phi}(D) = arctg\left(\frac{\Omega}{2r_k}\right) \tag{1.11}$$

where $\langle x^2 \rangle_0$ is the D-dependent variance of the stationary unperturbed system ($A_0 = 0$). From 1.10 we can see the direct dependence from the noise strength, thus the periodic response of the system can be manipulated by changing the noise level. Moreover, from a first closer analysis of 1.10, we notice that the amplitude $\bar{x}$ before increase with the noise level, up to reach a maximum, and then decreases again (see Fig. 1.3). By decreasing the driving frequency Ω, the position of that peak moves to smaller noise strength. This is the famous phenomenon of "stochastic resonance".

An alternative quantifier of SR is defined by the spectral amplification η, as the ratio between the integrated power stored in the delta spikes of the spectral density at $\pm\Omega$, $p_1 = \pi\bar{x}^2(D)$, and the total power of the modulation signal $p_A = \pi A_0^2$. Therefore:

$$\eta = \frac{p_1}{p_A} = [\bar{x}(D)/A_0]^2 \tag{1.12}$$

Considering small force amplitudes, $S_N(\omega)$ does not deviate much from the power spectral density $S_N^0(\omega)$, of the unperturbated system. Therefore, for a bistable system with relaxation rate $2r_k$, the hopping contribution $S_N^0(\omega)$ is:

$$S_N^0(\omega) = \frac{4r_k < x^2 >_0}{(4r_k^2 + \omega^2)} \tag{1.13}$$

It could be convenient also to extract the relevant phase-averaged power spectral density $S(\omega)$ Then, on adding the power spectral density of either component, we obtain:

$$S(\omega) = \left(\frac{\pi}{2}\right) \bar{x}(D)^2 \left[\delta(\omega - \Omega) + \delta(\omega + \Omega)\right] + S_N(\omega) \tag{1.14}$$

Then considering $S_N(\omega) = S_N^0(\omega) + O(A_0^2)$, SR can be envisioned as a particular problem of signal extraction from background noise $S_N(\omega)$. We adopt here the following definition of the signal-to-noise ratio (see Fig. 1.3)

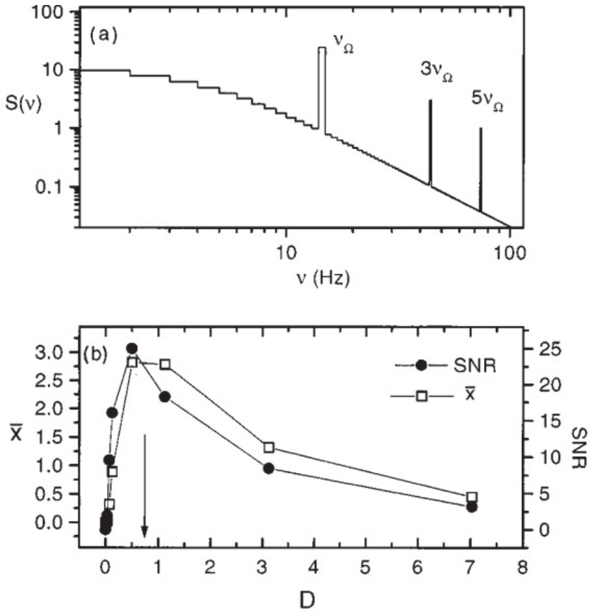

Figure 1.3: Characterization of stochastic resonance. (a) A typical power spectral density ($S\nu$) vs frequency n for the case of the quartic double-well potential. (b) Strength of the first delta spike, Eq. 1.14 , and the SNR, Eq. 1.15 , vs D (in units of Δ V). Reported from (2)

$$SNR = 2\frac{\left[\lim_{\Delta\omega\to 0}\int\limits_{\Omega-\Delta\omega}^{\Omega+\Delta\omega} S(\omega)d\omega\right]}{S_N(\Omega)} \tag{1.15}$$

1.5 Coherence Resonance

The problem presented by Stochastic Resonance phenomenon is to investigate the response of a bistable system to a periodic external force in the presence of noise. However, in many nonlinear systems the coherent motion of the system is not stimulated by an external force, but by the intrinsic dynamics of the nonlinear systems. For instance, limit cycles are very important dynamic states in self-organization processes of nonlinear systems in physics, chemistry, biology, and other fields. By adding an external control parameter beyond a critical value, the limit cycle of the system can be eliminated. However the intrinsic circulation of the system may still exist, and it can manifest in the transient process towards the equilibrium state. This transient circulation turns into an asymptotic coherent oscillation by introducing noise. For this phenomenon the term of: "Coherence Resonance" has been coined. Although the name of Coherence resonance phenomenon was firstly adopted in 1997 by Pikovsky and Kurths (3), Gang et al. in 1993 (114) were the first to to discover it. From then, many theoretical and experimental verification have been extensively investigated. Coherence resonance has been shown for a wide variety of systems such as stochastic and chaotic systems (115, 116), different formulations of FitzHugh-Nagumo model (3, 117), Belousov-Zhabotinsky reaction equations (118, 119), coupled Morris-Lecar models (120). Experimental evidence of coherence resonance phenomena is found in optical systems (121), electrochemical systems (122, 123), chaotic diode lasers (124), and semiconductor lasers (125). We briefly announce some works in optics and nonlinear systems, where CR has been observed: In (3), noise activates the system producing a sequence of pulses. The coherence of these noise-induced oscillations is shown to be maximal for a certain noise amplitude. In (121) it is shown that the regularity of the excitable pulses in the intensity of a laser diode with optical feedback increases when adding noise, up to an optimal value of the noise strength. While in (126) stochastic dynamics in a neural bistable system has been explored, where two spatially coupled noise sources (one was multiplicative and another additive) have been used in order to induce coherence resonance. Moreover, they experimentally confirmed that behaviour by using a nonlinear electronic circuit. Moreover, it has been found the strict relation between the correlation and the amplitude of the noise, and a coherent solution was selected by the system at intermediate values of feedback-coupling strength (127, 128). While in (129) Coherence Resonance (CR) it has been observed as clusters of ion channels generate neuronal action potentials depending of their size. It has been observed by numerical simulations in chemical reaction model and in the

Swift-Hohenberg model of fluid convection (130). Coherent oscillations have been also observed by building synthetic genetic network making use of an appropriate electronic elements linked in the same way as the original biochemical system (131).

1.5.1 Mechanism of Coherence Resonance

The phenomenon of CR appears in systems with a noise-induced limit cycle. A period of noise-induced limit cycle can be divided in two parts:

- First an activation time (T_a), which is the time needed for the phase trajectory to escape from the stable equilibrium to the excited state.
- Second an excursion time (T_e), needed to return to the equilibrium state.

The Arrhenius law rules the activation time, which is a function of the intensity noise, as: $< T_a > \propto exp(\Delta/D^2)$ where the parameter Δ is a threshold of excitation and D the noise strength. In the case of weak noise $D^2 \ll \Delta$, the period of noise-induced activation is dominated from the activation time and the statistic spiking is Poissonian. Then, large interspike intervals are detected for weak noise and the coefficient of variation approaches to 1. On the other hand for large noise the period is dominated by the excursion time and the Coefficient of Variation increases with the noise $CV \propto D$. Coherence resonance occurs for an intermediate noise intensity: where noise is weak enough to result in large fluctuations of the excursion time and large enough so that the activation time is short and the period is dominated by the excursion time.

The prototype model used in numerical simulations to show the coherence resonance, is based on the Fitz Hugh-Nagumo model:

$$\epsilon \frac{dx}{dt} = x - \frac{x^3}{3} - y \tag{1.16}$$

$$\frac{dy}{dt} = x + a + D\xi(t) \tag{1.17}$$

where $D\xi(t)$ is the noise term. Integrating this equation system a chaotic dynamics is found, with intensity pulses becoming much more regular at a well defined amount of noise strength. To quantify this behaviour usually the correlation function is taken into account:

$$C(\tau) = \frac{< \tilde{y}(t)\tilde{y}(t+\tau) >}{< \tilde{y}^2 >} \tag{1.18}$$

One can see from fig. 1.4 that the correlations are indeed much more pronounced for the moderate noise. To describe this effect the characteristic correlation time is usually calculated as follows:

$$\tau_c = \int_0^\infty C^2(t)dt \tag{1.19}$$

The process described from the above model, can be viewed as a sequence of pulses having durations t_p. it is convenient to look at the normalized fluctuations of pulse durations:

$$R_p = \frac{\sqrt{Var}t_p}{< t_p >} \tag{1.20}$$

As we already said, physically, the appearance of coherence resonance is deeply related to the excitable nature of the Fitz HughNagumo system. The system has two characteristic times: the activation time t_a and the excursion time t_e. The activation time is the time needed to excite the system from the stable fixed point $x = -a$, $y = a^3/3$; while the excursion time is the time needed to return from the excited state to the fixed point. The pulse duration t_p is the sum of these times $t_p = t_a + t_e$. The crucial point is that these times and their fluctuations have a different dependence on the noise amplitude. The activation time decreases rapidly with the noise amplitude according to the Kramers (Arrehnius) formula $< t_a >\sim exp(const \times D^{-2})$. It can be also shown that for small noise $Var(t_a) \approx < t_a >^2$. Thus for small noise, where $t_a \gg t_e$ and the period is dominated by the activation time $t_p \approx t_a$, the fluctuations of the pulse durations are relatively large: $R_p \approx R_a \approx 1$. For large noise the contribution of the activation time ta to the period is negligible, here the excursion time dominates $t_p \approx t_e$.

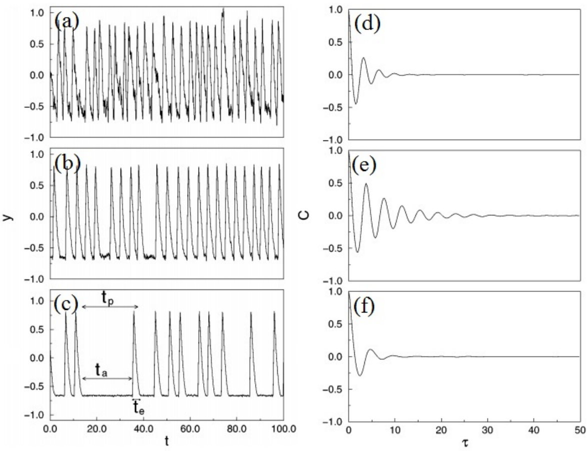

Figure 1.4: The dynamics of the Fitz HughNagumo system (Eqs. 1.16-1.17) for a=1.05, $\epsilon = 0.01$, and different noise amplitudes: (c) D= 0.02, (b) D= 0.07, and (a) D = 0.25. The mean durations of pulses are 7, 4, and 3.5, respectively.(d)-(e)-(f) are the respective autocorrelation function of (a)-(b)-(c). The activation and the excursion times for one pulse are depicted. Reproduced from (3)

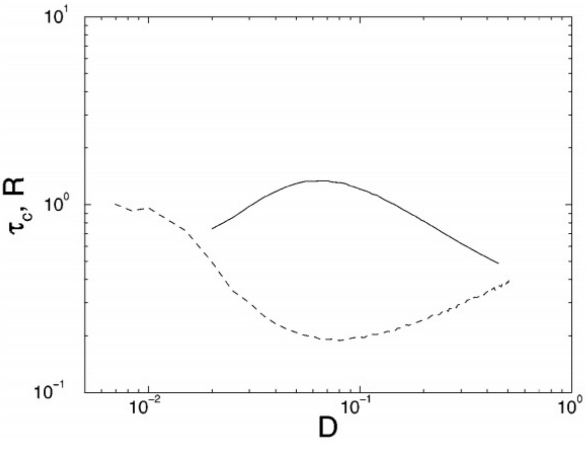

Figure 1.5: Correlation time t_c (solid line) and the noise-to-signal ratio R (Eq. 1.20, dashed line) vs noise amplitude for the Fitz HughNagumo system.Reproduced from (3)

1.6 Logical Stochastic Resonance

LSR was first reported by Murali and coworkers in Ref. (132). The main motivation for research performed in this direction, is due to the continuous shrinking in size of the computational devices and platforms, which does not allow to completely suppress or eliminate intrinsic fundamental noise. Therefore, an understanding of the cooperative behaviour and the background noise is needed, for the design the nonlinearity of the medium and the background between for the design and development of future computational concepts and devices. In nonlinear systems the interplay between bistability and noise can result in non-trivial noise-induced effects which can be potentially exploited for applications (2, 132, 133, 134). A recent example is the numerical demonstration of a stochastic logic gate using a vertical-cavity surface-emitting laser (VCSEL) that exploits the interplay between polarization bistability, noise, and pump current modulation (133, 135). VCSELs emit linearly polarized light with the direction of the polarization along one of two orthogonal directions associated with crystalline or stress orientations. Some VCSELs display, when the pump current increases, a Polarization Switching or Power Switching (PS) to the orthogonal polarization. The PS is often accompanied by hysteresis (15) and it has been shown that the switching points and the size of the hysteresis region depend on the pump current sweep rate (136, 137). When a VCSEL is subjected to optical injection, such that only the suppressed polarization receives injection, for appropriated injection parameters a polarization switching from the solitary laser polarization (in the following referred to as X) to the orthogonal one (Y) can also occur (138), either when the optical injection strength is increased (134, 139), or when the wavelength of the injected light is varied (140, 141). With this configuration, which has been referred to as orthogonal injection, polarization bistability and hysteresis cycles have also been observed, which can be exploited for all-optical buffer memories (142, 143). In the implementation of a VCSEL-based stochastic logic gate proposed in Ref (133), two logic inputs were encoded in an aperiodic three-level signal (i.e., the sum of two aperiodic square waves representing the two inputs) that was directly applied to the laser pump current, and the logic output was decoded from the polarization state of the emitted light (e.g., the output is a logic 0 if the laser emits the X polarization or a logic 1 if it emits the Y polarization). In Ref. (133) it was shown that the laser gives the correct logic response with a probability that was controlled by the level of noise, and that was equal to one in a wide range of noise levels. This phenomenon, which has been referred to as logic stochastic resonance (LSR) (132, 133, 135, 144),

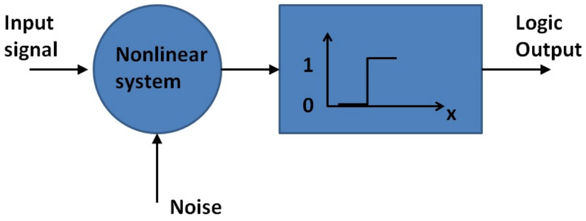

Figure 1.6: Schematic of a noisy nonlinear system forced by an input signal yielding a logic output.

is receiving a lot of attention because it occurs in several natural stochastic bistable systems (145, 146, 147).

Moreover, noise and nonlinearities have been exploited to build robust and tunable genetic regulatory networks that are capable of performing assigned operations, through the application of the logical stochastic resonance paradigm (146).

1.6.1 Mechanism of Logical Stochastic Resonance

Basically, the LSR is an application of the stochastic resonance phenomenon in some systems which present other peculiar effects. In some optical or electronic devices the intrinsic noise can play a certain role in order to switch between states. By means of a defined choice of initial threshold conditions the output response of these devices can be expressed as a logical combination of the input parameters (132) (see fig1.6). As for stochastic resonance, a right amount of noise can be exploited in order to synchronize the response. So that one can obtain very reliable logic circuit elements exploiting nonlinearity and tuning the noise strength. Logical Stochastic Resonance (LSR) has been extensively explored by means electronic circuits (132, 148). This behaviour has been also numerically found in semiconductor laser systems (133, 144).

Let us consider two logic inputs I_1 and I_2, which are encoded by 4 logical combinations. The output response in a bistable system in the case of an OR logic gate will be determined by the state of the system. In other words, the output can be considered a logical 1 if it is in one well, and logical 0 if its in the other well. Therefore, when the system switches wells, the output is toggled. It has been demonstrated that one observes, for a given set of inputs (I_1, I_2), a logical output from this nonlinear system, in accordance with the truth tables of the basic logic operations 1.1.

Table 1.1: Scheme of the AND, NAND, OR, NOR logical operations.

Logic inputs (I_1, I_2)	AND outputs	NAND outputs	OR outputs	NOR outputs
(0,0)	0	1	0	1
(1,0)	0	1	1	0
(0,1)	0	1	1	0
(1,1)	1	0	1	0

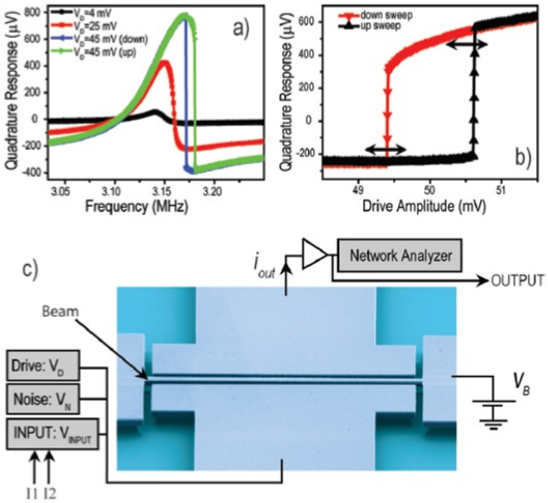

Figure 1.7: (a) Response in quadrature of the resonator as a function of the driving frequency for different values of the drive amplitude. (b) Response in quadrature of the resonator as a function of the drive amplitude for a fixed frequency (3.158 MHz) in the bistable regime. (c) Micrograph of the resonator and experimental setup. Reported from (4)

It has been demonstrated that in a reasonably wide band of moderate noise intensity, the system produces the desired logical outputs reliably. At this level the SR phenomenon provide a maximum in the probability of success operations (132, 148). In (4) a nanomechanical device, operating as a reprogrammable logic gate, and performing fundamental logic functions such as AND/OR and NAND/NOR was engineered and experimentally realized. The logic function could be programmed (e.g., from AND to OR) dynamically, by adjusting the resonator's operating parameters (see the schematic in Fig. 1.7).

Concluding, SR, CR, and LSR have been observed in many optical nonlinear systems (121, 124, 125, 126, 127, 128),(133, 134) and in the following chapters we present our results, which focus on stochastic resonant damping (Chapter 2, (149, 150)), stochastic logic gates (Chapter 4 (144)) and stochastic control of extreme pulses (Chapter 5, (151)).

2

Resonance phenomena in noisy systems by optical trap technique

2.1 Introduction

In this chapter, we illustrate the base principles of the optical trapping and calibration techniques, which have been the main tool employed in the first part of this thesis, in order to investigate some counterintuitive effects of noise, such as the SR and the Stochastic Resonant Damping (SRD), which will be presented in the next sections of this chapter.

Besides, we give some concept descriptions of the Photonic Force Microscope (PFM), which has been extensively used to study noise phenomena in nature (152, 153, 154, 155). More specifically, in this work the PFM has been used to trap nano and micrometer polystyrene beads with an infrared laser and also to detect in real time the position of the particle by interferometry of the light scattered by the particle. This has subsequently allowed us to study the random walk of the particle when it is submitted to a definite optical potential.

Thus, the results of this chapter include the main outcomes on resonance phenomena, such as maximization of the SNR detected in a monostable potential (156), resonance in a double well optical potential, the SRD (149)(157) and the comparison between the classical SR and the SRD (149). Finally, we reveal the novel technique that we used in almost all the cited previous works, to detect large displacements of the bead, up to 1500 nm, by using a QPD which usually only allows to detect displacements up to 150 nm (150).

2.2 Experimental techniques

2.2.1 Optical tweezers

In optics, a general assumption is that light photons carry linear momentum. This momentum can be transferred to an object upon collision; this phenomenon is called *radiation pressure* on the object. The radiation pressure exerted by typical light sources on a microscopic object can not be observed, because it is many orders of magnitude too small to get any measurable effect. Although later, Ashkin in 1970 (158) demonstrated that for an object of microscopic dimension ($< 100\mu m$) it can have considerable effects.

He used a focused argon laser of $\lambda = 0.51\mu m$ with 20 mW power, to trap micrometer polystyrene particles. Particles on the side of the beam seemed to be drawn inward to the focus, and were propelled further forward from there. When the laser beam was translated in a direction perpendicular to the axis of radiation, the particles stayed in the focus. From then, it has been realized that light can effectively exert a real force on microsphere particle, with a refractive index significantly different from that of the embedding medium, otherwise the gradient force does not come to be enough in order to trap the object inside its focus. The research further focussed on creating even atom traps (159, 160, 161), which of course, because the dimensions, it is still today quite a difficult task. Therefore, we know that a focused laser beam can be used to trap micrometer objects in a three dimensional landscape potential (158). A coherent laser beam focused by means of a high numerical aperture objective it is called optical trap or *optical tweezers*. Theoretically this effect is determined by the size of the trapped object and the wavelength λ of the light focused on. Therefore, depending on the object size d and the wavelength of the light λ, three different trapping regimes are considered (Figure 2.1):

1. Rayleigh regime, when $d \ll \lambda$;
2. an intermediate regime, when d is comparable to λ;

3. ray optics regime, when $d \gg \lambda$.

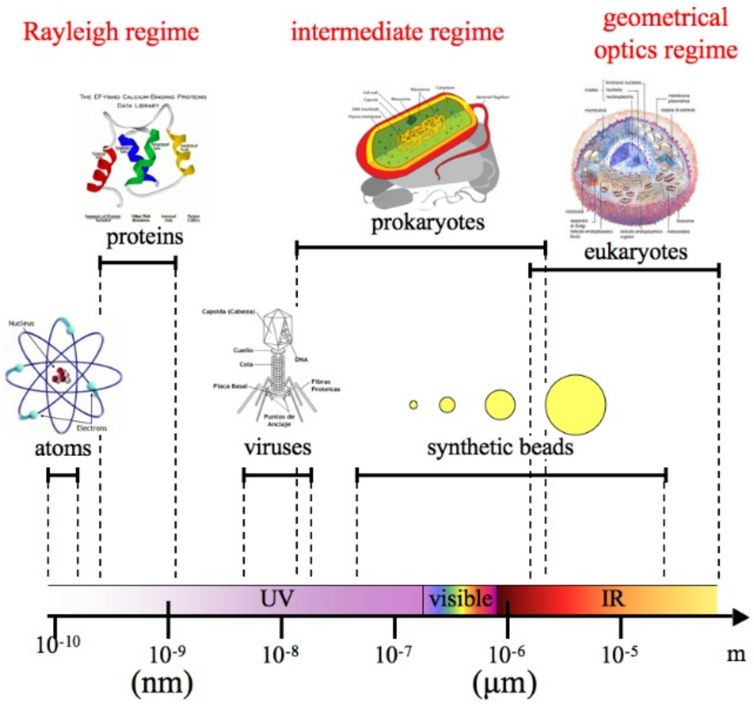
Rayleigh regime
intermediate regime
geometrical optics regime
proteins
prokaryotes
eukaryotes
Nucleus
Electrons
atoms
Capsida (Cabeza)
Cuello
Cola
DNA
Placa Basal
Fibras Proteicas
Puntos de Anclaje
viruses
synthetic beads
UV
visible
IR
10^{-10}
10^{-9}
10^{-8}
10^{-7}
10^{-6}
10^{-5}
m
(nm)
(µm)

Figure 2.1: Trapping regimes. Trapping regimes and typical objects that are trapped in optical manipulation experiments.

Unfortunately in many practical cases, the object is trapped by a source with wavelength similar to its size. In such cases an approximative approach between the two limits is used to obtain a quantitative estimate for the trapping forces (see (162)).

2.2.1.1 Ray optics regime

When the dimension of the object is much larger than the wavelength λ of the light, the geometrical optics can be applied. This regime can be easily explained in terms of refraction of light rays between media with different refractive indices ((158)(163)(164) and (165)). Figure 2.2 shows qualitatively the origin of the trapping force in the ray optics regime. The gradient restoring force (Figure 2.2a) can be explained considering that if the rays p_1 and p_2 reach the object with different intensity, then the momentum changes ($\Delta p_1, \Delta p_2$) will also be different in magnitude, causing a net reaction force on the refracting medium in the direction of the highest intensity. The displacement of the laser beam's axis is counteracted by the x-projection of this force related with Δp_x.

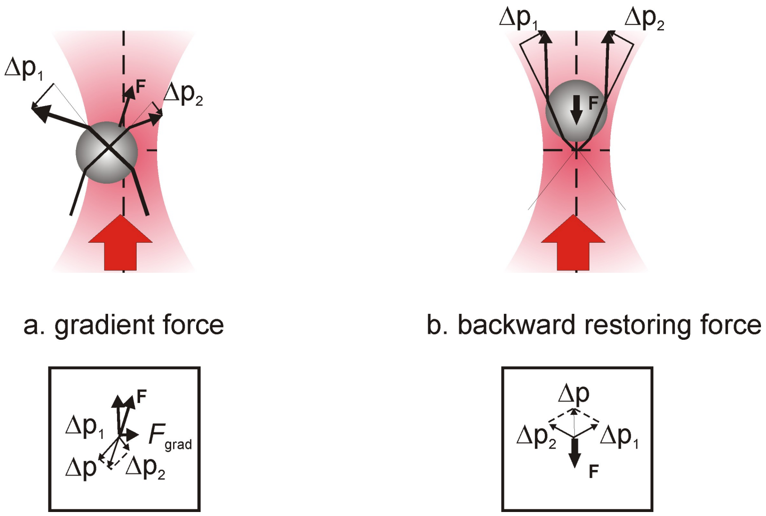

Figure 2.2: Principle of optical trapping of a microsphere. [a] A trapped bead in the laser focus, slightly displaced in a direction perpendicular to that of the laser light. Incoming rays with different intensities (arrows) are refracted by the transparent bead. Because of momentum conservation, the direction of the force on the bead is opposite to the momentum change of the photon field. The net force is composed of the inward gradient force F_{grad} and an upward component. [b] Forces acting on a bead positioned slightly above the laser focus. Due to refraction of high incident angle rays, the net force on the bead is in the downward direction. This force can overcome the upward pointing scattering force F_{scat} (not shown).

As can be seen in Figure 2.2b, the axial gradient force is also caused by momentum transfer upon refraction, resulting in a restoring force towards the focus. However, part of the incoming light is reflected rather than refracted - the scattering force. This light momentum reflection causes the object to be pushed out of the focus beam. If the scattering force along the +z-direction is compensated by the gradient force along the -z-direction, then the object is stably trapped. In (166) the optical forces on a dispersive sphere due to a light ray of power P have been computed, using the Fresnel reflection and transmission coefficients R and T (see (167)). For the scattering force they found

$$
\begin{aligned}
F_s &= \frac{n_1 P}{c}\left\{1 + R\cos 2\Theta - T^2 \frac{\cos(2\Theta - 2\phi) + R\cos 2\Theta}{1 + R^2 + 2R\cos 2\phi}\right\}\hat{\mathbf{u}}_{\|} \\
&\equiv \frac{n_1 P Q_s}{c}\hat{\mathbf{u}}_{\|}
\end{aligned}
\tag{2.1}
$$

where Θ and ϕ are the angles of incidence and refraction, n_1 is the index of refraction of the suspending medium, “c” the speed of light and $\hat{\mathbf{u}}_{\|}$ a unit vector parallel to the incident ray. The term $n_1 \frac{P}{c}$ represents the momentum per second of the light ray. The angles ϕ and Θ are related via Snellius‘refraction law: $\frac{n_2}{n_1} = \frac{\sin\Theta}{\sin\phi}$, with n_2 the refractive index of the object. In the same way, the gradient force is found as

$$
\begin{aligned}
F_g &= \frac{n_1 P}{c}\left\{R\sin 2\Theta - T^2 \frac{\sin(2\Theta - 2\phi) + R\sin 2\Theta}{1 + R^2 + 2R\cos 2\phi}\right\}\hat{\mathbf{u}}_{\perp} \\
&\equiv \frac{n_1 P Q_g}{c}\hat{\mathbf{u}}_{\perp}
\end{aligned}
\tag{2.2}
$$

The force exerted by a single ray of power P, is given by the vectorial addition of these two trapping force components:

$$
F_{tot} = \frac{n_1 P}{c}\sqrt[2]{Q_s^2 + Q_g^2} \equiv \frac{n_1 P}{c} Q\left(\Theta, \frac{n_2}{n_1}, R, T\right) \tag{2.3}
$$

The total force is obtained by summing the forces over all rays passing through the object. Ashkin worked out these calculations for a laser beam with a Gaussian profile (164).

r

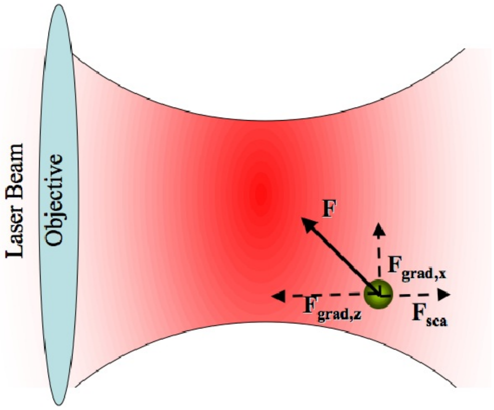

Figure 2.3: Forces in the Rayleigh. Scattering and gradient forces in the Rayleigh regime.

2.2.1.2 Rayleigh regime

For the case $d \ll \lambda$ we must consider the Rayleigh regime. The trapped objects are considered as point dipoles, so that the electromagnetic field is constant on the scale of the particle. A schematic is shown in Figure 2.3. The scattering force on the particle, is given by:

$$\mathbf{F}_s = n_1 \frac{\langle \mathbf{S} \rangle \sigma}{c} \tag{2.4}$$

where $\langle \mathbf{S} \rangle$ is the time-averaged Poynting vector of the electromagnetic wave and $\sigma = \sigma\left(d, \lambda, \frac{n_2}{n_1}\right)$ the scattering cross section of a particle of diameter d. The gradient force acting on the dipole induced by the electromagnetic wave (168):

$$\mathbf{F}_g = \frac{\alpha}{2} \nabla \langle E^2 \rangle \tag{2.5}$$

where E is the electric field and $\alpha = \alpha(d^3, \frac{n_2}{n_1})$ the *polarizability* of the object.

2.2.1.3 Optimization of trapping force

Considering the ray optics approach, it is obvious that the trapping force can be enlarged by increasing the laser power P, the refractive index of the surrounding medium n_1, or the Q-values. The laser power can not be increased beyond a certain limit due to unavoidable damages to the optics or/and the system (biomaterials in biophysical application). Increasing the refractive index is hardly ever an option, as most samples require an aqueous solvent of $n_1 \approx 1.3$. Another parameter that can be optimized is the geometric Q-values. The angle Θ_{max} is a parameter depended on the optics used. Specifically, it is determined from the microscope objective used to focus the laser beam into the sample chamber. Usually, one of the specifications of an objective is the numerical aperture (or NA, see references (169), (167)). This is a measure for the solid angle over which the objective lens can spread light. It is defined as:

$$NA = n_3 \sin \Theta_{max} \tag{2.6}$$

Table 2.1: Table of refractive index of plastic and polystyrene.

Material	**Index n_2**
Silica (SiO_2)	1.37 - 1.47
Polystyrene	1.57

where Θ is one-half the angular aperture (Figure 2.4) and n_3 is the refractive index of the *immersion medium.* Usually, the value of n_3 varies between 1.0 for air and ≈1.5 for most immersion oils. The NA of the objectives in the setups used to perform the experiments was 1.3 and 1.35. Additionally, the beam diameter d is another parameter which also influences Θ_{max}. As indicated in the Figure 2.4, an expanded beam yields a larger Θ_{max} and therefore a stronger intensity gradient in the focus. To optimize the trapping quality with a Gaussian profile beam, the beam should *overfill* the back aperture of the objective lens. The highly convergent rays increase the gradient compared to when the aperture is just filled. The gradient force $\mathbf{F}_g$, is largely increased by these convergent rays.

Moreover, the ratio n_2/n_1 determines how strong the incident rays are refracted, and then how strong the trapping force is.

The balance of the gradient and scattering forces such as required, yields an optimal refractive index of n_2= 1.69 (see (170), (162)). In the table 2.1 the refractive indices of the most used materials are listed. Polystyrene particles trap better than do silica particles, which is true considering a beam sufficiently expanded.

In many applications the objects size and the wavelength of the trapping light are often of the same order of magnitude, thus neither the ray optics nor the Rayleigh approach can be applied. The laser wavelengths that we used in our setup were λ= 1064 nm, and λ= 785 nm and the bead diameters for the experiments described here were either d = 600 nm or 2.1 μm.

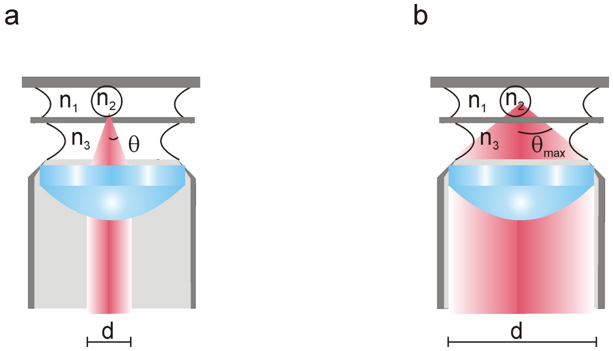

Figure 2.4: Objective NA and overfilling. [a] When the trapping laser does not (over)fill the back aperture of the objective, the highest-angle rays are smaller than Θ_{max} and thus the high NA is not fully exploited. [b] The scattering force is more efficiently counteracted by an expanded beam. The parameters used in Eq. 2.6 are depicted.

2.2.2 Force detection and calibration

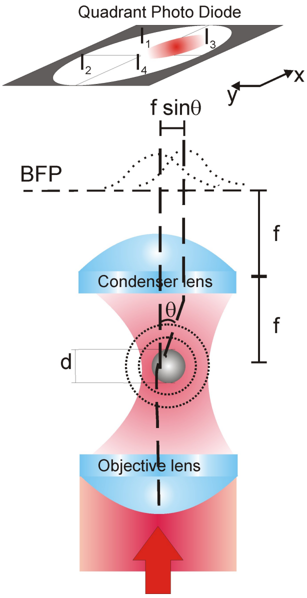

Figure 2.5: Back-focal-plane interferometry. Configuration for the detection of lateral displacement of a trapped sphere from the trap center. The condensers BFP is imaged onto a QPD. Reading out the differential signals $(I_1 + I_3) - (I_2 + I_4)$ and $(I_1+I_2)-(I_3+I_4)$ (both normalized by the total intensity), displacement signals for x and y are obtained, respectively.

The theoretical prediction of the force exerted by the laser beam upon the trapped object is an hard task, or in some cases even impossible to do it. Despite many limitations, it is possible to use the light scattered from the object, in order to accurately measure the trapping force. Additional forces are generated when the rays incident on the object, which push or pull it from the center trap. In (5) a model based on far-field interference of the outgoing laser light with the scattered light from the trapped particle has been developed. The lateral displacement of the particle induces an intensity shift. The movement of the trap around in the sample does not affect the intensity distribution. Only the motion of the trapped object affects the interference pattern created. So that, if the plane is imaged onto a quadrant photodiode, which can detect changes in the intensity distribution over the plane, the position of the particle can be measured. This method is known as back-focal-plane interferometry, and from now on we will refer always to this for the detection of the position of the particle(Figure 2.5).

Figure 2.5 illustrates the configuration for the detection of the lateral displacement from the trap center. In Figure 2.6 the intensity shifts as combination of the output signals from the four segments of the quadrant diode are defined. Considering a micrometer spherical object with diameter d, displaced of δ from the center of a beam of focal waist diameter ω_0, the following expression for the detector response can be derived ((5)).

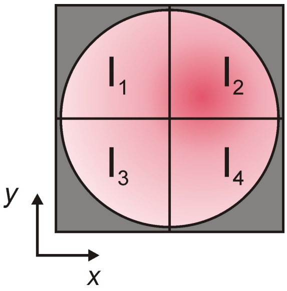

$$\left.\begin{aligned} I_{y^+} &= I_1 + I_2, \\ I_{y^-} &= I_3 + I_4, \end{aligned}\right\} \qquad D_y = \frac{I_{y^+} - I_{y^-}}{I_{y^+} + I_{y^-}}$$

$$\left.\begin{aligned} I_{x^+} &= I_2 + I_4, \\ I_{x-} &= I_1 + I_3, \end{aligned}\right\} \qquad D_x = \frac{I_{x^+} - I_{x^-}}{I_{x^+} + I_{x^-}}$$

Figure 2.6: Intensity distribution signals D_x and D_y constructed from the light intensities I_j on the four individual segments of a quadrant photodiode.

$$D_x \quad = \quad \frac{I_{x^+} - I_{x^-}}{I_{x^+} + I_{x^-}} \approx 32\sqrt{\pi}\frac{n_1\alpha}{\lambda\omega_0^2}\mathcal{H}\left(\frac{\delta}{\omega_0}\right) \tag{2.7}$$

$$\mathcal{H}(u) = exp(-2u^2)\int_0^u exp(t^2)dt$$

Where the terms α and λ represent the susceptibility and the wavelength of the laser. The expression was derived in the Rayleigh approximation (see section 2.2.1.2). However, it has been found a good agreement of the observed response also for particles with size in between the two regimes. In Figure 2.7 the response function from equation 2.7 for a 0.5 μm sphere diameter and a focal beam waist $\omega_0 = 0.53$ μm, which is the actual value for our objective and an unexpanded beam of 1.0 μm diameter is plotted. For small displacements ($\mid \delta \mid \leq 0.15 \mu m$), the response is approximately linear. The slope of the linear

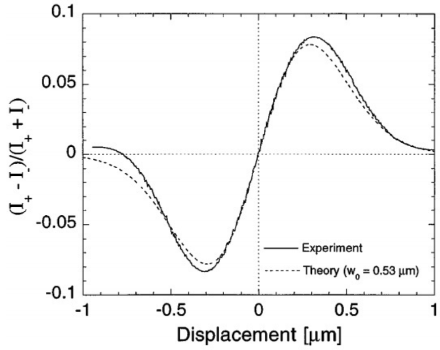

Figure 2.7: Detector response for ω_0 = 0.53 μm and d = 0.5 μm. Reported from (5)

range is a function of the bead diameter d, and scales as d^3, but its width is hardly affected by this parameter. By the application of a known force to the trapped bead, one can calibrate the detector to physically relevant units of force or displacements. This procedure will be explained in the next section.

2.2.2.1 Brownian motion and power spectral density

In order to measure the forces causing the displacements of the trapped object, the intensity shifts in the back focal plane can be used. Applying forces of known magnitude to the bead, it is possible to calibrate the detector response. One method consists in moving the sample in which the bead is trapped, at a constant velocity, then the bead will be dragged out of the trap due to the *viscous force* of the fluid on the bead. The force on the bead can be calculated by the following equation:

$$F = 3\pi\eta d\nu = \gamma\nu \qquad (2.8)$$

where η and ν are the viscosity and velocity of the fluid along a bead of diameter d, and γ is the drag coefficient. A more accurate calibration procedure is to make use of the diffusive Brownian motion of the bead due to the continuous and random bombardment by solvent molecules, which establishes a free diffusion regime of the particle. Then, after a time t, the mean square displacement of the spatial coordinate x will be (see (171), (172)):

$$Var(x) = \left\langle x^2(t) - \left\langle x(t) \right\rangle^2 \right\rangle = \frac{2k_B T}{\gamma} t = 2Dt \qquad (2.9)$$

with D the diffusion constant, T the temperature and k_B Boltzmann's constant. Therefore, a bead held in an optical trap will feel both the diffusional forces due to the solvent molecules and the restoring force from the optical trap which confines its motion towards the laser focus. Considering that displacement and the confining force have a linear correspondence by means a factor k, the Langevin equation (see (172)) for the bead's motion becomes

$$F(t) \quad = \quad \gamma \frac{dx}{dt} + kx \tag{2.10}$$

(Note that for very low Reynolds number $\Re$ (about 10^{-4} in this case) the inertial forces have been neglected.) $F(t)$ is the random thermal force, with a power spectrum $S_F(f)$, which contains the contribution to $F(t)$ of motions at different frequencies.

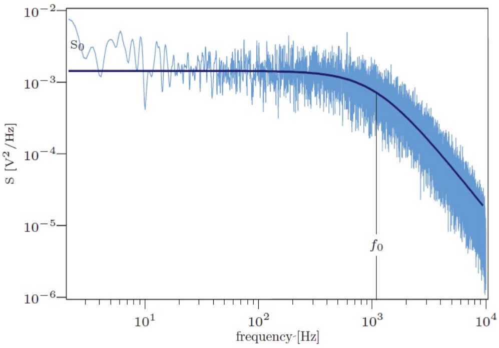

Figure 2.8: Power spectrum plus fit. The 'noise' is in fact the Brownian motion of the bead in the trap. The corner frequency f_0 of this spectrum is $\sim$ 1000 Hz, taken with a 2.1 μm polystyrene bead. This yields a trap stiffness of 125 pNμm^{-1}

The power spectrum, for an idealized Brownian motion (this is 'white noise) has a constant value (see (171)):

$$S_F(f) \quad = \quad |\mathcal{F}^2(f)| = 4\gamma k_B T \tag{2.11}$$

where $\mathcal{F}(f)$ is the Fourier transform of $F(t)$. Therefore the power spectrum of the displacement fluctuations given by the Langevin equation 2.10 —writing $\xi(f)$ as the Fourier transform for $x(t)$— is found to have a Lorentzian shape (see (171)):

$$S_x(f) \quad = \quad |\xi^2(f)| = \frac{k_B T}{\gamma \pi^2 (f_c^2 + f^2)} \tag{2.12}$$

where, $f_c \equiv k/2\pi\gamma$ is introduced as a characteristic frequency of the trap. At frequencies $f \ll f_c$, the power spectrum is grossly constant, $S(f) = S_0 = 4\gamma k_B T/k^2$. At $f \gg fc$, it falls off like $1/f^2$. For this reasons f_c is known as the corner frequency. The high frequency behavior is characteristic of free diffusion, meaning that at short time scales the particle does not feel the confinement of the trap. A typical power spectrum is shown in Figure 2.8

2.2.2.2 Conversion to physical units

By fitting of the observed power spectrum of a trapped particle it is possible to determine the values of S_0 and f_c (Figure 2.8), and these numbers can be used to find the trap stiffness k:

$$k \quad = \quad \frac{2k_B T}{\pi S_0 f_c} \qquad or \qquad k = 2\pi\gamma f_c \tag{2.13}$$

The stiffness k has the same units $[N/m]$ of a spring constant in a mechanical oscillator. Moreover, it must be noticed that the provided output signal is a voltage proportional to the displacement of the bead (section 2.2.2). Therefore it is essential to determine the conversion factor from voltage to nanometers in order to define exactly the bead displacements.

The Stokes formula for the viscous drag coefficient on a bead ($\gamma = 3\pi\eta d$), which gives γ from first principles, can be used to calibrate the response $R[m/V]$ of the detector if bead diameter and solvent viscosity are known:

$$R[m/V] \quad = \quad \left[\frac{k_B T}{\pi^2 \gamma S_0^V f_c^2}\right]^{1/2} \overset{25^\circ C}{=} \left[\frac{5.0 \cdot 10^{-20} m^3/s}{S_0^V f_c^2 d}\right]^{1/2} \tag{2.14}$$

where room temperature of $25°C$ and the viscosity of water at that temperature have been substituted. The quantity S_0^V is the low-frequency limit of the power spectrum of the voltage data.

To convert the data to forces, R should be multiplied by the trap stiffness k. Note that the power spectrum has 1/frequency units, which is due to the fact that the spectra are divided by their frequency resolution δf , to meet the normalization criterion

$$\sum_{i=1}^{N/2} S(f_i)\delta f \quad = \quad \left\langle x^2(t) - \langle x(t\rangle^2 \right\rangle = Var(x) \tag{2.15}$$

with N the number of samples (see: (171)).

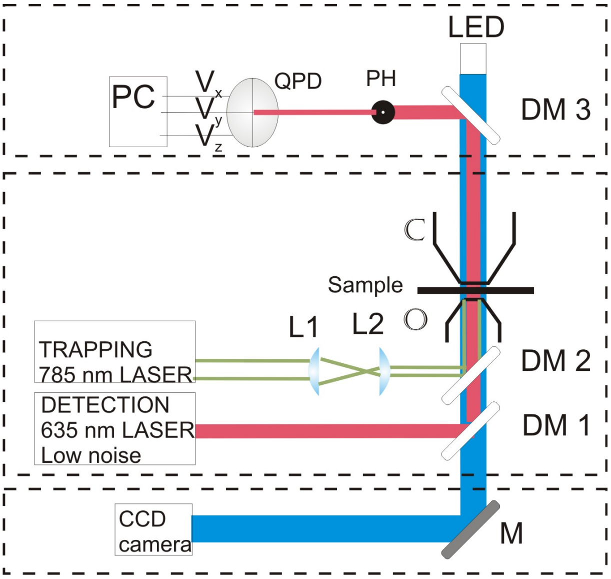
LED
PC
V_x
V_y
V_z
QPD
PH
DM 3
C
Sample
L1
L2
O
TRAPPING
785 nm LASER
DM 2
DETECTION
635 nm LASER
Low noise
DM 1
CCD
camera
M

Figure 2.9: Basic PFM setup. The main components are: laser, high-NA objective (O), sample, quadrant photo-detector (QPD), and CCD camera. Other optical components: telescope (L_1, L_2), Dichroic Mirror DM, mirror (M), and illuminating light source (LED).

2.2.3 The Photonic Force Microscope

In this section we briefly describe how a PFM is structured. A typical PFM setup comprises an optical trap to hold a probe - a dielectric or metallic particle of micrometer size - and a position sensing system. In the case of biophysical applications the probe is a small dielectric bead tethered to the cell or molecule under study. In a PFM it is possible to distinguish three main parts (Figure 2.9):

- Trapping,
- Position detection,
- Imaging.

2.2.3.1 Trapping optics

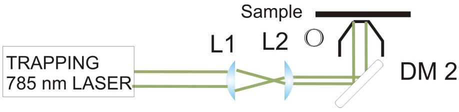

Figure 2.10: The trapping optics is constituted by two lenses which expand the laser beam to overfill an high-NA objective (O), which focused create the optical trap inside the liquid solution where the object to be trapped is suspended. Besides, a dichroic mirror (DM) is used to reflect the NIR beam and allowing to pass the visible light direct to the CCD camera and the detection beam.

As discussed in section 2.2.1 an optical trap is a 3-dimensional landscape potential generated by a strongly focusing laser beam. The main optical components to build this part (Figure 2.10) are: laser, telescope, objective and sample. Usually, in most applications, the laser has a wavelength in the near-infrared regime, because NIR light is less damaging to biological cells and molecules than visible and ultraviolet light. A couple of lenses forms a telescope in order to expand the laser beam and getting the objective overfilled (see section 2.2.1.3). The sample chamber is made of two very thin slide glasses (around 100 μm), because the focus point is very close to the objective. Usually the object to be trapped is a polystyrene particle and it is suspended in an aqueous solution sealed between the two glass slides. By a nano-positioning system the trapped object can be moved in all 3 dimensions. The refracted rays exert a very small force of the order of pico-Newton on it, drawing it towards the region of highest intensity. The optical potential is harmonic close to the focal point and the attractive force is proportional to the stiffness of the trap times the bead displacements from the center focus beam: $F_{opt} = k(x - x_0)$. The trap stiffness k: (1) is directly proportional to the power in the light beam; (2) for a given power beam, the trap stiffness increases with a decrease of the size of the focused spot. The intensity of the trap decreases proportionally with a increase of the size spot of the focused beam; (3) the trap is weakest in the direction of the beam propagation, in fact depending on how much light is reflected at the bead surface, the force due to the reflection can easily push the sphere out of a weak trap. Furthermore, in presence of damping, if the trap depth is not significantly greater than the kinetic energy characteristic of the Brownian fluctuations, the particle will easily escape. In order to optimize and making stronger possible the optical trap the objective must be overfilled by the NIR collimated laser beam, and the objective must have an high-Numerical Aperture (high-NA) (2.2.2).

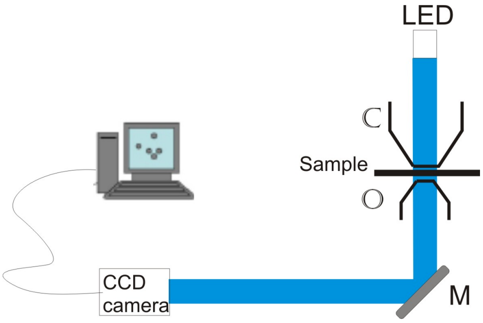

Figure 2.11: Imaging optics. An objective *C* (usually called condenser) focuses a white or green light (LED) on the sample. The light is then recollected by a second objective (*O*) and projected onto a CCD camera connected to a monitor.

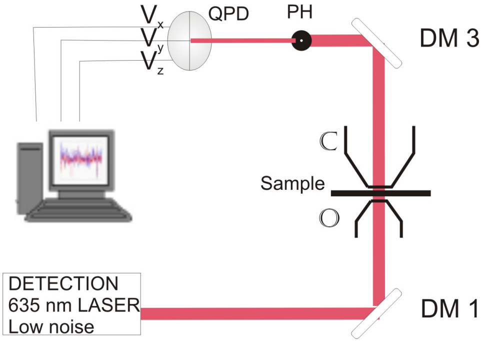

Figure 2.12: Detection optics. A QPD, connected to an acquisition system, receives the forward scattered laser light by a trapped particle, after it is collimated by an objective (*O*) and collected by a condenser C.

2.2.3.2 Imaging optics

Figure 2.11 shows the imaging optical section, which is necessary to observe in real time the trapped object. The light for the imaging is provided by a Light Emitted Diode (LED) lamp, and is collected by a condenser *C* and directed orthogonally towards the trapping region. The objectives *O* and *C* are on the same axis, as well as the light is projected on a CCD camera which is connected to a Personal Computer (PC) for imaging recording and to visualize in real time the position of the particle. In order to not saturate the camera due to the high intensity of the trapping beam, color filters are required.

2.2.3.3 Detection optics

As explained in section 2.2.2, the scattered light usually provided by the same trapping laser beam is collected from a condenser and directed into a QPD, which converts in voltage signal the pattern of the forward scattered light due to the changes in the particle's position [Figure 2.12].

2.2.3.4 Acousto-Optic Deflection

In order to create different potential shape, in the path from the IR laser to the objective O an AOD, is inserted with the aim to steer the beam light and then modulate the position of the optical trap, up to a few tens of kilohertz. The physical principle which acousto-optic deflectors are based on is called photo-elastic effect. It establishes that an elastic deformation of a solid body under strain causes a change of its refractive index. An acoustic wave can be considered as a local compression and expansion of the medium it is travelling through. Therefore, an acoustic wave travelling in a crystal will modulate the refractive index. In (173, 174) an extensive description is given, including the general case of *anisotropic* crystals — with a different index in all crystal directions. We will summarize the main results shown there. The refractive index n of a crystal with sound velocity v, will vary depending of the frequency ($f = \omega/2\pi$) and wavelength ($\Lambda = v/f$) of a plane acoustic wave with wave vector $\mathbf{K}$ (with $|\mathbf{K}| \quad K = \omega/v$):

$$\delta n = \delta n_0 \sin(\omega t - \mathbf{K} \cdot \mathbf{r}) \tag{2.16}$$

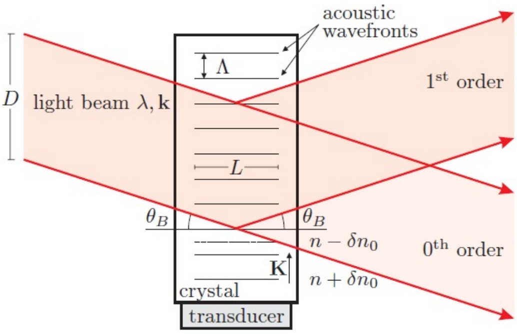

Figure 2.13: Light scattering off the wavefronts of a plane acoustic wave traveling through a crystal. The figure shows the case for Bragg diffraction, where the incidence angle should be the Bragg angle θ_B given by equation 2.18 The total beam deviation equals $2\theta_B$

. Reproduced from (174)

This behaves like an optical grating of spacing Λ, traveling along its direction with a speed v. However, because of the speed of light being much larger than the speed of sound, the grating can be considered static with respect to an incoming light beam. Figure 2.13 shows a typical configuration to illustrate the acousto-optic effect. An acoustic wave (usually in the radiofrequency region) is introduced in a crystal by a piezoelectric transducer, which converts an electric voltage to mechanical deformations (or vice versa).

An incident light beam (vacuum wavelength λ, wave vector $\mathbf{K} = \frac{2\pi}{\lambda}\hat{\mathbf{K}}$) diffracts on the acoustic wavefronts. Depending on the physical parameters

of the configuration (light incidence
angle, L, Λ, λ), two types of diffraction can occur. To distinguish, the following dimensionless parameter Q is often used:

$$Q = \frac{LK^2}{nk} = 2\pi \frac{\lambda L}{n\Lambda^2} \tag{2.17}$$

The case of $Q \ll 1$ is known as the *Raman-Nath diffraction*. The beam light arrives with normal incidence on the crystal surface. This kind of diffraction is characterized by the generation of many beams with comparable intensity. The diffracted light rays can not destructively interfere because the length L of the medium is so small compared with the other length scale.

On the other hand when $Q \gg 1$ the *Bragg diffraction* is obtained. The Bragg angle θ_B provides the condition for which only the first diffracted order is the result of constructive interference:

$$\theta_B = \arcsin \frac{\lambda}{2n\Lambda} \approx \frac{\lambda}{2n\Lambda} = \frac{\lambda f}{2nv} \tag{2.18}$$

The total deflected angle is equal to $2\theta_B$ (typically a few tenths of milliradiants) and it is proportional to the acoustic frequency. The diffraction efficiency η of the first order, has been obtained in ref. (174), and it is given by:

$$\eta = \frac{I_1}{I} = \sin^2 \left\{ \frac{2.22}{\lambda} \sqrt{M_2 P_a \frac{L}{H}} \right\} \tag{2.19}$$

where P_a is the average energy flow or *acoustic power* (in J/s), L/H is the length to height aspect ratio of the sound field, and M_2 the acousto-optic *figure of merit*, which is completely determined by the crystal's material properties. The efficiency of the first diffracted order can approach 100 %.

Nevertheless, this is a result valid only for the ideal Bragg case of $Q \gg 1$. Practically, the crystals interactions limits the Q-value, then the higher orders are not fully suppressed. Beside, if the beam steering is obtained by Bragg diffraction, then the Bragg angle for ideal operation changes (2.18), this implies that the first-order efficiency decreases accordingly (equation 2.19). Therefore power stability of the deflected beam is enhanced at the expense of the diffraction efficiency. By using *anisotropic* crystals, it is possible to reduce this efficiency decrease. In that crystals the diffraction efficiency can be stable over a relatively wide acoustic frequency band ($\lesssim$ one octave).

2.3 Introduction to the experimental theoretical outcomes

In this section we give the phenomenological description of the nonlinear dynamics of a micro or nanometric dielectric particle catched inside a landscape optical potential, created by an IR laser steered by means of an Acousto-Opto Deflector (AOD: see section 2.2.3.4). We have dedicated section 2.4 to theoretically derive and experimentally demonstrate the new effect discovered from us, named Stochastic Resonant Damping (SRD), which is in contrast with the phenomenon of stochastic resonance (SR). The SRD concerns a minimization of the variance of the detected output position, while the SR refers to a maximization of the SNR. Thus, in section 2.5, we report the experimental demonstration of the two phenomena (SR vs SRD), which coexist in the same system, but at different regimes. Afterwards, in section 2.6, we show that a maximization of the SNR can be observed even in a monostable optical system. We consider this phenomenon directly related with the stochastic resonance (SR). Therefore, we determine that such a behaviour is the same as that SR observed in a bistable system. Finally, in section 2.7 we give the details about the technique developed in order to exactly detect the position of the particle beyond the practical limit imposed by the sensitivity range of the electronic device used for this purpose (see section 2.2.2). This method exploits the channel crosstalk to 10-fold increase the spatial detection range, from 150 nm up to 1500 nm.

2.3.1 Optical setup

The optical trapping setup illustrated in Figure 2.14 is a PFM as the general one described in section 2.2.3, but with some modifications and additional elements to perform our experiments. In the next sections, we always refer to this optical geometry to describe the physical results obtained.

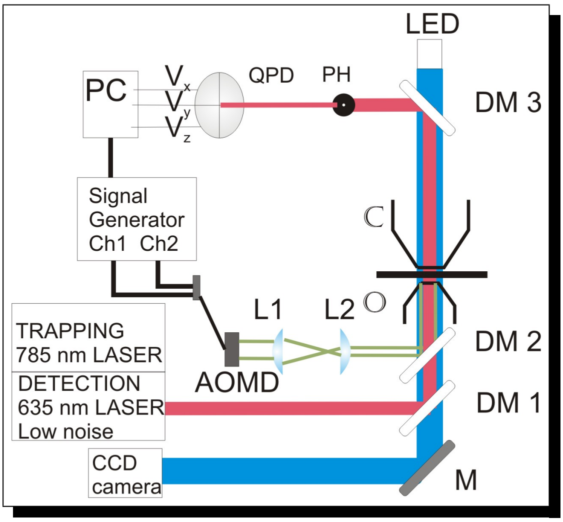

Figure 2.14: Experimental setup: O and C are objective and condenser, respectively; DM_1, DM_2, and DM_3 are dichroic mirrors; M is mirror; AOM/D is acousto-optic modulator/ deflector; L_1 and L_2 are lenses of an optical system which conjugates the output plane of the AOM/D and the input plane of the objective O; PH is a pinhole;

In this experimental assay a micrometer polystyrene particle is considered as the probe in the PFM geometry. The particle's forward scattering light is detected by a proper device. A NIR laser beam (Microlaser 785 nm, 30 mW at the sample) steerable along the x-direction by an AOD (AOM/D ISOMET LS55 NIR) was inserted into the beam path in order to create a movable optical trap. Two lenses, L_1 and L_2 were inserted along the IR light path, which conjugate the output plane of the AOD and the input plane of the objective O. The AOM/D input voltage was controlled by an arbitrary waveform generator (Tabor Electronics, WW 5062). The trap position depends linearly on the beam deflection, which we control through the AOD input voltage. The probe position detection is realized by a red beam (635 nm) proceeding from a low noise laser (Coherent, Lablaser 635 nm, ultralow noise), which is focused by a microscope objective (O, 100×, numerical aperture(NA) =1.3, Nikon). The forward scattered light was collected by a 40× objective (C, 40×, NA=0.75, Olympus UPlanFI) and detected by a Quadrant Photo Detector (QPD labeled as New Focus 2911). Besides, the sample probe was fixed on a piezoelectric stage which allows for

3D nanometric displacements. The resulting sum and differential signals are then transferred through an analog to digital conversion card to a computer for analysis (National Instruments 6270 A/D converter card). The white light proceeding from the LED into the probe, was collected by the objective, reflected by a dichroic hot mirror (cutoff wavelength 580nm, Thorlabs, FM02), and focused by a 200 mm lens onto a CCD camera (Rister, CCD 3035) [Figure 2.14]. The magnified image was then displayed on a Liquid Crystal Display (LCD) screen. We calibrated the trap displacement for small deflection angles, when the QPD response is linear, by using standard optical tweezers calibration techniques, (175)(176)(177), and then we linearly extrapolated the position of the trap to larger trap displacements (see section 2.7)(150).

2.4 Stochastic Resonant Damping: theory and experiments

2.4.1 Introduction

The presence of noise is ubiquitous in natural, social, and technological phenomena, ranging from nanoscopic systems such as biomolecules and nanodevices to macroscopic systems such as financial markets and human organizations. Noise introduces disorder and random fluctuations into any type of system; and often this is deleterious for the system's performance.

We report the theoretical study and the experimental observation of the situation when the confinement effort is increased at a fixed intrinsic and parametric noise level. Counter-intuitively, we show that in most cases an increased confinement effort over a certain threshold leads to a poorer system's performance. More specifically, we show that the minimum output variance is typically, but not always, achieved for a finite confinement effort, and therefore to increase the confinement effort over this threshold value leads to a poorer performance. This feature derives from the interplay between the *intrinsic noise*, whose characteristic frequency depends on the confinement effort, and the *parametric noise* of the confinement effort exerted on the system. We name this effect *stochastic resonant damping* because of its similarities to stochastic resonance; however, while stochastic resonance is concerned with the maximization of the SNR (2), stochastic resonant damping is concerned with the minimization of the system's output variance. We use a mathematical model that is linear and exactly solvable, but the main characteristics are also observed under more arbitrary conditions. We experimentally verify our prediction on a physical model system based on a colloidal particle held in an oscillating optical trapping potential. We finally show how stochastic resonant damping can be useful for the study of phenomena in various fields.

2.4.2 Mathematical Model

We consider a system whose behavior can be described by the following Langevin equation

$$\dot{x}(t) + C[x(t) - x_0(t)] \quad = \quad Dh(t). \tag{2.20}$$

The intrinsic noise is driven by a white Gaussian random process $h(t)$ such that $< h(t) >= 0$ and $< h(t+\tau)h(t) >= \delta(\tau)$; D determines the intensity of the noise. The system is constrained by the restoring term $C[x(t) - x_0(t)]$, whose equilibrium position $x_0(t)$ can vary over time either deterministically or randomly. The value C defines the confinement effort, *i.e.* a measure of the effort applied to the system for its confinement.

The choice of this model is motivated by the fact that it is exactly solvable and readily experimentally implementable. This permits us to directly compare theoretical and experimental results. As we will see in more detail in the experimental section, Eq. (2.20) describes an overdamped Brownian motion in the presence of an oscillating harmonic potential: $x(t)$ is the position of a Brownian particle with diffusion coefficient $D^2/2$ in the presence of a harmonic trapping potential characterized by a fixed stiffness proportional to C and an oscillating center $x_0(t)$. In the case this potential is generated by an optical trap, C is proportional to the optical trapping power and inversely proportional to the viscosity.

We are interested in studying the output variance σ_x^2 of the system with modulation of the trap position as a function of C for a given $x_0(t)$. $x_0(t)$ can be either a deterministic or a stochastic function. Solving (2.20) in the Fourier domain leads to:

$$X(f) = \frac{DH(f) + CX_0(f)}{C + i2\pi f}, \tag{2.21}$$

where $H(f)$, $X(f)$, and $X_0(f)$ are the Fourier transform of $h(t)$, $x(t)$, and $x_0(t)$. In absence of modulation, *i.e.* $x_0(t) \equiv 0$, the PSD is: $P_x(f) =< H(f)^\dagger H(f) >= D^2/(C^2 + 4\pi^2 f^2)$, where the dagger represents complex conjugation. It describes the intrinsic system noise in the presence of a confinement potential and is characterized by the cutoff frequency $f_c = C/2\pi$.

Using Parseval's theorem we obtain

$$\sigma_x^2 \;=\; \frac{D^2}{2C} + \int_{-\infty}^{+\infty} \frac{C^2}{C^2 + 4\pi^2 f^2} < |X_0(f)|^2 > df, \tag{2.22}$$

where the first term represents the *intrinsic noise* contribution, and the second term the *parametric noise* contribution. It follows straightforwardly that the total variance in the externally modulated system always exceeds the intrinsic noise. The output response depends on the power spectral density of x_0 describing the movement of the equilibrium position.

First we consider the case when $x_0(t)$ is a white Gaussian random process with $< |X_0(f)|^2 >= N^2$; then

$$\sigma_x^2 = \frac{D^2 + N^2 C^2}{2C} \tag{2.23}$$

For increasing confinement effort C, the output variance initially decreases and then it increases. This behavior can be explained as follows: while the confinement effort C increases, the intrinsic noise cutoff frequency f_c increases as well and therefore more components of the parametric noise have pronounced effect on the system. However, in this case the power of the noise is infinite, while in the real cases it is finite. In particular, the output variance in this case diverges for C tending to infinity, while this never happens for real noises that do have a cutoff frequency. Therefore, in the following examples we will consider noises with finite variance.

In the case of the equilibrium position moves harmonically, $< |X_0(f)|^2 >= A^2 \left[\frac{1}{2}\delta(f - f_0) + \frac{1}{2}\delta(f + f_0)\right]$ (notice that its variance is normalized to A^2) and

$$\sigma_x^2 = \frac{D^2}{2C} + A^2 \frac{C^2}{C^2 + 4\pi^2 f_0^2}. \tag{2.24}$$

In Fig. 2.15(a) the system variance σ_x^2 as a function of C and the forcing frequency f_0 is represented. The σ_x^2 diverges for vanishing C, because the confinement is lost. For very low forcing frequencies ($f_0 << \frac{C}{2\pi}$) as well as for high forcing frequencies ($f_0 >> \frac{C}{2\pi}$) σ_x^2 monotonically decreases with increasing the confinement effort C. However, there is a range of frequencies f_0 when a minimum of the output variance can be achieved for a finite value of C.

This effect, which we name *stochastic resonant damping*, is similar to stochastic resonance. Both indeed are due to a pseudo-resonance between the forcing frequency f_0 and a packet of frequencies from the range of intrinsic frequencies of the system noise, whose cutoff is $f_c = C/2\pi$. The difference is that stochastic resonance is concerned with a maximum in the SNR, while stochastic resonant damping is concerned with a minimum of the output variance. Interestingly enough, the two phenomena may occur simultaneously in the same system, although typically in quite different parameter regimes; this should be object of further studies. At a modulation frequency $f_0 = 1\,Hz$ the squeezing of the output variance is observed at $C = 2$, corresponding to the intrinsic system noise cutoff frequency $f_c = 1/\pi\,Hz$. Fig. 2.16 illustrates the counterintuitive aspects of ***stochastic resonant damping***: while the effort made to increase the confinement is increased the system output variance first diminishes (comparison between Fig. 2.16(i) and 2.16(ii) and then starts growing again (comparison between Fig. 2.16(ii) and 2.16(iii). Hence, in this simple case of harmonic modulation of the equilibrium position the system reveals a unexpected behavior: the more effort (over a certain threshold) is exerted to confine the system, the less confinement is achieved.

Noises occurring in nature are typically more complex than a harmonic modulation.

Biological transport phenomena work in the presence of thermal noise and internal, generally correlated, random noise of biological origin, such as the hydrolysis mechanism Adenosine triphosphate (ATP) (25). It is therefore important to analyze also the movement of the equilibrium position of the system governed by a colored noise. We therefore consider the simplest case of a colored Gaussian forcing with PSD $< |X_0(f)|^2 >= A^2 f_0/\pi(f_0^2 + f^2)$ (notice that its variance is again A^2 and f_0 is its characteristic frequency). The system variance is now

$$\sigma_x^2 \quad = \quad \frac{D^2}{2C} + A^2 \frac{C}{C + 2\pi f_0}. \tag{2.25}$$

In Fig. 2.15(b) the system variance σ_x^2 as a function of C and the characteristic frequency f_0 is represented. The overall behavior is similar to the one presented in Fig. 2.15(a) for harmonic forcing. The value of the confinement effort C_{opt} which provides a minimal variance as a function of the characteristic frequency f_0 and the noise power A^2 of x_0:

$$C_{opt} = \begin{cases} +\infty & \text{for } f_0 A^2 < D^2/4\pi \\ 2\pi f_0 D/(2\sqrt{\pi f_0} A - D) & \text{for } f_0 A^2 \geq D^2/4\pi \end{cases} \tag{2.26}$$

In Fig. 2.15(b) the thick curve shows the behavior of C_{opt}.

Until now we have only considered a noise of constant intensity, *i.e.* $A^2 =$ constant. If we now explore how output the variance σ_x^2 varies as a function of the noise intensity A^2, the σ_x^2 increases with the increase of the noise intensity A^2. We find that the variance minima becomes deeper as the noise intensity grows. The depth of the variance minima can be defined as $\sigma_x^2(C_{opt})/\sigma_x^2(C = +\infty)$. Hence, the present result is more evident for highly noisy systems.

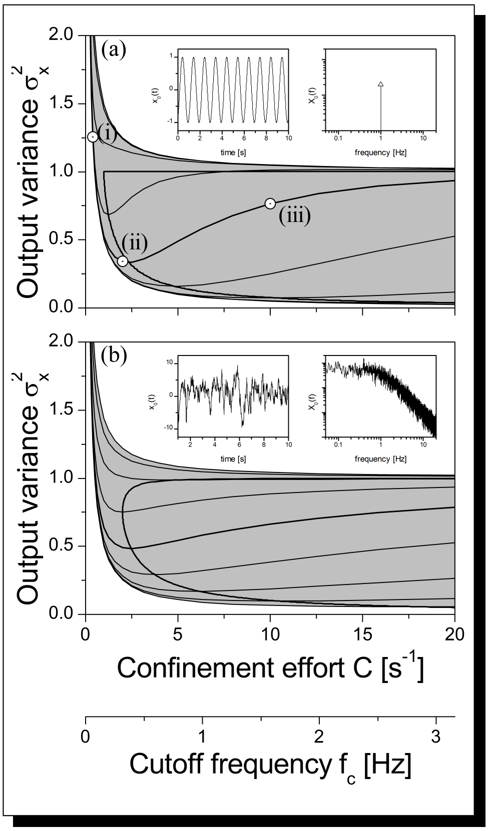

Figure 2.15: Output system variance σ_x^2 as a function of the confinement effort C ($D = 1$, $A = 1$) for harmonic (a) and colored Gaussian (b) parametric noise for various values of the frequency f_0: from bottom to top $f_0 = 100, 31, 10, 3, 1$ (thick curve), $0.3, 0.1, 0.03, 0.01 Hz$. The thick line indicates the σ_x^2 minima. The shaded area represent the range of accessible output variance for a given value of the confinement effort. The additional axis shows the system intrinsic noise cutoff frequency f_c. Insets: a typical example of x_0 in time and frequency domain ($f_0 = 1$).

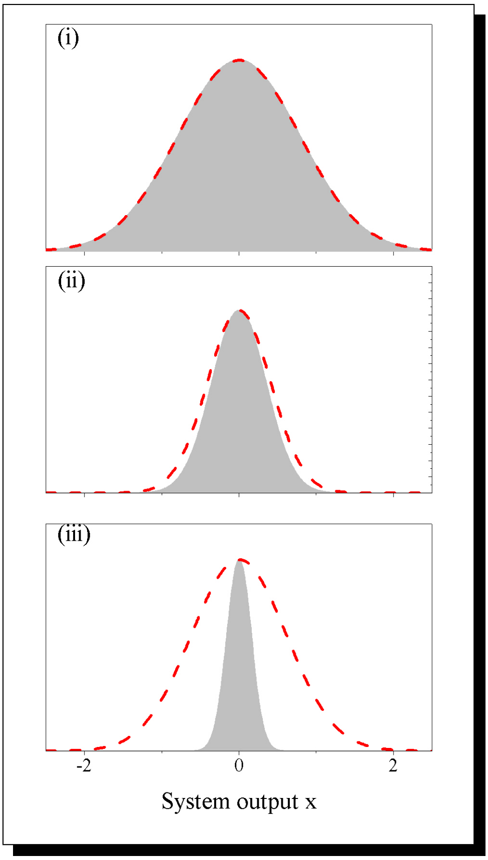

Figure 2.16: Intrinsic system output (gray filled area) and system output in the presence of a sinusoidal modulation (f_0 =1, D=1, A=1) (red dashed curve) for three states of the system, indicated by dots in Fig. 2.15(a) for the modulation frequency f_0=1Hz: (i) C=0.4 (f_c=0.064 Hz), (ii) C=2 (f_c=0.32 Hz) corresponding to the absolute variance minimum, and (iii) C=10 (f_c=1.6 Hz). The output variance always exceeds the intrinsic variance.

2.4.3 Experimental Verification

As we anticipated above, a paradigmatic system that behaves according to the presented theory is a Brownian particle held in an oscillating trapping potential. We have therefore used such a physical system in order to verify our predictions. We implemented this system using the optical trap whose instantaneous center position is controlled by steering the focussed optical beam. We employed the same optical configurations described in sections 2.3.1. For further details see (149). When equation (2.20) describes the Brownian motion of a particle in an oscillating potential, the parameters have the following physical meaning: $C = k/\gamma$, where k is the stiffness of the trap, γ is the friction coefficient of the particle, $D = \sqrt{2k_B T/\gamma}$, $k_B = 1.3807 \cdot 10^{-23}\, J/K$ is the Boltzmann constant, γ=$6\pi r\eta$ is the friction coefficient of the particle, r is the radius of the particle, η is the viscous coefficient of the liquid, and T is the absolute temperature of the system.

2.4.4 Experimental Setup

The optical geometry of the PFM employed for these experiments is the same of section 2.3.1 The sample solution was prepared by adding a small amount of polystyrene beads (radius $r = 295\, nm$, Kisker-Biotech GmbH) to a 10% sodium dodecyl sulphate sterile aqueous solution. A drop (about $10\, \mu l$) of the resulting solution was placed between two coverslips (thickness $80\, \mu m$) separated by a $50\, \mu m$ spacer and sealed with water insoluble silicone vacuum grease to prevent evaporation. This sample was placed onto a custom-made sample holder on top of an inverted microscope equipped with an oil immersion microscope objective (×100, $NA = 1.25$, Comar). The sample was illuminated from the top with white light for visualization by means of a CCD camera. The particle concentration was sufficiently low to guarantee that there was only a single particle within the field of view. A single bead was trapped by focusing the optical beam with the objective near the upper coverslip surface in order to increase the drag force acting on the particle and therefore to have a more stable trapping. This optical beam was produced by a laser ($\lambda = 785\, nm$, maximum power $95\, mW$, MicroLaserSystem). Nanometer position detection was achieved using the forward scattered light of a second beam, produced by a low-noise laser ($\lambda = 635\, nm$, maximum power $5\, mW$); its power at the sample was kept low in order to not affect the trapping of the probe.

The forward scattering of the detection beam was collected by a condenser objective (×40, $NA = 0.75$, UPlanFI) and projected onto a Quadrant Photo Detector

(QPD, New Focus 2911). The QPD measured the changes in the interference pattern and converted them into three signals proportional to the position of the particle in the trap. These signals were sampled and acquired into a computer by an acquisition card (62621E, National Instruments). The sampling rate was $f_s = 2\,kHz$. This is sufficiently higher than the corner frequency of the system f_c and permits us to acquire the dynamics of the particle motion for the optical trap calibration (176). In the study of the variance, since we are measuring the particle position distributions, we do not need to follow the dynamics of the particle. Therefore we can use a sampling rate that is much slower than the noise characteristic frequency. The modulation of the position of the optical potential was achieved by an AOD (AOM/D ISOMET LS55 NIR). This was inserted along the $785\,nm$ laser beam path and was used to steer it along the x direction. The y position of the trap was unaffected. The AOM/D input voltage was controlled by an arbitrary waveform generator (Tabor Electronics WW 5062) which allowed charging arbitrary signals. The power of the $785\,nm$ beam before the objective was adjusted between $3\,mW$ to $35\,mW$ by the AOD.

2.4.4.1 Colored Gaussian noise generation

A noisy sequence with any PSD can be generated starting from a sequence of independent normally distributed random variables $\zeta_{n\Delta T}$, *i.e.* $< \zeta_{n\Delta T} >= 0$ and $< \zeta_{n\Delta T}\zeta_{(n+m)\Delta T} >= \delta(m)$, where n and m are integers and ΔT is the sampling time. The most general approach involves: (1) to apply the Fourier-transformation to the signal ζ_{nT}; (2) to multiply the resulting signal by a frequency-domain filter with the desired PSD; (3) to perform the inverse Fourier-transformation of the resulting signal. The resulting signal has the desired PSD. A mathematically equivalent approach can be followed in time-domain by applying a time-domain filter. To generate the colored Gaussian noise, we used a Finite Impulse Response (FIR) filter of the first order:

$$x_{0,(n+1)\Delta T} = \alpha x_{0,n\Delta T} + A/\sqrt{1-\alpha^2}\zeta_{(n+1)\Delta T}, \tag{2.27}$$

where A is the variance of $x_{0,n\Delta T}$, and α is its autocorrelation. This filter produces a low-pass signal whose cutoff frequency depends on the value of T and α: $f_0 = -\ln\alpha/\Delta T$.

2.4.4.2 Data analysis

First for each value of the trapping power a series of data was acquired in absence of modulation with a sampling rate $f_s = 2kHz$. The stiffness of the optical trap was measured in the x and y directions using the autocorrelation function method (176). Furthermore, we have verified that no cross-correlation between the two direction exists, which shows that the modulation does not introduce a rotational force field and that the results along the y direction are independent from the data along the x direction (176), (178). The values of the stiffness constant were found to be linear with the trapping optical power: $k_x \approx k_y$. In the calibration process the value of the friction coefficient of the particle γ takes into account the correction of the viscosity coefficient due to the proximity of the surface (175).

For each data point in Figures 2.17, 2.19 and 2.18 (see below), 12 datasets of 10000 samples were acquired with a sampling rate $f_s = 2\,kHz$. The values of the output variance σ_x^2 and σ_y^2 are the average over these datasets. The error bars were calculated as the standard deviation of the measurements.

2.4.5 Experimental Results

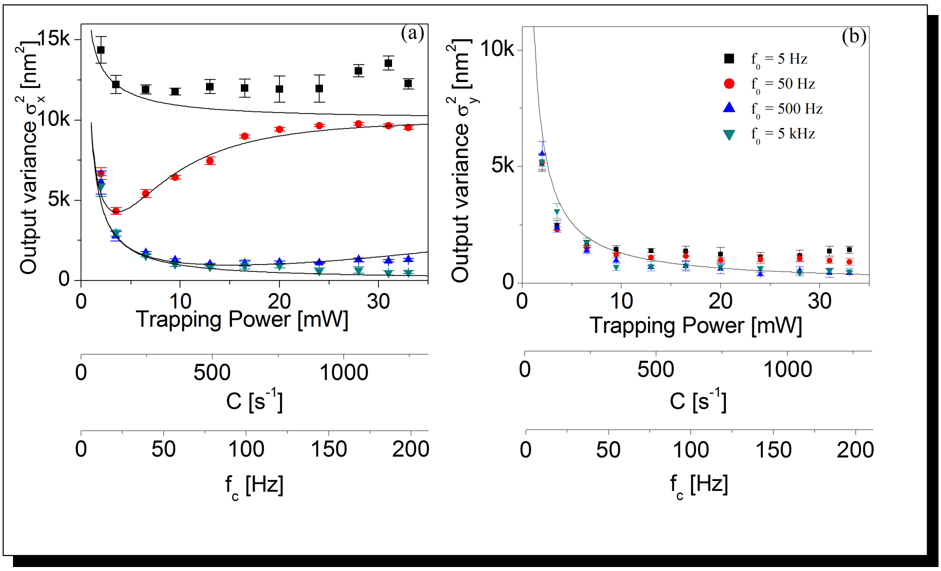

Figure 2.17: (a) Experimental and theoretical σ_x^2 as a function of the laser power in the presence of harmonic modulation of the trap center. From the bottom to the top the various sets of values correspond to $f_0 = 5,\ 50,\ 500,\ 5000,\ Hz$. The bar represent one standard deviation. The solid lines represent the theoretical prediction for the experimental parameters ($k = 0.4\,pN/\mu m\, mW \times$ TrappingPower $[mW]$, $\gamma = 1.1 \cdot 10^{-8}\, Ns/m$, $A = 100\, nm$). The disagreement between experimental data and theoretical results for right end of the $5\,Hz$ dataset is observed because for such values of the confinement effort and intrinsic noise frequency the trapping potential is not harmonic anymore. (b) Data for the non-modulated direction y. The two additional axes show the value of the confinement effort and the corresponding cutoff frequency of the intrinsic noise.

Fig. 2.17a illustrates the experimental results obtained with sinusoidal modulation of the trap center: $x_0(t) = \sqrt{2}A\sin(2\pi f_0 t)$ with $A = 100\, nm$ and $f_0 = 5,\ 50,\ 500,\ 5000\, Hz$. The continuous lines represent the theoretical prediction according to Eq. (2.24). The experimental results are in very good agreement with the theoretical predictions for all the range of the trapping power, except for very low values. The maximal value of the dip at the dependence was found at the modulation frequency $f_0 = 50\, Hz$ at the confinement effort of $C = 300\, s^{-1}$ when the corner frequency of the intrinsic noise of the system is $f_c = 60\, Hz$. As for the theoretical results, the modulation frequency to observe the stochastic resonant damping is higher than f_c. Hence, the stochastic resonant damping has a measurable value, when the external source of modulation induced the movement of the probe with frequencies that are not present in the spectrum of the unmodulated internal motion. To understand what physical quantities produce such phenomenon, we can give an intuitive picture of the situation. When there is *stochastic resonant damping* in an overdamped system the frequency of the intrinsic noise is such that in the time it takes the center of the trapping potential to move from one side to the other the particle has time to follow it only partially. Again this picture makes clear that stochastic resonant damping, such as stochastic resonance, is not a real resonance but only a pseudo-resonance.

The trap was modulated only along the x direction, and the y movement of the particle was used to monitor for the same experimental condition the behavior of the system in the presence of only the *intrinsic noise*. As expected the system variance σ_y^2 (Fig. 2.17b) increases with decreasing confinement effort and this behavior is independent from the modulation.

Fig. 2.19b illustrates the experimental results for the correlated Gaussian modulation of the trap center. In this case the trap position moves as illustrated in the inset of Fig. 2.15b with $A = 70\,nm$ and $f_0 = 5$, 50, 500, $5000\,Hz$.

There is very good agreement between the theoretical and experimental results. Again, as Fig. 2.19b shows, for the unmodulated direction the variance grows with decreasing confinement effort. Finally, in Fig. 2.18 the dependencies of the confinement with the noise amplitude are presented for $A = 55,\ 70,\ 85\,nm$. As it was mentioned in the theoretical part, the stochastic resonant damping decreases with decreasing noise amplitude.

As it can be seen in all the experimental figures, the agreement between experimental data and theoretical results gets worse for very low noise frequency and high confinement effort. For such parameters the optical trap cannot anymore be approximated as an harmonic potential, the system tends to become bistable, and Kramers transitions take place.

2.4.6 Conclusions

Usually in the presence of a background noise an increased effort put in controlling a system stabilizes its behavior. Rarely it is thought that an increased control of the system can lead to a looser response and, therefore, to a poorer performance. Strikingly there are many systems that show this weird behavior. Examples can be drawn from physical, biological (179), and social systems (180). In scanning probe microscopy techniques, such as Atomic Force Microscope or Photonic Force Microscope, an increased control over the probe position does not necessarily improve resolution. On ecosystems the implementation of conservation policies can have unintended and perverse consequences (179). Analogously, on social systems enforcement does not always achieve the desired effect, such as has been shown on ethnic/cultural conflicts (180) and economical systems (181, 182). We propose a simple and general mechanism underlying such behaviors: such a mechanism, named *stochastic resonant damping*, can be provided by the interplay between the background noise and the control exerted on the system.

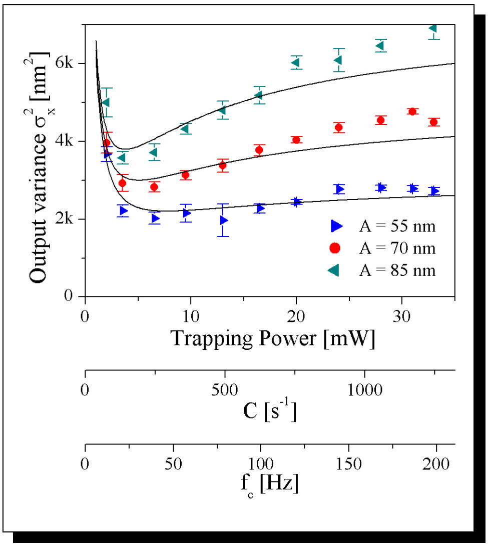

Figure 2.18: Experimental σ_x^2 as a function of the noise amplitude. Various sets of values are presented for $A = 55, 70, 85\, nm$. The bars represent one standard deviation. The solid line represent the theoretical prediction for the experimental parameters ($k = 0.7\, pN/\mu m\, mW \times \text{TrappingPower}\, [mW]$, $\gamma = 1.9 \cdot 10^{-8}\, Ns/m$). The two additional axes show the value of the confinement effort and the corresponding cutoff frequency of the intrinsic noise.

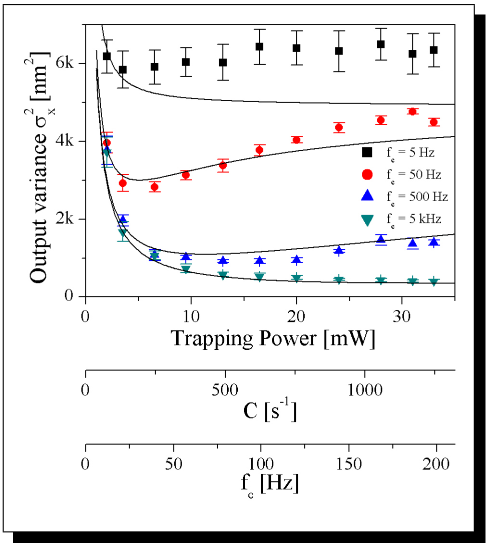

Figure 2.19: Experimental and theoretical σ_x^2 as a function of the trapping power obtained with colored Gaussian forcing of the equilibrium position. Various sets of values are presented for $f_0 = 5, 500, 50, 5, Hz$. The bars represent one standard deviation. The solid line represent the theoretical prediction for the experimental parameters ($k = 0.7\, pN/\mu m\, mW \times \text{TrappingPower}\, [mW]$, $\gamma = 1.9 \cdot 10^{-8}\, Ns/m$, $A = 70\, nm$). The disagreement between experimental data and theoretical results for right end of the $5\, Hz$ dataset is observed because for such values of the confinement effort and intrinsic noise frequency the trapping potential is not harmonic anymore. The two additional axes show the value of the confinement effort and the corresponding cutoff frequency of the intrinsic noise.

2.5 Stochastic Resonant Damping versus Stochastic Resonance

After having detected the new phenomenon that we called SRD, as described in the previous Section, we performed further experiments and numerical modelling with the aim of comparing, or contrasting, this phenomenon with that of the SR (157, 183) As previously pointed out, while SR is concerned with the maximization of the SNR, the SRD is concerned with the minimization of the output variance. We experimentally observed how in a system characterized by a harmonic potential only the SRD is present; there is no SR because the SNR diverges and therefore no maximum is present. In contrast, in a system characterized by a non harmonic potential, both SR and SRD may be found, however typically in different regimes. The experiments were performed by studying the behavior of a brownian particle in an optical potential.

2.5.1 Theoretical model and simulations of Stochastic Resonance in a double well system

In order to clearly elucidate that SRD and SR are two different effects coexisting in the same system, we performed some simulations of a brownian particle jiggling in a double well potential. An analytical formula of the SNR in a double well potential under the right hypothesis, has been obtained in previous works. Now let's consider the theoretical description of a double well system, where we suppose the particle is trapped and jiggling from one well to the other.

$$\begin{aligned}
D &= \frac{K_B T}{\gamma} && (2.28)\\
\dot{x}(t) &= -\frac{k}{\gamma} V'(x) + \varepsilon(t) && (2.29)\\
V(x) &= -\frac{(x-x_0)^2}{2} + \frac{(x-x_0)^4}{4} && (2.30)\\
\mathit{where:} & && \\
x_0 &= A_0 \cos(\Omega t + \phi) && (2.31)\\
\langle \varepsilon(t)\varepsilon(0)\rangle &= 2D\delta(t) && (2.32)
\end{aligned}$$

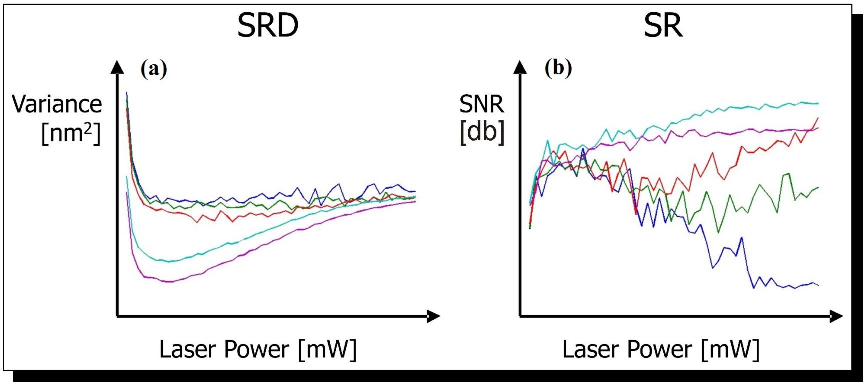

Figure 2.20: Panel (a) displays the numerical results of the Langevin equation for a monostable system described from the equation 2.20, while panel (b) shows the numerical results of the system from the equations set 2.28. In both situations, the center trap is modulated sinusoidally. The blue, green, red, blue-light and magenta curves (from the highest variance values to the lowest) represent modulation frequencies 1, 3, 5, 10, 20 Hz.

In the model (2.28) ε represents the thermal noise, k is the trap stiffness, and γ the friction coefficient of the particle in the medium. $V(x)$ is the mathematical description of the potential, which corresponds to an infinite double well system. x_0 is the center of the entire system, which is modulated sinusoidally.

We computed the Langevin equation 2.29 for a double well potential modulated by a sinusoidal external forcing at different frequencies. Our simulation shows clearly that SRD phenomenon is found in another frequency regime than SR (Figure 2.20). As it can be seen, at low frequencies (1 or 3 Hz) the output position variance decreases monotonically, contrarily the SNR shows a maximum for a certain trap stiffness. Another scenario is given for the SRD, which presents a minimum in the output variance at the frequencies of 20 or 10 Hz, whereas for the SR no maximum can be observed.

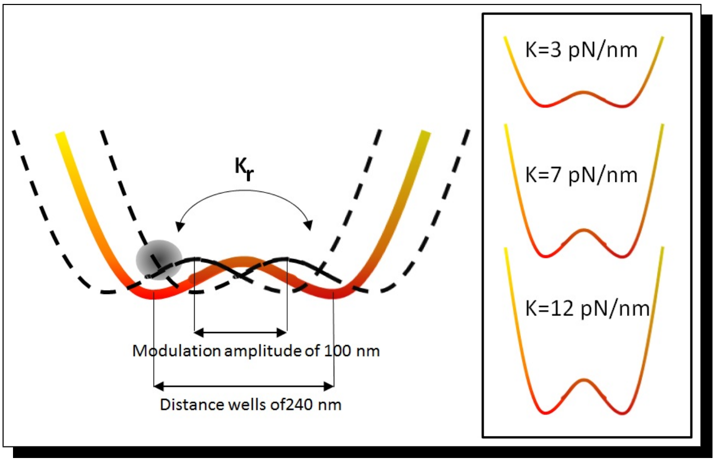

Figure 2.21: Concept of the double well optical landscape. The particle is jiggling from one well to the other. Dashed line indicate the movement of the center of 100 nm. The distance from the minimums is fixed at 240 nm. The sides graphs show the shapes changes due to the stiffness.

2.5.2 SR in a double well potential moved harmonically

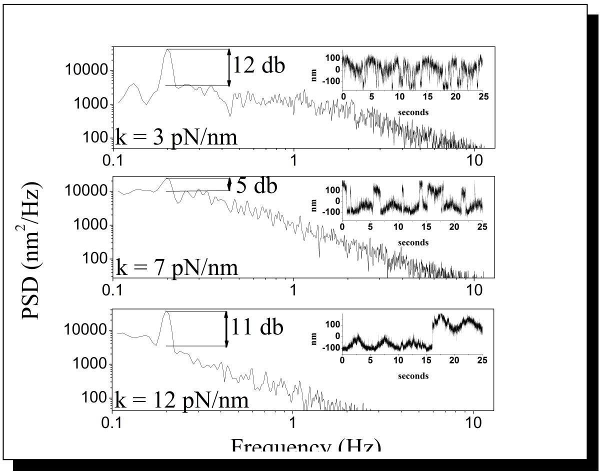

Figure 2.22: Power spectral density and traces of features SR. The particle is jiggling in a double well potential where the center trap is modulated sinusoidally at 0.2 Hz for three different powers (from the top to the bottom 3, 7, 12 pN/nm).

As explained in Chapter 1), the phenomenon of Stochastic Resonance (SR) has been extensively investigated in many systems (31, 38, 49, 52, 63, 86, 92, 94, 152, 184, 185). In the last decade, numerous experiments by means optical tweezers has been effectively conducted in order to observe kramers transitions and resonant phenomena. SR usually takes place in a bistable system, where a weak periodic signal applied in counter-phase to the depth of each well, can be boosted by adding a right amount of noise to the signal. The frequencies in the noise corresponding to the original signal's frequencies will resonate, amplifying only the original weak signal (45, 186, 187). With this work, we experimentally observed the phenomenon of SR in a double well system created by an optical potential as described in section 2.3.1. At difference to many other investigations, we apply a variant strategy to impose the resonance conditions, as shown in Figure 2.21.

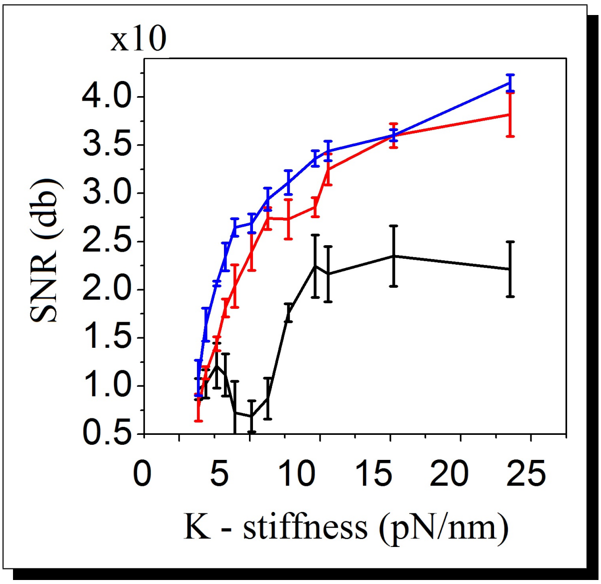

Figure 2.23: SNR of a double well optical potential versus the power stiffness "K", at three different frequency. Blue 200 Hz, red 20 Hz, black 0.2 Hz.

We modulated sinusoidally the center of the system with an amplitude (A) kept fixed at 100 nm, frequency of 0.2 Hz, the interwell distance was kept fixed at 240 nm with a potential barrier depending of the stiffness "K" (usually also depending from the distance between traps). The peak appearing in the power spectral density at the modulation frequency is a direct measure of signal to noise ratio. The stiffness value (K) is referred to each well. For a very low stiffness, the power of the intrinsic noise (Brownian motion) becomes stronger, then the particles could not feel anymore the modulation. The potential barrier is not high enough to prevent the free diffusion of the particle. Therefore, at stiffness from 1 to 2 pN, there is no modulation signal detected. At the modulation frequency applied the power spectral density appear flat. At K equal 3 pN/nm as shown in Figure 2.22(a), a strong signal is detected, which can be interpreted as a fingerprint of SR, because synchronized hopping events occur between the two wells. This assumption is confirmed when further increasing the stiffness to 7 pN/nm Figure 2.22(b), the delta spike measures 5 db, due to the fact that the signal is almost completely destroyed. The bottom plot in Figure 2.22(c) shows that the SNR measured is 11 db, so that for strong modulation in each well, no frequent hopping event occurs, because the potential barrier is so high compared with the intrinsic noise power. The complete description of the behaviour at different frequencies is reported in Figure 2.23, where it is possible to observe a clear maximum in the SNR at 5 pN and 20 Hz. While at 0.2 and 200 Hz only a monotonic behaviour is observed.

2.5.3 Experimental Results and discussion

A polystyrene particle of 0.6 μm diameter in a distilled water solution was trapped by a 785 nm IR laser beam. As described in section 2.2.3.4 an AOD was inserted in the optical path which steered the beam in x and y directions. An external sinusoidal forcing moved the center of the optical

Figure 2.24 shows our experimental results about a Brownian particle trapped in a single and double well potential modulated as described in the previous section. We compare Stochastic Resonant Damping with the classical Stochastic Resonance. We know that SRD is concerned with the minimization of the output variance, whereas SR is concerned with the maximization of the SNR.

The panel (a) clearly shows that in a single well the SNR is a monotonic function of the trap stiffness. Although the curve for lower frequency at higher K seems to go slightly down, no evidence of a maximum in the SNR is observed.

In (c) the output variance with the relative standard deviation is calculated. As the behaviour of the blue curve shows, a minimum in the output variance is observed, which is the main effect of SRD. Any curve in this plot has a small variance, even at 0.2 Hz where the hopping from the two wells starts to manifest.

The (b) plot shows SNR for a symmetric double well potential where the center is steered sinusoidally. A maximum is observed at 5 pN/nm of the 0.2 Hz curve. Decreasing still more the trap stiffness the SNR can only decrease, because the traps become weaker and the intrinsic noise is more powerful than the modulation strength.

The (d) panel displays the output variance of the double well potential for any stiffness values. The standard deviation takes higher values due to the shape of the potential. Actually, in the double well, the barrier not always allows a transition to the other state. This fact is evident looking the curves at lower frequency where the particle feels more the external forcing. At higher frequencies the Brownian motion does not feel strongly the potential movements, because that frequency starts to be out of the sensitivity range represented by the plateau region in the PSD, just before the corner frequency (Figure 2.8).

From these results we can conclude that both phenomena SRD and SR are present in the double well system. Contrarily, in the single well potential we detected only the SRD, while SR was not observed. We want to highlight that our findings show clearly that SRD is still a more general effect than SR, and it works at different frequency regimes.

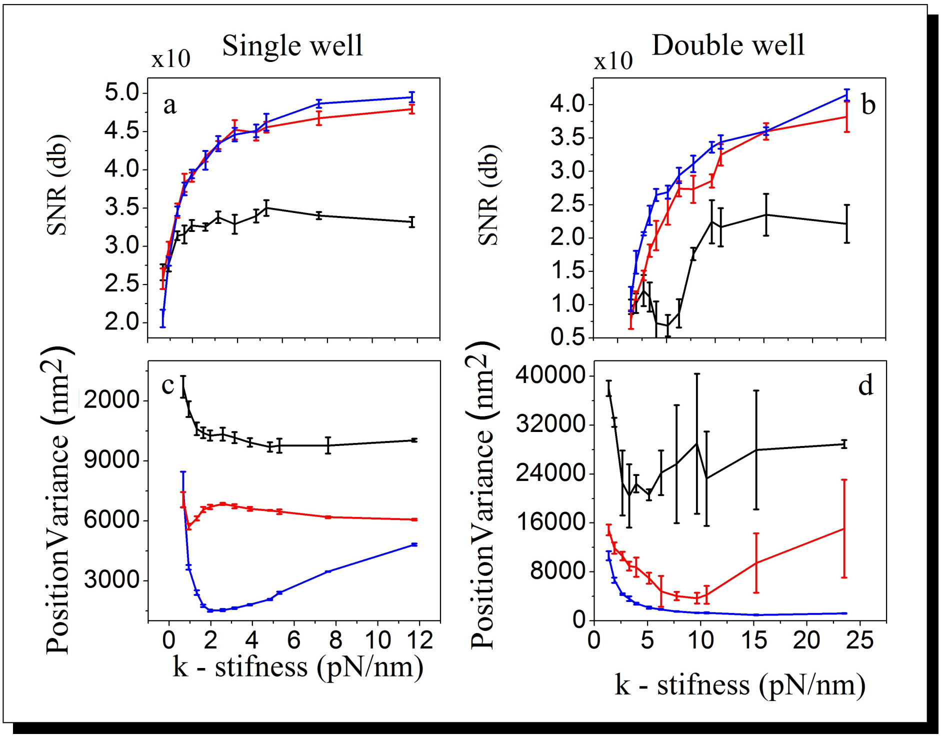

Figure 2.24: Experimental evidence of Stochastic Resonance vs Stochastic Resonant Damping: (a) SNR as a function of the trap stiffness for a single well system.(b) SNR as a function of K for a double well potential. (c) System output variance σ_x^2 for a single well. (d) System variance as a function of the trap stiffness for a double well potential. In each subplot, different curves are plotted for different values of the frequency f_0 of the external modulated forcing (blue 200 Hz, red 20 Hz, black 0.2 Hz).

2.6 Maximum in the Signal-to-Noise ratio in a monostable system

In the last decades, a long debate about the possibility to observe Stochastic Resonance in a monostable system, has been undertaken. A theoretical work of Vilar and Rubí in 1996 (6), has been a source of inspiration. The main results of that work are shown in Figures 2.25 2.26, which proved that SR can be achieved by means of a proper modulation of the potential shape. Actually, in Figures 2.25(a)(b), it is shown that the SNR for the three potential configurations is a divergent function. Anyway, for low noise, from 10^{-2} to 1, they have a distinct behaviour, thus it is normal to think that an oscillating potential between these three configurations, can present a maximum in the SNR function. As confirmed in the same work, the dynamics of a ferromagnetic particle under a modulated external magnetic field, exhibit a maximum in the signa-to-noise ratio as depicted in Fig. 2.26. Others works, which confirm the existence of stochastic resonance even in monostable systems, have been published by (96, 188). In the next sections we have experimentally proved that a maximum in the SNR can also be obtained in a nonlinear system represented by a paradigmatic brownian particle held in a cuartic monostable optical landscape.

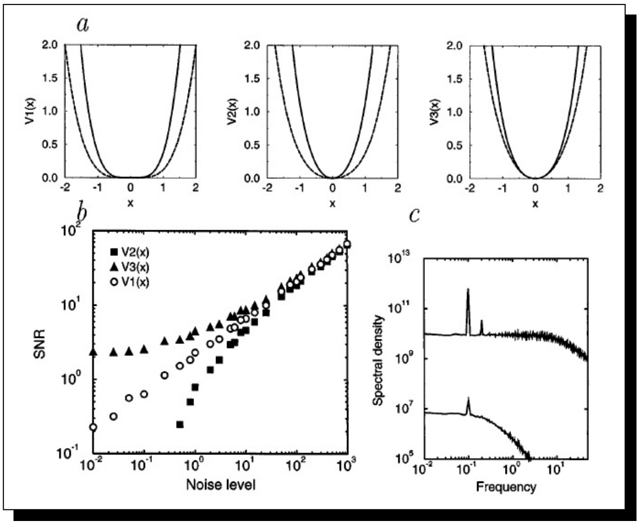

Figure 2.25: (a) Potentials $V_1(x)$, $V_2(x)$, $V_3(x)$ for the maximum value of $h_t(d)$ (solid line) and for the minimum value (dashed line).(b) Behavior of the SNR for the three potentials.(c) Power spectrum corresponding to $V_1(x)$ for noise strength D=0.1 and D=1000). Reported from (6)

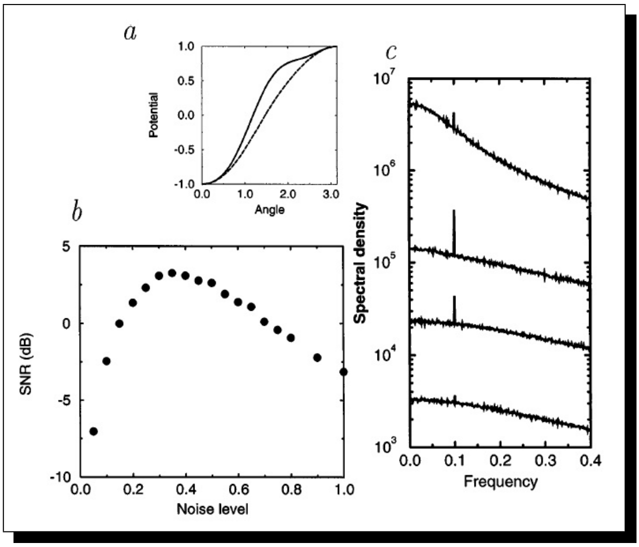

Figure 2.26: Potential energy of the ferromagnetic particle as a function of θ for the maximum value of $h_t(d)$ (solid line) and for the minimum (dashed line). (b) SNR for the previous values of the parameters obtained through computer simulations. (c) Power spectrum for noise strength D= 0.05, 0.15, 0.35, and 1. Reported from (6)

2.6.1 Mathematical description of a particle held in an oscillating cuartic optical potential

A mathematical description of a particle held in an oscillating monostable potential, can be provided by the classical langevin equation, which is often used to model dynamical systems such as a brownian particle in a given potential $V(x)$. In the equation 2.33 the term k represents the trap stiffness, γ is the coefficient friction and, considering the low Reynolds number (10^{-4}), we neglected the inertial term. The right-side of the eq. 2.33 $\eta(t)$ is a noise term driven from a gaussian random process. Furthermore, we consider the potential $V(x)$ as time-space dependent, with $V_1(x)$ in the case of an harmonic potential, while $V_2(x)$ when it is proportional to x^4. Besides, we assume that the center of the optical potential is a sinusoidal oscillating at frequency f_0, where $\omega_0 = 2\pi f_0$ and amplitude A 2.36.

$$\gamma\dot{x} + k\frac{dV(t)}{dx} = \eta(t) \tag{2.33}$$

$$V_1(x) = \frac{1}{2}(x - x_0)^2 \tag{2.34}$$

where $V_1(x)$ is an harmonic potential centered at x_0.

$$V_2(x) = \frac{1}{4}(x - x_0)^4 \tag{2.35}$$

where $V_2(x)$ is a potential proportional to x^4 and centered in x_0.

$$x_0 = A\sin(\omega_0 t) \tag{2.36}$$

2.6.2 Experimental procedures and Data analysis

The AOD inserted in the optical path, was driven by an input voltage signal proceeding from an arbitrary waveform generator. The latter was programmed by a custom built labview program, in order to modulate the deflection beam (see Fig. 2.14). For the data analysis, we employed the *power spectral density* method as described in section 2.2.2.1. At each position of the optical trap the PSD of the acquired time-series (sampling frequency $f_s = 2$ kHz, number of samples N_s=100000) was calculated and fitted to the theoretical Lorentzian shape, getting the value for the calibration parameters. The stiffness of the optical trap was measured in the "x" and "y" directions using the autocorrelation function method (176). Furthermore, we have verified that no cross-correlation between the two direction exists, which proves that the modulation does not introduce a rotational force field and that the results along the "y" direction are independent from the data along the "x" direction (176), (178). The values of the stiffness constant were found to be linear with the trapping optical power: $k_x \approx k_y$.

In the calibration process the value of the friction coefficient of the particle γ takes into account the correction of the viscosity coefficient due to the proximity of the surface (175).

2.6.3 Experimental outcomes

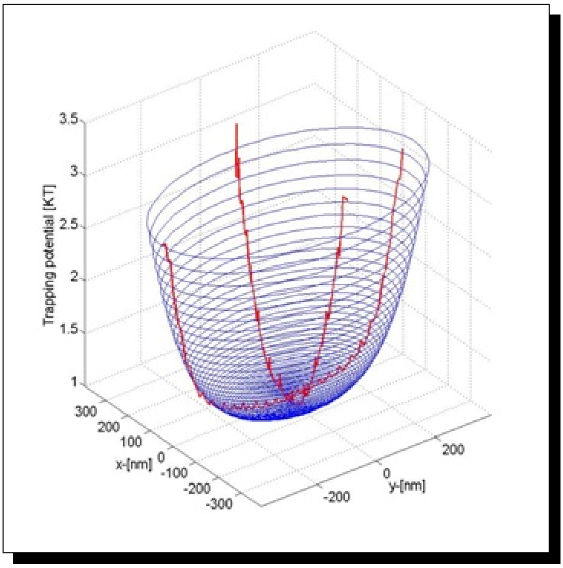

Figure 2.27: Experimental realization of an optical x^4 potential by an AOD.

Here, we report our experimental observation of a maximum in the Signal to Noise Ratio in a nonlinear monostable optical landscape potential (See Figure 2.27) (156) created by an AOD, as already described in section 2.3.1. In order to characterize our optical trap we performed a 3D position fluctuation analysis applying Boltzmann statistics to the movement of an optically trapped 600 nm polystyrene bead. The IR laser beam instead of remaining fixed (usually in a static harmonic optical trap it is focused onto one fixed point) is linearly steered at 50 KHz, forward an backward along a distance of 200 nm. The latter procedure allows us to create an homogeneous optical landscape for the diffusion particle. The application of sufficiently strong signal "x_0" drives the system out of the linear regime, going into the nonlinear region. Therefore, the SNR increases at the higher-order harmonics, *i.e.*, it results in a maximum of the SNR (Figure 2.28). Besides, it must be said that an experimental optical potential is intrinsically non linear, due to the very short focus distance into the fluidic chamber, and the numerical aperture of the objective. We use this nonlinearity to observe a maximum in the SNR. This is not a proper SR (such as from definition), because the intrinsic noise is not used in a cooperative way with the modulation signal in order to switch to another state, and no optical barrier is present. However, a maximum in the Signal to Noise Ratio has been observed, as never experimentally performed but only theoretically investigated (6, 96, 188).

In this experiment we modulate sinusoidally the center of the trap at a certain frequency and amplitude to detect a peak in the SNR. We determine that frequency about the corner frequency of the PSD of the particle position in the stationary optical potential. At each frequency we recorded the particle trace for 11 different amplitudes ranging from 80 to 640 nm. Figure 2.28 depicts the power spectral densities of the output intensity detected, at three different amplitude modulations $A_{mod} = 100, 240, 650$ nm, and frequency modulation of 20 Hz, which correspond to the points 1, 2, 3 in Figure 2.29. Finally, as displayed in Figure 2.28(a), we observed a clear maximum in the SNR of 38 db, for a modulation amplitude of 240 nm (Figure 2.29(a)). The same experiment was performed at 2 and 200 Hz but no evident maxima were observed. (Figure 2.29(b)).

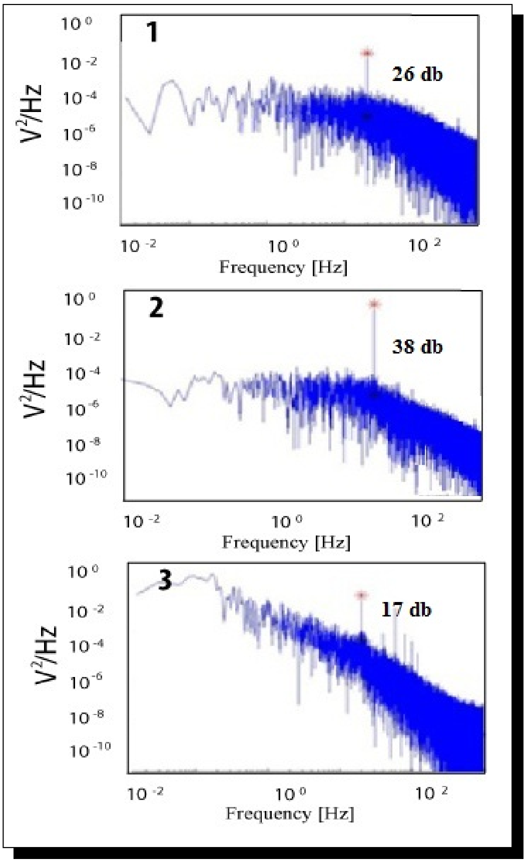

Figure 2.28: Power Spectral Densities for three amplitude sinusoidal modulation (from the top to the bottom A=100,240,650 nm)

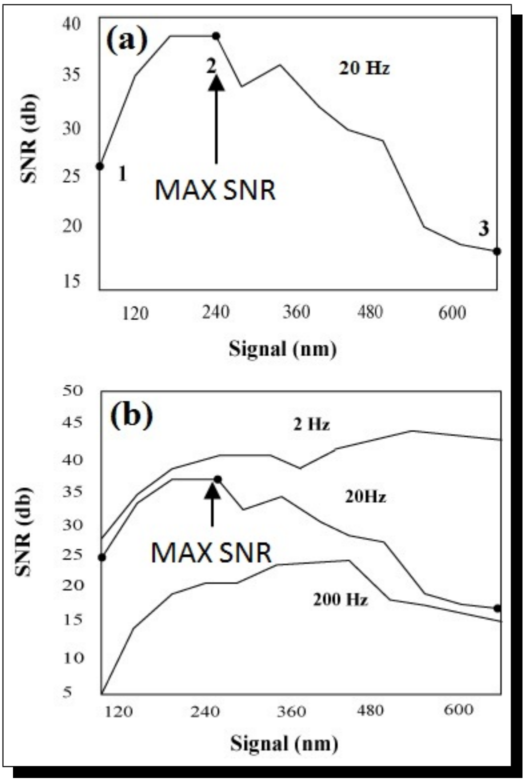

Figure 2.29: (a) SNR as a function of the modulation amplitude at 20 Hz frequency modulation. (b) SNR as a function of the modulation strength for three different frequencies (2, 20, 200 Hz).

2.7 10-fold increasing detection range in position sensing for photonic force microscope

2.7.1 Introduction

Since 1993 the PFM (189)(190) has become an important tool to measure forces and torques in microscopic systems and it has been used in many areas such as biophysics, colloidal physics, and hydrodynamics of small systems. A typical PFM setup comprises an optical trap (191)(192) that holds the probe particle, and a position sensing system, which uses the scattering of a beam illuminating the probe. The PFM relies on the analysis of the probe thermal fluctuations. (175)(176) The probe randomly moves due to the Brownian motion in the potential well formed by the optical trap. Near the center of the trap, the optical trapping potential is parabolic and the restoring force is linear in the displacement. The restoring force of the optical trap in each direction may be deduced from the three-dimensional (3D) position fluctuation spectrum. After this calibration procedure the measurement of an external force is reduced to the measurement of the position of the probe, in the range where the parabolic approximation is valid. The 3D position of the probe can be measured through the scattering of an auxiliary beam (detection beam) that illuminates the probe. The PFM has measured forces down to few femtonewtons, (193) and it has been lately applied to the measurement of torques in the range of few fN nm produced by vortex beams (194) or microscopic hydrodynamic flows (195). Usually the probe position is determined by measuring the Forward Scattering (FS) light transmitted through the probe. Backfocal plane interferometry with a QPD enables the 3D tracking of a trapped probe with nanometer precision at sampling rates up to megahertz (196)-(197). As pointed out in subsection 2.2.2 a QPD is a four-element photodiode array which gives three output signals-V_x, V_y, and V_z-proportional to the light intensity impinging upon it and associated with the displacement of the probe in the trap. In order to track the probe position unambiguously, the dependence of the output signals on the probe displacement must be known. Usually it is supposed that this dependence is linear, *i.e.*, V_x(x)=S_xx, V_y(y)=S_yy, and V_z(z)=S_zz, where (x, y, z) is the probe position and S_x, S_y, S_z are the conversion factors between the output QPD voltages and displacements [with units of (length/voltage)]. However, usually the linearity range of the QPD detection is limited to a few hundreds of nanometers. For many biophysical applications of the PFM, in particular, in the study of molecular motors, this range is not sufficient. One of the options in this case may be the tracking of the probe position by video microscopy which makes for a more computationally expensive and slow data processing.

Another problem arises due to a cross-talk between the three signals as an intrinsic feature of the Mie scattering(198). Here, we describe a technique that we have designed and implemented, which we have used in all the experiments reported in previous sections and has allowed us to increase by one order of magnitude the detection range for available PFM systems. This technique takes advantage of the unavoidable cross-talk between the output signals of the QPD and does not assume that the output signals are linear in the probe displacement. We demonstrate an increase in the detection range from 150 to 1400 nm for a trapped polystyrene sphere with radius 300 nm as probe. The main idea for the position detection calibration is the following. We record two QPD signals, say, V_x and V_z, while we scan the probe across the detection beam along the x-direction with known steps using an optical trap generated by a second beam. In this way we associate the detector signals (V_x ,V_z) to a given known probe position x (Figure 2.30a). This gives us the calibration curve, *i.e.*, a parametric plot $V_x(x_{trap})$ versus $V_z(x_{trap})$. Now for any output (V_x^* ,V_z^*) signals we can determine the probe position maximizing the likelihood function.(199)

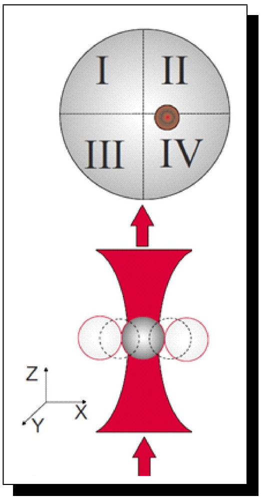

Figure 2.30: Concept of the detection. We record the QPD signals V_x and V_z while we scan the probe along the direction x through the detection beam. The QPD gives three signals that are proportional to the probe position in the trap: Vx=$(VI + VIII) - (VII + VIV)$, $Vy = (VI + V_{II}) - (V_{III} + V_{IV})$, and $V_z = V_I + V_{II} + V_{III} + V_{IV}$, where VI, V_{II}, V_{III}, and V_{IV} are the signals associated to the four quadrants of the QPD.

2.7.2 Experimental procedures and Results

The experimental optical setup is the same of section 2.3.1 We calibrated the trap displacement for small deflection angles, when the QPD response is linear by using standard optical tweezers calibration techniques, (175)(176)(177) and then we linearly extrapolated the position of the trap to larger trap displacements. We steered the trap position by applying a sinusoidal signal $x_trap(t) = A\sin(2\pi f_0 t)$ with various amplitudes A=18, 180, and 720 nm, and f_0=1 Hz. The frequency f_0 was kept low enough to permit the probe to be in a quasistationary state, i.e., $f_0 \ll f_c$, where f_c is the corner frequency of Brownian motion of the probe in the trap. In Figure 2.31(a)-Figure 2.31(c) we show the resulting signals V_x and V_z as functions of time. Due to the thermal fluctuations of the probe near the trap position only the probe position x averaged over time coincides with the position of the trap x_{trap}, i.e., ,$< x >= x_{trap}$. Therefore we need to average the recorded output signals. In Figs. 2.31(d)-2.31(f) we show the averaged signals $< V_x >$ and $< V_z >$ as functions of the trap position, when the signals were acquired during 60 s. These signals have variances σ_x^2 and σ_z^2 and correlation coefficient $\rho^2 = \sigma_{xz}^2/\sigma_x\sigma_z$ which depend on x_{trap}. When the steering amplitude is small [A=18 nm, Figs. 2.31a and 2.31d] the signal V_x is linear in the displacement and the signal Vz is uncorrelated with V_x.

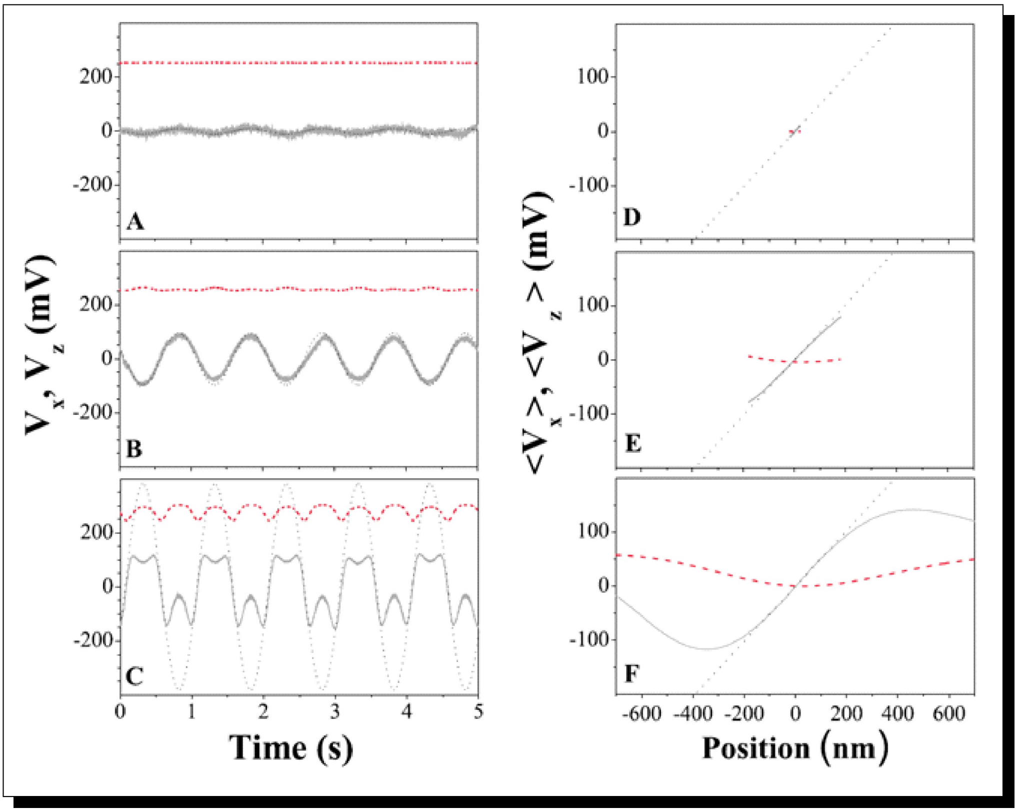

Figure 2.31: Experimental data. [(a)(c)] V_x (solid line) and V_z (dash line) signals obtained by moving the probe sinusoidally. [(d)(f)] Averaged signals $\langle V_x \rangle$ (solid line) and $\langle V_z \rangle$ (dash line) in function of the probe position x. The dotted lines represent the signals of the photo-detector if its response would be linear. The amplitude of the sinusoidal movement of the trap center is [(a) and (d)] A=18 nm, [(b) and (e)] A=180 nm, and [(c) and (f)] A=720 nm.

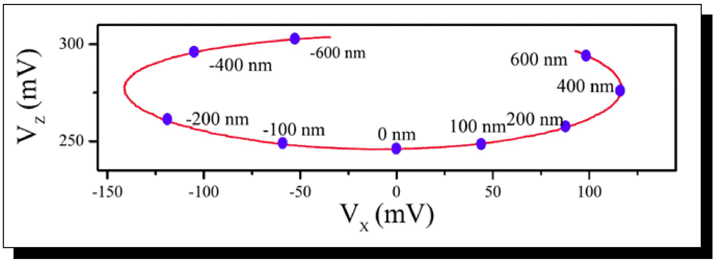

Figure 2.32: Calibration curve (solid line) $\langle V_x \rangle (x_{trap})$, $\langle V_z \rangle (x_{trap})$ parameterized on the trap position x_{trap} (dots).

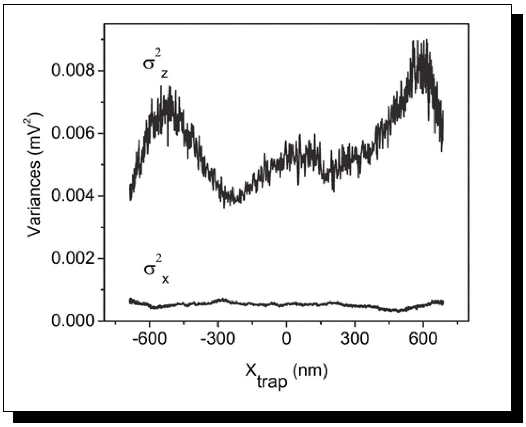

Figure 2.33: Variances of $\langle V_x \rangle$ and $\langle V_z \rangle$ depend on the position of the trap.

However, when the steering amplitude is increased up to A=180 nm [Figs.2.31(b) and Figs.2.31(e)] the signal V_x is distorted and a cross-talk between the signals V_x and V_z is observed. These effects become dominant when the steering amplitude is increased even further [A=720 nm, Figs. 2.31(c) and 2.31(f)]: the data do not give a reasonable estimation of the probe position anymore. If we continuously change the trap position by means of AOD, we can now plot the parametric curve for the PFM [$< V_x > (x_{trap})$ and $< V_z > (x_{trap})$] shown in Fig. 2.32. In Fig. 2.32 we demonstrate how the calibration curve can be used to measure unknown probe x-positions. For a given value of the QPD signals (V_x^* ,V_z^*), we apply a maximum likelihood estimator in order to find the best estimation of the probe position x^*. We assign the estimated particle position to the position value $x_t rap$ that maximizes the probability of obtaining the given QPD signals, *i.e.*, that maximizes the likelihood function (199) where $\langle V_x \rangle$, $\langle V_z \rangle$, σx, σz, and ρ were defined above and they are functions of the trap position. We measured the variances of ($\langle V_x \rangle$) and ($\langle V_z \rangle$) as a function of the trap position and we found that they are not constant and the variance of ($\langle V_x \rangle$) is larger than the variance of ($\langle V_z \rangle$)

(Fig. 2.33). Furthermore, a slight correlation between the two signals was observed, especially for large excursions of the particle position.

In Fig. 2.34 the reconstructed time dependencies of the probe position corresponding to the data presented in Fig. 2.31 are shown. For comparison the known trap center position is also depicted. Now the probe position may be measured with high accuracy over all the range of the steering amplitude of 1400 nm for a trapped probe with a radius of 300 nm. This represents a one order of magnitude improvement over the case when only the linear dependencies of the QPD signals from the probe displacement are used. The results obtained by maximizing the likelihood function are similar to the ones obtained by using the minimization of the Euclidean distance(see footnote).[1]

However, the former delivers much better results especially near the extremes of the probe position excursions.

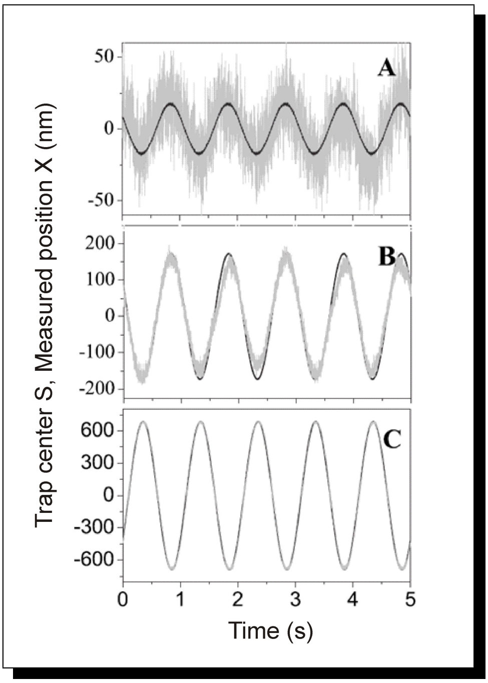

Figure 2.34: Calculated probe position x^* (gray line) for the signals presented in 2.31. The known trap center position (black line) is shown for comparison. The amplitude of the sinusoidal movement of the trap center are (a) A_1 =18 nm, (b) A_2=180 nm, and (c) A_3=720 nm.

2.7.3 Final comments

The method uses the cross-talk between the signals of the QPD, which

---

[1]

$$L(x_{trap}) = \frac{e^{-[1/2(1-\rho^2)][[(V_x^*-\langle V_x\rangle)^2/\sigma_x^2]-([2\rho(V_x^*-\langle V_x\rangle)(V_z^*-\langle V_z\rangle)]/\sigma_x\sigma_z)+[(V_z^*-\langle V_z\rangle)^2/\sigma_z^2]]}}{2\pi\sigma_x\sigma_z\sqrt{(1-\rho^2)}} \tag{2.37}$$

is normally considered as a nuisance. The experimental setup described is only one out of many possible realizations of this method. We have considered the FS detection with a QPD; however, the same method can be used also when experimental constraints prevent access to the forward-scattered light, forcing one to make use of the backward scattered light (200) or with other kinds of photodetectors, such as position sensing detectors. (201) Although we have used an optical trap controlled by an AOD to move controllably the probe across the detection beam and to get a calibration curve, other means can be used to achieve the same purpose: a galvomirror, a dielectric mirror, a piezostage moving a probe stuck on a surface, a fluid flow. Finally, although we used the V_x and V_z signals of the QPD, other kind of signals can be considered: two beams at different wavelengths or the forward and backward scattering of the same beam.

3

Semiconductor Laser with Optical Injection

3.1 Introduction

In this chapter we give a brief description of the working regimes that can appear in a SCL when it operates under OI. First of all, we briefly introduce the most common SCL which is known as the edge-emitting semiconductor laser (EEL), and then we consider a new type of SCL emerged in the last years, called *vertical-cavity surface-emitting laser* VCSEL, which is becoming a key component for telecommunication systems. Mostly, we report results obtained by different researchers in the last years, which will allow us to estimate the present degree of knowledge about the properties of the laser light generated in these systems. This will allow us to better understand and put in proper context the configuration, model and results that we have obtained on optically injected semiconductor lasers, which are described in detail in the next Chapters. It must be taken into account that different investigations of optically injected semiconductor lasers have considered different operation regimes (and even slightly different laser models), and have explored different parameter space regions. For this reason, it will often be difficult to establish direct relationships between results obtained by different authors. In the last subchapters of this chapter different results will be analysed separately.

Before going on, let us previously point out that in this chapter we describe the behaviour of OI semiconductor lasers, focusing particularly on the locking conditions and on the types of dynamics that can be generated, as a function of the input parameters, frequency detuning and injection ratio. The output dynamics behaviour can be interpreted and understood by using tools like power, optical and regenerative spectra. These methods are usually employed in experimental work. While, more often for theoretical calculations, bifurcation maps are used which highlight the different operation regimes. Moreover, we explain the advantage of the OI technique, such as enhancement bandwidth and chirp frequency suppression.

3.1.1 Historic overview and types of semiconductor laser

3.1.1.1 Basic physical principles of laser

In a semiconductor the forbidden energy gap between the valence band and the conduction band, is from 0.1 to 3 eV. The thermal excitation and/or the absorption of a photon whose energy $\hbar\omega$ is larger than the bandgap energy generates charge carriers in semiconductors: a valence band electron is excited to the conduction band and leaves behind a vacancy that effectively behaves as a positively charged free particle called hole. Conduction band electrons and valence band holes (electron-hole pairs) may recombine and release their energy in either nonradiative or radiative processes. Nonradiative recombination corresponds to the release of the electron-hole energy through heating (interaction with lattice photons). Radiative recombination corresponds to the release of the electron-hole energy through the emission of a photon. Radiative processes include spontaneous and stimulated emissions. Spontaneously generated photons are emitted in random directions and with a random phase relatively each other, hence they correspond to the emission of an incoherent light. On the other hand, Einstein reported in 1917 that an incoming photon of energy $\hbar\omega$ may stimulate the recombination of an electron hole pair and the emission of a second photon with energy $\hbar\omega$, keeping the polarization, phase and propagation direction of the incoming photon (202).

Stimulated emission processes form the basis of LASER operation, whose acronym means Light Amplification by Stimulated Emission of Radiation. Stimulated emission received little attention from experimentalists during the 1920's and 1930's when atomic or molecular spectroscopy was of central interest for many physicists. Later, in the 1940's, experiments to demonstrate stimulated emission were at least discussed informally but they seemed only rather difficult demonstrations and not quite worthwhile. Any amplification was swamped by losses due to other competing processes and their use for amplification seems not to have been seriously considered until the works of Basov (203), Weber (204), and Gordon, Zeiger and Townes (205). In 1954, these last researchers demonstrated population inversion in a system of ammonia molecules. Their system emitted in the microwave spectrum. Shortly after this, in 1958 (206), it was realized that the same laser principle could be used for the infrared and visible parts of the light spectrum. The first laser operation in the visible spectrum was reported by Maiman in 1960 (207). It was with the ruby laser, which exploits transitions between states of Cr^{3+} ions in an AL_2O_3 crystal.

Shortly afterwards, several researchers considered the possibility of laser emission from band to band transitions in semiconductors. In 1962, laser emission was demonstrated in p-n junctions by a number of laboratories (208, 209, 210, 211). In 1963 Kroemer and Alferov (212, 213) suggested that the semiconductor laser (SCL) could be improved by clamping of a semiconductor between two semiconductor layers with wider a bandgap. This was the first theoretical proposal of heterostructure lasers, with two different semiconductor materials. In these years it was difficult to match the lattice constants of the two semiconductor materials to built an heterostructure. In 1969, a semiconductor pulsed laser that could operate at room temperature was built (214). Only in 1970, the first heterostructure working at room temperature was built (215). In later devices, partially reflecting mirrors were formed from parallel cleaved semiconductor facets to form a Fabry-Perot cavity typically 500 μm in length. In 1975, a laser with emission wavelength of 1.1 μm was built, and until 1979 the wavelength of the emitted light was continuously increased up to 1.5 μm (216, 217, 218, 219, 220).

The simplest structure model of a semiconductor laser is a Positive doped-Negative doped (PN) junction, as showed in figure 3.1. A positive voltage is applied to the P side of the junction with respect to the N side. Because the semiconductor on the two sides has the same bandgap, the energy bands are continuous across the junction. The current applied in the PN junction produces the injection of electrons from the conduction band of the n-type material to the conduction band of the p-type material, while holes move in the opposite direction, in the valence band.

When an electron and a hole are located in the same region, recombination phenomena can be produced, giving rise to spontaneous emission, which is necessary to start the stimulated emission. The key of lasing is the transition of an electron from an occupied state at high energy to an empty state at lower energy, due to stimulated emission. The cleaved facets act as a mirror, reflecting the photons into the cavity, where they interact with the excited electrons. The cavity is designed in a fashion to resonate at the frequency corresponding to that of the stimulated-emission transition, amplifying the photons that propagate in the same direction. When the amplification is higher than the losses, lasing occurs. This occurs at a given threshold value of the pump current, and light is emitted in the plane of the junction.

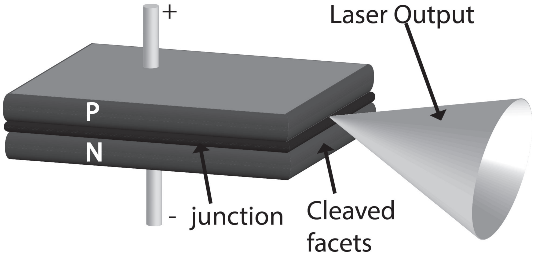

Figure 3.1: Schematic edge-emitting semiconductor laser diode. Lasing occurs in the plane of the junction.

The most common types of semiconductor lasers, according to the material composition, are depicted in figure 3.2; they are:

- Homostructure: it is a PN junction, made of the same semiconductor material (only the doping changes in the two sides of the junction). In the recombination region the concentration of carriers is quite low. The current threshold is very high.
- Heterostructure: there are two junctions, each one made of different semiconductor materials. This structure effectively reduces the current threshold. The active region is sandwiched between two oppositely doped semiconductors with higher bandgap and lower refractive index compared with the active layer. Electrons and holes are confined into the active layer where they can recombine more efficiently. On the other hand the difference in refractive index produces a waveguide effect, concentrating the generated light in the central region. All that leads to a much higher gain than in homostructure lasers.

In an heterostructure the active layer is about 100 nm. When this layer is still reduced, the structure becomes a Quantum Well (QW). In this kind of laser the vertical variation of the energy is quantized (221). Therefore the conduction and valence bands are divided in subbands, which implies that for a given current, more bands are excited, so that the gain amplification factor is higher and it is easier to reach the transparency (minimum number of carriers to have gain equal to the losses),

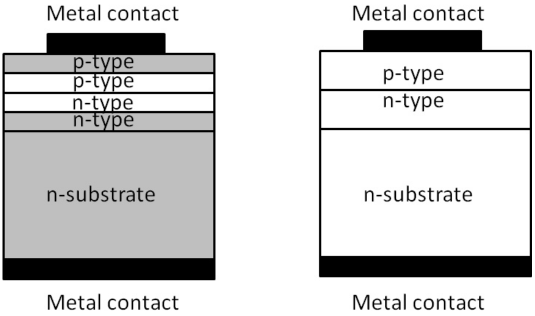

Figure 3.2: Schematic heterostructure (left) and homostructure (right) SCL. In heterostructure laser a layer of low bandgap materials (gray) is sandwiched between two layers of high bandgap material (white). Homostructure is a p-n union of the same type semiconductor materials.

and the current threshold becomes lower which allows higher modulation speed. As a result, quantum well lasers have narrower laser linewidth.

On the other hand, semiconductor lasers can also be classified according to their geometrical configuration, in particular according to the propagation direction with respect to the plane of the active area. The optical field can propagate and exit perpendicular or parallel to the junction plane. Then, heterogeneous semiconductor lasers can be classified into edge-emitting lasers, if the light is emitted through a surface plane perpendicular to the junction plane, or surface emitting laser VCSEL, Vertical Cavity Surface Emitting Laser) if the light is emitted through a surface plane parallel to the junction plane (the mirrors are built parallel to the junction plane). We describe this type of laser in the next subsection.

3.1.1.2 Vertical Cavity Surface Emitting Laser VCSEL

3.1.1.3 Advancement of VCSEL

As pointed out above, in VCSEL lasers the mirrors are grown parallel to the juntions plane, so that the generated laser light crosses the juntions perpendicularly to them, Fig. 3.3.

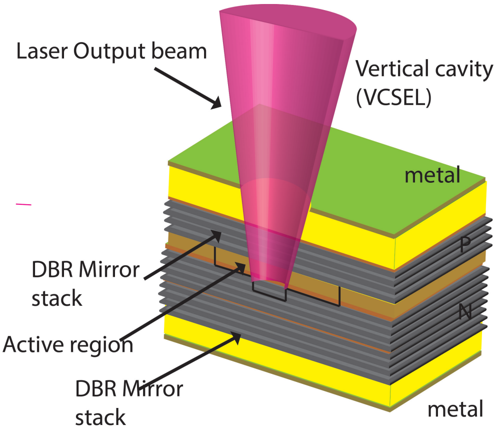

Figure 3.3: Schematic of VCSEL.

Nowadays, the total annual market of lasers is dominated by diode lasers, which represent over a billion dollars. The market of diode lasers includes telecommunications, optical storage (Compact Disc (CD) players, CD-ROM), image recording (including printing applications) and other markets such as applications of diode lasers for bar-code scanning, instrumentation, medicine, solid-state laser pumping. So far (but this is changing), any of these applications has been almost exclusively served by conventional EELs. So, why VCSEL should take a primary place in this market? The answer is mainly based on wether VCSELs, thanks to their unique features, will reach equal or superior performances than EELs, but at a much lower cost. Most importantly is whether the special features of VCSELs will allow new applications not easily addressed by EELs.

Special technological features of VCSELs, which allowed them to replace EELs in many applications, and to open up new applications are:

1. **Epitaxial growing of mirror facets.**

   unlike EELs lasers, to implement the mirrors several epitaxial layers are required during the construction process of VCSEL, which for sure represent an extra cost. Nevertheless, once the growing facility is developed, numerous advantages appear. The cleaving of mirror facets of EELs is not required. The narrow band reflective layers yield a narrow emission spectrum in a well-defined longitudinal mode, hence avoiding the demanding processing steps required for incorporating frequency selective gratings in conventional EELs.

2. **Surface emission.**

The emitted light, in VCSELs is perpendicular to the active layer. This property makes the devices well suited for fabrication in arrays, including two dimensional arrays, and allow on-wafer testing, which has been a significant aspect towards the use of VCSELs for low cost parallel data communications. Even if EELs can be turned into surface emitters by the incorporation of turning mirror gratings, VCSELs are better choice since they take less wafer area and extra processing steps are not required. The surface emission also makes easy the integration of VCSELs with other optoelectronic circuits, as well as the monolithic incorporation of microlenses on the surface.

3. **Low threshold.** VCSELs present a small active region which allows very small threshold current, of the order of mA or even less. On the other hand, VCSEL output power is in general around 1 mW at most. In low power systems (i.e. those which require only mW optical power), having a low threshold is important as it allows to increase the response speed of the device, decrease the turn-on delay, and decrease the power consumption. The combination of low threshold and high efficiency at power less than mW is better met with VCSELs than with EELs.

4. **Circular beam.**

   In conventional EELs, the output beam cross section is elliptical, with a large emission angle in the direction perpendicular to the layers and a small emission angle in the direction parallel to the layers. By contrast, VCSELs, with their circular aperture, put out a circular beam with lower divergence, which greatly simplifies the coupling into fiber cores and the coupling to optical components such as lenses.

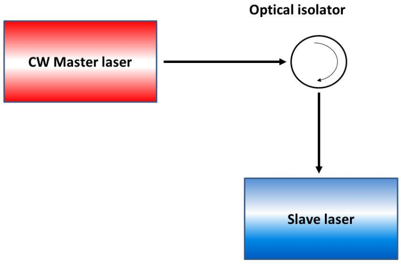

Figure 3.4: Typical setup of a CW master laser and a follower laser coupled by an optical isolator

3.2 Semiconductor Laser with Optical Injection

OI is a method to add a further degree of freedom to the system, which can lead to different working regimes with specific properties. The injection locking system is very simple, as shown in Fig. 3.4. In order to achieve this goal, light from an external source, which usually is another laser named “master laser” Master Laser (ML), is fed into the active layer of the laser that is going to generate the light (we are going to call it the “slave laser”, Slave Laser (SL)), to pump it. It is important to notice that the output dynamics we are going to study refers only to the output light emitted from the slave laser (the master laser emits in a steady state regime with constant intensity). Therefore the SL is the main laser to be considered. Usually, the two lasers are prepared to emit approximately at the same wavelength range, under appropriate conditions of frequency detuning and injection strength. Besides, in order to prevent mutual coupling between the two lasers, an optical isolator is inserted (Fig. 3.4). As we will discuss below, depending on the strength of the master laser and on the operating conditions of the slave laser, the last one can either lock its frequency to that of the ML, or to bring about more complicated dynamics.

Considering the vastity and diversity of laser types (222, 223, 224, 225, 226, 227), due to differences in the active media, originated from the fact that the α parameter (linewidth enhancement factor) has a non-zero definite value (228), and the continuously evolving cutting edge technology, it is difficult to give an idea of the enormous complexity involved in modeling laser dynamics.

The technique of the injection locking was discovered and used more than 30 years ago (229). It is of great interest in semiconductor laser design and technology, because it was shown that it can significatively improve the coherence of the emitted signal.

More in specifics, it can lead to reduction of the mode hopping and mode partition noise, reduction of the laser linewidth (α) and of the frequency chirping, and enhancement of the bandwidth modulation.

Essentially, as described below, it is possible to summarize the dynamics of an optically injected semiconductor laser in three regimes (223):

- **"Stable locking region"** in this parameter region the frequency of the SL is locked to the ML, and this corresponds to the "steady state" of the SL system. There are two conditions to be satisfied in order to locking occur:
    1. the detuning between the wavelength of the injected light and the wavelength of the light emitted by the free-running laser should be small enough
    2. the injected power should be larger enough.
- **"Non locking region"** Simply the SL does not manage to lock to the frequency of the ML. Anyway, the nonlinear interaction can bring to interesting wave mixing effects between the ML frequency component and that of the SL, which are amplified inside the SL active medium.
- **"Destabilized locking"** in which the stationary locked state is destabilized to a more complex dynamics such as time periodic dynamics, period doubling, quasi periodic or chaotic behaviors.

With the OI, dynamical states including period-1 oscillation (P1), period-2 oscillation (P2), chaos oscillation (CO), and stable locking (L) have been observed and applications in photonic microwave signal generation (227, 230), laser stabilization (231, 232, 233), and bandwidth enhancement (10, 11, 12, 234, 235, 236) have been explored. Interestingly in (237) it has been studied the chaotic regimes in injection-locked semiconductor lasers and they calculated the stability diagrams discriminating regular from chaotic laser emissions and indicating where multistability was to be expected. The response of an optically injected Quantum-dot semiconductor laser has been studied both experimentally and theoretically in (233). Moreover, in (238) they demonstrated that optically injected semiconductor quantum-dot lasers operated in the frequency-locked regime exhibit the phenomenon of coherence resonance.

In (239) the injected quantum cascade laser have been investigated analytically on the basis of current estimates of the laser parameters. Also recently, the dynamics of an optically injected quantum-dot laser accounting for excited states has been investigated, showing that the noise strength could act as ingredient to make the pulsation more periodic (240, 241), and that the dynamics often lead to the appearance of single and double-pulses excitability at one boundary of the locking region (242). Besides, various works in the last years have analyzed experimentally and theoretically the injection locking properties of VCSEL lasers (140, 243, 244, 245, 246, 247), where they have also intensively studied the polarization dynamics, which shows phenomena such as polarization switching accompanied by four-wave mixing, frequency pushing or chaotic regimes.

Optical injection was originally developed to stabilize the injected slave laser, so that it may be surprising that the laser is destabilized by the injection. This occurs because the optical injection represents the introduction of an extra degree of freedom, so that the perturbed laser is a candidate for a chaotic system.

Considering a typical bifurcation map of the output slave laser (3.11) as a function of the frequency detuning between master and slave, with a fixed optical injection rate, it is possible to identify on it stable and unlocking oscillations, as well as various unstable oscillation states. Therefore, in order to investigate the characteristics of optical injection locking, it is necessary to do first a linear stability analysis.

3.3 Rate equations and steady state solutions

The rate equations for the amplitude, phase and carrier density for a semiconductor laser optically injected takes the following form (8):

$$\frac{dA(t)}{dt} = \frac{1}{2}g[N(t)-N_{th}]A(t) + \kappa A_{inj} cos\phi(t) \tag{3.1}$$

$$\frac{d\phi(t)}{dt} = \frac{\alpha}{2}g[N(t)-N_{th}] - \kappa\frac{A_{inj}}{A(t)} sin\phi(t) - \Delta\omega_{inj} \tag{3.2}$$

$$\frac{dN(t)}{dt} = J - \gamma_n N(t) - \gamma_p + g[N(t)-N_{th}]A(t)^2 \tag{3.3}$$

Where the variable A is the slowly varying field amplitude, ϕ is the phase difference between the internal and the injected fields, expressed such as $\phi(t) = \varphi(t) - \Delta\omega_{inj}t - \varphi_{inj,c}$ where $\varphi(t)$ and $\varphi_{inj,c}$ are the temporal phase of the total field inside the cavity and the constant injected phase, while $\Delta\omega_{inj}$ is the frequency detuning between the two lasers. N is the carrier number, α is the linewidth enhancement factor, g the linear gain coefficient, N_{th} is the threshold carrier number for the solitary operation, γ_p and γ_n are the photon and carrier decay rates, and J is the pump current. A_{inj}, is the injected field amplitude. The condition of injection locking is namely explained by the equation 3.2. That equation describes a phase change of the slave laser induced by the resonance shift and the coupling between the internal and the injected fields. Therefore, when the sum of the relative changes in frequency is equal to the detuned frequency $\Delta\omega_{inj}$, the laser is injection-locked. Defining the amounts $A(t) = A_s$, $\phi(t) = \phi_s$, and $N_{th} - N_s = \Delta N_s$, that are the steady state values, and substituting into 3.2, we obtain the following injection locking conditions:

$$\Delta\omega_{inj} - \frac{\alpha}{2} g \Delta N_s + \kappa \frac{A_{inj}}{A_s} sin\phi_s = 0 \tag{3.4}$$

The term $\frac{\alpha}{2} g \Delta N_s$ is a frequency red-shift, caused by the change of the optical frequency of the laser oscillation after the optical injection. Then, from 3.4 the resonance between the two fields in the steady state is given by:

$$\omega_{res} = \Delta\omega_{inj} - \Delta\omega_{shift} = -\kappa \frac{A_{inj}}{A_s} sin\phi_s \tag{3.5}$$

Therefore the steady state solutions have been determined exactly from (236, 248):

$$\begin{aligned} A_s^2 &= \frac{A_{inj}^2 - \frac{\gamma_n}{\gamma_p \Delta N_s}}{1 + \frac{g \Delta N_s}{\gamma_p}} && (3.6) \\ \phi_s &= sin^{-1}\left\{ -\frac{\Delta\omega_{inj}}{\kappa\sqrt{1+\alpha^2}} \frac{A_s}{A_{inj}} \right\} - tan^{-1}\alpha && (3.7) \\ \Delta N_s &= -\frac{2\kappa}{g} \frac{A_{inj}}{A_s} cos\phi_s && (3.8) \end{aligned}$$

3.3.1 Stability analysis

The stability analysis is often used to study the resonance response in nonlinear systems, and it has been frequently applied in the analysis of semiconductor lasers with optical injection. The standard procedure consists in calculating the complex eigenvalues characterizing the (linear) response of the system to a small perturbation of the steady-state solution (10, 248, 249, 250). Let us thus consider a steady state solution x_s (with x=A, ϕ, and N) which, after a small perturbation, becomes (7):

$$\begin{pmatrix} \lambda + zcos\phi_s & zA_s sin\phi_s & -\frac{1}{2}gA_s \\ -\frac{zsin\phi_s}{A_s} & \lambda + zcos\phi_s & \cdot\frac{\alpha}{2}g \\ 2A_s(\gamma_p - 2zcos\phi_s) & 0 & \lambda + \gamma_n + gA_s^2 \end{pmatrix} \times \begin{pmatrix} \delta A \\ \delta\phi \\ \delta N \end{pmatrix} = 0$$

where $z = \kappa A_{inj}/A_s$. The solution of the equations require to have the determinant equal to zero:

$$\begin{aligned} D(\lambda) &= \lambda^3 + (\gamma_R + 2zcos\phi_s)\lambda^2 + \left[\omega_R^2\left(1 - \frac{2zcos\phi_s}{\gamma_p}\right) + z^2 + 2\gamma_R zcos\phi_s\right]\lambda + \\ &+ \gamma_R z^2 + z\omega_R^2\left(1 - \frac{2zcos\phi_s}{\gamma_p}\right) \times (cos\phi_s - \alpha sin\phi_s) = 0 \qquad (3.9) \end{aligned}$$

where $\omega_R = \sqrt{g\gamma_p A_s^2}$ and $\gamma_R = \gamma_N + gA_s^2$ correspond to the angular frequency and the damping rate of the relaxation oscillation of the free running laser. Dividing λ in real and imaginary parts such as $\lambda = \gamma + i\omega$, we can solve the equation 3.9. Obviously the stability condition for the steady state solution is that the real part γ be negative. The imaginary part ω gives the oscillation frequency of the relaxation oscillations around the steady-state solution. The obtained stable region in parameter space is represented in Fig. 3.6 ("stable locking" region).

Just as a double check that our results bring to the solution for the steady state analysis, we consider a very small fluctuation in the carrier δN with respect to the varying field A. In such a way, the carrier is fixed to its steady state and the perturbation of the carrier is mostly negligible compared with the field (because they are adimensional amounts): $\delta N \ll \delta A$ and $\delta\phi$. Therefore we can assume $\delta N = 0$, and the characteristic equation 3.9 (The stability conditions associated with the determinant of the first sub-matrix 3) reduces to the simple form:

$$\lambda^2 + 2zcos\phi_s\lambda + z^2 \;=\; 0 \tag{3.10}$$

then is easy obtain the analytical solution:

$$\lambda \;=\; -zcos\phi_s + izsin\phi_s \tag{3.11}$$

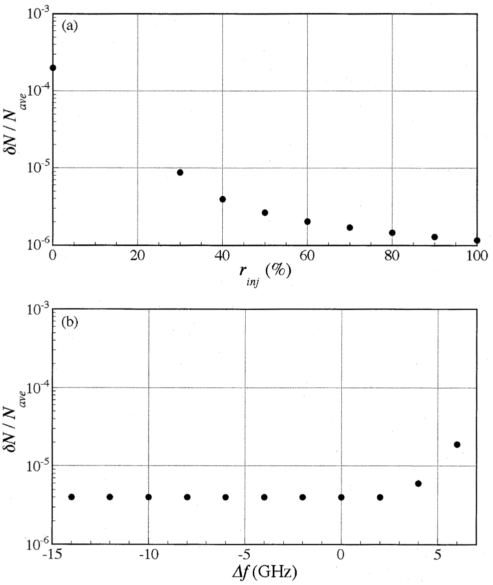

Figure 3.5: Carrier fluctuations normalized by the averaged value in injection-locked semiconductor laser modulated at resonance frequency for (a) different injection rates at Δf= 0.5 GHz and (b) different detuned frequencies at r_{inj} = 40%. Reported from (7)

The imaginary solution (*i.e.* the resonance frequency) is now the same expression of 3.5. In this case even the damping rate is given analytically, by the real part. This fact explains how damping can be enhanced from the strong injection current. From these theoretical results we can deduce the following scenario. Strong optical injection implies:

1. the carrier fluctuations are negligible compared with that of the field.
2. the interactions between carrier and field are weak. This fact causes the reduction of the relaxation oscillations frequency.
3. the enhanced resonance is caused by a transient interference due to the shifted cavity resonance, in the entire injection-locked SCL.

In order to examine the above assumptions in (7) it has been numerically confirmed such a behaviour of the carrier density by small modulation current. They calculated the fluctuation of the carrier density $\delta N = N_{max} - N_{ave}$, where N_{ave} is the average carrier density. Then, they modulated the current at 1% of the bias current and then it has been varied the injection ratio r_{inj} from 0 to 100%. As shown in figure 3.5 for the condition of solitary laser ($r_{inj} = 0$) the carrier density fluctuations have a maximum order of 10^{-4}.

The fluctuations decrease with the increased injection ratio up to reach 10^{-6}. For strong injection of 40% the variation of the fluctuations with the detuning is shown in Fig. 3.5(b). In this case the fluctuations are independent from the detuning and fixed to be 4 x 10^{-6}. At positive frequency detuning and closer to the Hopf-bifurcation boundary the fluctuations show some dependence from the frequency detuning. Therefore, these results conclude that the field-carrier coupling is mostly suppressed in strong injection locking regime, except for the Hopf-bifurcation boundary. Furthermore, carrier density fluctuations are considered as the main factor triggering the frequency chirp problem. Frequency chirp is a fluctuation of optical frequency occurring in laser diodes with high speed digital modulation of current and is considered to be the main cause limiting the bit rate for digital transmission (11, 249, 251, 252). Chirp can be considered resulting from the carrier fluctuations because carrier fluctuations alter the cavity resonance conditions during modulation, generating fluctuations in the optical frequency of the emitted light. We will discuss about the chirp problem, giving the definition and dependence of the laser parameters in section 3.7.

3.3.2 Injection locking conditions

In order to determine the condition of optical injection locking in real laser systems the following expression (related with equation 3.7), obviously must be less than unity.

$$sin(\phi_s + tan^{-1}\alpha) = -\frac{\Delta\omega_{inj}}{\kappa\sqrt{1+\alpha^2}}\frac{A_s}{A_{inj}} \leq 1 \tag{3.12}$$

$$\tag{3.13}$$

Then we obtain:

$$|\Delta\omega| \leq \Delta\omega_L = \kappa\sqrt{1+\alpha^2}\frac{A_{inj}}{A_s} \tag{3.14}$$

Successful optical injection occurs at a frequency satisfying the above relation for the injection fraction A_{inj}/A_s (in the following also named r_{inj}). Using the relation 3.14 inside the characteristic equation 3.9 we obtain the following equation:

$$\delta n = \frac{2\alpha\Delta\omega \pm 2\sqrt{\Delta\omega_L^2 - \Delta\omega^2}}{g(1+\alpha^2)} \tag{3.15}$$

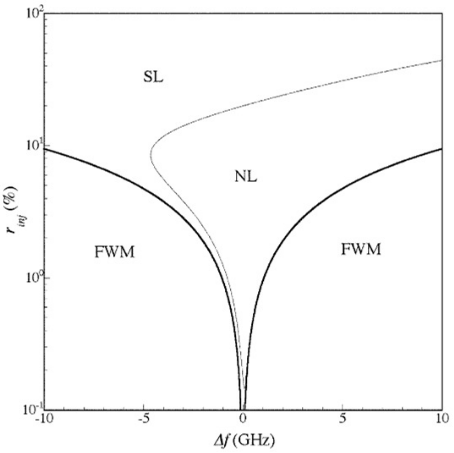

Figure 3.6: Locking and unlocking regions in the phase space of frequency detuning versus injection ratio. SL: stable locking. NL: nonlinear dynamics. FWM: Four-Wave Mixing. The FWM boundaries are obtained from the steady-state analysis of 3.12, and the SL boundary is calculated from the stability analysis of 3.15. The diagrams are drawn for pump current J = $1.3J_{th}$, where J is the threshold current. Reported from (7, 8).

For equation 3.15 two solutions exist for the same photon number S_s. One solution corresponds to a stable solution and the other is the unstable one. Figure 3.6, displays the areas of optical injection locking in the phase space defined by the frequency detuning between master-slave laser versus the injection ratio.

The solid curves show the boundary between Four-Wave Mixing (FWM) and stable or unstable locking regimes. As we said, in the non locking regions various interesting dynamics can be observed, such as chaotic oscillations and four-wave mixing when the detuning is not so far from zero.

The dashed line, denotes the boundary between the stable (left) and unstable (right) locking areas. In the latter we can observe roads to chaos for certain parameter ranges. The asymmetric feature of stable locking is due to the non zero value of α.

3.4 Nonlinear dynamics induced by optical injection

It is well established that a variety of perturbations over the laser system can bring the output laser to become unstable and yield oscillatory or chaotic output. Of all those perturbations, optical injection is the one which allows the greatest degree of control and most direct access to the mechanisms that lead to the instabilities. External optical injection allows one to perturb the slave output laser with a completely independent optical field. Besides, we know that for a laser operating at a given bias current, external optical injection can induce stable locked output, multiwave mixing, oscillatory power output due to the undamping of the carrier field resonance of the system, and chaotic dynamics depending on the offset frequency and amplitude of the external optical field (Figure 3.6). In the next section we are going to observe the laser dynamics in a specific case: that of a Distributed Feedback (DFB) laser subjected to optical injection when the injection ratio is increased, and the frequency detuning is fixed at 2GHz (Figures 3.93.10 reported from (9)).

3.4.1 Experimental mapping technique

In order to map the laser dynamics, in (9) three DFB lasers at 1557 nm have been used, as the schematic in figure 3.7. One laser was employed as master, optically injected to the slave laser by an optical circulator, and a third laser was a probe laser which was used to combine directly the output slave laser with its own output and even could be injected together with the master optical field into the slave laser. By means of this setup, three different optical spectra could be generated:

- If the probe laser is turned off, then the detected signal is a measure of the amplitude modulation of the slave laser and the spectrum analyzer measures the **amplitude (power) spectrum**.
- If the probe laser is on, but the frequency shifted output of the Acousto-Optic Modulator is blocked, then the probe laser acts as a local oscillator for a heterodyne measurement of the optical spectrum of the slave laser. To generate the optical spectrum the frequency of the microwave analyzer is fixed (generally at 33 MHz), then the bias current of the probe laser is ramp varied, which shifts its optical frequency. **The optical spectrum** is generated as the probe laser is sweept across the frequency components of the slave laser.

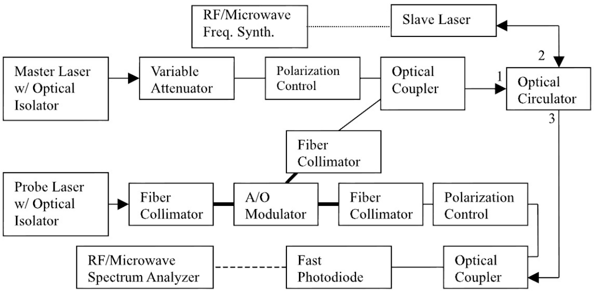
RF/Microwave Freq. Synth.
Slave Laser
Master Laser w/ Optical Isolator
Variable Attenuator
Polarization Control
Optical Coupler
1
2
Optical Circulator
3
Fiber Collimator
Probe Laser w/ Optical Isolator
Fiber Collimator
A/O Modulator
Fiber Collimator
Polarization Control
RF/Microwave Spectrum Analyzer
Fast Photodiode
Optical Coupler

Figure 3.7: Schematic of the apparatus used to build the spectra after shown. Reported from (9)

- Injecting simultaneously the frequency shifted output from the probe laser into the master laser, then a **regenerative amplification spectrum** can be generated. For this purpose it is essential to set the analyzer to match the frequency offset with a very narrow resolution (typically 10 KHz).

These three spectra yield complementary information about the free running and optically injected laser. Clearly, nonlinear dynamics, as frequency-mixing, chaos, instable locking or stable locking, could be obtained, observing the features appearing in these spectra. We next analyse some of these behaviours.

3.4.2 Optical injection induced dynamics

The mapping was made by relating a particular output dynamics to the spectral features displayed at a given injection level and offset frequency. In figure 3.8 it is shown the transition from free-running output to limit cycle dynamics as the injection strength is increased. Optical spectra are displayed to the left side while on the right side the regenerative spectra are represented. At relatively low injection the laser becomes locked to the master signal and the weak probe beam is no longer amplified at the free running frequency. As the injection is increased the sidebands become stronger until the Hopf bifurcation is passed and the laser output becomes unstable. Because there were no identified abrupt changes in the spectra to mark the boundary of the Hopf bifurcation, a criteria must be defined. They observed (as figure 3.8 shows), a change in level between the right and left parts around a power peak in the regenerative spectrum. This excursion (or discontinuity) indicates that the probe has a perturbing effect on the strong spectral characteristics of the signal, which is strongly blocked by the master laser. Therefore, this change with weakly resonant simultaneous oscillation at different optical frequencies is interpreted as an indicator of Hopf bifurcations. Associated with this transition there are sidebands approximately $15 \div 20$ dB below the resonant, locked feature in the optical spectrum.

Then, to distinguish the boundary regimes, the main information comes from the optical and power spectrum:

In Fig. 3.9(a) for a small level of the injection of 0.14, the output intensity of the slave laser shows four-wave and multiwave mixing components, because the slave laser remains unlocked. Besides, it shows a side peak in the spectrum due to the regenerative amplification, and the relaxation oscillation appears at a frequency of 4.7 GHz.

When the injection strength is increased to 0.33 (Fig 3.9(b)), the **multiwave mixing** effects become distinct. The relaxation oscillation component becomes non-vanishing and the oscillation close to the relaxation oscillation frequency is excited, and even the spectrum is much broadened, as well the features associated with the relaxation resonance sharpen and strengthen. The multiwave mixing effect is recognized as a phase-modulation like Adler frequency pulling towards locking (253).

As Fig. 3.9(c) shows, the frequency pulling multiwave components disappear at the injection strength of 0.41, and all the multiwave frequencies are pulled to the injection frequency. Therefore, a sharp and enhanced component of the relaxation oscillation is observed, and the laser shows a **stable oscillation** under these condi-

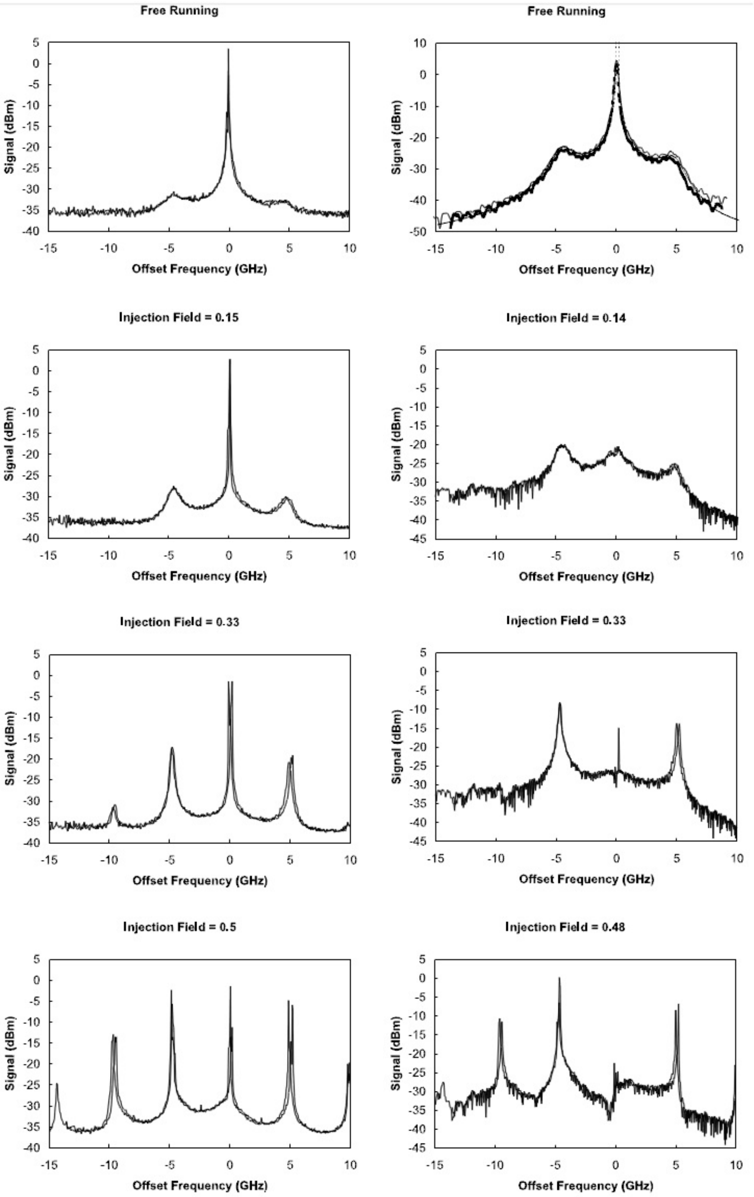

Figure 3.8: Spectra with injection at the free-running optical frequency showing the transition from stable to limit cycle dynamics. The left column contains the optical spectra and the right column consists of the regenerative amplification spectra. The Injection Field is proportional to the square root of the injected power. The free-running regenerative amplification spectrum has been corrected for background noise and the variation of local oscillator power during the scan so that it can be compared to the model calculation, shown as a thin line. Reported from (9)

tions.

In Fig. 3.9(d), the injection ratio is still increased to 0.52, and an incommensurate frequency is encountered. The background of the spectrum becomes broader and frequencies in the range 8-9 GHz start to appear. This is the typical onset of **quasi periodic bifurcation and chaos**, also predicted from numerical simulations (254).

The spectrum background becomes much broadened at injection strength of 0.77, as shown in Fig. 3.10(e). At the relaxation frequency component we can observe two visible peaks, which indicates that the emission corresponds to **period-3 oscillation and chaotic dynamics**.

In Figure 3.10(f) the laser shows **period-2 oscillation** and the relaxation oscillation spectrum becomes a single peak.

When the injection strength is large enough (1.3 in Fig. 3.10(g)), the laser oscillates with **period-1 oscillation**, with the main frequency corresponding to the relaxation oscillation. The higher harmonics of the period-1 oscillation are also visible.

Finally, at strong injection of 3.01 (Fig. 3.10(h)) the laser is completely locked to a certain frequency and show **period-1 oscillation**. At these high injection levels the resonance frequency is a function of the injection level and offset frequency of the master laser. Increasing still more the injection ratio is expected the laser to reestablish the stable locked operation.

This phenomenon is related with the cutoff frequency for the modulation bandwidth of the laser. Typically, these dynamics are not always the same, and depend on the frequency detuning. They exhibit chaotic routes when the absolute value of the frequency detuning is within several GHz.

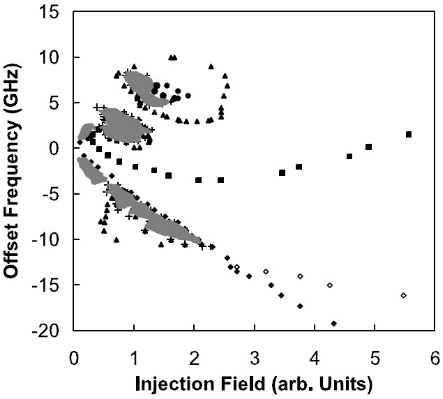

Figure 3.11: Mapping of the observed dynamics based on the experimentally measured spectra of the DFB laser under optical injection when biased at twice the threshold current. The full diamonds mark the saddle node bifurcation between stable and unlockedlocked operation while the open diamonds mark the unlockinglocking transition in a region of bistability (see (9)). Squares mark the Hopf bifurcation between stable and limit cycle operation. The triangles bound regions of period two operation. Within the period two regions are regions of complex dynamics marked by the shaded lines and crosses and a region of period four operation that is bounded by the circles. At injection levels below the saddle node bifurcation line and at low offset frequencies, multiwave mixing and Adler-type frequency pulling to locking are observed in the lightly shaded regions. Reported from (9)

The observed dynamics based on the previous observations of the regenerative, optical and amplitude spectra are mapped in figure 3.11 (reported from (9)). Stable injection locking is achieved for certain regions of the parameter space, but chaotic routes evolve when the laser is into the unstable region or unlocking regions. The laser is operating in single mode. Note that the axes in Fig. 3.11 are different than in Fig. 3.6. The full-diamonds marks represent the boundary between the stable and unstable operations, while the empty-diamonds show the unlocking-locking transition in a region of bistability and torus bifurcation. The square symbol marks close to zero detuning indicate the Hopf bifurcation boundary between stable locked and limit cycle dynamics. The triangles denote the boundaries for regions of period-2 dynamics. These period-2 regions include complex dynamics and they are shown by the shaded lines and crosses in the figure. Bounded by the circles is a region of period-4 operation. At injection levels below the saddle node bifurcation line and at low offset frequencies, multiwave mixing and Adler-type frequency pulling to locking are observed in the lightly shaded regions.

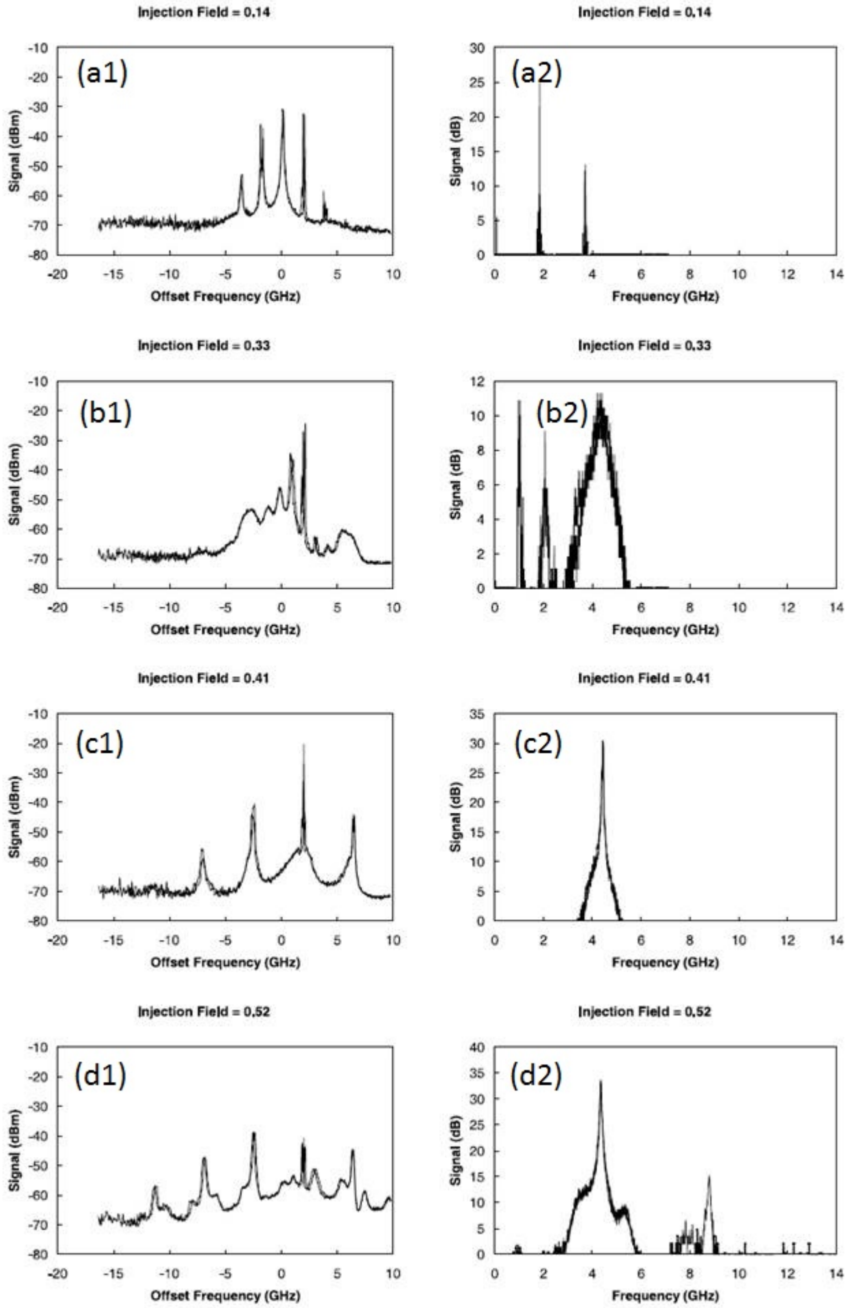

Figure 3.9: Experimental optical frequencies and rf power spectra corresponding to chaotic bifurcation in semiconductor lasers under optical injection. Left side are the optical spectra and in the right side the rf power spectra. The relaxation oscillation frequency at the solitary oscillation is 4.7 GHz. The injection current rate is changed as (a) 0.14, (b) 0.23, (c) 0.41 (d) 0.52. Reported from (9)

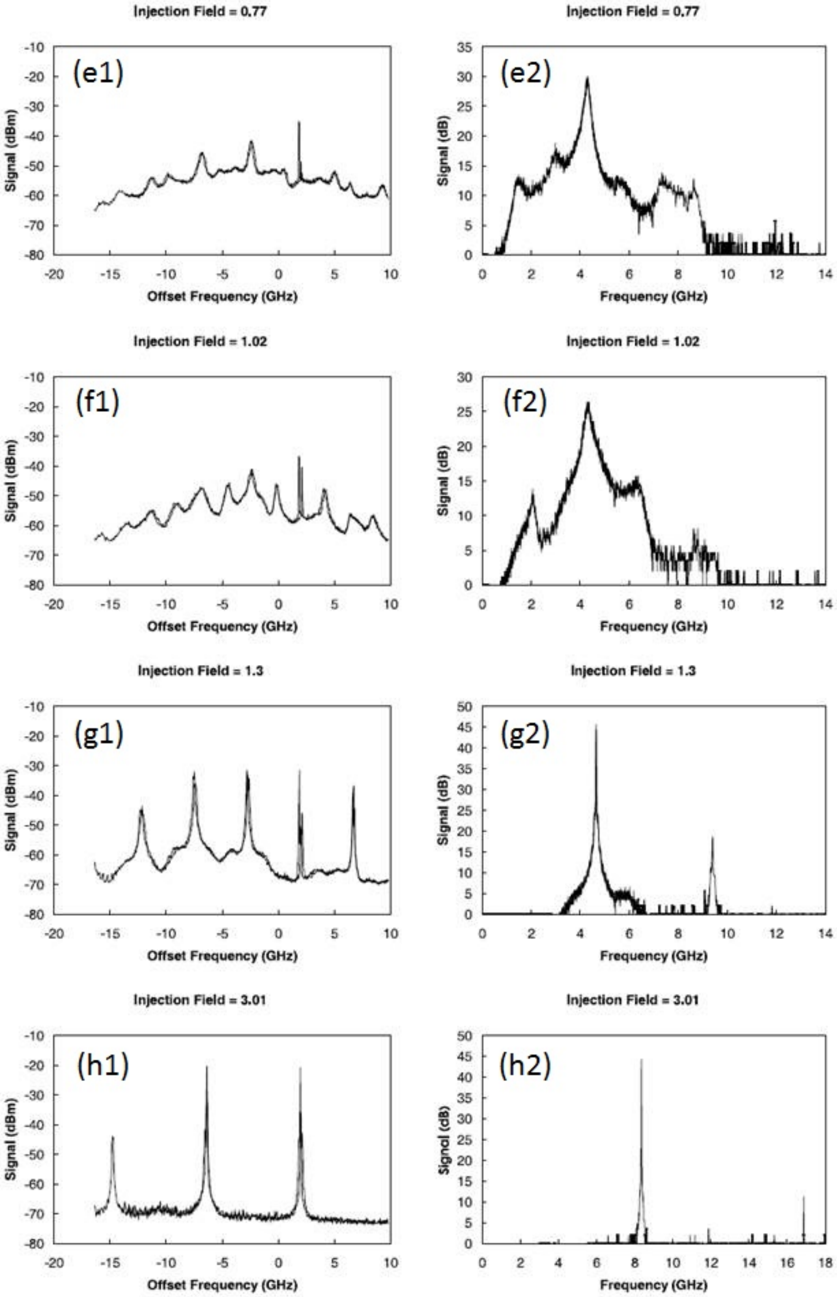

Figure 3.10: Experimental optical frequencies and rf power spectra corresponding to chaotic bifurcation in semiconductor lasers under optical injection. Left side are the optical spectra and in the right side the rf power spectra. The relaxation oscillation frequency at the solitary oscillation is 4.7 GHz. The injection current rate is changed as (e) 0.77, (f) 1.02, (g) 1.30 (h) 3.01. Reported from (9)

3.5 Influence of side mode excitation

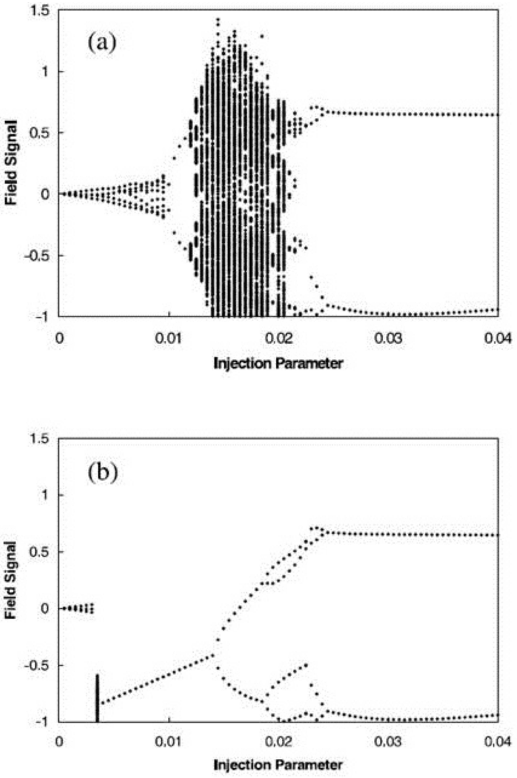

Figure 3.12: Bifurcation diagram as a function of the injection ratio at a frequency detuning of 2 GHz. (a) Bifurction diagram for large gain defect μ_d=0.1. The laser oscillates at a single mode. (b) Bifurcation diagram for small gain defect of μ_d=0.001. Reported from (9)

Generally, numerical calculations are a good method to compare with experimental results and to aim the research. In this case, in order to map the laser dynamics the bifurcation diagrams are especially suited and they can confirm the observed behaviour. Now, we briefly inspect the chaotic routes by numerical simulation performed in (9), taking into consideration the effects of side mode excitation. The chaotic evolution is observed for a frequency detuning of 2 GHz with respect to the free running frequency. Considering a large value of the gain defect of the secondary mode, $\mu_d = 0.1$ (Fig. 3.12(a)), the laser is assumed to oscillate at a single mode. The laser evolves from period-doubling to chaotic oscillations, then it takes an inverse period-doubling road, and finally it reduces to the period-1 state. For low values of the gain parameter, $\mu_d = 0.001$ (Fig. 3.12(b)), the laser shows evidence of power leaking out of the principal which leads to a strong change in the dynamics. Under this condition the laser shows no typical chaotic bifurcation.

With this work, the authors have found an excellent agreement with the experimental data. Therefore the proper rate equation model is an excellent tool to predict the nonlinear laser dynamics.

3.6 Enhancement of modulation bandwidth by strong optical injection

The relaxation oscillation frequency limits the bandwidth of an optical injected laser. However, in the case of a strong optically injection and under stable injection locking conditions, the modulation bandwidth of the slave laser is greatly enhanced. Although the laser noise is suppressed, the strong injection gives rise to frequency chirping in the laser oscillation, which is critical in laser operations (249). Depending in which parameter region it is working, a large modulation current can lock or unlock the laser. An enhancement of the bandwidth has been also demonstrated (7, 11, 235). For weak optical injection the cutoff frequency is enhanced ten percent at most. Under strong optical injection, the bandwidth is greatly enhanced up to several time the relaxation frequency of the free running laser.

An enhancement in the bandwidth of an optically injected laser is very useful considering the broadband light in the wide field of optical communications.

The enhancement of the modulation bandwidth in a semiconductor laser under strong optical injection has been numerically studied by means of the rate equations approach. The modulation response for a small signal to the bias injection current using a linear stability analysis has been investigated.

Figure 3.13 shows how the strong injection enhance the bandwidth. The cutoff frequency for the free running solitary laser is 3.4 GHz, while at strong injection of S_{inj}/S_s=0.44 the cutoff frequency becomes 12.6 GHz. The full bandwidth is enhanced four times compared with that of the free running laser. To obtain the equivalent modulation bandwidth of 12 GHz for the solitary free running laser, it would require the bias injection current to be seven times larger than that of the free running state. Which corresponds to 13 times the injection current threshold and it might damage the laser. Therefore, the technique of injection current is effective for greatly enhancing the bandwidth of a semiconductor laser.

We follow the analysis of bandwidth enhancement by optical injection reported in (10).

They conducted a linear stability analysis and obtained the approximate solution:

$$\nu_{enhanced} = \frac{1}{2\sqrt{3}\pi}\left[K_e - \left(\frac{{K_a}^2}{S_s}\right) + \left\{\left(\frac{{K_a}^2}{S_s}\right) - 4K_e\left(\frac{K_a}{S_s}\right)^2 + K_e^2 - 6K_aK_b\alpha G_n^2(n_s - n_0)\right\}^{1/2}\right]^{1/2} \tag{3.16}$$

where the parameters in the above equation are given by:

$$\begin{aligned} K_e &= \left(\frac{\kappa_{inj}}{\tau_{in}}\right)^2 \frac{S_m}{S_s} && (3.17)\\ K_a &= 2k_c\sqrt{S_m S_s}cos(\phi_s - \phi_m) = \\ &= -g(n_s - n_0)(1 - \varepsilon_s S_s) - \frac{1}{\tau_{ph}}S_s - R_{sp} && (3.18)\\ K_b &= k_c\sqrt{\frac{S_m}{S_s}}sin(\phi_s - \phi_m) = \frac{1}{2}\alpha g(n_s - n_0) - \Delta\omega && (3.19) \end{aligned}$$

Where we considered:

the photon number $S_m = |E_m|^2 = A_m^2$ for the injected power, such as for the slave laser $S_s = |E_s|^2 = A_s^2$. The phases ϕ_s and ϕ_m are generally time dependent functions, but the master laser is under steady-state operation therefore its phase can be imposed to be zero ($\phi_m = 0$). $\Delta\omega$ is the detuning between master and laser frequencies, τ_{in} is the round trip time of the light in the laser cavity, R_{sp} is the effective rate of the spontaneous emission, ε_s is the gain compression coefficient, τ_{ph} is the photon life time, n_0 is the carrier number for transparency, and κ_{inj} is the injection coefficient.

The enhancement of the cutoff frequency is linear with the injection current, and it is explained by the interference between the optical frequency of the original laser oscillation and the shifted frequency due to strong optical injection. Therefore, the bandwidth enhancement is strongly dependent on the frequency detuning between the master and slave lasers.

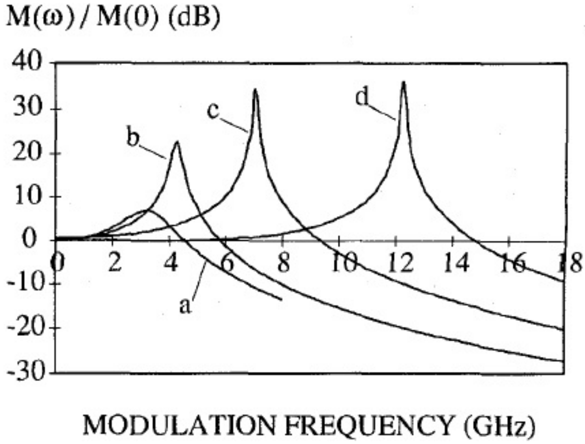

Figure 3.13: Experimental modulation response of a semiconductor laser at J=2.4J_{th}. (a) free running laser; (b) very weak injection of $S_{inj}/S_s = 0.011$;(c) $S_{inj}/S_s = 0.092$; (d) $S_{inj}/S_s = 0.44$. Where S_{inj} is the injected photon number and S_s steady state value of the free running laser. Reported from (10)

3.6.1 Origin of modulation bandwidth enhancement

The intrinsic modulation bandwidth of an SCL is approximately proportional to the relaxation oscillation frequency (ω_r).

The relaxation frequency can be increased by a proper design of the laser parameters. From the mathematical expression of the relaxation oscillation frequency ($\omega_R = \sqrt{g\gamma_p A_s^2}$), it seems that the bandwidth can be increased indefinitely, in principle by indefinite increase of the bias drive current. Unfortunately, facet damage and excessive heating will limit this increase of bandwidth. The technique of the injection locking reduces effectively any damage due to high current and heating because the bandwidth is increased by the beating frequency. It may be noted that injection locking also reduces chirp.

Recently, it has been investigated about the origin of the enhancement of the bandwidth in semiconductor laser by strong optical injection (7, 10). The expansion of the broadband has been realized by the interference between the slave solitary laser and the shifted frequency after the injection. The carrier density in the slave laser increase due to the strong optical injection. This change induces a variation in the optical frequency of the slave laser oscillations. In general, for a Fabry-Perot (FP) laser cavity, the $m-th$ longitudinal mode is given by the following expression:

$$\nu_0 = \frac{c}{2nl} \times m \tag{3.20}$$

where c is the light velocity in vacuum, n is the refractive index and l is the cavity length. Typically the refractive index n depends on the carrier number N in the cavity, namely $n(N)$.

The $\Delta\omega_{shift}$ of the laser angular frequency is given by:

$$\Delta\omega(N) = \frac{\alpha}{2} g \Delta N \tag{3.21}$$

therefore the change in the optical frequency is proportional to the carrier density ΔN. The injection locked laser can operate at a frequency which depends from its cavity resonance condition. Once the field corresponding to the shifted cavity resonance ω_{shift} is excited an interference between the two components of the angular frequencies ω_{shift} and ω_{inj} occurs. Then a frequency beat is induced between the two frequencies in the output of the slave laser. Figure 3.14 illustrates the resonance and emission frequencies in single-mode semiconductor lasers.

The frequency ω_0 and ω_{inj} are angular frequencies for solitary and injected fields without injection. When the laser is injection-locked the slave laser emits at the injected frequency ω_{inj}. Due to the optical injection the carrier density is reduced from its threshold value, thus the cavity resonance is shifted to lower frequency by $\Delta\omega(N)$. The latter does not mean that the laser can not operate at a frequency different from its cavity resonance condition, namely, operating at ω_{inj}, not at ω_{shift}. Then, we can assume that this frequency detuning can influence the bandwidth (248). Therefore, here we suppose that a transient field, corresponding with the shifted cavity resonance, can be generated and interfere with the locked field. The laser output can exhibit a damping oscillation due to the beating between the detuned frequency and the injected one. The oscillation of the mode rapidly decays out, because sufficient gain is not allocated, thus this is a transient field. The oscillation angular frequency of the slave laser is restored to ω_{inj}. The laser can exhibit damping oscillation at the beat frequency due to such transient interference. Therefore, the resonance angular frequency produced by the interference is given by:

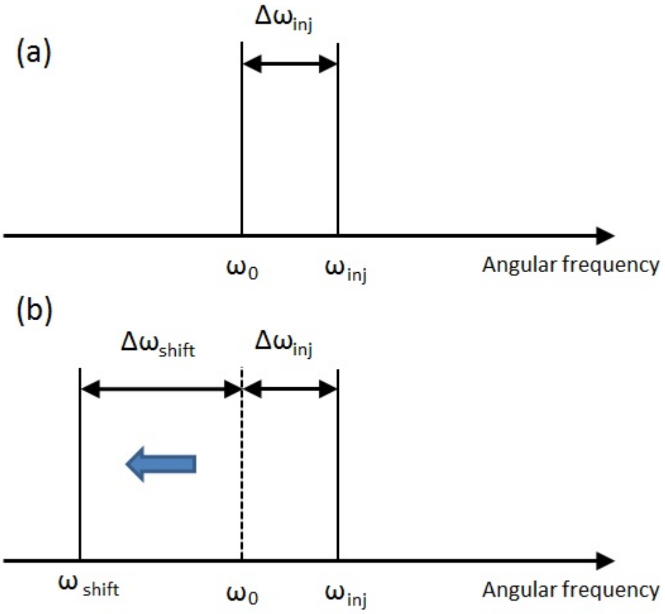
(a)
Δω_inj
ω_0
ω_inj
Angular frequency
(b)
Δω_shift
Δω_inj
ω_shift
ω_0
ω_inj
Angular frequency

Figure 3.14: Resonant condition of a semiconductor laser in the presence of optical injection. (a) Spectrum before optical injection. ω_0 is the angular frequency of the solitary laser, ω_{inj} is the frequency of the shifted light, and $\Delta\omega_{inj}$ is the frequency detuning between them. (b) Cavity resonant condition under injection locking. ω_{shift} is the cavity resonance frequency shifted from ω_0 by $\Delta\omega_{shift}(n)$ due to optical injection. Reported from (7)

$$\omega_{res} = \Delta\omega_{inj} - \Delta\omega(N) = -\kappa\sqrt{\frac{A_{inj}}{A_s}} sin\phi_S \tag{3.22}$$

Under strong optical injection, the cutoff frequency is linearly proportional to the injection ratio, in accordance with 3.21.

3.7 Frequency Chirping suppression by strong optical injection

As we said, a change in the carrier density causes a change in the refractive index of the gain medium. Therefore, this change in the index induces a frequency chirping, which can be a big limitation in the bandwidth and thus in the bit rate for communications applications.

A measure of frequency chirping has been given in (255), which is defined as follows:

$$CPR = \frac{1}{2\pi R_p}\left|\frac{d\phi}{dt}\right| \tag{3.23}$$

Where R_p is the modulation response. It has been found that frequency chirping originates from the α parameter, which has a non zero value in SCL laser (249). A stability analysis allows us to find the relation between the linewidth enhancement factor α and the CPR. This relation is expressed as follows:

$$\frac{1}{2\pi R_p}\left|\frac{d\phi}{dt}\right| \approx f_m\alpha\sqrt{\frac{f_m^2 + (u - v/\alpha)^2}{f_m^2 + (u + v/\alpha)^2}} \tag{3.24}$$

where u and v are given by:

$$u = \frac{\kappa_{inj}}{2\pi\tau_{in}}\left|\frac{A_m}{A_s}\right| cos\phi_L \quad (3.25)$$

$$v = \frac{\kappa_{inj}}{2\pi\tau_{in}}\left|\frac{A_m}{A_s}\right| sin\phi_L \quad (3.26)$$

and ϕ_L is the phase of the intracavity laser field relative to the injection field. Than, an effective linewidth enahancement factor can be defined, as:

$$\alpha_{eff} \approx \alpha\sqrt{\frac{f_m^2 + (u - v/\alpha)^2}{f_m^2 + (u + v/\alpha)^2}} \quad (3.27)$$

where for the case of solitary laser ($v = 0$ and $u = 0$) is reduced to the original α. Moreover, it is confirmed that a positive shift of the detuned frequency further reduces the frequency chirping. This fact can be seen in figure 3.15, where the injection locking of the laser at $\Delta\nu$ =-10 GHz reduces the effective chirping more than the injection locking at $\Delta\nu$=-18 GHz.

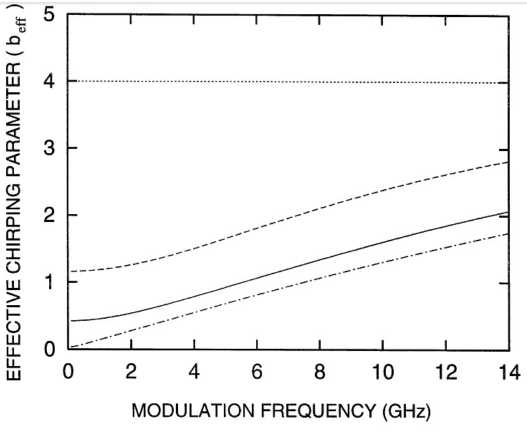

Figure 3.15: Effective chirping parameter. Dash-dotted curve: Injection locking at $\Delta\nu$=1 GHz. Solid curve: Injection locking at $\Delta\nu$=-10 GHz. Dashed curve: Injection locking at $\Delta\nu$=-18 GHz. Dotted curve: Free-running. Reported from (11)

When the power of the intrinsic noise is significantly high, then is no longer possible to use the simple relation from CPR and α. Therefore, the measure of the frequency chirping is better quantified directly from the CPR 3.23. However, when the modulation index is small reduction of the chirp coefficient is not guaranteed, and the chirp is dominated by the laser noise, following the same behaviour as the power noise. Therefore, an injected semiconductor laser operating in the stable locking regime has better modulation characteristics than a free running state.

3.8 High frequency chaotic oscillation by strong optical injection

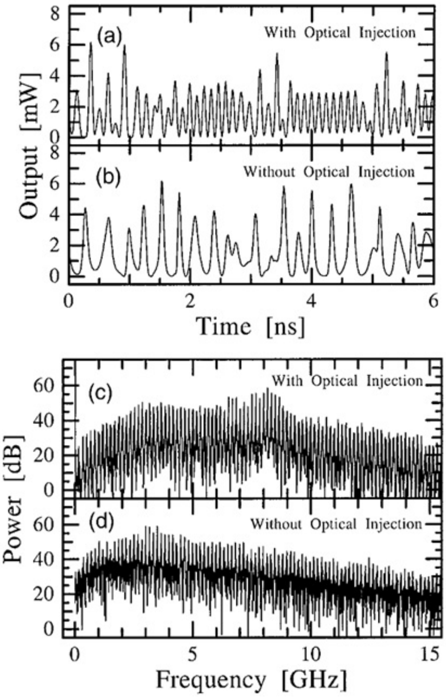

Figure 3.16: (a-b) Time series and (c-d) power spectra (respectively for (a) and (b)) of chaotic oscillations in the transmitter laser with and without optical injection. Reproduced from (12)

Typically, in a SCL the chaotic carrier frequency is near the relaxation oscillation frequency of the solitary laser, and obviously plays an important role in the chaotic dynamics. In particular, it can influence the bandwidth of the chaotic signal, which can be important for instance for secure communication systems (32, 256, 257). In this kind of applications the generation of a fast chaotic carrier signal is essential for an high bit rate of the transmitted message (258).

Figure 3.16 shows the time series of chaotic oscillations and power spectra with and without optical injection, numerically calculated by (12). The power spectrum in the case without optical injection presents a corner frequency around 2.7 GHz, while it is evident that in the case of strong optical injection the bandwidth is greatly expanded, up to about 10 GHz. However, it is difficult to calculate analytically the exact enhanced bandwidth of the carrier frequency.

The review, performed in this chapter, of published results concerning the optically injected semiconductor laser will allow us to better understand and better place in proper context the results that we have obtained about this class of laser and that are described in detail in the following chapter.

4

All optical implementation of Stochastic Logic Gate

In this chapter we present the results of our numerical simulations of VCSELs dynamics in an optically injected (OI) configuration (144). We introduce a general form of multimode rate equations for VCSELs, then we illustrate the spin-flip model for the circularly polarized and the linearly polarized rate equations for the two preferred oscillation modes. We describe the effects of bistability and the hysteresis, for both an opto-electronic and an all-optical configuration. Finally, we demonstrate how an OI VCSEL can be used as a stochastic logic gate, describing our numerical results and all implications in possible real applications.

4.1 Theoretical model for VCSELs

It is well known that VCSELs offer numerous advantages, but we must say that they also present some inconvenient, in particular they present unstable features in their operation, even without any external perturbation. Their spatial structure and polarization modes make them to often present chaotic oscillations. On the other hand spatial hole burning and multi-transverse mode oscillations bring the laser output to exhibit polarization switchings (PSs).

The field equations for a VCSEL are similar to those for an edge-emitting laser, exception for the spatial terms, which must take into account the different structure and propagation geometry. Considering a certain polarization mode, the field equation is given by (see: (8)):

$$\frac{dE_j(t)}{dt} = \frac{1}{2}(1+i\alpha)G_{nj}\{n(r,\phi,t)-n_{th,j}\}E_j(t) \tag{4.1}$$

where $n(r,\phi,z,t)$ is the space dependent carrier density expressed as a function of the cylindrical coordinates (r,ϕ,z) and $n_{th,j}$ is the threshold carrier density for the $j-th$ mode. E_j is the field amplitude for the laser oscillation of the $j-th$ component, and the total complex amplitude is given by

$$E_{total}(r,\phi,z,t) = \frac{1}{2}\sum_{j=1}^{M}\hat{e_j}E_j(t)\psi_j(r,\phi)A_0\sin(\beta_z z)e^{+i\omega_{th,j}t} + c.c. \tag{4.2}$$

where M is the total number of spatial modes, $\hat{e_j}$ is the polarization vector for the $j-th$ mode, ψ_j is the eigen-function for the j-th mode, β_z is the propagation constant along the z direction, and A_0 is the normalization coefficient. Since the carrier diffusion in the radial direction must be taken into account for the VCSEL oscillation, the rate equation for the carrier density is given by

$$\begin{aligned}\frac{d}{dt}n(r,\phi,t) &= D\nabla_T^2 n(r,\phi,t) + \frac{J(r,\phi)}{ed} - \frac{n(r,\phi,t)}{\tau_s} \\ &- \frac{\Gamma_d}{d}\sum_{j=1}^{M}G_{nj}\{n(r,\phi,t)-n_0\}|E_j(t)\psi_j(r,\phi)|^2 \end{aligned}\tag{4.3}$$

where D is the coefficient for carrier diffusion, the subscript T denotes the operation for the transverse coordinates, and Γ_d is the confinement factor for the longitudinal direction in the active layer, given by

$$\Gamma_d = \int_0^d |A\sin(\beta z)|^2 dz \tag{4.4}$$

Considering the thickness of the active layer d small compared with the laser cavity L, then $\Gamma_d < 1$. In the derivation of the carrier density we should consider the depletion term and take into account the interference terms for the external product of the vector polarizations. But the beating frequency between the i and j terms is of the order of several GHz, thus the corresponding term into the equation 4.3 can be neglected. The eigen-function for the modes "i-j" for a particular VCSEL structure is a function of the polar coordinate. For example for a weak index-guide cylindrical structure with two polarization states corresponding to the LP_{01} mode, they can be expressed in function of the Bessel function of the first kind $J_0(z)$ and the modified Bessel function of the second kind $K_0(z)$, taking the following form:

$$\psi_j(r,\phi) = \begin{cases} \frac{J_0(u_{1,j}/R_a)}{J_0(u1j)}, & \text{for } R \leq R_a \\ \frac{K_0(w_{1,j}/R_a)}{K_0(w1j)}, & \text{for } r > R_a \end{cases} \tag{B.F.}$$

where R_a is the radius of the active region and u_{1j} and w_{1j} are the first roots of the eigen-value equation for the j-th polarization mode.

$$\frac{u_j J_1(u_j)}{J_0(u_j)} = \frac{w_j K_1(w_)}{K_0(w_j)} \tag{4.5}$$

they have a relation of $u_{1j}^2 + w_{1j}^2 = V_j^2$. V_j is the normalized frequency defined by

$$V_j = \frac{2\pi R_a \sqrt{\eta_{1j}^2 - \eta_j^2}}{\lambda} \tag{4.6}$$

where λ is the wavelength of light in vacuum and η_{1j} and η_j are the refractive indices for the j-th mode in the active area and the clad region.

4.1.1 The spin-flip model

The general model above is able to describe the multi-transverse mode dynamics of the laser, but on the other hand some details concerning the polarization behaviour need a more specific description. In order to properly describe polarization effects in VCSELs, we must take into account that left and right circularly polarizations of laser light 4.2 are related to the spin states in the valence and conduct bands. This relation with the spin states is at the origin of the polarization oscillation, which includes a rich variety of polarization dynamics including polarization switching. A specific model has been proposed from (15, 259, 260, 261), which takes into account the interaction with spin states and the spin dynamics (although it can only be applied when the laser is operating at the lowest order spatial mode). This model, which is called Spin-Flip model (SFM), couples the polarization state with the magnetic sublevels of the valence and conduction bands. With it, it can be shown that laser dynamics depend significantly on the value of the relaxation rates. Polarization switching can be described by taking into account the population difference between carrier density with negative and positive spin values. With this model the results for the lower order spatial mode are entirely coincident with the full equation model, where all the modes are considered, and easily explained. For higher orders we should refer to the equation from the previous section.

Let us now briefly introduce the spin-flip model for lower order oscillation polarization modes. This is the model that we have used in our work to be described below, in this chapter. In Figure 4.1 the four-level model for the polarization dynamics of a quantum well semiconductor laser is represented. The magnetic quantum number in the lower edge conduction band is $J_z = \pm 1/2$, in accordance with the up and down spin states. On the other hand the quantum number for the heavy holes for the valence band have values $J_z = \pm 3/2$.

Conservation of angular momentum entails that photons emitted from state 1/2 to state 3/2 have left circular polarization light, while photons emitted from -1/2 to -3/2 have right circular polarization. In the model, a parameter γ_s takes into account the mixing effect between population of states with the same modulus of J but different sign of J_z.

It is well known that for VCSELs there are two preferred modes of linear polarization which coincide with the crystal axes. These two modes have a frequency splitting associated with the birefringence of the medium. These two modes can be modelled by the parameter of linear phase anisotropy γ_p, which represents the effect of different indexes of refraction for the orthogonal linearly polarized modes. On the other hand the two modes can have slightly different gain-to-loss ratios, which are related with the anisotropic gain properties of the crystal. These differences can be modelled by the parameter γ_a.

The SFM is defined for the slow-varying complex field E_+ and E_- corresponding to the orthogonal circular polarizations (see: (8)), the total carrier density N, and the carrier difference n:

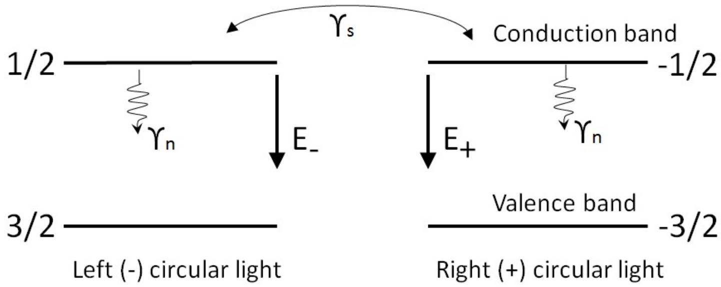

Figure 4.1: Four level model for polarization dynamics in QW VCSELs.

$$\frac{dE_\pm}{dt} = k(1+i\alpha)[(N \pm n - 1)E_\pm] - (\gamma_a + i\gamma_p)E_\mp, \tag{4.7}$$

$$\frac{dN}{dt} = \gamma_n[\mu - N(1 + |E_+|^2 + |E_-|^2) - n(|E_+|^2 - |E_-|^2)], \tag{4.8}$$

$$\frac{dn}{dt} = -\gamma_s n - \gamma_n[N(1 + |E_+|^2 + |E_-|^2) + n(|E_+|^2 - |E_-|^2)], \tag{4.9}$$

Where the variable $N = N_+ + N_-$ represents the total carrier number, given by the sum of the carrier populations with opposite spin in excess of its value at transparency, normalized to the value of that excess at the lasing threshold. The amount n is defined as $n = N_+ - N_-$, which takes into account the difference between the carrier numbers of the two magnetic sublevels, and it is normalized in the same way as N. Moreover, k is the field decay rate, γ_n is the decay rate of the total carrier population, γ_s is the spin-flip rate, α the linewidth enhancement factor, γ_a and γ_p are linear anisotropies representing dichroism and birefringence, and μ is the injection current parameter normalized such that the threshold in the absence of anisotropies is at $\mu_{th} = 1$. The projection of the circularly polarized states over the linearly polarized states is given by:

$$E_x = \frac{E_+ + E_-}{\sqrt{2}}, \quad E_y = -i\frac{E_+ + E_-}{\sqrt{2}} \tag{4.10}$$

Then, substituting eq. 4.10 into equations 4.7-4.9, we obtain the SFM equations in terms of the orthogonal linearly polarized states. Therefore, the SFM rate-equations for orthogonal linearly polarized fields are (15):

$$
\begin{aligned}
\frac{dE_x}{dt} &= k(1+i\alpha)[(N-1)E_x \pm inE_y] \mp (\gamma_a + i\gamma_p)E_x + \sqrt{\beta_{sp}\gamma_n N}\xi_x, && (4.11)\\
\frac{dE_y}{dt} &= k(1+i\alpha)[(N-1)E_y \pm inE_x] \mp (\gamma_a + i\gamma_p)E_y + \sqrt{\beta_{sp}\gamma_n N}\xi_y, && (4.12)\\
\frac{dN}{dt} &= \gamma_n[\mu(t) - N(1+|E_x|^2) + |E_y|^2) - in(E_y Ex^* - E_x E_y^*)], && (4.13)\\
\frac{dn}{dt} &= -\gamma_s n - \gamma_n[n(|E_x|^2) + |E_y|^2) + iN(E_y Ex^* - E_x E_y^*)], && (4.14)
\end{aligned}
$$

where E_x and E_y are linearly polarized slowly-varying complex amplitudes, and $\xi_{x,y}$ are uncorrelated Gaussian white noises with zero mean and unit variance. All the rest parameters have been defined in the previous section 4.1.1.

Although the SFM model makes strong simplifications regarding the dynamics of real VCSELs, many detailed comparisons between experimental measurements and simulations (262),(263),(264),(265), (266),(267),(268),(269),(270), have demonstrated that the model can indeed successfully capture the main features of the polarization-resolved nonlinear dynamics of VCSELs (stochastic polarization switching, current-induced polarization switching, two-mode emission, bistability and hysteresis phenomena). To characterize the mixing of the populations with different spin, this model introduces the spin-flip rate γ_s as a phenomenological parameter. The latter is even considered as a coupling parameter between the two populations of carriers in each pair of levels. For very slow mixing (i.e. $\gamma_s = \gamma_n$) the equations 4.11 can be decoupled in two sets of independent equations, one for E_+, N_+ and another for $E_- N_-$. In the limit of $\gamma_s \to \infty$, corresponding to an instantaneous mixing between the two populations, the orthogonal polarizations become independent of n and coupled through the same population N. The parameters γ_a and γ_p, as already said, represent the anisotropies, dichroism and birefringence. The frequency splitting of the linearly polarized modes is modeled by the parameter γ_p. Its value corresponds to the frequency detuning above and below a central frequency, then the frequency difference between the two modes x and y is given by $2\gamma_p$. While γ_a is the dichroism, which takes into account the different gain for the polarization modes of the cavity, the asymmetric position of the modes in the gain-frequency curve and different asymmetric geometries of the cavity (271). This parameter can be positive or negative depending on which mode has a larger gain-to-loos ratio. VCSELs can have different behaviours depending on the parameters and can show relatively large dispersion.

Table 4.1: Typical VCSEL parameters and values used in this chapter.

Parameter	Symbol	Range of values	Values used
Linewidth	α	2 to 5	3
Field decay rate	k	100 to 400 ns^{-1}	300 ns^{-1}
Carrier decay rate	γ_n	0.5 to 2 ns^{-1}	1 ns^{-1}
Spin-flip rate	γ_s	1 ns^{-1} to 100 ns^{-1}	50 ns^{-1}
Amplitude anisotropy	γ_a	> -1 ns^{-1} to < 1 ns^{-1}	0.5 ns^{-1}
Phase anisotropy	γ_p	1 to 150 ns^{-1}	30ns^{-1}
Bias current	μ	0 to 3	2.5
Noise strength	D	10^{-6} ns^{-1} to 10^{-3} ns^{-1}	10^{-6} ns^{-1}

4.1.2 Steady state solutions of the Spin-Flip Model

The steady state solutions for the orthogonal linear polarizations can be expressed as

$$E_{x,y} = Q_{x,y}e^{i(\omega_{x,y}t+\psi_{x,y})+i\theta}, \quad N = N_0, \quad n = n_0 \tag{4.15}$$

where θ is an arbitrary phase that can be set to zero and ψ is a relative phase between the polarizations. Therefore, by substituting eq. 4.15 into equations 4.11 we obtain the solutions for the x polarization

$$\begin{aligned} Q_x &= \sqrt{\frac{\mu - N_0}{N_0}}, && (4.16)\\ \omega_x &= -\gamma_p + \gamma_a\alpha, \quad \psi_x = 0, && (4.17)\\ N_{0,x} &= 1 + \frac{\gamma_a}{k} \quad n_0 = 0, && (4.18)\end{aligned}$$

and for y polarizations is given by:

$$\begin{aligned} Q_y &= \sqrt{\frac{\mu - N_0}{N_0}}, && (4.19)\\ \omega_y &= \gamma_p - \gamma_a\alpha, \quad \psi_y = 0, && (4.20)\\ N_{0,y} &= 1 + \frac{\gamma_a}{k} \quad n_0 = 0, && (4.21)\end{aligned}$$

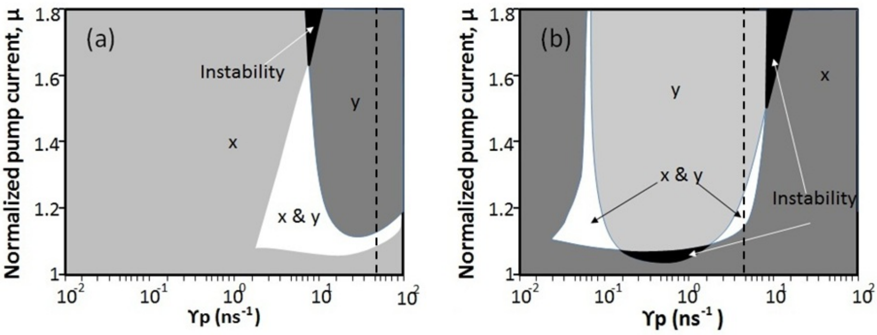

Figure 4.2: Polarizatyion stability diagram in the parameter space (γ_p, μ) for (a) $\gamma_a = 0.5$ and (b) $\gamma_a = -0.2\ ns^{-1}$. Reproduced from (13)

Observing these solutions it is clear that the amplitude anisotropy gives slightly different threshold solutions for the x and y polarizations. Figure 4.2 represents the stability map of the two polarization modes in the parameter space of γ_p and bias current μ. As shown in Fig. 4.2(a)(b), is easy to infer that for a fixed γ_p (along the dashed line) and varying the current μ, the stable output polarization mode can be either x or y and even between these two regions an intermediate region is found with bistability, where both modes can coexist. Increasing the bias current the first mode to turn on is the x mode, but when the current value is set to the boundary area then a small amount of spontaneous noise can allow to switch to the other modes y. Instead, for decreasing the bias current, considering the stable mode is the y one, then at the boundary of the bistable region, small spontaneous noise makes to switch to the other mode x. The section width of the bistable region between the two different stable regions, makes the VCSEL to exhibit hysteresis, which is an interesting feature that we exploit in order to build the stochastic OR logic gate illustrated in details in the next section.

Although the SFM model above described is a combination of phenomenological and detailed theoretical analysis of the light-matter interactions, it has a certain number of simplifications which must be considered and mentioned. Firstly, it is considered that the dipole polarizations have a much faster relaxation rate than the other characteristic time scales of the system and thus they can be adiabatically eliminated. Besides, we employed the simplest version of the SFM model which does not take into account the transverse modes of the emitted light, thus we restrict our study at low pump currents regime, not very far from the threshold, where the fundamental transverse mode dominates. Furthermore the model also neglects the thermal effects in the carrier and gain. Finally, the anisotropies are considered parallel, i.e. on the same axis x or y for simplicity. Therefore, the contribution of both parameters can be expressed, in the model, as a function of the same polarization.

4.2 Polarization switching and bistability

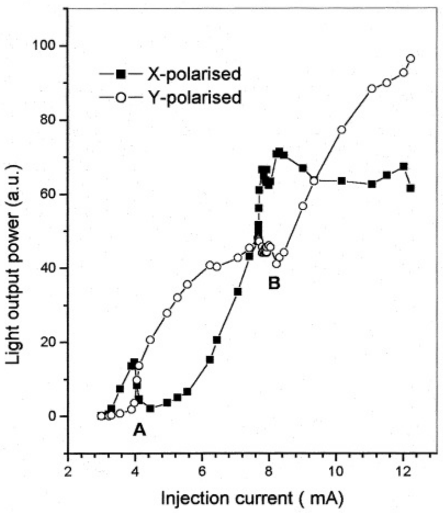

Figure 4.3: Polarization Resolved (PR) light-current characteristics of a solitary VCSEL. Reproduced from (14)

Because of the differences in the refractive index, the semiconductor material shows differences in its response for the polarization components for the principal axis and the orthogonal axis. These differences are included in the distortions and birefringence of the material, which are very small, of the order of $10^{-3} \div 10^{-4}$. For an edge-emitting laser these differences can be ignored due to the strongly asymmetric configuration for the TE and TM modes in the active layer, which make the laser to operate only at the Transverse Electric (TE) mode. However those differences play a crucial role in VCSELs lasers, because they have a relatively symmetric circular disk structure. Then, an ambiguity exists for the polarization direction of the laser oscillation. Therefore, an interesting feature of VCSELs is related to the stability of the two orthogonal linear polarization modes. At a low bias injection current, the fundamental transverse mode (higher frequency mode) starts to lase, then the orthogonal mode (lower frequency mode) grows up after a polarization switching point. Thus the main oscillation mode switches again from x to y mode well above the switching point 4.3. Nevertheless, stochastic polarization switching can also occur, which has been interpreted in terms of Kramers hopping in an effective 1D double well potential (262, 272).

In order to explain the physical mechanism about the described polarization switching (PS), several methods have been proposed, such as the one based on the different modal gain due to thermal effects, or another based on the diverse optical frequencies in birefringent media, and even on the combination of the birefringence and the spatial-hole burning. The first one explains the PS as an effect due to the increased pump current, which produces a self-heating of the device. Then a red shift of the cavity mode frequencies occurs as well as a red shift of the gain spectrum, which is larger than the red shift of the cavity resonances. As a consequence, the mode with larger gain changes. A second explanation is proposed in (273, 274). They consider that at low pump current one mode is suppressed because the cavity losses are larger than the material gain, while the orthogonal mode has a positive net gain. At high pump currents, the PS occurs when the modes exchange the sign of the net gain. Unfortunately, these theories do not explain some experiments involving hysteresis and PS at constant temperature (275, 276). An alternative way to explain the PS and the hysteresis has been developed from (15, 259, 277). They explain these phenomena as a combined effect of birefringence and saturable dispersion associated with the α factor. Therefore, the phenomenon of polarization switching can be described as follows: for low bias injection current, the carrier density has a maximum value at the center of the disk facet emitting light, and smoothly decreases towards the edge of the disk. When the injection current is increased, then the carrier density takes a maximum at a certain distance from the center, and in this way the orthogonal mode is excited and the original one is suppressed. Then the laser is switched from $x - mode$ to $y - mode$ 4.3.

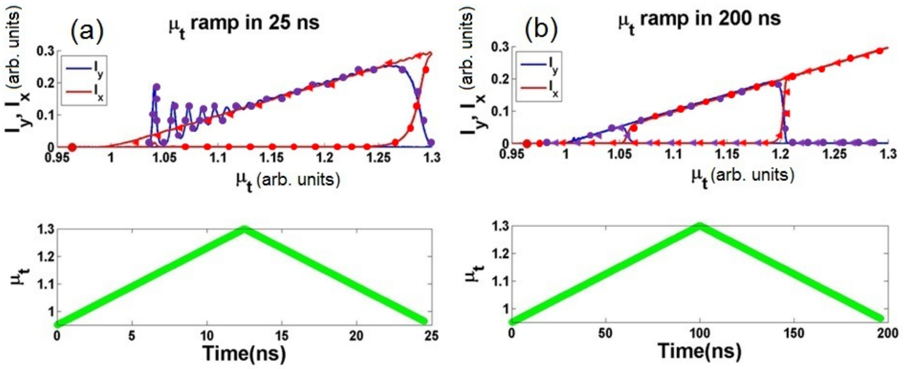

Figure 4.4: (Color online) Numerical calculated L-I curve for γ_a=0.5 and γ_p=30 GHz. (a) ΔT = 200 ns; (b) ΔT = 0.25 ns; circles identifies the dynamic for increasing current, while triangle identifies the dynamic for decreasing current. The green curve below the L-I characteristic is the current-time dependence.

As explained in section 4.1.2, usually the polarization switching does not appear at a given current value, but it occurs at two different currents depending on whether we are increasing or decreasing the bias current. Therefore the polarization mode describes an hysteresis cycle, as shown in Fig. 4.4. It can be seen that for increasing current, the polarization switches on at a given value, whereas for decreasing current, the same polarization mode switches off at a different current value. Besides, it is interesting to observe that the hysteresis cycle changes its size, depending on the velocity of the ramp current. Thus, the polarization switching is well reproduced from the simulations. Moreover, we are interested in the optical features of the output light as the bias current is changing. Figure 4.5(a), reported from (15), describes the light-current characteristic for the case $\gamma_p = 2\gamma$, where the light polarization changes at several bias current values. The average intensity for each polarization mode versus the value of the injection current it is plotted. As already discussed, two different L-I curves are obtained depending on which mode is selected, as the laser is brought above the threshold.

The x-polarized state is retained up to $\mu = 1.1$, where it loses its stability to elliptically polarized emission. After a further increase in the injection current, the output changes to the y-polarized state at $\mu = 1.2$. The switching involves intermediate states of different polarization, such as an elliptically polarized state (an example is labeled by β) and some other complex time-dependent intensity solutions (an example is labeled by γ). Each emission state can be also characterized by the optical spectrum (spectrum of the electric field amplitude). For the linearly polarized state (α and δ) and the elliptically polarized state (β), the spectra have one well-defined peak.

For the solution with time-varying intensities (γ) each of the spectra for the linearly polarized field amplitudes has a main peak (at the same frequency in the two cases) and many equally spaced sidebands, which is the signature of the periodic modulation of the intensity (and phase) for each component.

The $Re(E_x)$ versus the $Re(E_y)$ plots are shown beside the lightcurrent characteristics for the labeled states and clearly identify the different types of polarization; a curve or line is obtained because the solutions have a nonzero optical frequency relative to the rotating reference frame selected for the slowly varying amplitudes of the model.

The hysteresis cycle is also present for a VCSEL configuration master-slave, which we have considered in our Thesis work, and will be presented in the next Section. Figure 4.6 displays the numerically calculated polarization mode x and y curve where the intensity of the two modes is a function of the injected power E_{inj}. From these curves it is evident that at zero injected power only the $\hat{x}$-polarization mode turns on, while the $\hat{y}$-mode is almost zero. Also is displayed the schematic of the potentials referring to the polarization modes, around the cross over current points, because this phenomenon is strongly affected by the strength of the spontaneous emission noise.

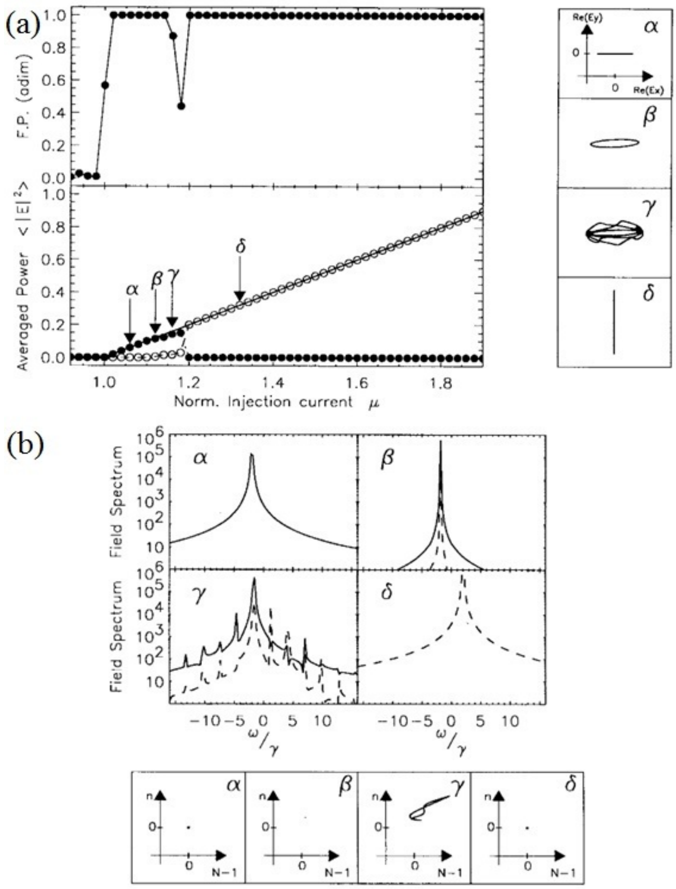

Figure 4.5: (a) Light-current characteristic for the intensity of each linearly polarized mode (solid dots: $\hat{x}$-polarized; open circles: $\hat{y}$-polarized) and the associated fractional polarization (FP). $Re(E_x)$ versus $Re(Ey)$ plots; (b) optical spectra of the field amplitudes E_x (solid line) and E_y (dashed line) for the solutions labeled on the light-current characteristic, and N-1 versus n. Reproduced from (15)

Thus an asymmetric bistable potential well describes the physical situation 4.6.

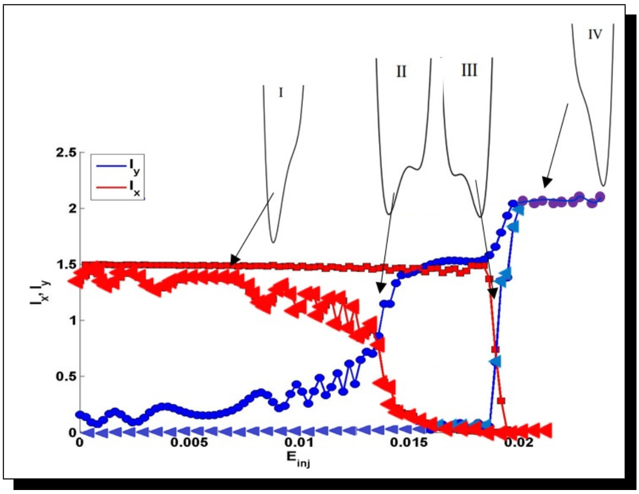

Figure 4.6: (Color online) Numerically calculated polarization resolved versus injection power curve. The red curve represents the x polarization mode, while the blue curve is the y mode. Red squares and blue dots represent the dynamics for increasing injected power. For both curves triangles indicate the dynamics for decreasing injected power. On the top a schematic of the optical potential referring to the polarization modes. The laser parameters are as in Table 4.1

4.3 Numerical results for all optical implementation of Stochastic Logic Gate

We study numerically the dynamics of a vertical-cavity surface emitting laser (VCSEL) with optical injection and show that the interplay between polarization bistability and noise yields a reliable logic output connected to two logic inputs. Specifically, by encoding the logic inputs in the strength of the light injected into the suppressed polarization mode of the VCSEL (the so-called "orthogonal" injection), and by decoding the output logic response from the polarization state of the emitted light, we demonstrate an all-optical stochastic logic gate that exploits the ubiquitous presence of noise. It gives the correct logic output response for as short as 5 ns bit times when the dimensionless spontaneous emission coefficient, β_{sp}, is within the range $10^{-4} \div 10^{-1}$. Considering that typical values of β_{sp} in semiconductor lasers are in the range $10^{-5} \div 10^{-4}$, the VCSEL-based logic gate can be implemented with nowadays commercially available VCSELs, exploiting either their intrinsic noise, or external and background noise sources.

4.3.1 Introduction

In nonlinear systems the interplay between bistability and noise can result in nontrivial noise-induced effects which can be potentially exploited for applications (2, 132, 133, 134). A recent example is the numerical demonstration of a stochastic logic gate using a vertical-cavity surface-emitting laser (VCSEL) that exploits the interplay between polarization bistability, noise, and pump current modulation (133) VCSELs emit linearly polarized light with the direction of the polarization along one of two orthogonal directions associated with crystalline or stress orientations. Some VCSELs display, when the pump current increases, a polarization switching (PS) to the orthogonal polarization. The PS is often accompanied by hysteresis (15) and it has been shown that the switching points and the size of the hysteresis region depend on the pump current sweep rate (136),(137). When a VCSEL is subjected to optical injection, such that only the suppressed polarization receives injection, for appropriated injection parameters a polarization switching from the solitary laser polarization (in the following referred to as X) to the orthogonal one (Y) can also occur (138), either when the optical injection strength is increased (134)(139), or when the wavelength of the injected light is varied (140),(141). With this configuration, which has been referred to as orthogonal injection, polarization bistability and hysteresis cycles have also been observed, which can be exploited for all-optical buffer memories (142),(143).

In the implementation of a VCSEL-based stochastic logic gate proposed in Ref (133), two logic inputs were encoded in an aperiodic three-level signal (*i.e.*, the sum of two aperiodic square waves representing the two inputs) that was directly applied to the laser pump current, and the logic output was decoded from the polarization state of the emitted light (*e.g.*, the output is a logic 0 if the laser emits the X polarization or a logic 1 if it emits the Y polarization). In Ref (133). it was shown that the laser gives the correct logic response with a probability that was controlled by the level of noise, and that was equal to one in a wide range of noise levels. This phenomenon, which has been referred to as logic stochastic resonance (LSR) (132), is receiving a lot of attention because it occurs in several natural stochastic bistable systems (145),(146),(147).

The aim of the present work is to demonstrate an all-optical implementation of the VCSEL-based logic gate. With this aim we use the spin-flip model (15) to simulate the polarization-resolved nonlinear dynamics of a VCSEL under orthogonal optical injection. We demonstrate the phenomenon of LSR, by which the laser gives the correct logic response (encoded in the polarization of the emitted light), to two logic inputs that are encoded in the injection strength. We find that the all-optical configuration can work almost one order of magnitude faster than the electro-optical counterpart described in (133). The model rate-equations are described in Sec. 4.1.1, and the results of the simulations are presented in Sec. 4.3.4. We show that for adequate parameters the polarization of the light emitted by the VCSEL switches between the X and Y polarizations in response to changes in the optical injection strength into the Y polarization. Three injection levels allow for codifying the two logic inputs and then obtaining the logic output of an OR gate (or of an AND gate) in the form of the emitted polarization, as displayed in Table 4.2.

Table 4.2: Input/output combinations for an OR gate: the input is codified with the injection strength on the Y polarization; the response is decoded from the output polarization.

OR Logic Gate			Output Laser Response	Signal level that codifies the input
Inputs		Output		
1	1	1	Y mode	Level 3
1/0	0/1	1	Y mode	Level 2
0	0	0	X mode	Level 1

Key model parameters are the angular frequency detuning between the lasers, $\delta\omega$, the strength of the optical power injected into Y polarization, $P_{inj} = |E_{inj}|^2$, the bit time T_{bit}, and the dimensionless spontaneous emission coefficient, β_{sp}., which will also be referred to as the noise strength. We show that an optimal value of the detuning $\Delta\omega$ allows operating the VCSEL-based logic gate with minimum switching injection power (i.e., minimum P_{inj}). We show that, as can be expected in a LSR phenomenon, an adequate value of β_{sp}, allows for the correct operation of the logic gate, *i.e.*, the laser emits the correct output polarization only when the noise strength is within a certain range of values, which depends on T_{bit}. If the noise is below this optimal range, errors occur in logic output, which are due to delays in the polarization switching; if the noise is stronger than the optimal range, errors can also occur due to the emission of both polarizations simultaneously. Typical values of the spontaneous emission coefficient in semiconductor media are of the order of $10^{-4} \div 10^{-5}$ (278),(8), and our simulations demonstrate that the VCSEL-based logic gate can correctly process bits with a bit-time of the order of $4-5$ ns when the noise strength is within the range of $10^{-4} \div 10^{-1}$. Therefore, the VCSEL-based logic gate proposed here could be implemented with nowadays commercially available VCSELs, exploiting either their intrinsic noise, or external and background noise sources.

4.3.2 Spin-Flip Model for optically injected VCSELs

Considering an optical injection on the orthogonal polarization mode, the Spin-Flip model previously described takes a sightly modified form:

$$\begin{aligned}
\frac{dE_x}{dt} &= k(1+i\alpha)[(N-1)E_x \pm inE_y] \mp (\gamma_a + i\gamma_p + i\Delta\omega)E_x + \\
&+ \sqrt{\beta_{sp}\gamma_n N}\xi_x, && (4.22)\\
\frac{dE_y}{dt} &= k(1+i\alpha)[(N-1)E_y \pm inE_x] \mp (\gamma_a + i\gamma_p - i\Delta\omega)E_y + \\
&+ \kappa E_{inj} + \sqrt{\beta_{sp}\gamma_n N}\xi_y, && (4.23)\\
\frac{dN}{dt} &= \gamma_n[\mu(t) - N(1+|E_x|^2) + |E_y|^2) - in(E_y Ex^* - E_x E_y^*)], && (4.24)\\
\frac{dn}{dt} &= -\gamma_s n - \gamma_n[n(|E_x|^2) + |E_y|^2) + iN(E_y Ex^* - E_x E_y^*)], && (4.25)
\end{aligned}$$

Where all the parameters take the same meaning that those in section 4.1.1. The optical power injected into the Y polarization is represented by $P_{inj} = E_{inj}$ The model equations are written in the reference frame of the injected field, and thus the detuning $\Delta\omega$ is the difference between the optical frequency of the injected field and the frequency intermediate between the X and the Y polarization. Without optical injection and with $\gamma_a = 0$, the angular optical frequencies of the X and the Y polarizations are $-\gamma_p$ and $+\gamma_p$ respectively, and therefore, $\Delta\omega = -\gamma_p$ ($\Delta\omega = +\gamma_p$) means that the injected field is resonant with the X (Y) polarized mode of the solitary VCSEL (134).

4.3.3 Encoding scheme of the logical response

In this section we analyze how two logic inputs can be encoded in a three level aperiodic modulation directly applied to the injected power from the master laser which is fed into the active layer of the slave laser. Then we characterize the laser logic response. The equations 4.22 have been integrated using the explicit Euler method with a time step of 10^{-1} ps, short enough to ensure the convergence of the integration method. The dynamics is studied in terms of the intensity for the two orthogonal polarizations $|E_x|^2$, $|E_y|^2$, and the total intensity as $|E_t|^2 = |E_x|^2 + |E_y|^2$. As said, the two logic inputs are encoded in the injected power via a three-level signal, with the injection levels defined as follows (see Fig. 4.7). Lets consider that $E_{inj}(t)$ is the sum of two aperiodic square-waves, $E_1(t) + E_2(t)$, that encode the two logic inputs.

Since the logic inputs can be either 0 or 1, we have four distinct input sets: (0, 0), (0, 1), (1, 0), and (1, 1). Sets $(0, 1)$ and $(1, 0)$ give the same value of E_{inj}, and thus, the four input sets reduce to three E_{inj} values. Then, it is more convenient to introduce as parameters E_c and ΔE, such that the three injection levels are $E_c - \Delta E$, E_c, and $E_c + \Delta E$. For simplicity we chose $E_c = \Delta E$, and therefore the 3 injection levels reduce to 0, ΔE, and $2\Delta E$. The duration of a bit is defined as $T_{bit} = T_1 + T_2$, where T_1 is the time interval during which the injected power is constant and T_2 is the duration of the ramp (up or down) to the injected power encoding next bit (with $T_2 \ll T_1$, as shown in Fig. 4.7). As will be discussed in the next sections, the value of T_1 strongly influences the reliability of the VCSEL logic gate, but the value of T_2 does not affect significantly the operation, as long as $T_2 \ll T_1$.

The laser response is determined by the polarization of the emitted light. We chose the parameters such that the laser emits either the x or y polarization (parameter regions where there is anti-correlated polarization coexistence or elliptically polarized light are avoided). The laser response is considered a logical 1 if, for instance the

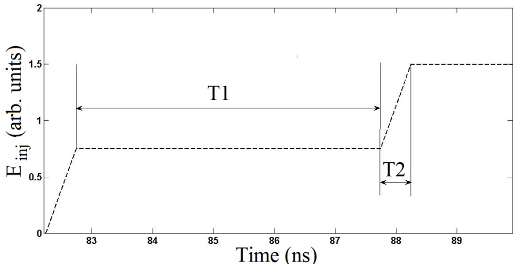

Figure 4.7: Time trace of the injected field amplitude within a bit.

x polarization is emitted, and a logical 0, if the y polarization is emitted. Which polarization represents a logic 1, and which represents a logic 0, depends on the logic operation, as will be discussed latter.

In this way the polarization emitted at the three injected powers (E_{inj}), encoding the four possible combinations of the two logic inputs, allows to implement the operation OR, AND, NOR, NAND, according to the table 4.5. It is evident that by detecting one polarization a logic response is obtained and, by detecting the orthogonal component, the negation of that logic response is obtained. We thus focus only on the operation OR and AND. In the section about the numerical results we study only the OR logic gate, the AND logic can be easily extrapolated from our outcomes.

There are two ways to associate the four possible logic inputs (0,0), (1,0), (0,1), (1,1) to three injected power strengths. The first one is schematically illustrated in Fig. 4.8, which we will refer all time for simplicity. The AND logic can be implemented by the three level current labels as E_I, E_{II}, E_{III}, while the levels E_{II}, E_{III}, E_{IV}, can lead to an OR logic operation. Table 4.3 briefly illustrates this criterion. The idea consists in assuming that the output response is encoded by (i.e) the output polarization which encodes the value 1 if the Y mode is on, otherwise is it 0. Let's describe the OR logic operation considering the only input combination (0,0) whose result is zero. This combination can be associated to the state E_{II}. The interesting feature which is the main idea behind the LSR is the possibility to tune and reliably control the transition between the two modes by the noise strength. Table 4.5 illustrates the relationship between the logic inputs, where the current levels encode these inputs, while the expected laser polarization gives the output response.

The main vantage of this scheme is that ΔE can be chosen constant for the three transitions, and by just changing the mean injected power (E_m) it is possible to change from AND to OR logic or viceversa. As we commented before, the hysteresis

Table 4.3: First scheme: Relationship between the two inputs and the output of the logical operations, and the encoding power levels.

Logic inputs	AND: Injected power	Output mode	Logic output	OR: Injected power	Output mode	Logic output
(0,0)	E_I	y	0	E_{II}	y	0
(1,0)/(0,1)	E_{II}	y	0	E_{III}	x	1
(1,1)	E_{III}	x	1	E_{IV}	x	1

Table 4.4: Second scheme: Relationship between the two inputs and the output of the logical operations, and the encoding power levels.

Logic inputs	AND: Injected power	Output mode	logic output	OR: Injected power	output mode	logic output
(0,0)	E_{IV}	x	0	E_{II}	y	0
(1,0)/(0,1)	E_{III}	x	0	E_{III}	x	1
(1,1)	E_{II}	y	1	E_{IV}	x	1

cycle has a shape and size which depend on the velocity of the injected power. This fact implies that for the encoding scheme, it does not allow very fast modulation for the AND operation, due to the fact that PS for decreasing injected power disappears (133). A second encoding possibility can be implemented (Table 4.4 illustrates this second criterion) where the power injected levels are the same E_{IV}, E_{III}, E_{II}, for both logic operations. Also the encoding criterion changes, in the sense that the lower power level E_{II} encodes the input (0,0) for the OR operation, while it encodes the input (1,1) for the AND operation: the highest power level E_{IV} encodes the input (1,1) for OR and encodes (0,0) for AND. the middle power level encodes (1,0) and (0,1) for both operations. Because the AND and OR operations are implemented with the same three current levels, such a encoding method allows high performance for both logic operations.

4.3.4 Results

The laser parameters used in the simulations of the model 4.22, which are kept constant unless otherwise specifically indicated, are: $k = 300\ ns^{-1}$, $\mu = 2.5$, $\alpha = 3$, $\gamma_a = 0.5\ ns^{-1}$, $\gamma_s = 50\ ns^{-1}$, $\gamma_p = 30$ rad/ns, $\gamma_n = 1\ ns^{-1}$. For these parameters

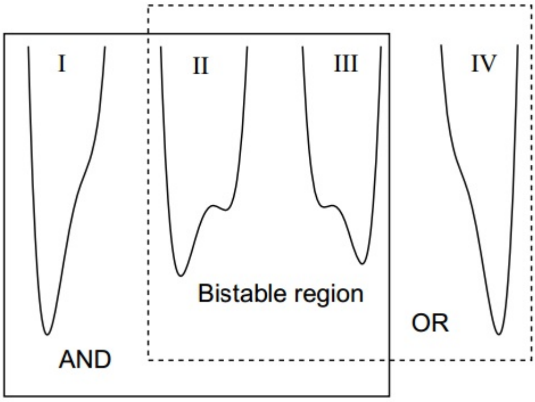

Figure 4.8: Schematic representations of the effective potential at four different pump current values, corresponding to the labels I to IV in Fig. The solid square indicates the three values that can be used for implementing a logic AND; the dashed square indicates the three values that can be used for implementing a logic OR.

Table 4.5: Relationship between the two inputs and the output of the logical operations.

Logic inputs	AND	NAND	OR	NOR
(0,0)	0	1	0	1
(1,0)/(0,1)	0	1	1	0
(1,1)	1	0	1	0

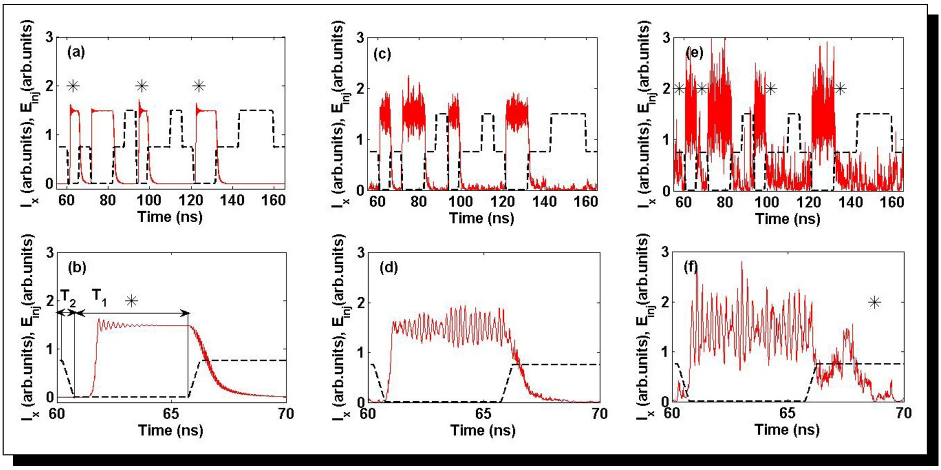

Figure 4.9: Time trace of the intensity of the X polarization (red line) for three noise levels (a), (b) $\beta_{sp} = 105$; (c),(d) $\beta_{sp} = 0.1$; and (e), (f) $\beta_{sp} = 1$; $T_{bit} = 5ns$, other parameters are as indicated in the text. The black dashed line represents the three-level injection strength and the stars mark bits with wrong logic output. The panels (b), (d) and (f) indicate a zoom of (a), (c) and (e).

the solitary laser emits the X polarization. Unless otherwise indicated, the injection parameters are $\Delta\omega = 12$ rad/ns, $\Delta E = 0.0015$, $T_{bit} = 5$ ns, and $T_2 = 0.5$ ns. Figure 4.9 shows a typical time-trace of the X polarization (red solid line) when a three level signal varies the injection strength (black dashed line). The dynamics is shown for three noise levels ($\beta_{sp} = 10^{-5}$ in Fig. 4.9(a), $\beta_{sp} = 0.1$ in Fig. 4.9(c) and $\beta_{sp} = 1$ in Fig. 4.9(e)). Notice that the X polarization turns on when the injected signal is in level 1 (i.e., no optical injection) and turns off in the other two levels, when the Y polarization turns on. The intensity of the Y polarization (not shown for clarity) is either off (when the X polarization is on) or displays fast oscillations (when the X polarization is off). In Fig. 4.9, the asterisks indicate the bits when the laser emits the wrong polarization. The criterion used to determine whether the laser emits the right polarization to a given input is as follows: The laser logic output response is considered correct if, when X is the polarization that has to be emitted according to Table 4.2, 80% or more of the total power is emitted in the X polarization; and in the bits when Y is the correct polarization, 20% or less of the total power is emitted in the X polarization. In other words, the response of the laser is determined only by detecting the intensity of the X polarization, being above or below a certain value. In Fig. 4.9(b) it can be observed that a wrong bit is due to the delay in the switching,

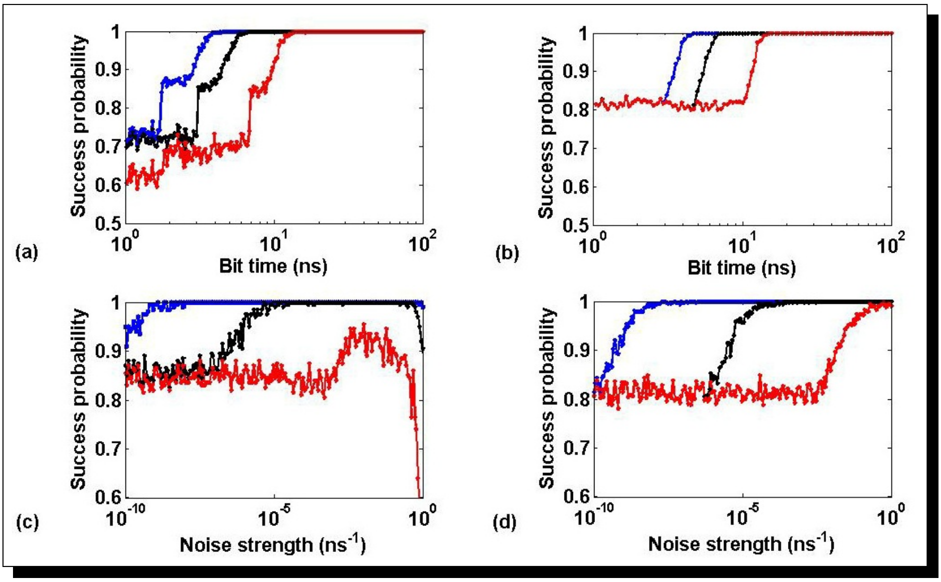

Figure 4.10: Probability of success of an OR logic gate as function of the bit time (a), (b) and as a function of the noise strength (c), (d). The red, black and blue lines indicate the probability calculated using the 90/10, 80/20 and 70/30 criteria respectively (see text for details). ΔE is 0.0015 in panels (a), (c); and 0.005 in (b), (d), the bit time is 7 ns in panels (c), (d), other parameters are as indicated in the text.

as there are oscillations during the switching, but with larger noise the polarization switching is faster Fig. 4.9(d), but increasing still more the noise strength it plays a worst effect with delays in switching off the polarization mode Fig. 4.9(f). Figure 4.10 displays the probability of success of the OR logic gate as a function of the bit time (Figs. 4.10(a) and 4.10(b)) and as a function of the noise strength (Figs. 4.10(c) and 4.10(d)). The success probability was calculated over seven realizations of 500 bits and using 3 criteria for determining if the laser logic output response is correct: 90/10; 80/20 and 70/30, where the first number indicates the minimum percentage of light emitted in the X polarization during a bit, if X is the correct polarization, and the second number, the maximum percentage emitted in X if X is the wrong polarization.

As a function of the bit time, in Figs. 4.10(a) and 4.10(b) one can observe that for the less strict criterion (70/30, blue line) the probability grows to one for smaller bit times as compared to the more restrictive criteria (80/20 and 90/10, black and red lines respectively). One can also observe that the minimum bit time, with the 80/20 criterion as employed in (133), is about $5-7$ ns depending on the noise strength, which is significantly lower than that found in (133), where the logic inputs were applied as a direct modulation of the pump current, which was about $20-30$ ns. As a function of the noise strength, one can observe in Figs. 4.10(c) and 4.10(d) that, for the 70/30 and 80/20 criteria, the probability of a correct response has a wide flat region where P = 1. Considering the criteria 80/20, in Fig. 4.10(c) the plateau with $P = 1$ occurs for $\beta_{sp} = 10^{-4} - 0.1$, which clearly demonstrates the robustness of the correct operation of the logic gate. Figure 4.11 displays the probability of correct logic operation represented with color code, in a two-dimensional parameter space: as function of the noise strength and the bit time, in Figs. 4.11(a) and 4.11(b); and as a function of the bit time and the injection strength, in Figs. 4.11(c) and 4.11(d). Figures 4.11(a) and 4.11(b) are done with two injection strengths (respectively $\Delta E = 0.0015$ and $\Delta E = 0.005$), and Figs. 4.11(c) and 4.11(d), with two noise levels ($\beta_{sp} = 10^{-4}$ and 0.1 respectively). The squares in Fig. 4.11(a) indicate the parameters used in Figs. 4.9(a), 4.9(c) and 4.9(e), and show that for a noise level of $\beta_{sp} = 10^{-5}$ the minimum bit time with probability of correct operation equal to 1 is 7 ns, counterintuitively with $\beta_{sp} = 0.01$ the minimum bit time decreases to 4 ns, and thus noise can improve the speed of the logic gate. Figure 4.11(b) shows that, with large enough optical injection, correct operation of the logic gate can be obtained even when the laser is under the influence of very strong noise, higher than $\beta_{sp} = 1$ (notice the difference in the right-top corner of Figs. 4.11(a) and 4.11(b)). In Figs. 4.11(c) and 4.11(d), which display the success probability as a function of the bit time and ΔE, for weak ($\beta_{sp} = 10^{-4}$) and for strong ($\beta_{sp} = 0.1$) noise respectively, one can observe that if the injection strength is below a threshold at about $\Delta E = 0.001$, the laser does not give the correct logic response, regardless of the bit time or the noise strength. The region with probability equal to 1 is wider in Fig. 4.11(d) (starting with bit times as low as 3 ns) than in Fig. 4.11(c) (that starts at 6 ns), because moderated noise levels (β_{sp} up to 0.01) are beneficial by reducing the switching delay and allowing for correct operation with shorter bit times. In order to demonstrate that the correct operation does not require a fine tuning of the laser parameters, in Fig. 4.12 we present the success probability as a function of various parameters: in captions (a) and (b), as a function of the injection strength and the frequency detuning, for two bit times (7 and 5 ns); in caption (c), as a function of the birefringence and spin-flip parameters, and in caption (d) as a function of the dichroism and the pump current parameters. In Fig. 4.12(a) where we used a bit

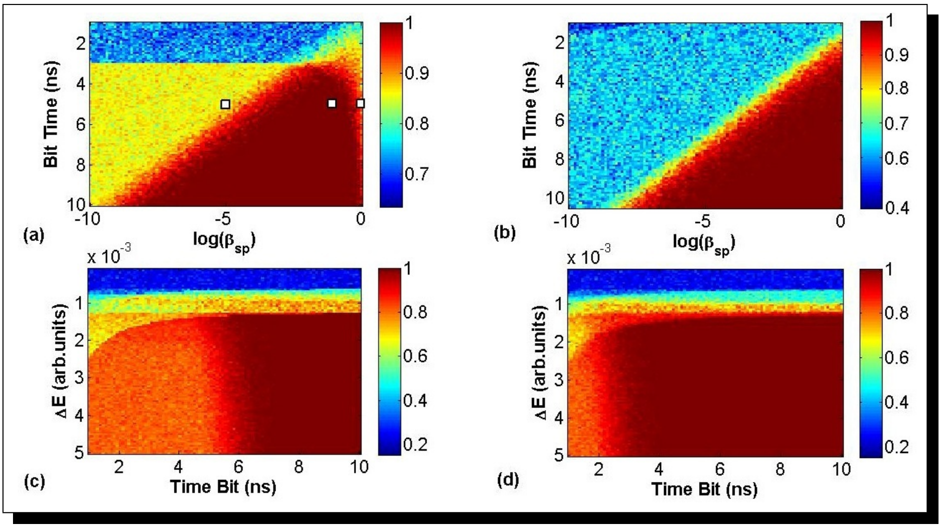

Figure 4.11: Probability of correct operation (in color code) as a function of the noise strength and the bit time (a), (b); and as a function of bit time and the modulation amplitude (c), (d). The probability is calculated over 500 bits using the 80/20 criterium of success logic OR operation. The parameters are $\Delta E = 0.0015$ (a), $\Delta E = 0.005$ (b), $\beta_{sp} = 10^{-4}$ (c) and $\beta_{sp} = 0.1$ (d), other parameters as in the text.

time of 7 ns, there is a wide red area where the success probability if equal to 1. But with a bit time of 5 ns (Fig. 4.12(b)), this red region becomes more narrow. One can also notice that this region is very similar to the stable injection locking region in a laser with cw optical injection. Since $\gamma_p = 30$ rad/ns and the optical frequency of the Y polarization $\approx \gamma_p$, in the red region the injected field is resonant with the Y polarization). Figures 4.12(c) and 4.12(d) show that the correct operation of the logic gate is robust to variations of the birefringence, dichroism, the spin-flip rate and the pump current parameters, as a wide red region is observed corresponding to a success probability equal to one.

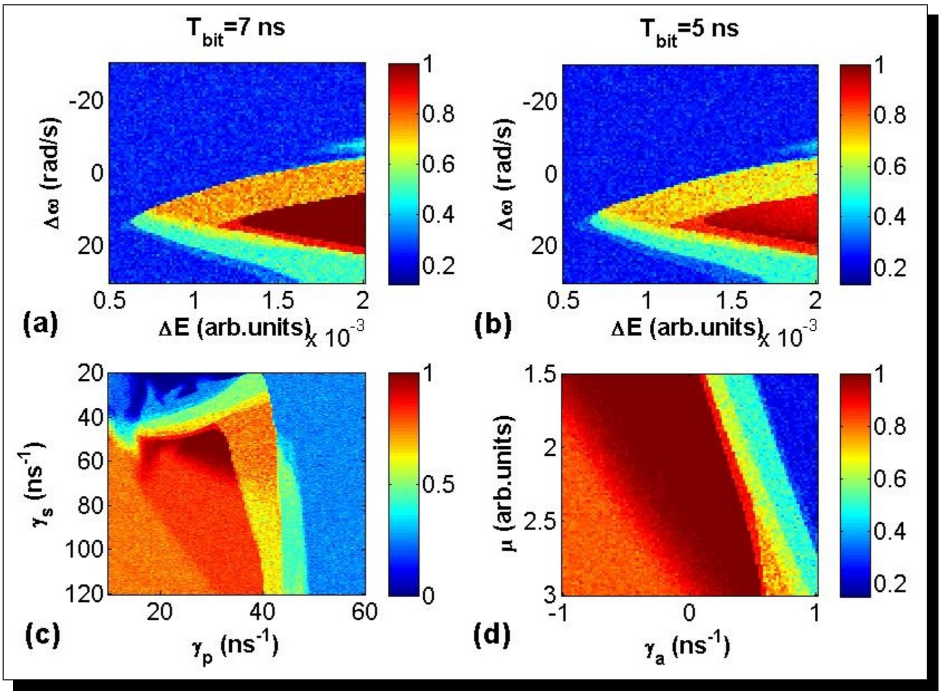

Figure 4.12: Success probability, P, as a function of the optical injection parameters (the injection modulation amplitude and the frequency detuning) for two bit times, 7 ns (a) and 5 ns (b); P as a function of the laser parameters (the birefringence and the spin-flip rate) (c), (the dichroism and the pump current) (d). The probability is calculated over 500 bits using the 80/20 criterium of success logic OR operation. The parameters are $\delta E = 0.003$, $\beta_{sp} = 10^{-4}$, other parameters are as indicated in the text.

4.3.5 Conclusions

In this chapter we briefly introduced the VCSEL laser, and gave the mathematical expressions that describe the rate equations and the SFM. We also explained what the bistability phenomenon and the hysteresis cycle consist in, as well how its characteristics could be exploited. Then, we have shown that in a VCSEL with orthogonal optical injection, there is a wide region of noise strengths where the probability of success of logic gate operation function is equal to 1. We also demonstrated that intrinsic laser noise and external noise can be exploited for improving the performance of the logic gate, giving a reliable and correct logic response, evenly robust to variations of the laser parameters. For too low or too high noise strength, some mistakes occur (see Fig. 4.9), which are due to either turn-on or turn-off delays. In the opto-electronic stochastic logic gate proposed in (133), the minimum bit time for successful operation was about $30 - 40$ ns, whereas in the optical implementation proposed here, the probability equals 1 for much shorter bit times, as $5 - 7$ ns (see Fig. 4.11). Therefore, the all-optical implementation presents a clear advantage for applications where noise is unavoidable and fast switching is required.

5

Rogue Waves in a semiconductor laser with optical injection and current modulation

5.1 Introduction

For centuries, tales of giant oceanic waves which suddenly appear and disappear in calm and safe seas, have been told. In the mid-1990s, one of these phenomena was recorded: for the first time an entire oil platform was "swallowed" by a rogue wave. After that episode, now it is retained that an unprecise number of maritime disasters were caused by these freak waves which disappear without leaving any trace. These phenomena of fast rising wall of water and fast falling down are generally named Rogue Waves (Rogue Wave (RW)s). Again, once not long ago we lived in an economy of financial growing and prosperity. Although politics, and some experts ensured us about the infinite resources of our planet, this new era could not last too long. Countless small and medium-sized financial bubbles have occurred over the years, which have inevitably driven the financial market towards well defined world economics-crash. As oceanic RWs, financial-crashes can be considered as extreme events. Many of these extreme events follow a typical trajectory as a fast exponential function which in some way describes exactly when an extreme events can occur. The term of Rogue Waves, as in oceanography, is also used in many other fields to describe extreme events. For example they have been observed in nonlinear optics, or in electronic circuits (279, 280). Nowadays, modern high-power multimode Continous Wave (CW) lasers are extensively investigated, because the complex dynamics of the output intensity exhibits irregular intensity fluctuations. The latter occurring on time scale of the order of the inverse of the laser linewidth enhancement factor. The analysis of the probability density function reveals the existence of extreme and rare events which have a probability higher than that predicted by Gaussian statistics (281, 282, 283, 284). An intensive research about the generation of optical Rogue Waves in laser systems has been initiated, and there is a widespread and rising interest in the observation of extreme optical events. However, up to now, not many experimental evidences have been reported. Recently, some experimental observations of optical Rogue Waves in several types of laser (Ti-sapphire, VCSELs) have been made (16, 284, 285). These extreme events have been interpreted and described as a collision of “breathers” (286, 287), and specific conditions for their formation have been reported in (288, 289). They demonstrated that two key elements are required for the formation of RWs; namely, granularity, (i.e.) fragmentation of the wave field into a large number of elementary objects of still finite size, named speckless, and inhomogeneity, which means clustering of speckless in spatial domains with different average intensities. Numerical simulations and theoretical studies predict their existence in VSCELs, Ti:sapphire, Raman and mode-locked fiber lasers (290, 291, 292). Also numerical studies by simple equation model describe how the chaotic behaviour could be suppressed by a periodic modulation current (35, 36, 293). An experimental demonstration of control of nonlinear dynamics by slow parametric modulation in a loss-modulated CO_2 laser is also given in (294). As well as an experimental suppression of chaos has been achieved in an optically pumped far-infrared $^{15}NH_3$ laser which displays Lorenz-like chaos (293).

The main characteristics of a Rogue Wave is a very high amplitude, with fast rise and fast falling side, which imply that the system must be highly nonlinear. Besides, the appearance of RWs as directly connected with the existence of a modulational instability has been investigated by employing the nonlinear Schrodinger Nonlinear Schrödinger (NLS) equations (295). In spite that behaviour has been confirmed for large scale, that equation can not explain ocean waves in short scale (287, 296).

One open question is about the role of noise in the occurrence of these extreme events. Could RWs be observed even in the pure deterministic case? and under which conditions?. It has been proved that even in the absence of noise RWs can be detected. They develop in a certain regions of input parameters, where the dynamics is completely chaotic (16). In (16) they calculated the Lyapunov exponent stability map 5.1a, which displays regions where deterministic chaos, hopf bifurcation from period-1 to period-2 oscillations have been observed together with stable and unstable locking. At the same time, they numerically calculated the number of Rogue Waves for the deterministic case (noise strength D=0) 5.1b, and they found that the domain where the RWs developed corresponds with the chaotic region predicted from the Lyapunov exponent 5.1a. In the chaotic region one can observe irregular oscillations and sporadic very high pulses, which by a defined criterium can be identified as RWs. A major challenge is to predict them and, if possible, to control them, making safer environments and systems. It is useful to point out that these phenomena, as opposed to tsunamis or solitons, can disappear in a short spatial length and not necessarily propagate for large distance. An interesting question that we have addressed is if these events could be totally or partially suppressed by a weak periodic perturbation. In this chapter we study the complex generation dynamics of RWs and the associated statistical behavior in the specific case of an optically injected (OI) semiconductor laser with a periodic external forcing via a direct modulation of the bias laser pump current. As it will be shown, we have found that the interplay of intrinsic noise and external modulation can significantly modify the probability of RW occurrence. By shedding light into the role of periodic forcing in a physical system that generates RWs, our findings could be helpful to build future prediction and control models.

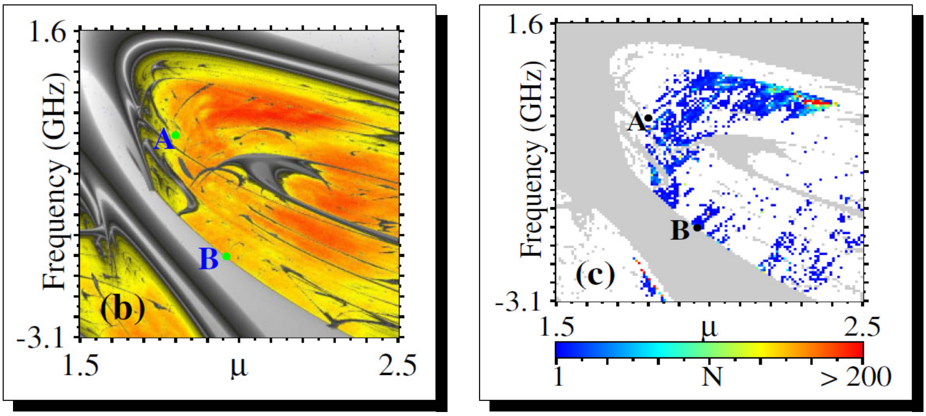

(a) Lyapunov exponents as function of slave laser pump current and the master-laser frequency detuning. The color code indicates negative exponents as gray scale and positive exponents as black-white (yellow-red) scale.

(b) Number of RWs "N" vs the slave laser pump current and the frequency detuning, over a time series of $10\mu s$, with D=0.

Figure 5.1: Both figures are reproduced from (16)

5.2 Rate equation model for a seminconductor laser with optical injection and current modulation

A rate equations model for an optically injected single-mode laser which describes well the dynamics induced by optical injection is the following set of equations (16, 297).

$$\begin{aligned} \frac{dE}{dt} &= \kappa(1+i\alpha)(N-1)E + i\Delta\omega E \qquad (5.1)\\ &+ \sqrt{P_{inj}} + \sqrt{D}\xi(t) \\ \frac{dN}{dt} &= \gamma_N(\mu(t) - N - |E|^2) \qquad (5.2)\\ \\ \mu(t) &= \mu_0 + \mu_{mod} sin(\omega_0 t) \qquad (5.3) \end{aligned}$$

where E and N are the complex field amplitude and carrier density for the laser (which we will call the “slave” laser), P_{inj} is the injection strength (coming from another laser kept all the time in a steady state regime, which we will call the “master” laser), $\Delta\omega = \omega_s - \omega_m$ is the detuning between the two lasers, D is the noise strength, and ξ is a complex Gaussian white noise representing spontaneous emission. Other parameters are the field decay rate, κ, the carrier decay rate, γ_N, the line-width enhancement factor, α, and the injection current, μ. The bias current μ can be sinusoidally modulated with an amplitude μ_{mod} and frequency of $f_{mod} = \omega_0/2\pi$. The parameters kept fix in all simulations are: $P_{inj} = 60\, ns^{-2}$, $\kappa = 300\, ns^{-1}$, $\gamma_n = 1\, ns^{-1}$, and $\alpha = 3$. The frequency detuning is defined as $\Delta\nu = \Delta\omega/2\pi$. These equations are equivalent, for a single-mode laser, of those used in the previous chapter, for a VCSEL with two orthogonal polarized modes. Then, the frequency (Ω_{ro}) of the (Relaxation Oscillation (RO)s) can be calculated as (8):

$$f_{ro} \simeq \frac{\sqrt{2k\gamma(\mu-1)}}{2\pi} \qquad (5.4)$$

We will use this expression in the next section in order to calculate the frequency relaxation oscillation component for the free running laser, and taking it as reference for our discussions.

5.3 Statistical description

The major feature of the Rogue Waves is their unpredictable appearance, thus a method to detect them can be based on the analysis of the probability density function of the output amplitudes (Probability Density Function (PDF)), which turns out to be the more appropriate measure for our purpose. Systems that exhibit rogue waves have long-tailed PDFs. In this work, to define a RW, we use a criterium for which an intensity pulse is detected as a RWs only if its maximum value is higher than a defined threshold. Any other values will be not considered as RW, then they will not provide neither information to the statistics that we will develop here. We define the threshold, τ, as the mean value of the total intensity in the temporal range considered, plus a number (const=6 or 8) of variances σ_I of the probability density function (PDFs)of pulse amplitudes. 5.5.

$$\tau \quad = \quad < I > + const \cdot \sigma_I \tag{5.5}$$

Where $< I >$ represent the intensity mean value, and *const* is a factor that multiplies the PDF intensity variance σ_I. In previous works, the factor *const*, it has taken values from 2 to 8. In the calculations below we have used “const” equal to 6. Despite we calculated the threshold (τ) by means the intensities values, all the next calculations concerning the detection events refer to amplitude values. This difference is due to practical reasons whose for high noise strength and without any filtering to the dynamic, can bring to real differences between the two ways to calculate the threshold. Otherwise, however not appreciable differences can be noticed.

In Fig. 5.2 are reported two examples of the output temporal dynamics of a semiconductor laser optical injected. Although Fig. 5.2(a) for a given set of input parameters (frequency detuning between master and slave laser and, slave injection current) does not shows any RWs, Fig. 5.2(c), for another input parameters, exhibit a chaotic dynamic with pulses much higher than the defined threshold. We will apply always in the next calculation this criterium to define the RWs occurrences.

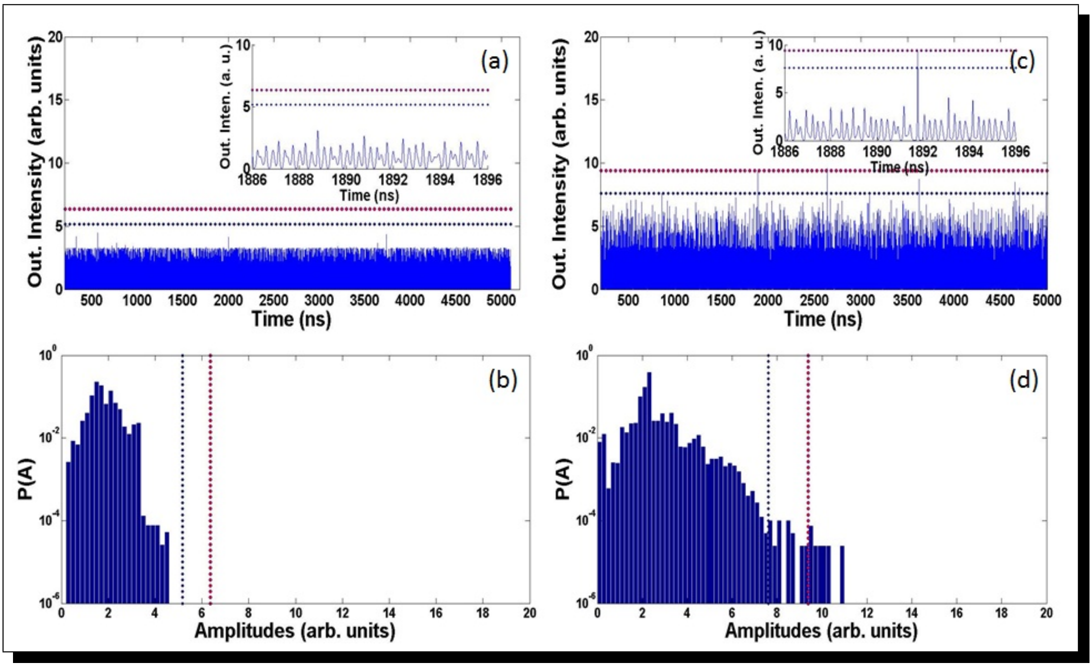

Figure 5.2: Output time traces (a-c), and corresponding probability function of the amplitudes detected over the threshold (b-d). The red dot line correspond with the threshold defined with “const” equal to 6. While for the blue dot line “const” is equal to 8. The figure (a) and (c) are relative to the set of input parameters $\Delta\nu$=0 GHz, μ = 1.8, and (b) and (d) to the set $\Delta\nu$=-1.86 GHz, $\mu = 1.96$

5.4 Numerical Results

In order to investigate the spectral features of our system, we calculate the power spectral density (PSD) of the system response. The PSD function is defined as the module square of the real part of the fourier spectrum of the output intensity $|\chi(f)|^2$, thus it can be considered as an amplitude spectrum such as the one described in chapter 3. The power spectral density gives us information about the characteristic time scales of the system. In particular, we expect the PSD to give us information about which frequencies for the modulated bias current could more efficiently induce or suppress RWs, depending of the input parameters ($\Delta\nu$, μ, f_{mod}, A_{mod}). First of all, and as a milestone for the future development, we will analyze the PSD for the free running (or solitary) lasers, where we expect to obtain a power spectrum with a peak at the relaxation oscillation frequency (which is given analytically by the equation 5.4). Then we will introduce the optical injection (OI) and we will discuss about some different regimes that can be observed, always referring to the amplitude spectra and to the temporal series. We want to identify the chaotic nonlinear region (see chapter 3), as thanks to a previous work we know that Rogue Waves can be detected in that region (16). Subsequently, we will focus on the influence of a periodic modulation of the bias current of the slave laser, which could dramatically change the dynamics. It is fine to remark that, although some regions with period-one or period-two oscillations can have very high peak intensities, the given definition of a RW, as a phenomenon with a deviation above Gaussian prediction, allow us to not consider these oscillations as RWs. Interestingly, we will condense our observations by mapping the detected RWs in the parameter subspace defined by the frequency detuning $\Delta\nu$ versus the bias current μ, at different strengths of noise, including the case of absence of noise. And finally, we will apply a periodic modulation to the bias current μ of the slave laser, and we will study how frequency and amplitude modulation can influence the occurrence of these extreme events.

5.4.1 Relaxation oscillation frequency of the free running laser

We now study the intensity fluctuations of the free running slave laser; therefore, in this subsection the terms representing optical injection and current modulation in equations 5.3 have been removed. As previously said, we now study the situation with the slave laser as free running or solitary laser, so that for this configuration the terms relative to the optical injection (E_{inj}, $\Delta\omega$) and to the modulation current (A_{mod}, f_{mod}) in the equations 5.3 have been removed. Figure 5.3 displays the PSD of the system just described in the absence of bias current modulation and without optical injection ($E_{inj} = 0$), at three different bias currents ($\mu_1 = 1.8$, $\mu_2 = 2.4$, $\mu_3 = 3$). From panel (a) it can be noticed how the PSD exhibits a peak at the frequency corresponding to the relaxation oscillation frequency. The peak is shifted in frequency as the bias current is increased. It is important to notice that the main peak (labeled with the arrow) is shifted proportionally to the bias current, as suggested by equation 5.4. In fact, for the currents $\mu_1 = 1.8$, $\mu_2 = 2.4$, $\mu_3 = 3$ the theory predicts a peak located respectively around $3.48, 4.61, 5.51$ GHz. The inset in panel (a) displays the time trace for a current μ of 1.8, where the relaxation fluctuations around the mean value of 0.8 are highlighted. Panel (b) displays the time traces for a longer time of 800 ns, and from this figure it is evident that the intensity fluctuations due to the relaxation oscillations are very small compared with the mean output power, which can basically be considered constant for the three bias currents respectively at 0.8, 1.4, and 2.

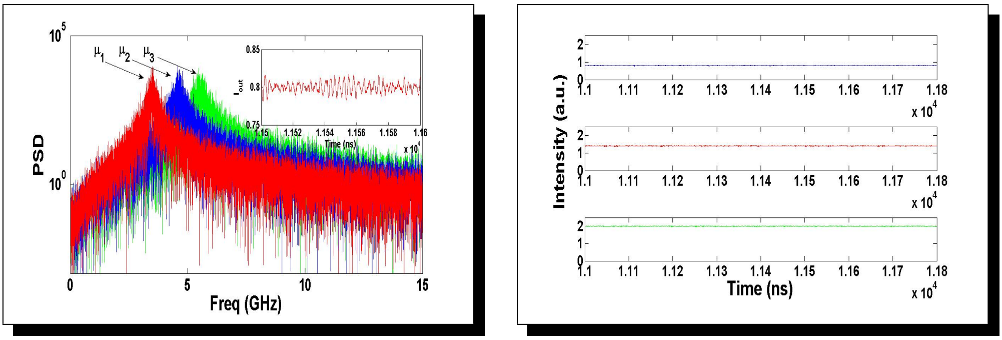

(a)

(b)

Figure 5.3: Numerical calculated Power Spectral Density (a) and respective temporal series (b), without OI ($E_{inj} = 0$) and in the absence of periodic current modulation A_{mod}=0%, f_{mod}=0. Constant bias current with value of μ=1.8; 2.4; 3; respectively red, blue, green curves. Frequency detuning between master and slave $\Delta\nu = 0$ GHz; Power injected $E_{inj} = 0$.

5.4.2 Dynamic regimes with optical injection and without current modulation

Now lets consider the situation where the free running laser (the slave laser) is optically injected from a master laser. Therefore, in the slave-laser equations 5.3 the terms proportional to the injected power E_{inj} and frequency detuning $\Delta\omega$ must be added, but still considering a constant value of the bias current. As done in the previous section, we observe the output dynamics for three fixed bias currents 1.8, 2.4, 3. For each one of them, we calculate the PSD and the respective time traces as shown in figure 5.4 and 5.5. Figures 5.4a-5.4b were obtained setting the injected power at $E_{inj} = 60$ and $\Delta\nu = 0.22$ GHz, while for the curves shown in figures 5.5a-5.5b another set parameters has been chosen $E_{inj} = 60$ and $\Delta\nu = -0.24$ GHz, both with noise strength of 10^{-4}. These two sets of parameters will also be used for further calculations in our work. The input parameters from the master laser have been chosen in a fashion that more dynamics could be revealed. In fact from Fig. 5.4 we clearly see that for input current of 1.8 the power spectral density exhibits a peak at the relaxation oscillation frequency of the solitary laser and two further peaks at lower frequencies which indicate period-3 oscillations as the panel (e2) of Figure 3.10. At current of 2.4 as predicted from the Lyapunov exponent in figure 5.1a it is found chaos, where irregular oscillations dominate the dynamics, and some sporadic pulses can be boosted, and in some case detected as RWs. Interestingly enough, at $\mu = 2.4$ the shape of the PSD has changed, as the two peaks at frequencies lower than the relaxation oscillation frequency have disappeared. We want to remark this fact because this is the typical shape feature of chaos concurrently with extreme events. At higher current of $\mu = 3$, period-1 oscillations appear, in fact the time trace reveals a dynamics locked to the relaxation oscillation of the solitary laser, and a huge peak in the PSD at 5.5 GHz is exhibited. For each case figures 5.4-5.5 also report the behaviour with a noise strength of 10^{-2}, which clearly reveals an increase in the power background which leads to the detection of more RWs due to the nonlinear nature of the system.

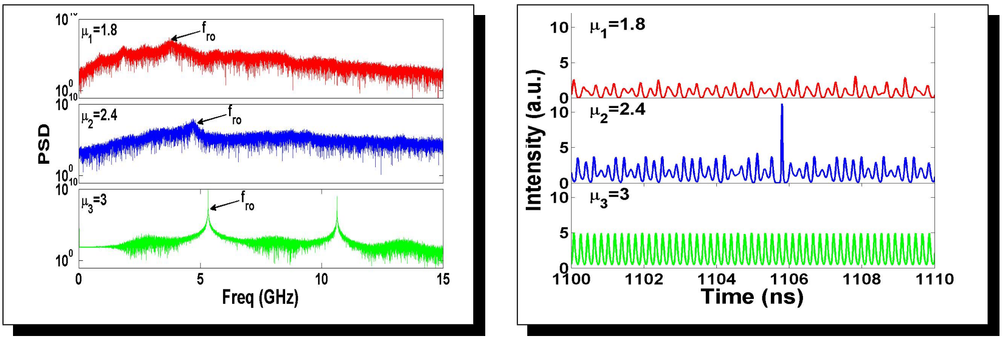

(a) Noise strength D=10^{-4} **(b)** Noise strength D=10^{-4}

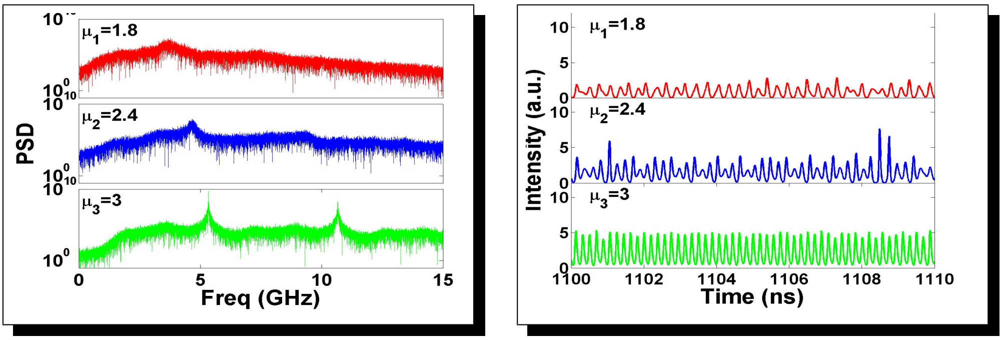

(c) Noise strength D=10^{-2} **(d)** Noise strength D=10^{-2}

Figure 5.4: Numerical calculated Power Spectral Density (a-c) and respective temporal series (b-d), without periodic current modulation A_{mod}=0%, f_{mod}=0. Constant bias current with value of μ=1.8; 2.4; 3; respectively red, blue, green curves. Frequency detuning between master and slave $\Delta\nu$ = 0.22 GHz; Power injected E_{inj} = 60.

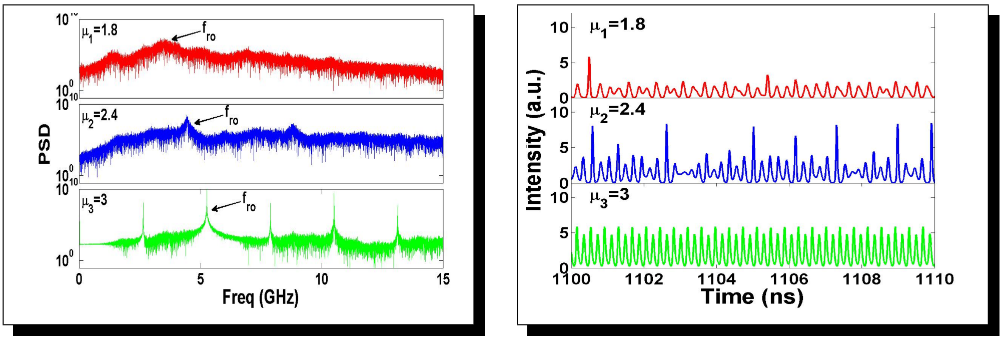

(a) Noise strength D=10^{-4} **(b)** Noise strength D=10^{-4}

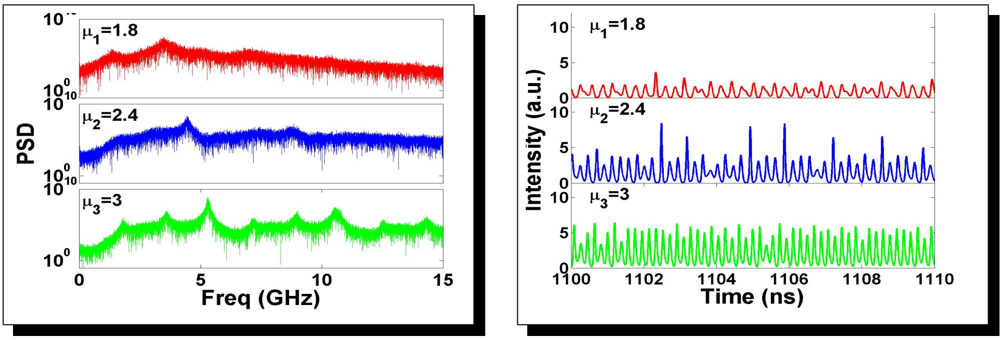

(c) Noise strength D=10^{-2} **(d)** Noise strength D=10^{-2}

Figure 5.5: Numerical calculated Power Spectral Density (a-c) and respective temporal series (b-d), without periodic current modulation A_{mod}=0%, f_{mod}=0. Constant bias current with value of μ=1.8; 2.4; 3; respectively red, blue, green curves. Frequency detuning between master and slave $\Delta\nu = -0.24$ GHz; Power injected $E_{inj} = 60$.

5.4.3 Dynamics at strong current modulation

Finally, in this section we study the effects of a strong modulation of the bias current, for the slave laser. Thus, we must add the periodic component into the term of the bias current μ, making the set equations 5.3 fully equipped for our future analysis. The main goal of this section is to answer to the following questions: *Applying a strong periodic bias current modulation at a certain frequency, will the dynamics change with respect to the case of constant bias current? and how does it changes? Could we inhibit the generation of RWs?* Lets compare the two cases, with strong periodic modulation of the bias current and with bias constant current. For our purpose we again consider three bias current values of 1.8, 2.4 and 3, at which we know from the previous analysis that correspond relaxation oscillation frequencies of 3.5, 4.5, 5.5 GHz, respectively. Moreover we have also considered a lower modulation frequency of 2.5 GHz. First of all we apply a strong sinusoidal modulation current, with an amplitude of 16% of the bias current μ, at the frequencies of 2.5 and 3.5 GHz. Figures 5.6a-5.6b-5.6c-5.6d display the PSD and the respective time traces for the usual three bias currents (μ=1.8, 2.4, 3). In order to visually compare, we report below in Figures 5.6e-5.6f, the PSD and traces for the case without modulation already discussed in the previous section. We must take into account, as previously revealed, that 3.5 GHz was the relaxation oscillation frequency for the bias current of 1.8. Therefore, it could be natural to expect, as main effect of the modulation current at 3.5 GHz, a change of the dynamics corresponding to this latter curve (red curves in Figures 5.6c-5.6d). Despite the modulation frequency coincides with the relaxation oscillation frequency of the free running laser with bias current of 1.8, the dynamics does not show any appreciable change. However, the PSD exhibits several very narrow peaks corresponding to the frequency components at multiples of the modulation frequency at all the three bias currents considered and both modulation frequencies of 2.5 and 3.5 GHz. Surprisingly, the case relative to the bias current of 3 (the green curve in Figures 5.6c-5.6d), it has dramatically changed. The change can even be evidenced from the time trace, which clearly shows as for the bias current $\mu = 3$ the dynamic behaviour slough from periodic to chaotic. However, the output dynamics corresponding to the case $\mu = 1.8$ displays more regular chaos, which could help to boost some RWs. From this bias current, the PSD displays the main components of the modulation frequency but without other ripples which actually make the dynamic more regular. These features of the power spectra under current modulation have a particular interest and they will be retrieved in the results shown in the next sections. Using the same conditions we also calculated the power spectral density for frequency modulations of 4.5 and 5.5 GHz (Figures 5.7). As in the previous cases we observe that the dynamics which it is more affected corresponds to the bias current of 3. However, it is clear how the dynamics of the bias current $\mu = 2.4$ exhibits peaks at 4.5 GHz, as well as its multiple components 9, 13.5 GHz. Moreover, it is noticed that in between these peaks other ripples appear, making all the PSD as a waves-bed. In this case, observing the time traces it is evident that the effect of the modulation is to suppress RWs, because the threshold will be higher. Though the dynamics for a current of 1.8 exhibits a peak at 4.5 and 5.5 GHz, no evidence of dramatic changes from the PSD or temporal traces are observed. Therefore, we can infer that the distance in frequency between the periodic modulation and the nearer periodic solution is proportional to the chaos degree of the system. The relation between the chaotic regime and the frequency modulation can be deeper investigated by means more sophisticated tools such as bifurcation maps and Poincaré section. In this way more direct links between the the output optical field and carrier density could be highlighted. Especially, because we know that an injected field leads to a frequency shift ($\Delta\omega_{shift}$) proportional to the variation of carrier density (δn, as extensively explained in chapter 3). Therefore, modulating the bias current entails that we are introducing a further complexity degree, in this way we obtain a modulated frequency shift such as:

$$\Delta\omega_{shift} \sim \frac{\alpha}{2} g A_{mod} sin(2\pi f_{mod}) * \delta n \tag{5.6}$$

This equation evidences how complex dynamics can be induced from an external periodic forcing. Therefore, it could be ambitious to figure out the output dynamics under different input conditions. Nevertheless we, at least, will try to do observations to identify some strong guide lines.

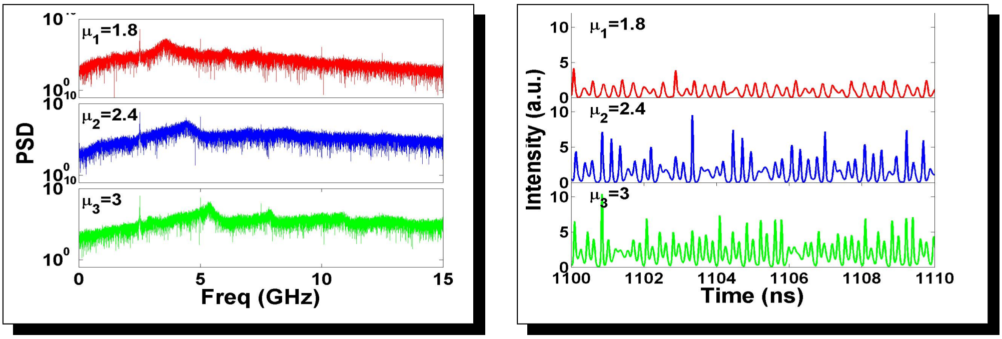

(a) f_{mod}=2.5 GHz **(b)** f_{mod}=2.5 GHz

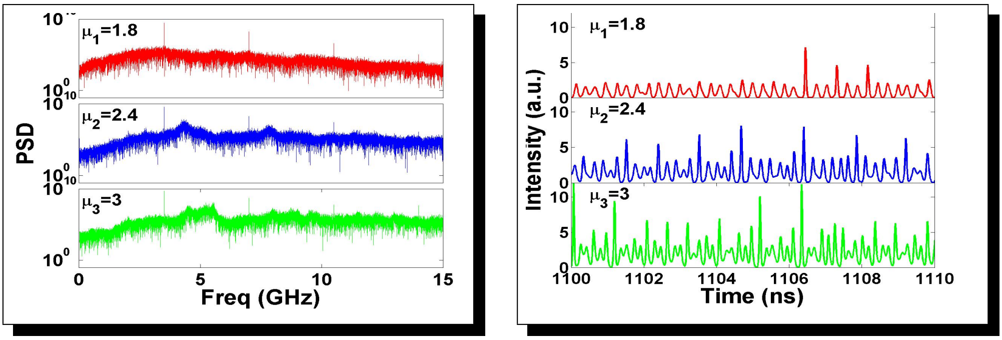

(c) f_{mod}=3.5 GHz **(d)** f_{mod}=3.5 GHz

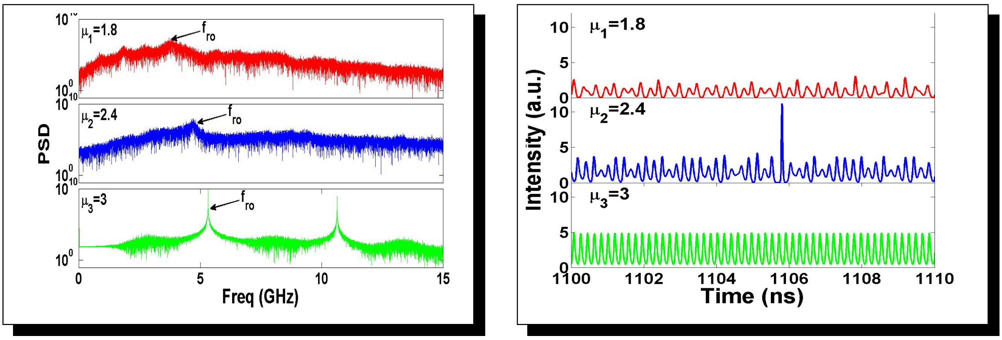

(e) A_{mod}=0% **(f)** A_{mod}=0%

Figure 5.6: Numerical calculated Power Spectral Density and respective temporal series with OI in the cases of modulation bias current and with constant bias current. Average currents values of μ=1.8; 2.4; 3; respectively red, blue, green curves. Noise strength $D = 10^{-4}$; $\Delta\nu$=0.22 GHz; $E_{inj} = 60$; A_{mod}=16% of the μ_{bias};

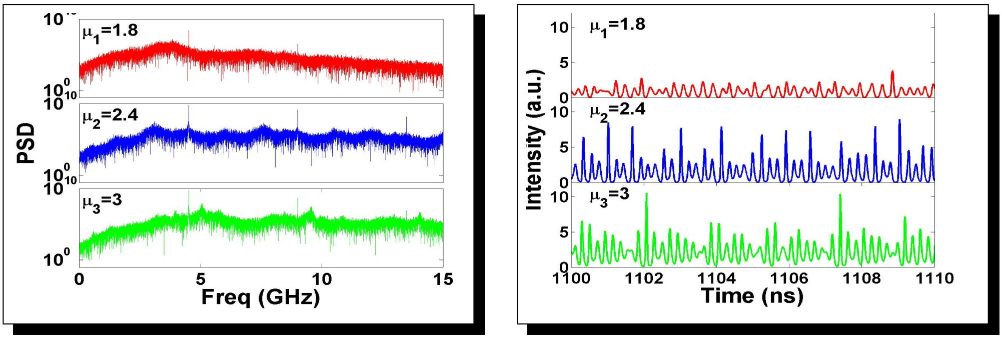

(a) f_{mod}=4.5 GHz **(b)** f_{mod}=4.5 GHz

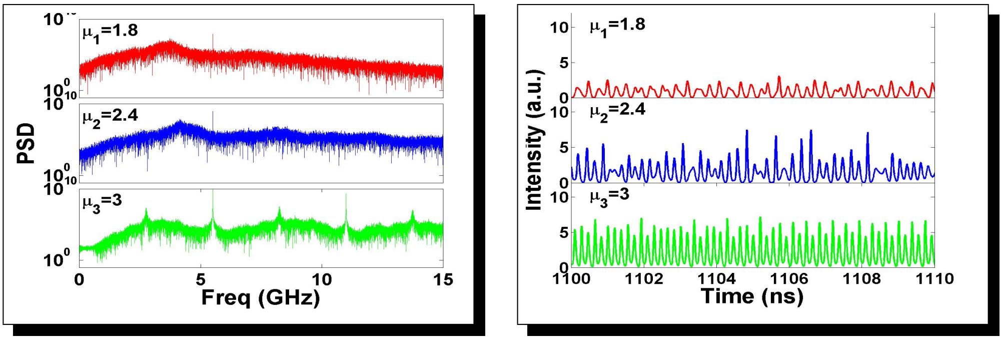

(c) f_{mod}=5.5 GHz **(d)** f_{mod}=5.5 GHz

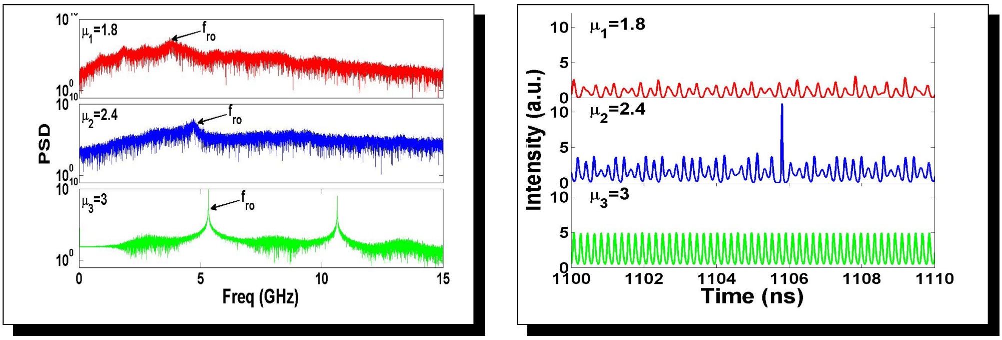

(e) A_{mod}=0% **(f)** A_{mod}=0%

Figure 5.7: Numerical calculated Power Spectral Density and respective temporal series with OI in the cases of modulation bias current and with constant bias current. Average currents values of μ=1.8; 2.4; 3; respectively red, blue, green curves. Noise strength $D = 10^{-4}$. $\Delta\nu$=0.22 GHz; $E_{inj} = 60$; A_{mod}=16% of the μ_{bias};

In Figures 5.8 and 5.9 we consider the case with frequency detuning $\Delta\nu$ of -0.24 GHz. Interestingly and contrarily to the case with frequency detuning of 0.22 GHz, the dynamics corresponding to the bias current of 1.8 (Figures 5.8a-5.8b-5.8c-5.8d) at the frequency modulation of 2.5 and 3.5 GHz makes the PSD to exhibit periodicity and quasi-periodicity . The dynamics corresponding to the bias current of 2.4 does not display significative changes with respect to the case without modulation. However, the PSD exhibits peaks at the modulation frequency and its multiple frequencies. On the other hand the dynamics at the bias current of μ=3 reveals a strong mutation, the output response switching from periodic (without modulation) to chaotic oscillations (with modulation). Increasing more the modulation frequencies at 4.5 and 5.5 GHz (Figures 5.9a-5.9b-5.9c-5.9d), at current of μ=3 (green curves) we can observe again, as in the case with $\Delta\nu = 0.22$ GHz, a switch from periodic to chaotic oscillations dynamics. The PSD function reveals a dramatic change, and for the modulation frequency of 4.5 GHz the power spectrum exhibits peaks at 5 and 9 GHz, which could appear because of some frequency shift of the characteristic time scale of the system. Although the dynamic is not significatively changed, at bias currents of 1.8 and 2.4 we observe spikes at the modulation frequency and its multiple frequencies. As well, interestingly in absence of modulation, a peak around 2 GHz at current of 1.8 is disappearing due to the modulation.

Remarks

Concluding, thanks to this first analysis, we can remark that the effect of the modulation current is important to change the output dynamics. It can force the dynamics towards periodic oscillation or, contrarily, into a pseudo-chaos region depending basically on the input parameters: frequency detuning $\Delta\nu$, bias current μ, and obviously strength and frequency of the applied modulation. We can not discard the possibility that more complex entanglement for example between the frequency shift (given from the change of the carrier density δn) and the frequency of the injected optical field could play a primarily role to select a route to chaos. On basis to this approach it seems promising to further investigate increasing the insight into the routes which define the generation of optical RWs. However, we must say that the generation of optical RWs is not caused by the drastic dynamic change from periodic behaviour to chaos due to the modulation, but rather to a power spectral concentration at the expenses of other components. Let us illustrate that by highlighting figures 5.6a-5.6c where, at bias current of 1.8, the modulation leads to a power spectral concentration at 3.5 GHz, making extreme events to arise. Contrarily, at $\Delta\nu = -0.24$ GHz (Figures 5.8a-5.8c) that behaviour is suppressed by the applied periodic modulation. Therefore, depending on the input parameters region, the modulation current can provide a background potential which favours developing RWs or a frequency power distribution leading to periodic oscillations. Especially, we highlight the case where the modulation provokes suppression of RWs as in Figures 5.7a-5.7c. Observe that the depression immediately after the peak is pulled up from the modulation spike. Therefore, we can conclude that the current modulation can effectively suppress the RWs dynamics in the sense that the energy absorbed from the high pulses can be equilibrated by an increase in the spectral components which have yielded energy during the process. Just to give a phenomenological description about the role of the modulation, we can think of a boat in a calm sea where at some moment RWs appears. By adding an external periodic forcing near to the characteristic frequency of the background waves (but not exactly at that frequency), then the sea will become more agitated at expenses of the Rogue Waves. In other words, the calm and safe environment will be destroyed by the modulation, but at least you will not be killed by an anomalous wave.

From the other hand, our findings leaded that the applied modulation can induce RWs. With a full understanding of this process it could create mechanisms of discharge of the stored energy as a sort of lightning rods. One method would be the introduction of instability which would aim the system out of the defined paths for the establishment of a rogue waves. More concretely it could prevent these phenomena simply inducing them periodically on a smaller time scale. Then, extreme events could be used to produce energy in a controlled form. From our results RWs could be modulated and controlled with a periodic forcing, then in order to understand if it is still an exergonic process a detailed analysis of the energetic approach to define a ratio between the provided energy and the output response could be developed.

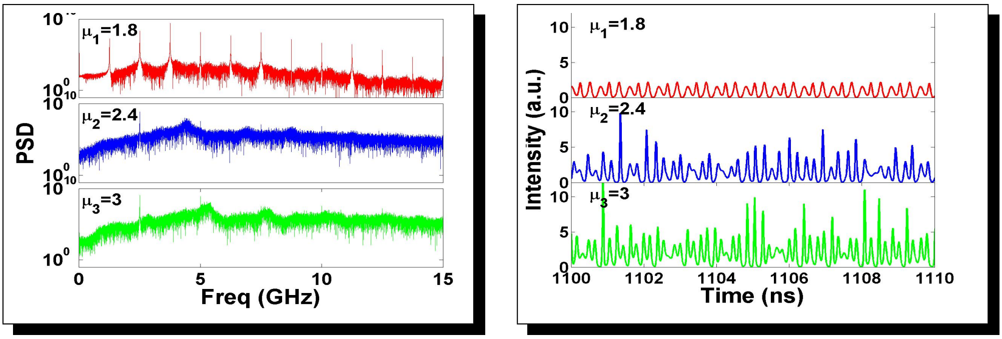

(a) f_{mod}=2.5 GHz **(b)** f_{mod}=2.5 GHz

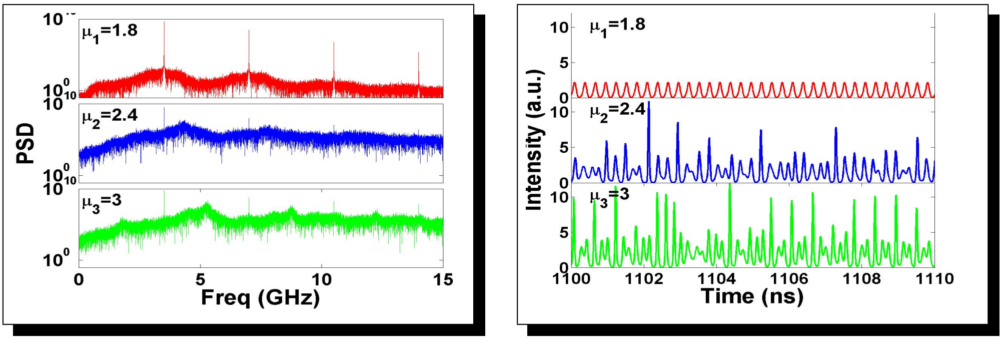

(c) f_{mod}=3.5 GHz **(d)** f_{mod}=3.5 GHz

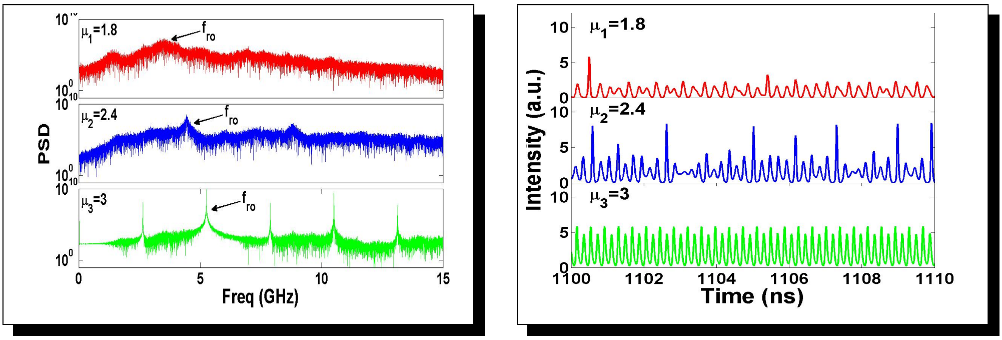

(e) A_{mod}=0% **(f)** A_{mod}=0%

Figure 5.8: Numerical calculated Power Spectral Density and respective temporal series of the output intensity with OI, in the cases of modulation bias current and with constant bias current. Average currents values of μ=1.8; 2.4; 3; respectively red, blue, green curves. Noise strength $D = 10^{-4}$. $\Delta\nu$=-0.24 GHz; $E_{inj} = 60$; A_{mod}=16% of the μ_{bias};

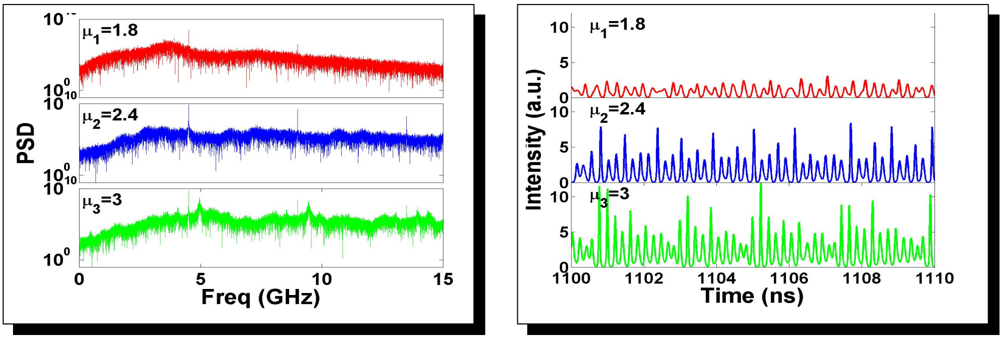

(a) f_{mod}=4.5 GHz **(b)** f_{mod}=4.5 GHz

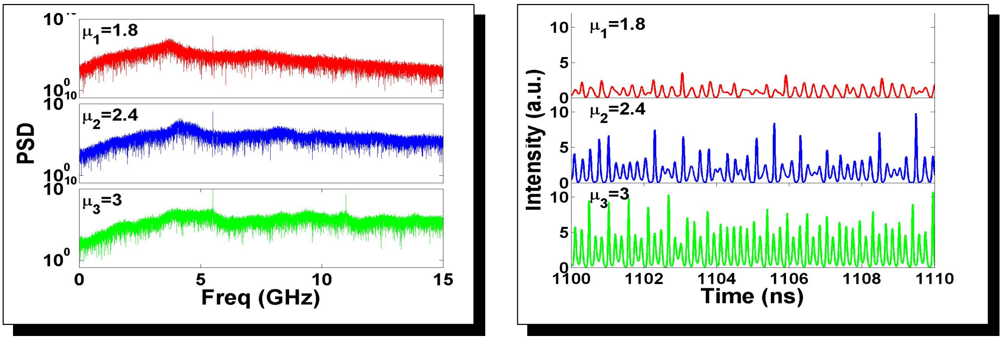

(c) f_{mod}=5.5 GHz **(d)** f_{mod}=5.5 GHz

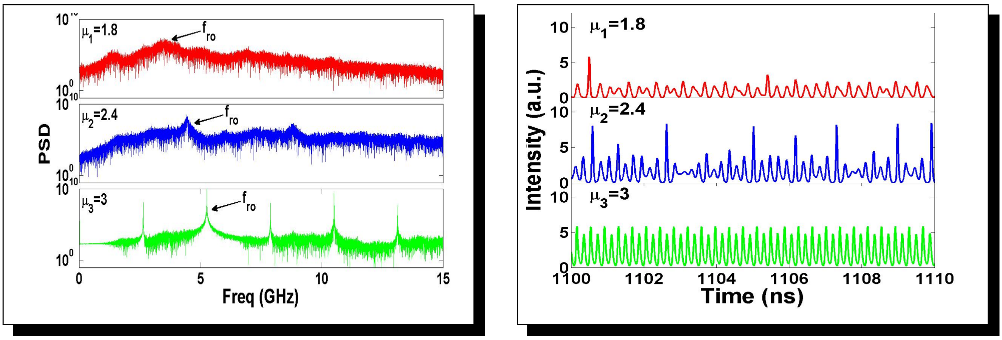

(e) A_{mod}=0% **(f)** A_{mod}=0%

Figure 5.9: Numerical calculated Power Spectral Density and respective temporal series with OI, in the cases of modulation bias current and with constant bias current. Average currents values of μ=1.8; 2.4; 3; respectively red, blue, green curves. Noise strength $D = 10^{-4}$. $\Delta\nu$=-0.24 GHz; $E_{inj} = 60$; A_{mod}=16% of the μ_{bias};

5.4.4 RWs maps in the parameter space ($\Delta\nu$, μ), without modulation

Figures 5.10 reveal the RWs-dynamics in the parameter space current μ versus frequency detuning $\Delta\nu$ as the noise strength is varying from 0 to 10^{-2} , for the system without current modulation (in the next subsection the influence of modulation will be considered). As we already said in the introduction, because of the medium-nonlinearity present in the semiconductor laser, optical RWs can appear even in the absence of noise (D=0), which we will refer to as deterministic optical RWs (16), and as shown in figure 5.10(a). The parameters region where RWs manifest is strictly related with the chaotic region in the parameter space frequency detuning ($\Delta\nu$) versus injection ratio for the OI laser, as confirmed by the calculation of the Lyapunov exponent in (16).

Interestingly enough, for a small amount of noise, of 10^{-4}, no evidence of an increase in the occurrence of RWs has been detected such as shown in panel 5.10(b). More specifically, in certain region as for example the ones highlighted with the dashed boxes, apparently the occurrence of RWs decreases, which could be interpreted as a resonance phenomenon. Particularly, this behaviour could be the fingerprint of the phenomenon of Coherence Resonance (CR). The CR mechanism depend of the specific input parameters region, it appears where the noise can play the role of maximizing the regularity of the oscillations, which makes the dynamics to show more regular oscillations. This obviously increases the threshold needed to detect such extreme events.

At an higher noise strength, of 10^{-3}, as shown in Fig. 5.10(c), it is clearly noticed that the color regions are wider, as compared with the case of lower noise strength. Further increasing one order of magnitude the noise strength up to 10^{-2}, the number of RWs becomes more and more pronounced in regions where the number of RWs was already more significant. At the same time, RWs start also to appear in new areas which were totally devoid of extreme events, as shown in Fig. 5.10(d).

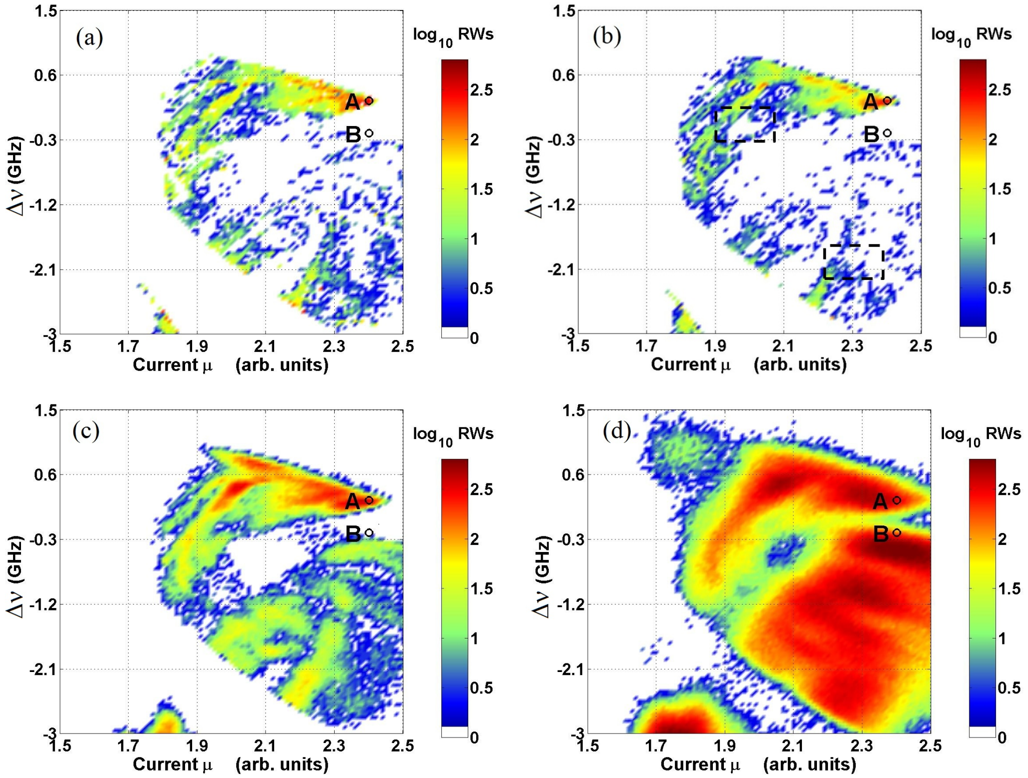

Figure 5.10: Number of detected RWs in the parameter space μ, $\Delta\nu$, when no current modulation is applied. The color code is plotted in logarithmic scale in order to increase the contrast of the regions with a small number of RWs. (a) Noise strength $D = 0$, (b) Noise strength $D = 10^{-4}$, (c) Noise strength $D = 10^{-3}$,(d) Noise strength $D = 10^{-2}$. The two parameters to be used in next section are labeled as A ($\mu = 2.4$, $\Delta\nu = 0.22$ GHz) and B ($\mu = 2.4$, $\Delta\nu = -0.24$ GHz).

5.4.5 RWs maps in the parameter space (f_{mod} A_{mod})

We choose the two points A and B, corresponding to the input parameters $\Delta\nu = 0.22$ GHz and $\mu = 2.4$, which are labeled in Figures 5.10, and, in these operating conditions, we apply a sinusoidal modulation current. Then, we map the number of RWs detected in the parameter space frequency modulation (f_{mod}) versus amplitude modulation (A_{mod}), as it is displayed in Figures 5.11 (Point A)-5.12 (Point B). Moreover, we add another complexity degree varying the noise strength (D) in four steps: 0, 10^{-4}, 10^{-3}, 10^{-2}, whose respective maps are displayed in Figures 5.11(a)-5.11(b)-5.11(c)-5.11(d) (and similarly for Fig. 5.12). Lets start to comment Fig. 5.11, arises from to point A in Fig. 5.10. First of all, we want to highlight that, for zero value of the modulation amplitude and frequency (lower left-hand-side corner of the figures), the operating conditions are the same as in the case displayed in Fig. 5.10. Besides, It is also convenient to remind that as already determined in section 5.2, the relaxation oscillation frequency for this bias current of $\mu = 2.4$ is of about 4.5 GHz. In order to compare the relative effects of different levels of modulation, we take as reference the value of the number of RWs at zero modulation frequency or amplitude. In Fig. 5.11(a), where the noise strength is 0, increasing the modulation frequency up to 5 GHz we observe a dramatic suppression of RWs (white region around 4.5 GHz, for a wide range of modulation amplitudes), exactly at the relaxation oscillation frequency. Actually, suppression of the number of extreme events occurs in a wide domain of modulation frequencies, as all colors different form red (which is the color for the case of absence of modulation, for which the number of RWs is of the order of $10^{2.5}$) correspond to a much lower number of RWs. Fig. 5.11(b) shows, as discussed before, how for the specific noise strength corresponding to this figure a sort of coherence resonance phenomenon occurs. Particularly, the region from 0 to 2 GHz and currents from 4 % to the highest value considered, seems to be the most affected. It reveals a clear diminishing of the number of RWs, as compared with the case of absence of noise (Fig. 5.11(a)).

Interestingly, at noise strength of 10^{-3} Fig. 5.11(c) region with reduction in the number of RWs becomes narrower again. Finally, in the case with a the strongest noise of 10^{-2}, the dynamics evolves as predicted from the previous level of noise of 10^{-3}, that is the number of RWs still continues to increase. The white region corresponding to the suppression events becomes more narrow around the relaxation oscillation frequency. What occurs at this frequency value, in all subfigures in Fig. 5.11, is that the system resonates with the external forcing, exhibiting a multi-wave mixing output response, which leads to a pulsed dynamic behaviour with less dispersion in the pulse peak amplitudes. Thus the threshold value for RWs increases, so that less RWs will be detected. It is also interesting to notice in all subfigures in Fig. 5.11 that, as at noise strength of 10^{-3}, there are frequency values (as 2.3 or 2.9 GHz) at which still traces of suppression events remain. Furthermore between 2 and 4 GHz and for amplitude higher than 16% the occurrence of events becomes higher than in the case without modulation. Therefore, by this first analysis we can conclude that the number of RWs can be suppressed in certain ranges of modulation frequencies and amplitudes. Besides, at high noise strength more RWs events can be induced. Finally, it is worth pointing out that this increase in the number of RWs with noise is not monotonous: we expect that, further increasing the noise level, beyond the values considered in Fig. 5.11, would eventually lead to a reduction in the number of RWs, as in the limit of very high noise the behaviour should be close to a gaussian statistical function, so that essentially no peaks would exceed the threshold value we established for RWs.

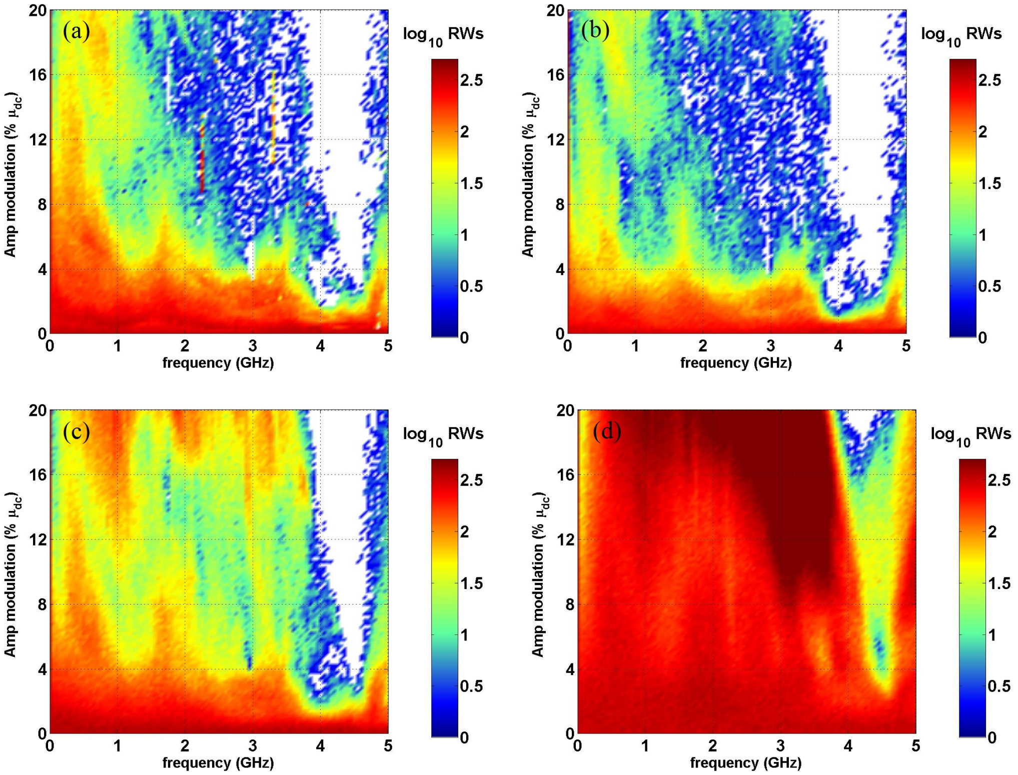

Figure 5.11: Number of detected RWs in the parameter space f_{mod}, A_{mod}. The color code is plotted in logarithmic scale in order to increase the contrast of the regions with a small number of RWs. (a) Noise strength $D = 0$, (b) Noise strength $D = 10^{-4}$, (c) Noise strength $D = 10^{-3}$,(d) Noise strength $D = 10^{-2}$. The input parameters used for the master laser are those labeled with A ($\mu = 2.4$, $\Delta\nu = 0.22$).

Let's now figure out the situation when the frequency detuning is changed at $\Delta\nu = -0.24$ and $\mu = 2.4$. This set of parameters is labelled in Figures 5.10 as B. We have chosen this point because, in the deterministic case (as well as for the lowest considered noise level), no RWs are detected, as shown in Fig. 5.10(a)-(b). As usual, Fig. 5.12(a) depicts the deterministic case. We can observe that almost for all the range of modulation frequencies considered spots of RWs appear (except, as before, for modulation frequencies near the relaxation oscillation frequency of the free.running laser -ca. 4.5 GHz-). Moreover, at frequencies of 0.8 and 1.8 GHz some tongues of detected RWs appear, which could be caused from a sort of modulation-induced chaos or instabilities. As also happened for the point A, noise strength of 10^{-4} provokes a diminishing of RWs occurrences, at least in some parameters region. This coherence resonance effect is clear in Fig. 5.12(b), just observing that the tongues of the RWs detected becomes smaller than in Fig. 5.12(a). As the amount of noise is increased at 10^{-3}, the regions of induced RWs expand, as shown in Fig. 5.12(c). Finally, at the strongest noise of 10^{-2}, , Fig. 5.12(d), a large number of RWs appear, at almost any region in the figure. At many of these points the number of RWs is larger than in the case without modulation with the same noise level (i.e., it is larger than at point (0,0) in the subfigure, or at point A in Fig. 5.10(d)). The only region where still no RWs are detected, is located around 4.5 GHz, corresponding, as indicated, with the relaxation oscillation frequency of the free running laser, but it occurs only in a reduced range of modulation amplitudes.

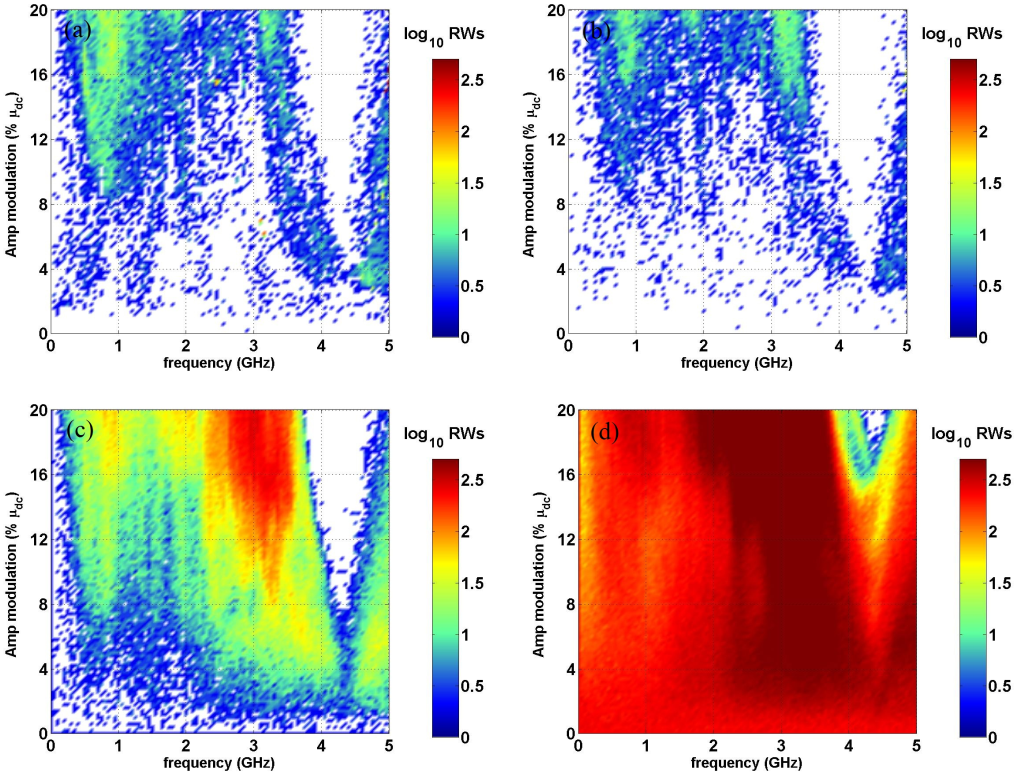

Figure 5.12: Number of detected RWs in the parameter space f_{mod}, A_{mod}. The color code is plotted in logarithmic scale in order to increase the contrast of the regions with a small number of RWs. (a) Noise strength $D = 0$, (b) Noise strength $D = 10^{-4}$, (c) Noise strength $D = 10^{-3}$,(d) Noise strength $D = 10^{-2}$. The input parameters used for the master laser are those labeled, in Fig. 5.10, with B ($\mu = 2.4$, $\Delta\nu = -0.24$ GHz).

5.5 Conclusions

In this chapter we have investigated the nonlinear dynamics of an optical injected laser subjected to an external periodic forcing, which in our specific case is represented by a sinusoidal modulation of the laser bias current. We focused our studies into the generation of extreme events named rogue waves (RWs). They are sudden pulses which appear as fast rising up to huge intensity as well fast fall down in the order of hundred picoseconds. Our outcomes are related with the role of noise and modulation (and of the interplay between them) on the output dynamics. Concerning noise, it usually increases the system's response. Although noise boost the output intensity, we noticed that the interplay between noise and modulation can lead, in some circumstances, to an opposite effect. For small amount of noise of 10^{-4} a counterintuitive phenomenon of the type of coherence resonance is observable as a diminishing of the RWs occurrences (see Figures 5.12(b)-5.11(b)-5.10(b)). Importantly, we also characterized the role of the current modulation by the analysis of the Power Spectral Density (PSD) of the output intensities and the respective temporal dynamics. We observed how the modulation acts as a forcing at certain modulation frequencies mutating the dynamics from chaotic to periodic. As well as, depending on the input parameters region, current modulation can provide a background potential which favours developing RWs or otherwise a frequency power distribution leading to periodic oscillations and an increased threshold for RWs. Therefore, we can conclude that the modulation can effectively suppress the RWs dynamics in the sense that the energy absorbed from the high pulses can be equilibrated by an increased of the spectral components which have yielded energy during the process. Just to give a phenomenological description about the role of the modulation, we can imagine a boat in a calm sea where at some instant RWs can appear. By adding an external periodic forcing near the characteristic frequency of the background waves (but not at exactly at that frequency), then the sea will become more agitated at expenses of the Rogue Waves power. In other words, the calm and safe environment will be destroyed by the modulation, but at least you will not be killed by an anomalous wave.

On the other hand the applied modulation can induce RWs. A full understanding of this process might allow us to create mechanisms of discharge of the stored energy as a sort of lightning rods. One method could be the introduction of instability which would aim the system out of the defined paths for the establishment of rogue waves. More concretely, it could prevent these phenomena simply by inducing them periodically on a smaller time scale. Then, extreme events could be used to produce energy in a controlled form. Our results indicate that RWs could be modulated and controlled with a periodic forcing, then a detailed analysis of the energetic approach to define a ratio between the provided energy and the output response could be developed. Finally, with this original theoretical work, we have been able to induce or contrarily suppress RWs in a VCSEL laser by a periodic modulation of the bias current. Therefore it is interesting to study the temporal edge of prediction of these phenomena. As future works, we trust that this kind of behaviour can deeper be investigated even by means other tools, as bifurcation and Poincaré maps. On the other hand, an experimental confirmation of these behaviours and predictions would be convenient, and we will push to try to do it somewhere. Obviously, for what concerns optics, very fast and sensitive instrumentation would be required.

6

Conclusions: Summary of results and future work

The work contained in this thesis was devoted to improve the understanding of how the interplay of stochastic and nonlinear phenomena in optical systems, under specific constrains, can be exploited in novel ways. The interplay between external deterministic forcing and intrinsic nonlinear dynamics in the presence of noise has been experimentally and numerically investigated. This interaction of noise and nonlinearity can lead to several resonance phenomena, such as Stochastic Resonance, Coherence Resonance, and Logic Stochastic Resonance.

In statistical physics, colloidal particles are often referred to as model systems to address novel concepts in a convenient way. This is particularly true for the study of noisy phenomena, because colloidal particles are continuously moving randomly due to the presence of thermal fluctuations. Such fluctuations — responsible for the Brownian diffusion of the particles— introduce a noisy background. The presence of some deterministic force acting on the particles can affect the random walk of the particles producing a drift. As described in Chapter 2, it is possible to make use of optical forces to introduce deterministic perturbations acting on the particle in a controllable way. Optically trapped particles can, therefore, be a very powerful tool to study statistical physics phenomena, relying both on the presence of a natural intrinsic noisy background and on a finely controllable deterministic force field.

However, noise is ubiquitous in nature and, despite the fact that it is often considered as a drawback, it is unavoidable for life. An example is further given by the semiconductor laser, where spontaneous emissions are indispensable to turn on the laser. In fact, one of the main point of this thesis is to demonstrate that the combination of nonlinearities and noise can be useful for novel applications where the nuisances can be employed in a constructive way.

6.1 Summary of results

In Chapter 2 we presented our results related with stochastic resonances phenomena by using optical trap techniques. We have shown that a maximization of the Signal to Noise Ratio (SNR) is also observable in a monostable optical system. Despite in this system no potential barrier is present, we consider this phenomenon directly related with the classical Stochastic Resonance phenomenon(SR) which is usually observed in a double well system. About this issue no previous experimental evidence by using optical trap techniques had never been made.

The main outcome of this chapter comes from the experimental and theoretical investigation of the dynamics of a brownian particle kept trapped in an harmonic potential, and where the considered output response was the position of that particle. It is well known that, in the presence of a background noise, an increased effort put in controlling a system stabilizes its behavior. Rarely it is thought that an increased control of the system can lead to a looser response and, therefore, to a poorer performance. We have studied theoretically and experimentally the situation where the confinement effort is increased at a fixed intrinsic and parametric noise level. We have shown that, counterintuitively in most cases an increased confinement effort over a certain threshold leads to a poorer system performance. This feature derives from the interplay between the intrinsic noise and the parametric noise of the confinement effort exerted on the system, a kind of a resonance that produces a damping of the system - henceforth we named it resonant damping.

Afterwards, we have experimentally demonstrated that the Stochastic Resonant Damping (SRD), and Stochastic Resonance (SR) are two distinct phenomena. While the SRD concern a minimization of the variance of the detected output position, the SR refer to a maximization of the SNR. We report the experimental demonstration about the diversity of the two phenomena, which coexist in the same system but at different frequency regimes.

Finally, in subchapter 2.7 we have described a detection technique that we developed in order to exactly define the position of the particle beyond the practical limit imposed in principle, by the sensitivity range of the electronic device used for this purpose. Essentially, this method exploits the channel crosstalk in order to 10-fold increase the spatial detection range from 150 nm up to 1500 nm. Because the spatial modulation of the optical potential up to 1 μm, this more powerful technique has been adopted in all the previous outcomes described in that chapter. The technique demonstrated in this thesis allows a significant increase of the detection range in 2D or 3D systems.

One of the aspects that has motivated our research is the technological importance of semiconductor lasers,as well as their rich variety of nonlinear dynamical phenomena and the role of spontaneous emission noise in them. Numerical simulations of rate equations which describe the nonlinear dynamics in an optically injected semiconductor laser have been implemented to predict and better understand these devices. In Chapter 3 we presented an introduction to the physics of semiconductor lasers, and we discussed the most important features of the dynamics of optically injected lasers, in particular their working regimes and the enhanced bandwidth obtained thanks to the injected field, which we used in subsequent chapters for the analysis of the results.

In Chapter 4 we demonstrated the phenomenon of Logic Stochastic Resonance (LSR) in an optically injected semiconductor laser. LSR has been shown to be a reliable mechanism to obtain a nonlinear logic operator due to the interplay between bistability, noise and an aperiodic modulation. Our work in Chapter 4 has been devoted to exploit bistable and nonlinear effects present in an optically injected VCSEL laser in order to generate all-optically signals that can codify logical inputs and output response. VCSEL lasers exhibit bistability and hysteresis cycle in the output polarization modes as the current is increased. In the same way an optically injected laser shows bistability and hysteresis as the injected power is increased and successively decreased. In Chapter 4 we have shown how these properties can act as a stochastic logic operators due to the effect of the spontaneous emission noise. Two logical input signals have been codified from three levels of the injected power from the driven laser (master laser). Therefore, the polarization of the emitted light is varied from the injected power. A logical response encoded in the two orthogonal linear polarizations has been obtained when the injected power modulation is adjusted to favor one polarization for two modulation levels and to favor the opposite polarization for the third modulation level. We numerically demonstrated that the VCSEL-based logic operator allows to reproduce the truth table for the OR and NOR logic operators. From our results the extension to the rest of operators (AND, NAND) is easy to be implemented. With the optically injected configurations we have been able to reduce the minimum bit time required to perform a correct operation from 30 ns, obtained for an opto-electronic configuration, to only 5 ns with our all optical logic gate. Moreover, we have demonstrated that VCSELs can act as reliable logic operators in a wide range of noise strengths, and could be a promising technique for logic operations under strong background noise.

As extensively investigated and reported in previous works, optically injected semiconductor lasers (SCLs) show several parameter regions where the dynamics is chaotic and irregular pulses appear. By using a proper definition, some of these pulses can be considered as extreme events. In the last years, in optics, as well as in oceanography, these extreme events have been named Rogue Waves (RWs). The motivation to study such class of phenomena in semiconductor lasers is because it has been proved that the laser model could be employed to explain natural phenomena as that of freak waves. In chapter 5, we have numerically studied, by using the rate equations for the semiconductor laser, the nonlinear dynamics of a SCL optically injected underlying the mechanism which provide these huge peak intensities. Ours findings bring us to conclude that by adding noise, the number of RWs increase, and the region in the parameter space where they have been detected becomes always wider. This behaviour is registered for high noise, but for very low noise, of the order of 10^{-3}, we discovered a sort of coherence resonance which provides a diminishing in the number of events in certain defined regions of the parameters space.

In order to suppress or induce extreme events, we investigated the effects of an external periodic modulation of the bias current of the free running laser. We observed how the modulation acts as a forcing at certain modulation frequencies mutating the dynamics from chaotic to periodic. As well as, depending on the input parameters region, current modulation can provide a background potential which favours developing RWs or otherwise a frequency power distribution leading to periodic oscillations and an increased threshold for RWs. Therefore, we can conclude that the energy that was concentrated in the high pulses is partially transferred and distributed over many new spectral components brought about by the modulation. Just to give a phenomenological description about the role of the modulation, we can imagine a boat in a calm sea, where at some instants RWs can appear. By adding an external periodic forcing near the characteristic frequency of the background waves (but not exactly at that frequency), then the sea will become more agitated (many frequencies brought about by the beating between those frequencies appear) at the expenses of the Rogue Waves power. In other words, the calm and safe environment will be destroyed by the modulations, but at least you will not be killed by an anomalous wave.

In conclusion, with this original work we have theoretically been able to induce or suppress RWs in a VCSEL laser by a periodic modulation of the bias current.

6.2 Perspectives for future work

We consider that the research presented in this thesis has clarified many aspects of nonlinear dynamics, but at the same time it has been for us a source of inspiration for new possible future developments. We propose here a list of possible interesting aspects that could be developed and could lead to new scenarios:

- The Stochastic Resonant Damping (SRD) has been proven to be a mechanism able to maximize the confinement of a colloidal particle (to minimize the variance of its position) only adding an external noise to the position of the trap. The natural question is: Is it possible to control or stabilize random dynamics with high variance even in other systems by means the effect of SRD? Therefore it could be interesting to apply this mechanism in real world problems such as financial markets, social science, or even in geophysics or climatology.
- The Stochastic Logic Gate has been numerically demonstrated to be implemented in a VCSEL semiconductor laser as a reliable and fast logic operation. Could it be possible to implement a VCSEL configuration that can consume less energy obtaining faster transmission? Also, it would be interesting to try an experimental verification of an all optical logic gate in a VCSELs laser.
- Extreme events in nature are often considered as destructive phenomena. In principle it is commonly thought that predicting them could prevent disasters, as economic crises due to financial crashes or oceanic RWs that shoot-down platform in the sea, or could limit the damages when an earthquake is going to manifest. Any of these events are essentially due to energy concentration at some defined characteristic spatial and temporal scales. In this sense, one of the future challenge could be how to predict them, to avoid disasters that could come across anywhere. Therefore it would be interesting to study the temporal edge of prediction of these phenomena. With this information, discharge mechanisms of the stored energy could be created, as a sort of lightning rods. One method could be the introduction of an instability which, would aim the system

out of the paths defined for the establishment of rogue waves. More concretely it could prevent these phenomena simply applying a modulation current at a given frequency near to the relaxation oscillation frequency.

On the other hand, extreme events could also be beneficial. For instance, they could be used to produce energy in a controlled form. From our results, RWs could be modulated and controlled with a periodic forcing, then a detailed analysis of the energetic approach to define a ratio between the provided energy and the output response could be developed.

Moreover, based on an idea from Pisarchick and at. (294) we would like to stabilize the chaotic solution at the boundary to the stable one, by means a slow and strong external modulation.

A

Brownian motion

The Brownian motions was described for the first time by the botanist Robert Brown, in the year 1828. He observed that pollen of different plants was dispersed in water in a uncounted number of small particles (called pollen grains). The movements of these pollen grains was perceived as an irregular and continuous swarming motion. He also found that all kinds of inorganic substances show the same behaviour, then he was concluding that all matter was built up of ‘primitive molecules’. Before the theory of Einstein other investigations were been bring up from Weiner (1863), Jevons (1870), Dancer (1870), Delsaux (1877). However, the first precise investigation was performed by Gouy in the year 1888. He observed that the motion is more likely the smaller the viscosity of the liquid. Moreover, he described the matter motion was due essentially to the thermal molecular fluctuations of the liquid. Exner in the year 1900 was demonstrating that the velocity of the movement decreases with the size of the particle and increases with the rise of temperature. Einstein was the first in the 1905 to give a correct explanation of the whole problem.

A.1 Diffusion relation

Considering the irregular movement of the particle due to the thermal molecular liquid movement, this process give rise to diffusion. Then, there are two important assumptions. Firstly, that each particle displacement is independent from the other particle movements. Secondly, that for a finite size interval of time the particles movement must be considered mutually independent process. Therefore considering an interval τ so that it will be shorter than the observation time but large enough such that the motion executed in two consecutive intervals τ are independent. Now, supposing a solution with n suspended particles, each particle after a time τ, it will be move of Δ (with Δ positive or negative). If dn is the number of particles which experience a displacement between Δ and $\Delta + d\Delta$ in an interval of time τ, then it is possible to formulate the following relation:

$$\frac{dn}{n} = \phi(\Delta)d\Delta \tag{A.1}$$

where $\phi(\Delta)$ is the probability of jump of magnitude Δ, and it differs from zero only for very small values of Δ. Moreover it fullfills the phase symmetry condition:

$$\phi(\Delta) = \phi(-\Delta) \tag{A.2}$$

Confining the motion in one dimension (x), we specify as $\nu = f(x,t)$ the number of particles per unit volume. Now we calculate, the distribution of the particles a time $t + \tau$, from a distribution at time t. After some integrations (see (99, 298, 299)), we obtain the diffusion differential equation:

$$\frac{\partial f(x,t)}{\partial t} = D\frac{\partial^2 f(x,t)}{\partial x^2} \tag{A.3}$$

where D is named diffusion coefficient. Moreover, if we suppose that at time $t = 0$ alla the particle are concentrated at the point $x = 0$ then the density of the distribution will be infinite at this point and zero every where. Then after some calculations (see (299)) the diffusion distribution in space-time is given by:

$$f(x,t) = \frac{n}{\sqrt{4\pi Dt}}e^{-x^2/4Dt} \tag{A.4}$$

From the above equation is easy to calculate the square root of the arithmetic mean of the squares of the displacement:

$$\langle x^2 \rangle = 2Dt \tag{A.5}$$

Therefore the mean displacement is proportional to the square root of time, which is a typical feature of brownian motion.

A.2 Diffusion and mobility

Considering the suspended particles inhomogeneous dispersed in a liquid, and further we consider the equilibrium state depending from a force k, which acts on the particles and it depends, only of position but not on time. The dynamic equilibrium condition can be looked as a superposition of two processing which act in the opposite directions.

- The particle immersed in the liquid experience an opposing force due to the molecules of the liquid. The balancing between the external force k and the opposing force, then the particles falls with a constant terminal velocity v_0. Therefore if the opposing force is $6\pi\kappa\rho v_0$, then:

  $$v_0 = \frac{k}{6\pi\kappa\rho} \tag{A.6}$$

  If the number of particle per unit of volume is ν, then the number of particle which pass a unit area per unit of time is: νv_0.

- The thermal movement of the liquid lead to a diffusion process as result of the irregular movement. Then, considering D the coefficient of diffusion and μ the mass of the particle, then the number of particle passing per unit of time in a unit of volume is:

  $$-D = \frac{\partial \nu}{\partial x} \tag{A.7}$$

  Therefore the dynamic equilibrium is given by:

  $$\frac{\nu k}{6\pi\kappa\rho} = -D\frac{\partial v}{\partial x} \tag{A.8}$$

  At the equilibrium the particles density (ν) under the gravity (k) takes a Boltzmann distribution:

  $$\nu = \nu_0 exp\left[-\frac{k(x-x_0)N}{RT}\right] \tag{A.9}$$

  where is R the universal gas constant and N the Avogadro number. Therefore, after a substitution of A.9 in A.8

  $$D = \frac{RT}{N}\frac{1}{6\pi\kappa\rho} \tag{A.10}$$

Then the coefficient diffusion depends only of the coefficient of the viscosity of the liquid and the size of the suspended particle. If we name the term $\frac{1}{6\pi\kappa\rho}$ as "mobility" of the particle, and we labeled as B, then, the following expression is the relation between the mobility and the diffusion coefficient.

$$D = \frac{RT}{N} B \tag{A.11}$$

B

Numerical integration techniques

There are several possible numerical methods to solve the semiconductor laser rate equations by temporal discretization. Here, we briefly explains some of that, we employed in this thesis, that are the Heun method (or improved Euler method) or second order Runge-Kutta.

The Heun method refer to the explicit trapezoidal rule, and it is a numerical procedure to solve ODE equations (Ordinary Differential Equations), with given initial conditions.

The Heun method consist to calculate first an intermediate value of the solution which than will be used for the final approximation. The general form of a first order ODE system is:

$$y'(t) = f(t, y(t)) \tag{B.1}$$

Then since we need a second-order method, we have to expand:

$$y(t+h) = y(t) + hy'(t) + \frac{h^2}{2}y''(t) + O(h^3) \tag{B.2}$$

The first derivative can be replaced by the right-hand side of B.1, and differentiating B.1 it is possible to obtain the second derivative:

$$\begin{aligned} y''(t) &= f_t(t,y) + f_y(t,y)y'(t) && \text{(B.3)} \\ &= f_t(t,y) + f_y(t,y)f(t,y), && \text{(B.4)} \end{aligned}$$

with f_y the Jacobian. Neglecting the dependence of y and t when it is appear as argument to f, the expansion becomes:

$$\begin{aligned} y(t+h) &= y(t) + hf(t,y) + h^2/2[f_t(t,y) + f_y(t,y)f(t,y)] + O(h^3) && \text{(B.5)} \\ &= y(t) + h/2f(t,y) + h/2[f_t(t,y) + hf_t(t,y) + hf_y(t,y)f(t,y)] + O(h^3) && \text{(B.6)} \end{aligned}$$

We know from the multivariate expansion that:

$$f(t+h, y+k) = f(t,y) + hf_t(t,y) + f_y(t,y)k + ... \tag{B.7}$$

It is evident that the expression of B.5 can be interpreted as:

$$f(t+h, y+hf(t,y)) = f(t,y) + hf_t(t,y) + hf_y(t,y)f(t,y) + O(h^2) \tag{B.8}$$

Therefore:

$$y(t+h) = y(t) + h/2f(t,y) + h/2f(t+h, y+hf(t,y)) + O(h^3) \tag{B.9}$$

or the numerical method

$$y_{n+1} = y_n + h\left(\frac{1}{2}k_1 + \frac{1}{2}k_2\right) \tag{B.10}$$

with

$$\begin{aligned} k_1 &= f(t_n, y_n) && \text{(B.11)} \\ k_2 &= f(t_n + h, y_n + hk_1) && \text{(B.12)} \end{aligned}$$

The values k_1 and k_2 are also known as stages of the Runge-Kutta method. They are different estimations of the slope of the solution. The accuracy of this method improves quadratically with the step size, while for the Euler method improves only linearly. This method is named predictor-corrector method where the predictor is based on the Euler's method and the corrector is the trapezoidal method.

The general form of the explicit second-order Runge Kutta methods can be written as:

$$y(t+h) = y(t) + h\left[b_1\tilde{k}_1 + b_2\tilde{k}_2\right] + O(h^3) \tag{B.13}$$

$$\begin{aligned} \tilde{k}_1 &= f(t,y) && \text{(B.14)} \\ y_{i+1} &= f(t + c_2 h, y + h a_{21}\tilde{k}_1) && \text{(B.15)} \end{aligned}$$

This correspond to a generalization of the classical Runge-Kutta method since the choice of the parameters $b_1 = b_2 = 1/2$ and $c_2 = a_{21} = 1$ yields that case. The coefficients $a_{i,j}$, b_i, and c_i are arranged by the *Butcher tableaux*, as follows:

c	A
	b^T

Therefore the Butcher tableaux, for the classical second-order Runga-Kutta method:

0	0	0
1	1	0
	1/2	1/2

Explicit Runge-Kutta methods are characterized by a lower triangular matrix A, *i.e.* $a_{ij} = 0$ if $j > i$. The coefficient c_i and a_{ij} are connected by the condition:

$$c_i = \Sigma_{j=1}^{\nu} a_{ij} \quad i = 1, 2, ..., \nu$$

This is a condition of consistency for method of order one. For An explicit second -order method we necessarily have a_{11}=a_{12}=a_{22}=$c_1 = 0$.

Then we can now study the combinations of the coefficients b_1, b_2, c_2 and a_{21}B.10 Therefore, the general second-order Runge-Kutta becomes:

$$y(t+h) = y(t) + h\left[b_1 f(t,y) + b_2\{f(t,y) + c_2 h f_t(t,y) + h a_{21} f_y(t,y) f(t,y)\}\right] + O(h^3) \tag{B.16}$$

$$= y(t) + (b_1 + b_2) h f(t, y + b_2 h^2)\left[c_2 f_t(t,y) + a_{21} f_y(t,y) f(t,y)\right] + O(h^3) \tag{B.17}$$

To match the general expansion B.5 we want:

$$\begin{aligned} b_1 + b_2 &= 1 \\ c_2 b_2 &= 1/2 \\ a_{21} b_2 &= 1/2 \end{aligned}$$

This is a three equation system for a four unknowns variables. A popular solution is given by the choice of: $b_1 = 0$; $b_2 = 1$; $c_2 = a_{21} = 1/2$. This is the modified Euler method

$$y_{n+1} = y_n + hk_2$$

with:

$$\begin{aligned} k_1 &= f(t_n, y_n) \\ k_2 &= f(t_n + h/2, y_n + h/2k_1) \end{aligned}$$

with the Butcher tableaux:

$$\begin{array}{c|cc} 0 & 0 & 0 \\ 1/2 & 1/2 & 0 \\ \hline & 0 & 1 \\ \hline \end{array}$$

References

At the end of each reference we indicate the pages where it is cited in this Memory.

[1] I. Poberaj D. Babic, C. Schmitt and C. Bechinger. Stochastic resonance in colloidal systems. *Europhysics Letters*, 67:158, 2004. 9, 44

[2] P. Jung L. Gammaitoni, P. Hänggi and F. Marchesoni. Stochastic resonance. *Rev. Mod. Phys.*, 70:223–287, 1998. 9, 40, 48, 53, 79, 161

[3] Arkady S. Pikovsky and Jürgen Kurths. Coherence resonance in a noise-driven excitable system. *Phys. Rev. Lett.*, 78:775–778, Feb 1997. 9, 10, 49, 52

[4] Diego N. Guerra, Adi R. Bulsara, William L. Ditto, Sudeshna Sinha, K. Murali, and P. Mohanty. A noise-assisted reprogrammable nanomechanical logic gate. *Nano Letters*, 10(4):1168–1171, 2010. PMID: 20218630. 10, 55

[5] F. Gittes and C.F. Schmidt. Interference model for back-focal-plane displacement detection in optical tweezers. *Optics Letters*, 23:7–9, 1998. 11, 65, 66

[6] J. M. G. Vilar and J.M. Rubi. Divergent signal-to-noise ratio and stochastic

resonance in monostable systems. *Phys. Rev. Lett.*, 77(14):4, 1996. 16, 40, 99, 100, 103

[7] A. Murakami, K. Kawashima, and K. Atsuki. Cavity resonance shift and bandwidth enhancement in semiconductor lasers with strong light injection. *Quantum Electronics, IEEE Journal of*, 39(10):1196–1204, 2003. 18, 21, 124, 125, 128, 138, 140, 142

[8] J. Ohtsubo. Semiconductor lasers: Stability, instability and chaos. volume 48, pages 203 – 341. Springer, Berlin, 2005. 18, 122, 128, 148, 150, 163, 179

[9] T.B. Simpson. Mapping the nonlinear dynamics of a distributed feedback semiconductor laser subject to external optical injection. *Optics Communications*, 215:135–151, 2003. 18, 19, 20, 129, 130, 132, 134, 135, 136, 137

[10] L. Li J. Wang, M. K. Haldar and F. V. C. Mendis. Enhancement of modulation bandwidth of laser diodes by injection locking. *IEEE Photon. Technol. Lett.*, 8:34, 1996. 20, 121, 124, 138, 140

[11] H.F. Chen, J.M. Liu, and T.B. Simpson. Response characteristics of direct current modulation on a bandwidth-enhanced semiconductor laser under strong injection locking. *Optics Communications*, 173(16):349 – 355, 2000. 21, 121, 126, 138, 144

[12] Y. Takiguchi, K. Ohyagi, and J. Ohtsubo. Bandwidth-enhanced chaos synchronization in strongly injection-locked semiconductor lasers with optical feedback. *Opt. Lett.*, 28(5):319–321, Mar 2003. 21, 121, 146

[13] J. Zamora-Munt. Nonlinear and stochastic dynamics of semiconductor lasers: modulation, transient dynamics and synchronization. *PhD thesis*, Jun 2011. 21, 154

[14] S. Bandyopadhyay, Y. Hong, P.S. Spencer, and K.A. Shore. VCSEL polarization control by optical injection. *Lightwave Technology, Journal of*, 21(10):2395–2404, 2003. 21, 156

[15] J. Martín-Regalado, F. Prati, M. San Miguel, and N. B. Abraham. Polarization properties of vertical-cavity surface-emitting lasers. *Quantum Electronics, IEEE Journal of*, 33(5):765–783, 1997. 22, 53, 150, 151, 157, 158, 159, 161, 162

[16] Cristian Bonatto, Michael Feyereisen, Stéphane Barland, Massimo Giudici, Cristina Masoller, José R. Rios Leite, and Jorge R. Tredicce. Deterministic optical rogue waves. *Phys. Rev. Lett.*, 107:053901, Jul 2011. 23, 176, 177, 178, 179, 182, 195

[17] J. García-Ojalvo, A. M. Lacasta, F. Sagus, and J. M. Sancho. Noise-sustained signal propagation. *EPL (Europhysics Letters)*, 50(4):427, 2000. 37

[18] Francesc Sagués, José M. Sancho, and Jordi García-Ojalvo. Spatiotemporal order out of noise. *Rev. Mod. Phys.*, 79:829–882, Jul 2007. 38

[19] Alexei Zaikin, Jordi García-Ojalvo, Lutz Schimansky-Geier, and Juergen Kurths. Two-fold role of noise in doubly stochastic effects, (proc. SPIE), 2003. 38

[20] J. García-Ojalvo and J. M. Sancho. Colored noise in spatially extended systems. *Phys. Rev. E*, 49:2769–2778, Apr 1994. 38

[21] JoseM. Sancho and Jordi García-Ojalvo. Noise-induced order in extended systems: A tutorial. In JanA. Freund and Thorsten Pschel, editors, *Stochastic Processes in Physics, Chemistry, and Biology*, volume 557 of *Lecture Notes in Physics*, pages 235–246. Springer Berlin Heidelberg, 2000. 38

[22] Jose M. Sancho, Oliver Carrillo, Marta Ibanes, Jaume Casademunt, and Jordi García-Ojalvo. Multiplicative white-noise-induced phase transitions: the role of the stochastic interpretation, 2004. 38

[23] E. Ullner, A. Zaikin, J. García-Ojalvo, and J. Kurths. Noise-induced excitability in oscillatory media. *Phys. Rev. Lett.*, 91:180601, Oct 2003. 38

[24] R. D. Astumian. Thermodynamics and kinetics of a brownian motor. *Science*, 276:917–922, 1997. 38

[25] S. Leibler. Moving forward noisly. *Nature*, 370:412–413, 1994. 38, 82

[26] R. D. Astumian and M. Bier. Fluctuation driven ratchets: molecular motors. *Phys. Rev. Lett.*, 72:1766–1769, 1994. 38

[27] Jordi García-Ojalvo. Physical approaches to the dynamics of genetic circuits: a tutorial. *Contemporary Physics*, 52(5):439–464, 2011. 38

[28] J. Grau-Moya, A. J. Pons, and J. García-Ojalvo. Noise-induced up/down dynamics in scalefree neuronal networks. *International Journal of Bifurcation and Chaos*, 22(07):1250175, 2012. 38

[29] J. M. G. Vilar and J. M. Rubi. Noise suppression by noise. *Phys. Rev. Lett.*, 86:950–953, 2001. 38

[30] C. R. Doering and J. C. Gadoua. Resonant activation over a fluctuating barrier. *Phys. Rev. Lett.*, 69:2318–2321, 1992. 38

[31] C. Schmitt, B. Dybiec, H. Hänggi, and C. Bechinger. Stochastic resonance vs. resonant activation. *Europhys. Lett.*, 74:937–943, 2006. 38, 94

[32] Atsushi Uchida, Fabien Rogister, Jordi García-Ojalvo, and Rajarshi Roy. Synchronization and communication with chaotic laser systems. volume 48 of *Progress in Optics*, pages 203 – 341. Elsevier, 2005. 38, 146

[33] C. Serrat, M. C. Torrent, J. García-Ojalvo, and R. Vilaseca. Synchronization-induced noise reduction in spatially coupled microchip lasers. *Phys. Rev. A*, 64:041802, Sep 2001. 39

[34] Jordi García-Ojalvo, David J. DeShazer, and Rajarshi Roy. Stochastic modeling of bursting dynamics in an injected fiber laser, (proc. SPIE), 2003. 39

[35] A. Kul'minskii, R. Vilaseca, and R. Corbalán. Tracking unstable steady states by large-amplitude low-frequency periodic modulation of a control parameter: Phase-space analysis. *Phys. Rev. E*, 61:2500–2505, Mar 2000. 39, 176

[36] R. Vilaseca, A. Kul'minskii, and R. Corbalán. Tracking unstable steady states by large periodic modulation of a control parameter in a nonlinear system. *Phys. Rev. E*, 54:82–85, Jul 1996. 39, 176

[37] J. García-Ojalvo and R. Roy. Noise amplification in a stochastic ikeda model. *Physics Letters A*, 224(12):51 – 56, 1996. 39

[38] A. Sutera Benzi, R. and A. Vulpiani. The mechanism of stochastic resonance. *Journ. Phys. A*, 14:L453, 1981. 39, 44, 94

[39] G. Parisi A. Sutera Benzi, R. and A. Vulpiani. Stochastic resonance in climatic change. *Tellus*, 34:10, 1982. 39

[40] G. Parisi Benzi R., A. Sutera and A. Vulpiani. A theory of stochastic resonance in climatic change. *SIAM J. Appl. Math.*, 43:565, 1983. 39

[41] Nicolis C. Solar variability and stochastic effects on climate. *Sol. Phys.*, 74:473–478, 1981. 39

[42] C. Nicolis. Stochastic aspects of climatic transitions. *Tellus*, 34:1, 1982. 39

[43] C. Nicolis. Long-term climatic transitions-response to a periodic forcing. *Journ. Stat. Phys.*, 70:3, 1993. 39

[44] P. Jung and P. Hänggi. Resonantly driven brownian motion: Basic concepts and exact results. *Phisic. Rev. A*, 41:2977, 1989. 39

[45] S. Fauve and F. Heslot. Stochastic resonance in a bistable system. *Phys. lett. A*, 97A:5, 1983. 39, 95

[46] Chua LO Anishchenko VS, Safonova MA. Stochastic resonance in chua's circuit driven by amplitude or frequency-modulated signals. *International Journal of Bifurcation and Chaos*, 4:441–446, 1994. 39

[47] A. A. Zaikin, J. García-Ojalvo, L. Schimansky-Geier, and J. Kurths. Noise induced propagation in monostable media. *Phys. Rev. Lett.*, 88:010601, Dec 2001. 39, 40

[48] G. Nicolis Hu, G. and C. Nicolis. Periodically forced fokker-planck equation and stochastic resonance. *Phys. Rev. A*, 42:2030, 1990. 39

[49] K. Wiesenfeld McNamara, B. and R. Roy. Observation of stochastic resonance in a ring laser. *Phys. Rev. Lett.*, 60:2626, 1988. 39, 94

[50] Chen TR Zhuang YH Iannelli JM, Yariv A. Stochastic resonance in a semiconductor distributed feedback laser. *Applied Physics Letters*, 65:1983–1985, May 1994. 39

[51] Francesco Marino, Massimo Giudici, Stéphane Barland, and Salvador Balle. Experimental evidence of stochastic resonance in an excitable optical system. *Phys. Rev. Lett.*, 88:040601, Jan 2002. 39

[52] F. Marchesoni E. Menichella-Saetta Gammaitoni, L. and S. Santucci. Stochastic resonance in bistable systems. *Phys. Rev. Lett*, 62:349, 1989. 39, 42, 94

[53] B. McNamara and K. Wiesenfeld. Theory of stochastic resonance. *Phys. Rev. A*, 39:4854, 1989. 39

[54] P. Jung and P. Hänggi. Stochastic nonlinear dynamics modulated by external periodic forces. *Europhys. Lett.*, 8:505, 1989. 39

[55] Toshio Mori and Shoichi Kai. Noise-induced entrainment and stochastic resonance in human brain waves. *Phys. Rev. Lett.*, 88:218101, May 2002. 39, 40

[56] Zhou T Bulsara A, Jacobs EW. Stochastic resonance in a single neuron modeltheory and analog simulation. *Journal of Theoretical Biology*, 152:531555, May 1991. 39

[57] Moss F Longtin A, Bulsara A. Time-interval sequences in bistable systems and the noise-induced transmission of information by sensory neurons. *Physical Review Letters*, 67:656659, May 1991. 39

[58] Pantazelou E-Moss F. Douglass JK, Wilkens L. Noise enhancement of information transfer in crayfish mechanoreceptors by stochastic resonance. *Nature*, 365:337–340, Sept. 1993. 39

[59] Miller JP. Levin JE. Broadband neural encoding in the cricket cercal sensory system enhanced by stochastic resonance. *Nature*, 380:165–168, Mar. 1996. 39

[60] Verschueren S-Collins JJ Merfeld DM et al. Cordo P, Inglis JT. Noise in human muscle spindles. *Nature*, 383:769, 1996. 39

[61] J.K. Douglass; L. Wilkens; E. Pantazelou; and F. Moss. Noise enhancement of information transfer in crayfish mechanoreceptors by stochastic resonance. *Nature*, 365:337, 1993. 39, 40

[62] R. P. Morse and E. F. Evans. Enhancement of vowel coding for cochlear implants by addition of noise. *Nature Medicine*, 2:928, 1996. 39

[63] J. E. Levin and J. P. Miller. Broadband neural encoding in the cricket cereal sensory system enhanced by stochastic resonance. *Nature*, 380:165, 1996. 40, 44, 94

[64] Mark D. McDonnell and Derek Abbott. What is stochastic resonance? definitions, misconceptions, debates, and its relevance to biology. *PLOS computational biology*, May 2009. 40

[65] Neel EJ-Ditto WL Spano ML et al. Gluckman BJ, Netoff TI. Stochastic resonance in a neuronal network from mammalian brain. *Physical Review Letters*, 77:40984101, May 1996. 40

[66] Reichl LE Leonard DS. Stochastic resonance in a chemical-reaction. *Physical Review E*, 49:17341737, May 1994. 40

[67] Voydanoy I Bezrukov SM. Noise-induced enhancement of signal transduction across voltage-dependent ion channels. *Nature*, 378:362364, May 1995. 40

[68] Russell DF-Neiman A Moss F Greenwood PE, Ward LM. Stochastic resonance enhances the electrosensory information available to paddlefish for prey capture. *Physical Review Letters*, 84:47734776, May 2000. 40, 44

[69] Moss F Russell DF, Wilkens LA. Use of behavioural stochastic resonance by paddle fish for feeding. *Nature*, 402:291294, May 1999. 40

[70] Beisner B Neiman A Russell DF et al. Freund JA, Schimansky-Geier L. Behavioral stochastic resonance: How the noise from a daphnia swarm enhances individual prey capture by juvenile paddlefish. *Journal of Theoretical Biology*, 214:7183, May 2002. 40

[71] Doebeli M Blarer A. Resonance effects and outbreaks in ecological time series. *Physical Review Letters*, 2:167177, May 1999. 40

[72] Ehrenberg M Paulsson J, Berg OG. Stochastic focusing: Fluctuation-enhanced sensitivity of intracellular regulation. *Proceedings of the National Academy of Sciences of the USA*, 97:71487153, May 2000. 40

[73] Ehrenberg M Paulsson J. Random signal fluctuations can reduce random fluctuations in regulated components of chemical regulatory networks. *Physical Review Letters*, 84:54475450, May 2000. 40

[74] Ouyang Q Mao XM, Sun K. Stochastic resonance in a financial model. *Chinese Physics*, 11:11061110, May 2002. 40

[75] Grigg P Collins JJ, Imhoff TT. Noise-enhanced tactile sensation. *Nature*, 383:770, May 1996. 40

[76] E. Simonotto et al. Visual perception of stochastic resonance. *Physical Review Lett.*, 78:1186, 1997. 40

[77] Ward LM. Psychophysics of stochastic resonance. *Fluctuation and Noise Letters*, 4:11–21, 2004. 40

[78] Moss F Ward LM, Nieman A. Stochastic resonance in psychophysics and in animal behavior. *Biological Cybernetics*, 87:91101, 2002. 40

[79] M. Piana, M. Canfora, and M. Riani. Role of noise in image processing by the human perceptive system. *Phys. Rev. E*, 62:1104–1109, Jul 2000. 40

[80] Zhou C Kosko B Lee I, Liu X. Noise-enhanced detection of subthreshold signals with carbon nanotubes. *IEEE Transactions on Nanotechnology*, 5:613–627, 2006. 40

[81] Kosko B Zhou CW Lee IY, Liu XL. Nanosignal processing: Stochastic resonance in carbon nanotubes that detect subthreshold signals. *Nano Letters*, 3:1683–1686, 2003. 40

[82] Bulsara AR. No-nuisance noise. *Nature*, 437:962963, 2005. 40

[83] Mohanty P Badzey RL. Coherent signal amplification in bistable nanomechanical oscillators by stochastic resonance. *Nature*, 2005. 40

[84] Riddick BS Cullen WG Reutt-Robey J et al. Tao C, Liu Q. Dynamic interfaces in an organic thin film. *Proceedings of the National Academy of Sciences of the USA*, 105:1641816425, 2008. 40

[85] Andrews H Wallace R, Wallace D. Aids, tuberculosis, violent crime, and low birthweight in eight us metropolitan areas: Public policy, stochastic resonance, and the regional diffusion of inner-city markers. *Environment and Planning A*, 29:525555, 1997. 40

[86] R. Löfstedt and S. N. Coppersmith. Quantum stochastic resonance. *Phys. Rev. Lett.*, 72:1947, 1994. 40, 94

[87] R. Löfstedt and S. N. Coppersmith. Stochastic resonance: Nonperturbative calculation of power spectra and residence-time distributions. *Phys. Rev. E*, 49:4821, 1994. 40

[88] M. Grifoni and P. Hänggi. Nonlinear quantum stochastic resonance. *Phys. Rev. E*, 54:1390, 1996. 40

[89] M. Grifoni and P. Hänggi. Coherent and incoherent quantum stochastic resonance. *Phys. Rev. Lett.*, 76:1611, 1996. 40

[90] P. Jung and G. Mayer-Kress. Spatiotemporal stochastic resonance in excitable media. *Phys. Rev. Lett.*, 74:2130, 1995. 40

[91] Marchesoni F.; L. Gammaitoni; and A. Bulsara. Spatiotemporal stochastic resonance in a ϕ^4 model of kink-antikink nucleation. *Phys. Rev. Lett.*, 76:2609, 1996. 40

[92] Löcher M.; G. A. Johnson; and E. R. Hunt. Spatiotemporal stochastic resonance in a system of coupled diode resonators. *Phys. Rev. Lett.*, 77:4698, 1996. 40, 94

[93] H. S. Wio. Stochastic resonance in a spatially extended system. *Phys. Rev. E*, 54:3075, 1996. 40

[94] J. M. G. Vilar; and J. M. Rubi. Spatiotemporal stochastic resonance in the Swift-Hohenberg equation. *Phys. Rev. Lett.*, 78:2886, 1997. 40, 94

[95] F.; Castelpoggi and H. S. Wio. Stochastic resonance in extended systems: enhancement due to coupling in a reaction-diffusion model. *Europhys. Lett.*, 38:91, 1997. 40

[96] N. V. Agudov; A. V. Krichigin; D. Valenti; and B. Spagnolo. Stochastic resonance in a trapping overdamped monostable system. *Physical Review E*, 81:051123, 2010. 40, 99, 103

[97] McClintock PVE Moss F. In *Noise in nonlinear dynamical systems*, volume 2 of *Theory of noise induced processes in special applications*. Cambridge University Press., 1989. 40

[98] V.S. Anishenko; A.B. Neiman; F.Moss; L.Shimansky-Geier. Stochastic resonance: noise enhanced order. *Uspehi Fizicheskih Nauk*, 169:1, 1999. 40

[99] P. Talkner Hänggi, P. and M. Borkovec. Reaction-rate theory: fifty years after kramers. *Rev. Mod. Phys.*, 62:251, 1990. 42, 212

[100] H.A. Kramers. Brownian motion in a field of force and the diffusion model of chemical reactions. *Physica*, 7:284, 1940. 42

[101] Robert Rozenfeld, Alexander Neiman, and Lutz Schimansky-Geier. Stochastic resonance enhanced by dichotomic noise in a bistable system. *Phys. Rev. E*, 62:R3031–R3034, Sep 2000. 44

[102] P. Imkeller and I. Pavlyukevich. Model reduction and stochastic resonance. *Stochastics and Dynamics*, 02(04):463–506, 2002. 44

[103] J. J. Collins, Carson C. Chow, and Thomas T. Imhoff. Aperiodic stochastic resonance in excitable systems. *Phys. Rev. E*, 52:R3321–R3324, Oct 1995. 44

[104] A. Neiman, L. Schimansky-Grier, F. Moss, B. Shulgin, and J. J. Collins. Synchronization of noisy systems by stochastic signals. *Phys. Rev. E*, 60:284– 292, 1999. 44

[105] Bohou Xu, Fabing Duan, and Fran çois Chapeau-Blondeau. Comparison of aperiodic stochastic resonance in a bistable system realized by adding noiseand by tuning system parameters. *Phys. Rev. E*, 69:061110, Jun 2004. 44

[106] M. E. Inchiosa, V. In, A. R. Bulsara, K. Wiesenfeld, T. Heath, and M. H. Choi. Stochastic dynamics in a two-dimensional oscillator near a saddle-node bifurcation. *Phys. Rev. E*, 63:066114, May 2001. 44

[107] J. W. C. Robinson, J. Rung, A. R. Bulsara, and M. E. Inchiosa. General measures for signal-noise separation in nonlinear dynamical systems. *Phys. Rev. E*, 63:011107, Dec 2000. 44

[108] Mark D. McDonnell, Nigel G. Stocks, and Derek Abbott. Optimal stimulus and noise distributions for information transmission via suprathreshold stochastic resonance. *Phys. Rev. E*, 75:061105, Jun 2007. 44

[109] P. Hänggi C. Schmitt, B. Dybiec and C. Bechinger. Stochastic resonance vs resonant activation. *Europhysics Letters*, 74:937, 2006. 44

[110] Michael Gribskov and Nina L. Robinson. Use of receiver operating characteristic (roc) analysis to evaluate sequence matching. *Computers and Chemistry*, 20(1):25 – 33, 1996. 44

[111] V. Galdi, V. Pierro, and I. M. Pinto. Evaluation of stochastic-resonance-based detectors of weak harmonic signals in additive white gaussian noise. *Phys. Rev. E*, 57:6470–6479, Jun 1998. 44

[112] Steeve Zozor and Pierre-Olivier Amblard. On the use of stochastic resonance in sine detection. *Signal Process.*, 82(3):353–367, March 2002. 44

[113] R. J. Urick. Principles of underwater sound. page 423. 1967. 44

[114] Hu Gang, T. Ditzinger, C. Z. Ning, and H. Haken. Stochastic resonance without external periodic force. *Phys. Rev. Lett.*, 71:807–810, Aug 1993. 49

[115] A. Nikitin, Z. Néda, and T. Vicsek. Collective dynamics of two-mode stochastic oscillators. *Phys. Rev. Lett.*, 87:024101, Jun 2001. 49

[116] Coherence resonance in coupled chaotic oscillators. 49

[117] Thomas Kreuz, Stefano Luccioli, and Alessandro Torcini. Double coherence resonance in neuron models driven by discrete correlated noise. *Phys. Rev. Lett.*, 97:238101, Dec 2006. 49

[118] P. Parmananda, Hitoshi Mahara, Takashi Amemiya, and Tomohiko Yamaguchi. Resonance induced pacemakers: A new class of organizing centers for wave propagation in excitable media. *Phys. Rev. Lett.*, 87:238302, Nov 2001. 49

[119] L. Q. Zhou, X. Jia, and Q. Ouyang. Experimental and numerical studies of noise-induced coherent patterns in a subexcitable system. *Phys. Rev. Lett.*, 88:138301, Mar 2002. 49

[120] Seung Kee Han, Tae Gyu Yim, D. E. Postnov, and O. V. Sosnovtseva. Interacting coherence resonance oscillators. *Phys. Rev. Lett.*, 83:1771–1774, Aug 1999. 49

[121] Giovanni Giacomelli, Massimo Giudici, Salvador Balle, and Jorge R. Tredicce. Experimental evidence of coherence resonance in an optical system. *Phys. Rev. Lett.*, 84:3298–3301, Apr 2000. 49, 55

[122] Gerardo J. Escalera Santos, M. Rivera, and P. Parmananda. Experimental evidence of coexisting periodic stochastic resonance and coherence resonance phenomena. *Phys. Rev. Lett.*, 92:230601, Jun 2004. 49

[123] István. Z. Kiss, John L. Hudson, Gerardo J. Escalera Santos, and P. Parmananda. Experiments on coherence resonance: Noisy precursors to hopf bifurcations. *Phys. Rev. E*, 67:035201, Mar 2003. 49

[124] Jhon F. Martinez Avila, Hugo L. D. de S. Cavalcante, and J. R. Rios Leite. Experimental deterministic coherence resonance. *Phys. Rev. Lett.*, 93:144101, Sep 2004. 49, 55

[125] O. V. Ushakov, H.-J. Wünsche, F. Henneberger, I. A. Khovanov, L. Schimansky-Geier, and M. A. Zaks. Coherence resonance near a hopf bifurcation. *Phys. Rev. Lett.*, 95:123903, Sep 2005. 49, 55

[126] A. Zaikin, J. García-Ojalvo, R. Báscones, E. Ullner, and J. Kurths. Doubly stochastic coherence via noise-induced symmetry in bistable neural models. *Phys. Rev. Lett.*, 90:030601, Jan 2003. 49, 55

[127] J. García-Ojalvo, J. Casademont, M. C. Torrent, C. R. Mirasso, and J. M. Sancho. Coherence and synchronization in diode-laser arrayswith delayed global coupling. *International Journal of Bifurcation and Chaos*, 09(11):2225–2229, 1999. 49, 55

[128] J. M. Buldú, J. García-Ojalvo, Claudio R. Mirasso, M. C. Torrent, and J. M. Sancho. Effect of external noise correlation in optical coherence resonance. *Phys. Rev. E*, 64:051109, Oct 2001. 49, 55

[129] Shangyou Zeng and Peter Jung. Mechanism for neuronal spike generation by small and large ion channel clusters. *Phys. Rev. E*, 70:011903, Jul 2004. 49

[130] O. Carrillo, M. A. Santos, J. García-Ojalvo, and J. M. Sancho. Spatial coherence resonance near pattern-forming instabilities. *EPL (Europhysics Letters)*, 65(4):452, 2004. 50

[131] J. M. Buldú, J. García-Ojalvo, A. Wagemakers, and M. A. F. Sanjuán. Electronic design of siynthetic genetic networks. *International Journal of Bifurcation and Chaos*, 17(10):3507–3511, 2007. 50

[132] K. Murali, Sudeshna Sinha, William L. Ditto, and Adi R. Bulsara. Reliable logic circuit elements that exploit nonlinearity in the presence of a noise floor. *Phys. Rev. Lett.*, 102:104101, Mar 2009. 53, 54, 55, 161, 162

[133] J. Zamora-Munt and C. Masoller. Numerical implementation of a VCSEL-based stochastic logic gate via polarization bistability. *Opt. Express*, 18(16):16418–16429, Aug 2010. 53, 54, 55, 161, 162, 166, 170, 173

[134] Sylvain Barbay, Giovanni Giacomelli, and Francesco Marin. Noise-assisted binary information transmission in vertical cavity surface emitting lasers. *Opt. Lett.*, 25(15):1095–1097, Aug 2000. 53, 55, 161, 164

[135] M.F. Salvide, C. Masoller, and M.S. Torre. All-optical stochastic logic gate based on a vcsel with tunable optical injection. *Quantum Electronics, IEEE Journal of*, 49(10):886–893, 2013. 53

[136] Masoller C. Hong Y.-Spencer P.S. Paul, J. and K.A. Shore. Experimental study of polarization switching of vertical-cavity surface-emitting lasers as a dynamical bifurcation. *Optics Letters*, 31:748–750, 2006. 53, 161

[137] C. Masoller, M. S. Torre, and Paul Mandel. Influence of the injection current sweep rate on the polarization switching of vertical-cavity surface-emitting lasers. *Journal of Applied Physics*, 99(2):026108, 2006. 53, 161

[138] Z. George Pan, Shijun Jiang, Mario Dagenais, Robert A. Morgan, Keisuke Kojima, Moses T. Asom, Ronald E. Leibenguth, Gregory D. Guth, and Marlin W. Focht. Optical injection induced polarization bistability in vertical-cavity surface-emitting lasers. *Applied Physics Letters*, 63(22):2999–3001, 1993. 53, 161

[139] M. Sciamanna and K. Panajotov. Two-mode injection locking in vertical-cavity surface-emitting lasers. *Opt. Lett.*, 30(21):2903–2905, Nov 2005. 53, 161

[140] A. Hurtado, I.D. Henning, and M.J. Adams. Wavelength Polarization Switching and Bistability in a 1550-nm VCSEL Subject to Polarized Optical Injection. *Photonics Technology Letters, IEEE*, 21(15):1084–1086, 2009. 53, 122, 161

[141] M. Torre, A. Hurtado, A. Quirce, A. Valle, L. Pesquera, and M. Adams. Polarization Switching in Long-Wavelength VCSELs Subject to Orthogonal Optical Injection. *Quantum Electronics, IEEE Journal of*, 47(1):92–99, 2011. 53, 161

[142] H. Kawaguchi. Polarization-bistable vertical-cavity surface-emitting lasers: application for optical bit memory. *Opto-Electronics Review*, 17(4), 2009. 53, 162

[143] T. Katayama, T. Ooi, and Hitoshi Kawaguchi. Experimental demonstration of multi-bit optical buffer memory using 1.55- μm polarization bistable vertical-cavity surface-emitting lasers. *Quantum Electronics, IEEE Journal of*, 45(11):1495–1504, 2009. 53, 162

[144] Sandro Perrone, Ramon Vilaseca, and Cristina Masoller. Stochastic logic gate that exploits noise and polarization bistability in an optically injected VCSEL. *Opt. Express*, 20(20):22692–22699, Sep 2012. 53, 54, 55, 147

[145] F. Hartmann, A. Forchel, I. Neri, L. Gammaitoni, and L. Worschech. Nanowatt logic stochastic resonance in branched resonant tunneling diodes. *Applied Physics Letters*, 98(3):032110, 2011. 54, 162

[146] Anna Dari, Behnam Kia, Xiao Wang, Adi R. Bulsara, and William Ditto. Noise-aided computation within a synthetic gene network through morphable and robust logic gates. *Phys. Rev. E*, 83:041909, Apr 2011. 54, 162

[147] Kamal P. Singh and Sudeshna Sinha. Enhancement of “logical” responses by noise in a bistable optical system. *Phys. Rev. E*, 83:046219, Apr 2011. 54, 162

[148] Adi R. Bulsara, Anna Dari, William L. Ditto, K. Murali, and Sudeshna Sinha. Logical stochastic resonance. *Chemical Physics*, 375(23):424–434, 2010. Stochastic processes in Physics and Chemistry (in honor of Peter Hänggi). 54, 55

[149] G. Volpe; S. Perrone; J. M. Rubi; and D. Petrov. Stochastic resonant damping in a noisy monostable system: Theory and experiments. *Phys. Rev. E*, 77:051107, 2008. 55, 57, 58, 85

[150] Perrone S.; Volpe G. and Petrov D. 10-fold detection range increase in quadrant-photodiode position sensing for photonic force microscope. *Review Scient. Instr.*, 79:10, 2008. 55, 58, 78

[151] S. Perrone. J. Zamora-Munt, R. Vilaseca and C. Masoller. Rogue waves in a periodically forced semiconductor laser system. *in preparation*, 2014. 55

[152] K. Hayashi, S. de Lorenzo, M. Manosas, J. M. Huguet, and F. Ritort. Single-molecule stochastic resonance. *Phys. Rev. X*, 2:031012, Aug 2012. 57, 94

[153] Shafigh Mehraeen and Andrew J. Spakowitz. Intrinsic fluctuations lead to broad range of transduced forces in tethered-bead single-molecule experiments. *Phys. Rev. E*, 86:021902, Aug 2012. 57

[154] David B. Ruffner and David G. Grier. Optical forces and torques in nonuniform beams of light. *Phys. Rev. Lett.*, 108:173602, Apr 2012. 57

[155] N. Koumakis and R. Di Leonardo. Stochastic hydrodynamic synchronization in rotating energy landscapes. *Phys. Rev. Lett.*, 110:174103, Apr 2013. 57

[156] S. Perrone; G. Volpe; J. M. Rubi; and D. Petrov. Maximum in the signal-to-noise ratio in an oscillating potential: an experimental study. *conference: "Stochastic Resonance 1998-2008, Perugia (Italy) (2008)*, Perugia (Italy) 2008. 57, 102

[157] G. Volpe; S. Perrone; J. M. Rubi; and D. Petrov. Stocastic resonence vs stochastic resonant damping: theory and experiments. *conference: "Stochastic Resonance 1998-2008, Perugia (Italy) (2008)*, Perugia (Italy) 2008. 57, 92

[158] A. Ashkin. Acceleration and trapping of particles by radiation pressure. *Physical Review Letters*, 24:156–159, 1970. 58, 59

[159] J. D. Thompson, T. G. Tiecke, A. S. Zibrov, V. Vuletic, and M. D. Lukin. Coherence and Raman sideband cooling of a single atom in an optical tweezer. *Phys. Rev. Lett.*, 110:133001, Mar 2013. 58

[160] Michael J. Gibbons, Christopher D. Hamley, Chung-Yu Shih, and Michael S. Chapman. Nondestructive fluorescent state detection of single neutral atom qubits. *Phys. Rev. Lett.*, 106:133002, Mar 2011. 58

[161] T. Aoki H. Lee E. Ostby K. Vahala H. Kimble D. Alton, N. Stern. Strong interactions of single atoms and photons near a dielectric boundary. *Nature Physics*, 7:159–165, Mar 2011. 58

[162] K. Svoboda and S.M. Block. Biological applications of optical forces. *Annual review of Biophysics and Biomolecular Structure*, 23:247–285, 1994. 59, 64

[163] Dziedzic J.M. Bjorkholm J.E. Ashkin, A. and S. Chu. Observation of a single-beam gradient force optical trap for dielectric particles. *Optics Letters*, 11:288–290, 1986. 59

[164] A. Ashkin. Forces of a single-beam gradient laser trap on a dielectric sphere in the ray optics regime. *Biophysical Journal*, 61:569–582, 1992. 59, 61

[165] B.A. Brown and P.R. Brown. Optical tweezers: theory and current applications. *American Laboratory Articles*, Novemeber issue:13–20, 2001. 59

[166] G. Roosen and C. Imbert. Optical levitation by means of 2 horizontal laser beams-theoretical and experimental study. *Physics Letters*, 59A:6–8, 1976. 60

[167] E. Hecht and A. Zajac. Optics. *Addison-Wesley Publishing Inc.*, Reading:MA, 1987. 60, 63

[168] Craig F.; Donald R. Huffman Bohren. Absorption and scattering of light by small particles. Springer, Berlin, 1983. 62

[169] M.W. Davidson and M. Abramowitz. Optical microscopy. *Online PDF-resource*, See also the Microscopy Primer at http://micro.magnet.fsu.edu/primer., 1999. 63

[170] Gittes F. Kopelman R. Agayan., R.R. and C.F. Schmidt. Optical trapping near resonance absorption. *Applied Optics*, 41:2318–2327, 2002. 64

[171] F. Gittes and C.F. Schmidt. Signals and noise in micromechanical measurements. *Methods in Cell Biology*, 55:129–156. Book chapter., 1998. 67, 68, 70

[172] F. Reif. Fundamentals of statistical and thermal physics. *McGraw-Hill Ltd.*, Tokyo, 1965. 67

[173] J. Sapriel. Acousto-optics. *John Wiley and Sons*, New York, 1979. 74

[174] J. Xu and R. Stroud. Acousto-optic devices: Principles, design and applications. *John Wiley and Sons*, New York, 1992. 74, 75

[175] K. Berg-Sorensen and H. Flyvbjerg. Power spectrum analysis for optical tweezers. *Rev. Sci. Instrumen.*, 75:594–612, 2004. 78, 87, 102, 105, 107

[176] G. Volpe G. Volpe and D. Petrov. Brownian motion in a nonhomogeneous force field and photonic force microscope. *Phys. Rev. E*, 76:061118, 2007. 78, 86, 87, 101, 102, 105, 107

[177] K. C. Vermeulen; J. van Mameren; G. J. M. Stienen; E. J. G. Peterman; G. J. L. Wuite; and C. F. Schmidt. *Rev. Scient. Instrum.*, 77:013704, 2006. 78, 107

[178] G. Badenes G. Volpe, R. Quidant and D. Petrov. Surface plasmon radiation forces. *Phys. Rev. Letters*, 96:238101, 2006. 87, 102

[179] J. Liu, T. Dietz, S. R. Carpenter, M. Alberti, C. Folke, E. Moran, A. N. Pell, P. Deadman, T. Kratz, J. Lubchenco, E. Ostrom, Z. Ouyang, W. Provencher, C. L. Redman, S. H. Schneider, and W. W. Taylor. Complexity of coupled human and natural systems. *Science*, 317:1513–1516, 2007. 90

[180] M. Lim, R. Metzler, and Y. Bar-Yam. Global pattern formation and ethnic/cultural violence. *Science*, 317:1540–1544, 2007. 90

[181] R. N. Mantegna and H. E. Stanley. *An Introduction to Econophysics: Correlations and Complexity in Finance.* Cambridge University Press, Cambridge, England, 2000. 90

[182] W. M. Saslow. An economic analogy to thermodynamics. *Am. J. Phys.*, 67:1239–1247, 1999. 90

[183] S. Perrone; G. Volpe; J. M. Rubi; and D. Petrov. Experimental observation of resonant damping in a parametrically-driven noisy system. *conference: "New Frontiers in Micro and Nano Photonics, Florence (Italy) (2008)*, Florence (Italy) 2008. 92

[184] D. Nozaki, D. J. Mar, P. Grigg, and J. J. Collins. Effects of colored noise on stochastic resonance in sensory neurons. *Phys. Rev. Lett.*, 82:2402–2405, 1999. 94

[185] G. Mato. Stochastic resonance using noise generated by a neural network. *Phys. Rev. E*, 59:3339–3343, 1999. 94

[186] C. Nicolis. Stochastic resonance in multistable systems: The role of intermediate states. *Physical Review E*, 82:011139, 2010. 95

[187] R. Rozenfeld; A. Neiman; and L. Schimansky-Geier. Stochastic resonance enhanced by dichotomic noise in a bistable system. *Phis. Rev. E*, 62:3031–34, 2000. 95

[188] Bartlomiej Dybiec. Lévy noises: Double stochastic resonance in a single-well potential. *Physical Rev. E*, 80:041111, 2009. 99, 103

[189] Lucien P. Ghislain, Neil A. Switz, and Watt W. Webb. Measurement of small forces using an optical trap. *Review of Scientific Instruments*, 65(9):2762–2768, 1994. 105

[190] E. L. Florin; A. Pralle; J. K. H. Hrber; and E. H. K. Stelzer. Photonic force microscope based on optical tweezers and two-photon excitation for biological applications. *J. Struct. Biol.*, 119:202, 1997. 105

[191] A. Ashkin. History of optical trapping and manipulation of small-neutral particle, atoms, and molecules. *Selected Topics in Quantum Electronics, IEEE Journal of*, 6(6):841–856, 2000. 105

[192] K. C. Neuman and S. M. Block. Optical trapping. *Rev. Scient. Instrum.*, 75:2787, 2004. 105

[193] Alexander Rohrbach. Switching and measuring a force of 25 femtonewtons with an optical trap. *Opt. Express*, 13(24):9695–9701, Nov 2005. 105

[194] G. Volpe and D. Petrov. Torque detection using brownian fluctuations. *Physical Rev. Letters*, 97:210603, 2006. 105

[195] Giorgio Volpe, Giovanni Volpe, and Dmitri Petrov. Singular-point characterization in microscopic flows. *Phys. Rev. E*, 77:037301, Mar 2008. 105

[196] Frederick Gittes and Christoph F. Schmidt. Interference model for back-focal-plane displacement detection in optical tweezers. *Opt. Lett.*, 23(1):7–9, Jan 1998. 105

[197] Simon F. Tolic-Norrelykke, Erik Schaffer, Jonathon Howard, Francesco S. Pavone, Frank Julicher, and Henrik Flyvbjerg. Calibration of optical tweezers with positional detection in the back focal plane. *Review of Scientific Instruments*, 77(10):–, 2006. 105

[198] H. C. van de Hulst. Light scattering by small particles. *(Dover, New York, 1981).* 106

[199] S. M. Kay. Fundamentals of statistical signal processing: Estimation theory. *(Prentice-Hall, New Jersey, 1993)*, 1993. 106, 109

[200] Giovanni Volpe, Gregory Kozyreff, and Dmitri Petrov. Backscattering position detection for photonic force microscopy. *Journal of Applied Physics*, 102(8), 2007. 111

[201] J. H. G. Huisstede; K. O. van der Werf; M. L. Bennink; and V. Subramaniam. *Opt. Express*, 13:1113, 2005. 111

[202] A. Einstein. Quantentheorie der strahlung. *Physikalische*, 18:121–128, 1917. 114

[203] A.M. Prokhorov Basov, N.G. *J. Exp. Theor. Phys. USSR*, 27(431), 1954. 115

[204] J. Weber. Ire professional group on electron devices pged-3. *IRE Trans. Electron DevicesQuantum*, (1), 1953. 115

[205] H.J. Zeiger J.P. Gordon and C.H. Townes. Molecular microwave oscillator and new hiperfine structure in microwave spectrum of nh_3. *Phys. Rev. Lett.*, 95, 1954. 115

[206] A.L. Schawlow and C.H. Townes. Infrared and optical masers. *Phys. Rev.*, 112, 1958. 115

[207] T.H. Maiman. Stimulated optical radiation in ruby. *Nature*, 187, 1960. 115

[208] O.N. Krokhin N.G. Basov and Y.M. Popov. Application of molecular beams to the radiospectroscopi study of the rotation spectrum of molecules. *Sov. Phys. JEPT*, 13, 1961. 115

[209] G. Burbs F.H. Dill M.I. Nathan, W.P. Dumke and G.J. Lasher. Stimulated emission of radiation from gaad p-n junction. *Appl. Phys. Lett.*, 1, 1962. 115

[210] W.E. Krag B. Lax A.L. McWhorter R.H. Rediker T.M. Quist, R.J. Keyes and H.J. Zeiger. Semiconductor maser of GaAs. *Appl. Phys. Lett.*, 1, 1962. 115

[211] J.D. Kingsley T.J. Soltys R.N. Hall, G.E. Fenner and R.O. Carlson. Coherent light emission from GaAs junctions. *Phys. Rev. Lett.*, 9, 1962. 115

[212] Zh. I. Alferov and R.F. Kazarinov. Semiconductor laser with electrical pumping. *USSR Patent*, 1963. 115

[213] H. Kroemer. A proposed class of heterojunction injection laser. *Proc. IEEE*, 51, 1963. 115

[214] E.L. Portnoi Zh. Alferov, V.M. Andreev and M.K. Trukan. AlAs-GaAs heterojunction injection lasers with low room-temperature threshold. *Fiz. Tekh. Poluprov*, 3, 1969. 115

[215] T. Ikegami Y. Nishimura, K. Kobayashi and Y. Suematsu. Hole-burning effect in semiconductor laser. *Proc. Int. Quantum Electronics Conf., Kyoto, Japan*, 20, 1970. 115

[216] S. Akiba T. Yamamoto, K.Sakay and Y. Suemalsu. Fast pulse behavior of InGaAsP/InP double heterostructure lasers emitting at 1.27 *μm*. *Electron. Lett.*, 13:142–143, 1977. 115

[217] Y. Suematsu S. Arai, M. Asada and Y. Itaya. Room temperature cw operation gainasp/inp dh laser emitting at 1.51 *μm*. *Jpn. J. Appl. Phys.*, 18:2333–2334, 1979. 115

[218] Y. Matsushima S. Akiba, K. Sakai and T. Yamamoto. Room-temperature c.w. operation of InGaAsP/InP heterostructure lasers emitting at 1.56 *μm*. *Electron. Lett.*, 15:606–607, 1979. 115

[219] M.A. Pollack L.W. Stulz I.P. Kaminow, R.E. Nahory and J.C. DeWinter. Single-mode c.w. ridge waveguide laser emitting at 1.55 *μm*. *Electon. Lett.*, 15:763–765, 1979. 115

[220] Y. Toyoshima H. Nagai H. Kawaguchi, T. Takahei and G. Iwane. Room temperature c.w. operation of InP/InGaAsP/InP double heterostructure diode lasers emitting at 1.55 *μm*. *Electron. Lett.*, 15:669–700, 1979. 115

[221] J.M. Liu. Photonic devices. *University pressed, Cambridge*, 2005. 116

[222] K.F. Huang K. Tai T.B. Simpson, J.M. Liu. Nonlinear dynamics induced by external optical injection in semiconductor. *lasers, Quant. Semiclass. Opt.*, 9:765784, 1997. 120

[223] T.B. Simpson D. Lenstra S. Wieczorek, B. Krauskopf. The dynamical complexity of optically injected semiconductor lasers. *Physics Reports*, 416:1–128, 2005. 120, 121

[224] I I Zolotoverkh and E G Lariontsev. Characteristic features of the dynamics of a solid-state laser with injection of an optical signal frequency-shifted from the gain-line centre. *Quantum Electronics*, 28(8):655, 1998. 120

[225] Haleh Karkhaneh, Ayaz Ghorbani, and Jia-Ming Liu. Broadband transmission over injection-locked optical ofdm systems: Theory and design. *J. Opt. Commun. Netw.*, 5(5):475–483, May 2013. 120

[226] S.K. Hwang and J.M. Liu. Dynamical characteristics of an optically injected semiconductor laser. *Optics Communications*, 183(14):195 – 205, 2000. 120

[227] C. I. Laidler and S. Eriksson. Microwave sidebands for atomic physics experiments by period one oscillation in optically injected diode lasers. *EPL (Europhysics Letters)*, 96(5):53001, 2011. 120, 121

[228] A Gavrielides, V Kovanis, and T Erneux. Analytical stability boundaries for a semiconductor laser subject to optical injection. *Optics Communications*, 136(34):253 – 256, 1997. 120

[229] H. L. Stover and W. H. Steier. Locking of laser oscillators by light injection. *Appl. Phys. Lett.*, 8:91–93, 1966. 120

[230] Jun-Ping Zhuang and Sze-Chun Chan. Tunable photonic microwave generation using optically injected semiconductor laser dynamics with optical feedback stabilization. *Opt. Lett.*, 38(3):344–346, Feb 2013. 121

[231] Stefan Eriksson and sa Marie Lindberg. Observations on the dynamics of semiconductor lasers subjected to external optical injection. *Journal of Optics B: Quantum and Semiclassical Optics*, 4(2):149, 2002. 121

[232] Puccioni G.P. Arecchi F.T., Lippi G.L. and J.R. Tredicce. Deterministic chaos in laser with injected signal. *Optics Communications*, 51(5):308–314, 1984. 121

[233] T. Erneux, E. A. Viktorov, B. Kelleher, D. Goulding, S. P. Hegarty, and G. Huyet. Optically injected quantum-dot lasers. *Opt. Lett.*, 35(7):937–939, Apr 2010. 121

[234] Erwin K. Lau, Xiaoxue Zhao, Hyuk-Kee Sung, Devang Parekh, Connie Chang-Hasnain, and Ming C. Wu. Strong optical injection-locked semiconductor lasers demonstrating &gt; 100-ghz resonance frequencies and 80-ghz intrinsic bandwidths. *Opt. Express*, 16(9):6609–6618, Apr 2008. 121

[235] T. B. Simpson and J.M. Liu. Enhanced modulation bandwidth in injection-locked semiconductor lasers. *Photonics Technology Letters, IEEE*, 9(10):1322–1324, 1997. 121, 138

[236] J.M. Liu et al. Modulation bandwidth , noise and stability of a semiconductor laser subject to strong optical injection. *Optics Communications*, 9(269):1325–1327, 1997. 121, 123

[237] Kovanis, V., Gavrielides, A., and Gallas, J. A.C. Labyrinth bifurcations in optically injected diode lasers. *Eur. Phys. J. D*, 58(2):181–186, 2010. 121

[238] Ziemann, D., Aust, R., Lingnau, B., Schöll, E., and Lüdge, K. Optical injection enables coherence resonance in quantum-dot lasers. *EPL*, 103(1):14002, 2013. 121

[239] Thomas Erneux, Vassilios Kovanis, and Athanasios Gavrielides. Nonlinear dynamics of an injected quantum cascade laser. *Phys. Rev. E*, 88:032907, Sep 2013. 121

[240] Lukasz Olejniczak, Krassimir Panajotov, Hugo Thienpont, and Marc Sciamanna. Self-pulsations and excitability in optically injected quantum-dot lasers: Impact of the excited states and spontaneous emission noise. *Phys. Rev. A*, 82:023807, Aug 2010. 122

[241] B. Kelleher, C. Bonatto, G. Huyet, and S. P. Hegarty. Excitability in optically injected semiconductor lasers: Contrasting quantum- well- and quantum-dot-based devices. *Phys. Rev. E*, 83:026207, Feb 2011. 122

[242] D. Goulding, S. P. Hegarty, O. Rasskazov, S. Melnik, M. Hartnett, G. Greene, J. G. McInerney, D. Rachinskii, and G. Huyet. Excitability in a quantum dot semiconductor laser with optical injection. *Phys. Rev. Lett.*, 98:153903, Apr 2007. 122

[243] J. P. Toomey, C. Nichkawde, D. M. Kane, K. Schires, I.D. Henning, A. Hurtado, and M. J. Adams. Stability of the nonlinear dynamics of an optically injected VCSEL. *Opt. Express*, 20(9):10256–10270, Apr 2012. 122

[244] Antonio Hurtado, Ana Quirce, Angel Valle, Luis Pesquera, and Michael J. Adams. Nonlinear dynamics induced by parallel and orthogonal optical injection in 1550 nm Vertical-Cavity Surface-Emitting Lasers (VCSELs). *Opt. Express*, 18(9):9423–9428, Apr 2010. 122

[245] M. Sciamanna and K. Panajotov. Route to polarization switching induced by optical injection in vertical-cavity surface-emitting lasers. *Phys. Rev. A*, 73:023811, Feb 2006. 122

[246] Y. Hong, P.S. Spencer, S. Bandyopadhyay, P. Rees, and K.A. Shore. Polarisation-resolved chaos and instabilities in a vertical cavity surface emitting laser subject to optical injection. *Optics Communications*, 216(13):185 – 189, 2003. 122

[247] Y. Hong, P.S. Spencer, P. Rees, and K.A. Shore. Optical injection dynamics of two-mode vertical cavity surface-emitting semiconductor lasers. *Quantum Electronics, IEEE Journal of*, 38(3):274–278, 2002. 122

[248] T. B. Simpson and J. M. Liu. Small signal analysis of modulation characteristic in a semiconductor laser subject to a stong optical injection. *IEEE J. Quantum Electron.*, 32:1456–1468, 1996. 123, 124, 141

[249] G. Yabre. Effect of relatively strong light injection on the chirp-to-power ratio and the 3 db bandwidth of directly modulated semiconductor lasers. *Lightwave Technology, Journal of*, 14(10):2367–2373, 1996. 124, 126, 138, 143

[250] Li L. Static and dynamic properties of injection-locked semiconductor lasers. *IEEE J. Quantum Electron*, (30):1701–1708. 124

[251] N.A. Olsson, C.H. Henry, R.F. Kazarinov, H. J. Lee, and B.H. Johnson. Relation between chirp and linewidth reduction in external bragg reflector semiconductor lasers. *Applied Physics Letters*, 51(2):92–93, 1987. 126

[252] S. Mohrdiek, H. Burkhard, and H. Walter. Chirp reduction of directly modulated semiconductor lasers at 10 gb/s by strong cw light injection. *Lightwave Technology, Journal of*, 12(3):418–424, 1994. 126

[253] A.F. Siegman. Lasers. *University Science books. Mill Valley*, Chapter 29, 1986. 131

[254] N. Tollenaar B. Krauskopf and D. Lenstra. Tori and their bifurcations in an optically injected semiconductor laser. *Optics Communications*, 156:158–169, 1998. 133

[255] Tamburrini T Piazzolia S, Spano P. Small signal analysis of frequency chirping in injection-locked semiconductor laser. *IEEE J. Quantum Electron.*, 22:2219–2223, 1986. 143

[256] J. García-Ojalvo and Rajarshi Roy. Spatiotemporal communication with synchronized optical chaos. *Phys. Rev. Lett.*, 86:5204–5207, May 2001. 146

[257] J. García-Ojalvo and R. Roy. Parallel communication with optical spatiotemporal chaos. *Circuits and Systems I: Fundamental Theory and Applications, IEEE Transactions on*, 48(12):1491–1497, 2001. 146

[258] L. Larger V. Annovazzi-Lodi P. Colet I. Fischer J. García-Ojalvo C. R. Mirasso L. Pesquera A. Argyris, D. Syvridis and K. A. Shore. Chaos-based communications at high bit rates using commercial fibre-optic links. *Nature*, 438:343–346, 2005. 146

[259] M. San Miguel, Q. Feng, and J. V. Moloney. Light-polarization dynamics in surface-emitting semiconductor lasers. *Phys. Rev. A*, 52:1728–1739, Aug 1995. 150, 157

[260] M. Sciamanna, Rogister F., Deparis O., Mégret P., Blondel M., Erneux T. Bifurcation to polarization self-modulation in vertical-cavity surface-emitting laser. *Optics Letters*, 27(261):1–4, 2002. 150

[261] M. Sciamanna, Erneux T., Rogister F., Deparis O., Mégret P., Blondel M. Bifurcation bridges between external-cavity modes lead to polarization self modulation in vertical-cavity surface-emitting laser. *Physical Rev. A*, 65(041801):1–4, 2002. 150

[262] F. Prati, G. Giacomelli, and F. Marin. Competition between orthogonally polarized transverse modes in vertical-cavity surface-emitting lasers and its influence on intensity noise. *Phys. Rev. A*, 62:033810, Aug 2000. 152, 156

[263] S. Balle, E. Tolkachova, M. San Miguel, J. R. Tredicce, J. Martín-Regalado, and A. Gahl. Mechanisms of polarization switching in single-transverse-mode

vertical-cavity surface-emitting lasers: thermal shift and nonlinear semiconductor dynamics. *Opt. Lett.*, 24(16):1121–1123, Aug 1999. 152

[264] Ethan Blansett, Michael Raymer, Galina Khitrova, Hyatt Gibbs, Darwin Keith Serkland, A. Allerman, and Kent Geib. Ultrafast polarization dynamics and noise in pulsed vertical-cavity surface-emitting lasers. *Opt. Express*, 9(6):312–318, Sep 2001. 152

[265] M. Sondermann, M. Weinkath, T. Ackemann, J. Mulet, and S. Balle. Two-frequency emission and polarization dynamics at lasing threshold in vertical-cavity surface-emitting lasers. *Phys. Rev. A*, 68:033822, Sep 2003. 152

[266] J. Danckaert, M. Peeters, C. Mirasso, M.S. Miguel, G. Verschaffelt, J. Albert, B. Nagler, H. Unold, R. Michalzik, G. Giacomelli, and F. Marin. Stochastic polarization switching dynamics in vertical-cavity surface-emitting lasers: theory and experiment. *Selected Topics in Quantum Electronics, IEEE Journal of*, 10(5):911–917, 2004. 152

[267] G. Van der Sande, M. Peeters, I. Veretennicoff, J. Danckaert, G. Verschaffelt, and S. Balle. The effects of stress, temperature, and spin flips on polarization switching in vertical-cavity surface-emitting lasers. *Quantum Electronics, IEEE Journal of*, 42(9):898–906, 2006. 152

[268] Jon Paul, Cristina Masoller, Paul Mandel, Yanhua Hong, Paul S. Spencer, and K. Alan Shore. Experimental and theoretical study of dynamical hysteresis and scaling laws in the polarization switching of vertical-cavity surface-emitting lasers. *Phys. Rev. A*, 77:043803, Apr 2008. 152

[269] C. Masoller, D. Sukow, A. Gavrielides, and M. Sciamanna. Bifurcation to square-wave switching in orthogonally delay-coupled semiconductor lasers: Theory and experiment. *Phys. Rev. A*, 84:023838, Aug 2011. 152

[270] R. Al-Seyab, K. Schires, N.A. Khan, A. Hurtado, I.D. Henning, and M.J. Adams. Dynamics of Polarized Optical Injection in 1550-nm VCSELs: Theory and Experiments. *Selected Topics in Quantum Electronics, IEEE Journal of*, 17(5):1242–1249, 2011. 152

[271] M. San Miguel. Semiconductor quantum optoelectronics. *Eds. A. Miller, M. Ebrahimzadeh and D.M. Finlayson*, (Bristol 339-366), 1999. 152

[272] M. B. Willemsen, M. U. F. Khalid, M. P. van Exter, and J. P. Woerdman. Polarization Switching of a Vertical-Cavity Semiconductor Laser as a Kramers Hopping Problem. *Phys. Rev. Lett.*, 82:4815–4818, Jun 1999. 156

[273] A. Valle, K.A. Shore, and L. Pesquera. Polarization selection in birefringent vertical-cavity surface emitting lasers. *Lightwave Technology, Journal of*, 14(9):2062–2068, 1996. 157

[274] K. Panajotov, B. Ryvkin, J. Danckaert, M. Peeters, H. Thienpont, and I. Veretennicoff. Polarization switching in VCSEL's due to thermal lensing. *Photonics Technology Letters, IEEE*, 10(1):6–8, 1998. 157

[275] Kent D. Choquette, Kevin L. Lear, Richard P. Schneider, Jr., Ronald E. Leibenguth, Jeffrey J. Figiel, Sean P. Kilcoyne, Mary H. Crawford, and John C. Zolper. Polarization characteristics, control, and modulation of vertical-cavity surface emitting lasers. *Proc. SPIE*, 2382:125–136, 1995. 157

[276] J. Martín-Regalado, J. L. A. Chilla, J. J. Rocca, and P. Brusenbach. Polarization switching in vertical-cavity surface emitting lasers observed at constant active region temperature. *Applied Physics Letters*, 70(25), 1997. 157

[277] J. Martín-Regalado, S. Balle, M. San Miguel, Estudios Avanzados, Departament De F'isica, A. Valle, and L. Pesquera. Polarization and transverse mode selection in quantum well vertical-cavity surface-emitting lasers: Index- and gain-guided devices. *Quantum Semiclas. Opt.*, 9:713–736, 1997. 157

[278] S. Barland, Piernicola Spinicelli, G. Giacomelli, and F. Marin. Measurement of the working parameters of an air-post vertical-cavity surface-emitting laser. *Quantum Electronics, IEEE Journal of*, 41(10):1235–1243, 2005. 163

[279] Solli, D.; R. Ropers, C.; Koonath, P.; Jalali, B. Optical rogue waves. *Nature*, 450:1054–1057, Dic 2007. 176

[280] Hugo L. D. de S. Cavalcante, Marcos Oriá, Didier Sornette, Edward Ott, and Daniel J. Gauthier. Predictability and suppression of extreme events in a chaotic system. *Phys. Rev. Lett.*, 111:198701, Nov 2013. 176

[281] Stéphane Randoux and Pierre Suret. Experimental evidence of extreme value statistics in Raman fiber lasers. *Opt. Lett.*, 37(4):500–502, Feb 2012. 176

[282] Dmitriy V. Churkin, Sergey V. Smirnov, and Evgenii V. Podivilov. Statistical properties of partially coherent cw fiber lasers. *Opt. Lett.*, 35(19):3288–3290, Oct 2010. 176

[283] Dmitry V. Churkin, Oleg A. Gorbunov, and Sergey V. Smirnov. Extreme value statistics in Raman fiber lasers. *Opt. Lett.*, 36(18):3617–3619, Sep 2011. 176

[284] M. Kovalsky, A. A. Hnilo, and J. R. Tredicce. Experimental evidence of extreme value statistics in Raman fiber lasers. *Optics Letters*, 36, 2011. 176

[285] Alexander N. Pisarchik, Rider Jaimes-Reátegui, Ricardo Sevilla-Escoboza, G. Huerta-Cuellar, and Majid Taki. Rogue waves in a multistable system. *Phys. Rev. Lett.*, 107:274101, Dec 2011. 176

[286] J.M. Dudley, C. Finot, G. Millot, J. Garnier, G. Genty, D. Agafontsev, and F. Dias. Extreme events in optics: Challenges of the manureva project. *The European Physical Journal Special Topics*, 185(1):125–133, 2010. 176

[287] Fatome J. Finot C. Millot G.-Dias F. Genty G. Akhmediev N. Dudley-J. M. Kibler, B. The peregrine soliton in nonlinear fibre optics. *Nature Phys.*, (1):790–795, 2010. 176

[288] F. T. Arecchi, U. Bortolozzo, A. Montina, and S. Residori. Granularity and inhomogeneity are the joint generators of optical rogue waves. *Phys. Rev. Lett.*, 106:153901, Apr 2011. 176

[289] N. Akhmediev, J. M. Soto-Crespo, and A. Ankiewicz. How to excite a rogue wave. *Phys. Rev. A*, 80:043818, Oct 2009. 176

[290] J. M. Soto-Crespo, Ph. Grelu, and Nail Akhmediev. Dissipative rogue waves: Extreme pulses generated by passively mode-locked lasers. *Phys. Rev. E*, 84:016604, Jul 2011. 176

[291] Alexandr Zaviyalov, Oleg Egorov, Rumen Iliew, and Falk Lederer. Rogue waves in mode-locked fiber lasers. *Phys. Rev. A*, 85:013828, Jan 2012. 176

[292] C. Lecaplain, Ph. Grelu, J. M. Soto-Crespo, and N. Akhmediev. Dissipative rogue waves generated by chaotic pulse bunching in a mode-locked laser. *Phys. Rev. Lett.*, 108:233901, Jun 2012. 176

[293] R. Dykstra, A. Rayner, D. Y. Tang, and N. R. Heckenberg. Experimentally tracking unstable steady states by large periodic modulation. *Phys. Rev. E*, 57:397–401, Jan 1998. 176

[294] Alexander N. Pisarchik, V. N. Chizhevsky, Ram*ó*n Corbal*á*n, and Ramon Vilaseca. Experimental control of nonlinear dynamics by slow parametric modulation. *Phys. Rev. E*, 55:2455–2461, Mar 1997. 176, 210

[295] A.I. Dyachenko and V.E. Zakharov. Modulation instability of stokes wave freak wave. *Journal of Experimental and Theoretical Physics Letters*, 81(6):255–259, 2005. 176

[296] Alfred R Osborne, Miguel Onorato, and Marina Serio. The nonlinear dynamics of rogue waves and holes in deep-water gravity wave trains. *Physics Letters A*, 275(56):386 – 393, 2000. 176

[297] Jordi Zamora-Munt, Bruno Garbin, St*é*phane Barland, Massimo Giudici, Jose R. Rios Leite, Cristina Masoller, and Jorge R. Tredicce. Rogue waves in optically injected lasers: Origin, predictability, and suppression. *Phys. Rev. A*, 87:035802, Mar 2013. 179

[298] A. Einstein. Investigation on the theory of brownian movement. *edited by R. Furth, Dover New York*, Ppapers I and IV, 1956. 212

[299] Deb Shankar Ray. Notes on brownian motion and related phenomena. *ARXIV*, May 1999. 212

Honours, Publications and Conferences

Publications

Journal Papers

- Title: "10-fold detection range increase in quadrant-photodiode position sensing for Photonic Force Microscope"
  Authors: Sandro Perrone, Giovanni Volpe, and Dmitri Petrov
  Journal: Review of Scientific Instruments, 79, 106101, 2008.

- Title: "Stochastic Resonant Damping in a Noisy Monostable System: Theory and Experiment"
  Authors: Giovanni Volpe, Sandro Perrone, J. Miguel Rubí, and Dmitri Petrov
  Journal: Physical Review E, 77, 051107, 2008
  Also featured in Virtual Journal of Biological Physics Research (May 15, 2008).

- Title: "Stochastic logic gate that exploits noise and polarization bistability in an optically injected VCSEL"
  Authirs: Sandro Perrone, Ramon Vilaseca, and Cristina Masoller
  Journal: Optics Express, Vol. 20, Issue 20, pp. 22692-22699 (2012)
  DOI: http://dx.doi.org/10.1364/OE.20.022692

- Title: "Extreme events in a periodically forced laser system"
  Authors: Sandro Perrone, Jordi Zamora-Munt, Ramon Vilaseca and Cristina Masoller
  Journal: In preparation

Conferences and Conference Proceedings

- Title: "Stochastic Resonance vs. Stochastic Resonant Damping: Theory and Experiment"
  Authors: Giovanni Volpe, Sandro Perrone, J. Miguel Rubí, and Dmitri Petrov
  Conference: Stochastic Resonance 1998-2008,
  Place: Perugia (Italy),
  Date: 17-21 August 2008.

- Title:"Maximum in the signal-to-noise ratio in an oscillating potential: an experimental study"

Authors: Sandro Perrone, Giovanni Volpe, J. Miguel Rubí, and Dmitri Petrov
Conference: Stochastic Resonance 1998-2008,
Place: Perugia (Italy),
Date:17-21 August 2008.

- Title: "Experimental Observation of Resonant Damping in a Parametrically-driven Noisy System"
  Authors: Sandro Perrone, Giovanni Volpe, J. Miguel Rubí, and Dmitri Petrov
  Conference: New Frontiers in Micro and Nano Photonics,
  Place: Florence (Italy),
  Date: 23-26 April 2008.

- Title: "All optical implementation of a stochastic logic gate using a VCSEL with external optical injection"
  Authors: Sandro Perrone, Cristina Masoller, Ramon Vilaseca
  Conference: ICTON 2012,
  Place: Warwick, (UK)
  Date: May 2012
  Digital Object Identifier (DOI): 10.1109/ICTON.2012.6253828

- Title: "All optical implementation of a stochastic logic gate using a VCSEL with external optical injection"
  Authors: Sandro Perrone, Cristina Masoller, Ramon Vilaseca
  Workshop: Workshop NDSL12,
  Place: Berlin (Germany),
  Date: September 2012

- Title: "Extreme events in a periodically forced laser system"
  Authors: Sandro Perrone, Jordi Zamora-Munt, Ramon Vilaseca and Cristina Masoller
  Conference: European Conference on Complex Systems - ECCS 2013,
  Place: Barcelona (Spain),
  Date: September 2013

- Title: "Extreme intensity pulses in a semiconductor laser with a short external cavity"

Authors: Jordi Zamora-Munt, Sandro Perrone, José Reinoso, and Cristina Masoller
Workshop: Workshop NDSL13
Place: Berlin (Germany),
Date: October 2013

Reports in Leading Magazines and Newspapers

- NATURE PHYSICS, Volume 4, page 438, "Soft grip", June 2008.
- SCIENCE NEWS, Online edition, "Less is more", May 7, 2008

Membership

- Active council members of the Complex Systems Society (CSS).
(http://css.csregistry.org/)

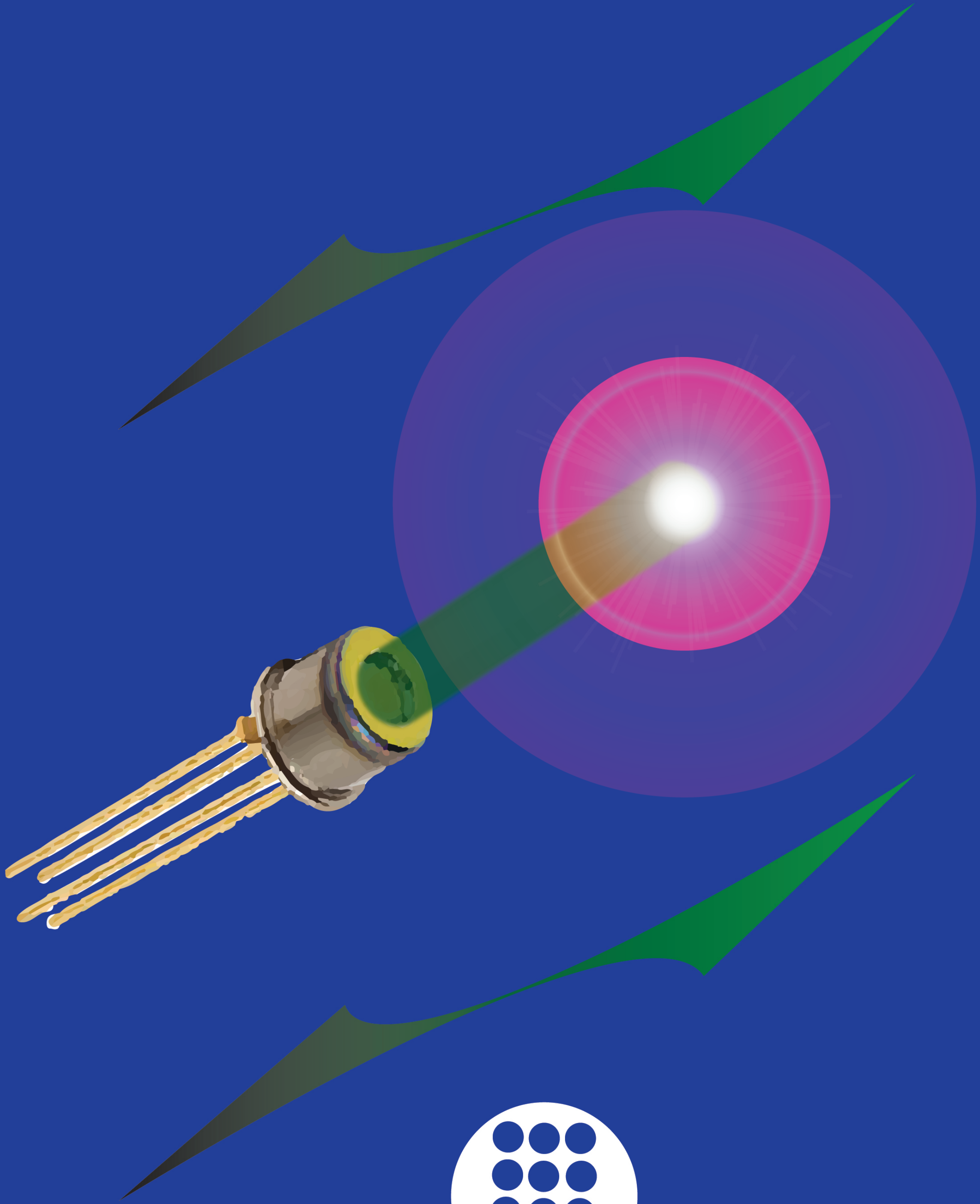

Departament de Fisica i Enginyeria Nuclear

Universitat Politècnica de Catalunya